

J-PAS: The Javalambre-Physics of the Accelerated Universe Astrophysical Survey

N. Benítez^{a,b}, R. Dupke^{b,c,d}, M. Moles^{e,a}, L. Sodré^f, A. J. Cenarro^e, A. Marín-Franch^e, K. Taylor^b, D. Cristóbal^e, A. Fernández-Soto^l, C. Mendes de Oliveira^f, J. Cepa-Nogué^h, L.R. Abramoⁱ, J.S. Alcaniz^b, R. Overzier^b, C. Hernández-Monteagudo^e, E. J. Alfaro^a, A. Kanaan^j, J. M. Carvano^b, R. R. R. Reis^k, E. Martínez González^l, B. Ascaso^a, F. Ballesteros^g, H. S. Xavierⁱ, J. Varela^e, A. Ederoclite^e, H. Vázquez Ramio^f, T. Broadhurstⁿ, E. Cypriano^f, R. Angulo^e, J. M. Diego^l, A. Zandivarez^o, E. Díaz^o, P. Melchior^p, K. Umetsu^q, P. F. Spinelli^r, A. Zitrin^s, D. Coe^{an}, G. Yepes^t, P. Vielva^l, V. Sahni^u, A. Marcos-Caballero^l, F. Shu Kitaura^v, A. L. Maroto^w, M. Masip^{at}, S. Tsujikawa^x, S. Carneiro^y, J. González Nuevo^l, G. C. Carvalho^b, M. J. Rebouças^{av}, J. C. Carvalho^{b,z}, E. Abdallaⁱ, A. Bernui^b, C. Pigozzo^y, E. G. M. Ferreiraⁱ, N. Chandrachani Devi^b, C. A. P. Bengaly Jr.^b, M. Campista^b, A. Amorim^g, N. V. Asari^{aa}, A. Bongiovanni^h, S. Bonoli^e, G. Bruzual^{ab}, N. Cardiel^l, A. Cava^{ac}, R. Cid Fernandes^j, P. Coelho^{ai}, A. Cortesi^f, R. G. Delgado^a, L. Díaz García^e, J. M. R. Espinosa^h, E. Galliano^b, J. I. González-Serrano^l, J. Falcón-Barroso^h, J. Fritz^{ad}, C. Fernandes^b, J. Gorgas^l, C. Hoyos^f, Y. Jiménez-Teja^{ab}, J. A. López-Aguerre^h, C. López-San Juan^e, A. Mateus^j, A. Molino^a, P. Novais^f, A. O'Mill^f, I. Oteo^h, P.G. Pérez-González^l, B. Poggianti^{af}, R. Proctor^b, E. Ricciardelli^g, P. Sánchez-Blázquez^t, T. Storchi-Bergmann^{ag}, E. Telles^b, W. Schoenell^a, I. Trujillo^h, A. Vazdekis^h, K. Viironen^e, S. Daflon^b, T. Aparicio Villegas^{b,a}, D. Rocha^{ah}, T. Ribeiro^{ai}, M. Borges^b, S. L. Martins^{ah}, W. Marcolino^{ah}, D. Martínez-Delgado^{iaj}, M.A. Pérez-Torres^f, B.B. Siffert^k, M.O. Calvão^k, M. Sako^m, R. Kessler^{ak}, A. Álvarez-Candal^b, M. De Prá^b, F. Roig^b, D. Lazzaro^b, J. Gorosábel^a, R. Lopes de Oliveira^{al}, G. B. Lima-Neto^f, J. Irwin^d, J. F. Liu^{aj}, E. Álvarez^t, I. Balmésⁱ, S. Chueca^e, M.V. Costa-Duarteⁱ, A. A. da Costaⁱ, M.L.L. Dantas^f, A. Y. Díaz^e, J. Fabregat^g, F. Ferrari^{ao}, B. Gavela^t, S. G. Gracia^f, N. Gruel^{ae}, J. L. L. Gutiérrez^f, R. Guzmán^{ap}, J. D. Hernández-Fernández^e, D. Herranz^h, L. Hurtado-Gil^q, F. Jablonsky^{au}, R. Laporte^{au}, L.L. Le Tiran^f, J. Licandro^h, M. Limaⁱ, E. Martín^{aq}, V. Martínez^g, J. J. C. Montero^f, P. Penteado^f, C.B. Pereira^b, V. Peris^g, V. Quilis^g, M. Sánchez-Portal^{ar}, A. C. Soja^f, E. Solano^{ao}, J. Torra^{as}, L. Valdivielso^e

^aInstituto de Astrofísica de Andalucía-CSIC, Granada, Spain

^bNational Observatory, Rio de Janeiro, Brazil

^cThe University of Michigan, Ann Arbor, MI, USA

^dThe University of Alabama, Tuscaloosa, AL, USA

^eCentro de Estudios de Física del Cosmos, Teruel, Spain

^fInstituto de Astronomia, Geofísica e Ciências Atmosféricas, Universidade of São Paulo, Brazil

^gUniversitat de Valencia, Spain

^hInstituto de Astrofísica de Canarias, Spain

ⁱInstituto de Física, University of São Paulo, Brazil

^jFederal University of Santa Catarina, Brazil

^kInstituto de Física, Federal University of Rio de Janeiro, Brazil

^lInstituto de Física de Cantabria, Spain

^mUniversity of Pennsylvania, PA, USA

ⁿIkerbasque, Spain

^oUniversidad de Córdoba, Argentina

^pOhio State University, OH

^qAcademia Sinica, Institute of Astronomy and Astrophysics

^rMuseu de Astronomia e Ciências Afins, Brazil

^sCaltech, Pasadena, USA

^tUniversidad Autónoma de Madrid, Spain

^uIUCAA: Inter-University Centre for Astronomy and Astrophysics, India

^vLeibniz-Institut für Astrophysik Potsdam, Germany

^wUniversidad Complutense de Madrid, Spain

^xTokyo University of Science, Japan

^yFederal University of Bahia, Brazil

☆This documents describes J-PAS and outlines its main scientific goals

^zFederal University of Rio Grande do Norte, Brazil
^{aa}LUTH, Observatoire de Paris, CNRS, France
^{ab}Centro de Investigaciones de Astronomía, Venezuela
^{ac}Geneva Observatory, University of Geneva, Switzerland
^{ad}University of Ghent, Belgium
^{ae}University of Sheffield, UK
^{af}Astronomical Observatory of Padova, Italy
^{ag}Federal University of Rio Grande do Sul, Brazil
^{ah}Valongo Observatory, Brazil
^{ai}Southern Astrophysical Research (SOAR) Telescope, Chile
^{aj}Max-Planck-Institut für Astronomie, Germany
^{ak}KICP, University of Chicago, IL
^{al}Federal University of Sergipe, Brazil
^{am}National astronomical Observatory, Chinese academy of Sciences, China
^{an}Space Telescope Science Institute, Baltimore, Maryland
^{ao}Federal University of Rio Grande, Brazil
^{ap}University of Florida, Gainesville, FL, USA
^{aq}Centro de Astrobiología (CAB-INTA-CSIC)
^{ar}Herschel Science Center - ESAC
^{as}Universitat de Barcelona, Spain
^{at}University of Granada, Spain
^{au}Instituto de Pesquisas Espaciais, São José dos Campos, Brazil
^{av}Centro Brasileiro de Pesquisas Físicas, Rio de Janeiro, Brazil

Abstract

The Javalambre-Physics of the Accelerated Universe Astrophysical Survey (J-PAS) is a narrow band, very wide field Cosmological Survey to be carried out from the Javalambre Observatory in Spain with a purpose-built, dedicated 2.5m telescope and a 4.7° camera with 1.2Gpix. Starting in 2015, J-PAS will observe 8500° of Northern Sky and measure 0.003(1+z) precision photometric redshifts for 9×10^7 LRG and ELG galaxies plus several million QSOs, about 50 times more than the largest current spectroscopic survey, sampling an effective volume of $\sim 14 \text{ Gpc}^3$ up to $z = 1.3$. J-PAS will be the first radial BAO experiment to reach Stage IV.

J-PAS will also detect and measure the mass of 7×10^5 galaxy clusters and groups, setting constraints on Dark Energy which rival those obtained from BAO measurements. Thanks to the superb characteristics of the Javalambre site (seeing $\sim 0.7''$), J-PAS is expected to obtain a deep, sub-arcsec image of the northern sky, which combined with its unique photo-z precision will produce one of the most powerful cosmological lensing surveys before the arrival of Euclid. In addition, J-PAS unprecedented spectral time domain information will enable a self-contained SN survey that, without the need for external spectroscopic follow-up, will detect, classify and measure $\sigma_z \sim 0.5\%$ redshifts for ~ 4000 SNIa and ~ 900 core-collapse SNe.

The key to the J-PAS potential is its innovative approach: the combination of 54 145Å filters, placed 100Å apart, and a multi-degree field of view (FOV) is a powerful “redshift machine”, with the survey speed of a 4000 multiplexing low resolution spectrograph, but many times cheaper and much faster to build. Moreover, since the J-PAS camera is equivalent to a very large, 4.7° “IFU”, it will produce a time-resolved, 3D image of the Northern Sky with a very wide range of Astrophysical applications in Galaxy Evolution, the nearby Universe and the study of resolved stellar populations. J-PAS will have a lasting legacy value in many areas of Astrophysics, serving as a fundamental dataset for future Cosmological projects.

Keywords: Dark Energy, Cosmology, SNIa, Large Scale Structure, Baryonic Acoustic Oscillations, Lensing, Dark Matter, Galaxy Evolution, Stars, Solar System, Transients, Telescopes, Instrumentation, Photometric Redshifts

Contents

1	Introduction	7
1.1	<i>Quasi</i> -Spectroscopy: Wide field Narrow Band Imaging as a Redshift Machine	7
2	J-PAS survey description	10
2.1	The filter system	10
2.2	Observing strategy	11
2.2.1	Exposure time and filter distribution	11
2.2.2	Limiting magnitudes	12
2.3	J-PAS Survey Area Definition	19
2.3.1	Area Selection	19
2.3.2	Raw observability from Javalambre	19
2.3.3	Correction by dust column extinction	19
2.3.4	Definition of the survey area	21
2.3.5	Overlap with SDSS and SDSS Stripe 82	23
2.4	Expected performance	25
2.4.1	Inputs for the empirical mocks	25
2.4.2	Empirical mocks	25
3	Scientific Goals I: Cosmology	30
3.1	The J-PAS Redshift Survey	30
3.1.1	Cosmology with galaxy surveys	30
3.1.2	The Fisher matrix approach	32
3.1.3	Baryonic Acoustic Oscillations	34
3.1.4	Forecasts for constraints from BAOs	38
3.1.5	Field reconstructions from the redshift survey	42
3.1.6	Morphology of the Cosmic Web	42
3.1.7	N-body Mocks	43
3.2	The J-PAS Cluster Survey	45
3.2.1	Self-contained mass calibration	48
3.2.2	Figure of Merit	48
3.3	Joint constraints on Dark Energy from BAOs and cluster counts	52
3.4	The J-PAS SN Cosmological Survey	53
3.5	The J-PAS Lensing Survey	56
3.5.1	Cosmic shear	56
3.5.2	Galaxy-galaxy lensing	57
3.5.3	Cluster Weak Lensing	57
3.5.4	Cluster strong lensing	59
3.5.5	Cross-correlation with Herschel	60
3.6	Correlations with the Cosmic Microwave Background Anisotropies (CMB)	61
3.6.1	Integrated Sachs Wolfe effect	61
3.6.2	The thermal history of the Universe	66
3.6.3	Bulk flows, missing baryons and redshift space distortions	66
3.6.4	CMB lensing maps	67
3.7	Alternative Cosmologies and Theories of gravity	67
3.7.1	Quintessence	67
3.7.2	Interaction in the dark sector	68

3.7.3	Unified models of dark matter and dark energy	69
3.7.4	The Lemaître-Tolman-Bondi Models	70
3.7.5	Most general scalar-tensor theories	70
3.7.6	$f(R)$ – Gravity	74
3.7.7	Vector-tensor theories of gravity	75
3.7.8	Higher dimensions and massive gravity	76
3.8	Inflation	77
4	Scientific Goals II: the J-PAS Galaxy Evolution Survey	80
4.1	Measurement Techniques	81
4.1.1	Redshifts and Sample size	81
4.1.2	Stellar Population Modeling and Emission Line Measurements	81
4.1.3	Density Field Construction	90
4.1.4	Morphological measurements	92
4.2	Science Themes	94
4.2.1	Theme I. The Nearby Universe	94
4.2.2	Theme II. Evolution of the Galaxy Population since $z \sim 1$	98
4.2.3	Theme III. The Growth of Large-scale Structure and Environment	101
4.2.4	Theme IV. The High Redshift Universe	105
4.2.5	Theme V. Active Galactic Nuclei	111
4.3	Synergy with other surveys	115
5	Scientific Goals III	124
5.1	Stars and the Galaxy	124
5.1.1	Stellar Populations	124
5.1.2	Additional topics	132
5.2	Stellar Variability	132
5.3	Minor planet science with J-PAS	136
5.3.1	Detection	136
5.3.2	Physical properties: phase parameters	136
5.4	A target of opportunity program for the T80: Responding to GRB alerts provided by <i>Swift</i> and <i>FERMI</i>	137
6	Photometric calibration	139
6.1	Calibrating J-PAS with J-PLUS	142
6.1.1	Description of J-PLUS	142
6.1.2	Calibration of J-PLUS	142
6.1.3	Determination of the atmospheric extinction	143
6.1.4	Stellar spectral fitting	144
6.1.5	Calibration of the J-PAS exposures	145
6.2	Improvements to the J-PAS calibration	145
6.2.1	Ubercalibration	145
6.2.2	Stellar locus and spectro-ubercalibration	146
6.2.3	Photometric redshifts	147

7	Survey Operation	147
7.1	Introduction	147
7.2	Daytime Operation	147
7.2.1	Data Transfer and Analysis	147
7.2.2	Data Validation	147
7.2.3	Night Scheduling	147
7.2.4	OAJ Telescopes' Afternoon Calibrations	148
7.3	Night-time Operation	148
7.3.1	The Weather and the Astronomical Conditions Monitoring	148
7.3.2	The observing queue	148
7.3.3	Observation Execution	148
7.3.4	Data Quick Look	149
7.3.5	The calibration plan	149
7.4	Data Publication	149
8	Data Management	150
8.1	Image Format, Data Rates and Data Volumes	150
8.2	Data Rates	150
8.2.1	Total data volumes	151
8.3	OAJ-UPAD Data Flow	151
8.4	Image processing pipeline	152
8.4.1	Daily pipeline	152
8.4.2	Tile combination	153
8.5	Final products for J-PAS	153
8.6	Photometric pipeline	154
8.7	Storage and Processing Facilities (UPAD)	154
9	The Observatorio Astrofísico de Javalambre	162
9.1	Site and infrastructures	162
9.2	The OAJ Telescopes	163
9.2.1	JST/T250	163
9.2.2	JAST/T80	165
10	The J-PAS Cameras	166
10.1	T80Cam, the wide field camera for the JAST/T80 telescope	166
10.1.1	The Camera System	167
10.1.2	The FSU System	168
10.2	JPCam, the 1.2Gpixel camera for the J-PAS survey	168
10.2.1	The Hexapod Actuator System (HAS)	170
10.2.2	The Filter and Shutter Unit (FSU)	170
10.2.3	The Camera System(Cryocam)	175
11	The J-PAS Collaboration	177
11.1	A Brief History of J-PAS	177
11.2	Organizational structure	178
11.2.1	The Collaboration Board	178
11.3	The Survey Management Committee	178
11.3.1	Scientific Directors	178
11.3.2	Science Working Groups and Science Groups	178

11.4 Authorship Policy	178
11.5 Data Policy	180
12 Acknowledgments	180

1. Introduction

The last decade has seen an accumulation of very large field Astrophysical Surveys (area $> 5000\text{Mpc}^2$). A key factor in this development has been the undoubted success of the Sloan Digital Sky Survey which has spawned significant advances in almost all the fields in Astrophysics. The quest for the origin of Dark Energy has also been a powerful motivator, fostering many of the current projects like Pan-STARRS (Kaiser et al., 2002), DES (DES, 2008), and BOSS (Schlegel et al., 2009), and also being one of the main goals of the very large extragalactic surveys planned to start around the beginning of the next decade LSST (LSST Science Collaboration et al., 2009), Euclid (Refregier et al., 2010) and DESI (Levi et al., 2013).

All these surveys are based on two traditional, one century-old, astronomical methods: broad-band imaging ($R \sim 6$)¹ supplemented by moderate resolution spectroscopy ($R \sim 500$).

Optical broad-band imaging with traditional astronomical filter systems is observationally efficient but yields very limited redshift information, with, typically, $dz/(1+z) \gtrsim 3\%$, see e.g. Hildebrandt et al. (2010) and references therein. Spectroscopy for cosmological purposes provides higher resolution, $dz/(1+z) \sim 0.0005 - 0.001$ but to be competitive requires very high object multiplexing $\gtrsim 1000$, making state-of-the-art spectrographs extremely expensive and very complex to develop. In addition, the information provided by low-resolution, cosmologically-oriented spectroscopy is relatively limited for other purposes, since the spectra are usually low S/N and for efficiency reasons only objects of direct cosmological interest are systematically targeted.

Several projects like COMBO-17 (Wolf et al., 2008), ALHAMBRA (Molino et al., 2014) and COSMOS (Ilbert et al., 2009) have carried out medium band imaging over a few square degrees, hinting at the potential of this approach. These surveys, with $\sim 300\text{\AA}$ medium band filters reach precisions of $dz/(1+z) \approx 0.8\%$ and of 0.6% for the highest quality photo- z . This is already not far from the 0.35% precision required for radial BAO measurements.

Benítez et al. (2009) showed that medium band ($R \sim 20$) and narrow band ($R \sim 60$) filter systems are much more effective, in terms of *photometric redshift* depth, than what a naive extrapolation from pure *photometric* depth would imply. However systematic, multiple-narrow band wide field imaging has not been attempted so far. One objective reason is that until quite recently, it was not possible to build homogeneous filters with a large enough scale. But perhaps the main objection is that NB imaging is quite inefficient for individual objects, since it requires repeated observations to cover a large spectral range; if prompted to consider a NB cosmological survey many would dismiss the idea out of hand (Tversky & Kahneman, 1974). However, as explained below, when NB imaging is combined with a large enough FoV, the result is a redshift machine more powerful than any existing spectrograph.

Moreover, with a system of contiguous $\sim 100\text{\AA}$ -width filters it is possible to reach $\approx 0.3\%$ redshift precisions for enough LRGs to competitively measure the radial Baryonic Acoustic Oscillation (BAO) scale at $z < 1$ (Benítez et al., 2009). J-PAS will observe with an improved version of that system, with the goal of maximizing the effective volume over which we can measure the BAO scale using not only LRGs ($z < 1.1$), but also blue galaxies ($z < 1.35$) and QSOs ($z < 3$), while presenting several features which make the data much more powerful for a wide range of Cosmological and Astrophysical goals.

1.1. Quasi-Spectroscopy: Wide field Narrow Band Imaging as a Redshift Machine

To understand the power of the J-PAS approach, it is instructive to look at the “raw” relative efficiencies of imaging and spectroscopy when observing an object’s SED within a particular wavelength range. Let’s assume that we have a source with a spectral energy distribution flux F_λ , observed against a background B_λ .

¹For imaging, we define the wavelength resolution as $R_\lambda = \lambda/\Delta_\lambda$, where Δ_λ is the filter width. Another alternative definition would be $R_z = (1+z)/\delta_z$, the inverse of the redshift error. This is usually much higher than R for photometric redshifts, for instance, for broadband imaging $R_z \sim 25$, for J-PAS-like Narrow Band(NB) imaging $R_z \sim 333$

The imaging system is defined by an average throughput η_I , a filter width $\Delta\lambda$ and a number of filters n_f . The spectrograph is defined by a throughput η_S . In both cases, we consider a detector with a spatial pixel scale p_s and readout noise σ_{ron} . The full total exposure time is t , divided into n_r individual read outs, and the covered wavelength range is $L = \lambda_{max} - \lambda_{min}$. The central wavelength is thus $\bar{\lambda} = (\lambda_{max} + \lambda_{min})/2$.

For the spectrograph, we have that the signal-to-noise (S/N) reached for a fixed time t , defined as $q_S = (S/N)_S$ is

$$q_S = \frac{\bar{F}L\eta_S t}{\sqrt{\bar{B}L\eta_S t + A_S n_r \sigma_{ron}^2}} \quad (1)$$

where \bar{F} and \bar{B} are, respectively, the average object flux and background flux in the spectral range L and A_S is the number of pixels covered by the object spectrum on the CCD. For a spectral resolution $R = \lambda/\delta_\lambda$, the pixel scale in the wavelength direction will be $p_\lambda \sim \bar{\lambda}/(2R)$, where we assume at least two pixels per resolution element. If we use a slit of spatial scale D , the total number of pixels covered by the spectrum will be $A_S = (L/p_\lambda) \times (D/p_s) \approx 2RD/p_s$ for the typical wavelength range considered here ($L \approx \bar{\lambda}$).

For the imaging case, we are using n_f different filters, and we don't cover the whole spectrum in a single shot, only a section $\Delta\lambda$. Therefore the exposure time for each wavelength segment will be smaller, $t_{exp} = t/n_f$, and $q_I = (S/N)_I$ will be equal to:

$$q_I = \frac{\bar{F}\Delta\lambda\eta_I t}{\sqrt{\bar{B}\Delta\lambda\eta_I t + A_I n_r \sigma_{ron}^2}} \quad (2)$$

Here we assume that $\bar{F}\eta_I \approx \sum(F_i\eta_i)/n_f$ and $\bar{B}\eta_I \approx \sum(B_i\eta_i)/n_f$, where the i values correspond to the individual filters. The total number of pixels covered by the n_f apertures of diameter D is $A_I = n_f \pi (\frac{D}{2p_s})^2$.

Let's examine the limit case in which both spectroscopy and imaging are totally background dominated. Then

$$q_{SB} \approx \frac{\bar{F}}{\sqrt{\bar{B}}} \sqrt{L\eta_S t} \quad (3)$$

and

$$q_{IB} \approx \frac{\bar{F}}{\sqrt{\bar{B}}} \sqrt{\Delta\lambda\eta_I t} \quad (4)$$

Therefore, the relatively S/N ratio of spectroscopy vs. imaging for the background-dominated observation of a single object is

$$\frac{q_{SB}}{q_{IB}} \approx \sqrt{\frac{L\eta_S}{\Delta\lambda\eta_I}} \quad (5)$$

If we take as fiducial values $L = 9100 - 3600 = 5500\text{\AA}$, $\Delta\lambda = 145\text{\AA}$, $\eta_I = 0.7$, $\eta_S = 0.25$, we have $\frac{q_{SB}}{q_{IB}} \approx 3.7^2$. Thus, as most astronomers will say intuitively, spectroscopy is significantly more efficient than NB imaging (as described here) for a single object observation, since it requires 13.5 times longer to reach the same S/N .

The inclusion of readout noise barely changes this result. Let's define, for the imaging case, the ratio r_I between the total readout and background noise

$$r_I^2 = \frac{A_I n_r \sigma_{ron}^2}{\bar{B}\Delta\lambda\eta_I t} \quad (6)$$

Then

$$q_I \approx \frac{\bar{F}}{\sqrt{\bar{B}}} \sqrt{\frac{\Delta\lambda\eta_I t}{1 + r_I^2}} \quad (7)$$

²To make a comparison which focuses on the effects of the filter width, we have not taken into account fiber aperture effects which are not present in imaging, and which in practice would reduce the ratio by a factor of ~ 2 in favor of NB imaging

For the spectroscopic case, since we are assuming the same number of readouts per wavelength segment n_r and the same readout noise σ_{ron} , we can write

$$r_S^2 = \frac{A_S n_r \sigma_{ron}^2}{\bar{B} L \eta_S t} = \frac{A_S \Delta \lambda \eta_I}{A_I L \eta_S} r_I^2 \quad (8)$$

And therefore

$$q_S = \frac{\bar{F}}{\sqrt{\bar{B}}} \sqrt{\frac{L \eta_S t}{1 + \frac{A_S \Delta \lambda \eta_I}{A_I L \eta_S} r_I^2}} \quad (9)$$

For our fiducial values, the ratio $(L \eta_S)/(\Delta \lambda \eta_I) \approx 13.5$. The ratio $A_S/A_I = (8Rp_s)/(n_f \pi D) \approx (R_S/100)$, where we have assumed $D = 2''$, $p_s = 0.4''$ and $n_f = 54$

Therefore we have

$$\frac{q_S}{q_I} = \sqrt{\frac{L \eta_S}{\Delta \lambda \eta_I}} \sqrt{\frac{1 + r_I^2}{1 + 0.07(R_S/100)r_I^2}} \quad (10)$$

In the J-PAS case, assuming $\sigma_{ron} \approx 6e^-$ (as we have done, to be conservative, for all the calculations and mocks presented throughout the paper, although the goal for the camera is $4e^-$), we get $r_I \approx 0.5$. Thus, the inclusion of readout noise for realistic cases does not change things significantly, since the r_I -containing factor on the right goes from 1.10 to 0.85 for resolutions $R_S = 250 - 4000$.

However, the relevant quantity to decide which approach is better as a redshift machine is not the efficiency for an individual object, but the survey speed v , which is defined as the total number of objects which can be observed per unit time, with the same signal-to-noise q .

$$v = \frac{N}{t_q} \quad (11)$$

And thus

$$\frac{v_I}{v_S} \propto \frac{N_I t_S}{N_S t_I} \quad (12)$$

where t_I and t_S are, respectively, the time required for a spectrograph and the imaging system to reach $S/N = q$. Disregarding the readout noise factors, we have $t_I/t_S = (L \eta_S)/(\Delta \lambda \eta_I)$, therefore

$$\frac{v_I}{v_S} \propto \frac{N_I \Delta \lambda \eta_I}{N_S L \eta_S} \quad (13)$$

The most efficient spectrographs, like BOSS (Schlegel et al., 2009), have $N_S \sim 1000$. In the case of NB imaging, the effective ‘‘multiplexing’’ can be extremely large depending on the camera FOV and the density of objects of interest. J-PAS can estimate highly precise photo- z , valid to measure line-of-sight BAOs for $N_I = 52,000$ galaxies in $4.7 \square^\circ$.

Thus, for $\leq 0.3\%$ photo- z , an instrument like the one which will be used by J-PAS is about 4 times faster, in terms of survey speed, than a 1000-x spectrograph, and it is comparable with a 4000-x spectrograph.

$$\frac{v_I}{v_S} \approx 4 \left(\frac{n_g}{11000 \text{ gals}/\square^\circ} \right) \left(\frac{FOV}{4.7 \square^\circ} \right) \left(\frac{1000}{N_S} \right) \quad (14)$$

where n_g is the galaxy density per square degree and FOV is the Field of view of the camera in square degrees.

We have endeavored to compare both imaging and spectroscopic techniques in a numerically balanced way, however, there are several ‘‘hidden variables’’ favoring imaging techniques which are more difficult to quantify but are nevertheless important to be aware of. We list some of these here:

1. Selection effects in spectroscopy: The necessity of object pre-selection for multi-object spectrographs introduces many unintended biases to a spectroscopic survey. These include effects due to morphology, magnitude and surface density limits all of which have effects on completeness and window function uncertainties which are largely eliminated in an imaging survey.

2. Astrometry: Astrometric errors which can be induced by systematic epoch effects and proper motion uncertainties may lead to small position errors which critically impact aperture coupling efficiencies. Uniform magnitude selection: Spectroscopic optimization of detector real estate requires selection of objects of uniform brightness which can introduce further selection biases.

3. Sky subtraction: Object multiplex has always to be traded with sampling of the sky both for multi-fibre and multi-slit spectroscopy. Sky subtraction for imaging, if done carefully, is generally a much more robust technique which minimally impacts both stochastic and systematic errors.

4. Acceptance aperture: Spectroscopic apertures are always limited by the design of the spectrograph and cannot generally be optimized for particular atmospheric conditions. The size of the instrument scales linearly with aperture; the cost is a much steeper function. There is thus always a strong driver for limiting the size of the aperture which is especially demanding for large telescope spectrographs. For point sources this simply means reduced aperture coupling ratios which are determined by variable seeing conditions, while for marginally resolved sources this leads to incomplete sampling of the intrinsic morphology.

6. Atmospheric dispersion and differential atmospheric refraction: These effects can strongly perturb spectroscopic efficiency as a function of wavelength thus producing errors in the observed source SEDs which are very difficult to impossible to calibrate out.

7. Fibre effects: Spectrograph efficiencies are a function of fibre properties such as throughput, focal ratio degradation and non-telecentric feeds. The first two effects can be a function of fibre placement and telescope orientation (and consequently time) and are very difficult to quantify. Non-telecentric feeds can be well determined but inevitably lead to reductions in efficiency. Many large telescope fibre systems also require multi-fibre connectors which again impact efficiency; it is indeed a fact that very few instrumentation papers actually quote the overall fibre spectrograph efficiency as measured on the sky.

Of course there are negatives for multi-band imaging surveys the most prominent of which is the fact that different wavelength samples are taken sequentially which introduce variable efficiencies and PSFs. However, this information can be recovered from the data itself with carefully monitoring of the photometric conditions and by tying the photometry to an all-sky photometric calibration survey, supplied in the case of J-PAS by the T80 telescope. Another limitation is in the effective spectral resolution given by wave-band limitations. However a concerted effort has been made to optimize the band-pass of the J-PAS survey through exhaustive S/N modeling; it is incidental but fortunate that this optimization has led to band-passes which are obtainable through a standard interference filter fabrication processes.

But perhaps the main advantage of NB imaging lies in the relative simplicity and low cost (about an order of magnitude lower) of the required instrumentation, specially when compared with a spectrograph with several thousand multiplexing.

2. J-PAS survey description

2.1. The filter system

As it was shown by Benítez et al. (2009), a contiguous set of filters spaced by $\sim 100\text{\AA}$ width is able to produce photometric redshifts with a precision of $0.003(1+z)$ for Luminous Red Galaxies. The original and main scientific goal of PAU-Consolider project, the origin of J-PAS, was measuring the radial scale of the Baryonic Acoustic Oscillations using these LRG population. However, the photo- z for Blue Galaxies are also precise enough to use them as BAO probes, significantly increasing the effective volume of the survey. QSOs can also be detected and their redshifts measured with excellent precision (Abramo et al., 2012). The J-PAS filter system and observing strategy has also been carefully optimized to maximize the returns of the survey in

other areas of Astrophysics without compromising the main goal of constraining the Dark Energy equation of state.

These are the main modifications we have introduced with respect to the filter system of Benítez et al. (2009):

1. The extension of the NB observations blue-wards to 3785\AA : this will enable a detailed and unique study of the galaxy properties in the local Universe, and the central wavelengths of the filters (and therefore of the whole system) have been chosen accordingly. It also improves slightly the photo- z precision of the higher redshift galaxy population.

2. Extension of the NB filter range to 9100\AA . This increases significantly the effective volume covered by the Survey by extending the redshift range at which we are able to measure photo- z for both LRG and ELGs. Going much further to the red becomes inefficient because of the fast increase with wavelength of the sky background.

3. To avoid duplications, our total number of filters has to be a multiple of 14, the number of CCDs in our camera. Putting together all the above considerations we arrive to 56 main filters, 54 of them NB, 1 medium-band (which covers the UV edge) and 1 broad band (which covers the interval red-wards of 9100\AA), with the NB filters spaced by 100\AA . Our simulations (Benítez et al., in preparation) show that photo- z precision and depth are more sensitive to the filter spacing than to the filter width (provided it is narrow enough). The width of our filters is set to 145\AA , the minimum width required by the manufacturer, to ensure filter homogeneity across our field of view. The resulting filter system is shown in Figure 1.

In addition, we include three regular broad band filters in our observations, u , g and r . The first filter has a redder cutoff than the SDSS u band, the other two are similar to the ones used in that survey. These BB observations will be quite deep compared to the NB imaging (5σ limiting magnitude in a $3''$ aperture of 23.1, 23.7 and ≈ 24 respectively). The r -band plays a special role, because it will be the main filter used for detection and weak lensing measurements. The BB filters are all contained in a single tray, and will be used only when the image quality is in the top 10% of the observatory range. Given the superb seeing at the Javalambre site, and the exquisite care being taken to make sure that neither dome nor camera significantly degrade it, we expect to get a deep $< 0.8''$ imaging of $\sim 8500\text{deg}^2$ of the Northern Sky which will be extremely useful for lensing analyses.

2.2. Observing strategy

2.2.1. Exposure time and filter distribution

Despite the use of drift scan by previous surveys, as SDSS, we have decided to use a traditional “point and shoot” mosaicking strategy. We found that drift scan is only marginally more efficient (once all the factors, as overlaps, etc. are taken into account) and therefore does not warrant the extremely strict—and therefore risky—technical requirements it imposes on both camera and telescope design. The simpler imaging strategy we have adopted gives us more flexibility in the observing strategy and makes possible to re-use the reduction software of other surveys like ALHAMBRA, which was mostly developed by members of the J-PAS collaboration (Molino et al, 2014; Cristóbal-Hornillos et al., 2009).

We are using a 14 CCD, 4.7deg^2 camera, and 56+3 filters. It is not currently possible to build a NB filter of the required width and homogeneity over the whole 4.7deg^2 ; even covering all the CCDs simultaneously with copies of the same individual filter, would require us to purchase 826 filters, surpassing the full cost of the camera. We therefore employ a single copy of the main 56 filter system, spreading them into 4 different trays (T1-4), each with 14 different filters. An additional broad band filter tray (T5) contains 8 r -band filters, 3 g -band filters and 3 u -band filters. Within the NB trays, T1-4, the filters are distributed as contiguously as possible in wavelength, although some scrambling among trays is needed to minimize the presence of image ghosts due to reflections. Tables 3., 4. and 5. list the filters, indicating which trays they belong to. Since the filters will be distributed parallel to each other, is quite straightforward to cover the whole observing area homogeneously

with all of them. It is sufficient to follow a pattern which tiles the full J-PAS sky with the CCD having the smallest effective area: that ensures that all the filters in each tray will also tile the sky with no gaps.

Our basic exposure is 60 seconds, and we will carry out at least 4 exposures in each filter, following a $2 + 1 + 1$ pattern whenever is possible, i.e. taking initially 2 almost simultaneous exposures, and then leaving an interval of a month before the third and approximately 20 days between the 3rd and 4th exposures. This is close to the optimum strategy for SNeI detection, giving J-PAS the opportunity of carrying out one of the most powerful ground-based SN surveys. For the filters in the 4th, and reddest tray, we will repeat the 4x60 observations. The u , g and r filters, which will be included in a 5th tray will be exposed by, respectively 225, 225 and 600 seconds, using 6, 6 and 16 exposures.

The total effective exposure time on any point of the sky will therefore be $1050s$ (the BB tray) + $56 \times 240s$ (one pass with all the 56 filters in T1-4) + 14×240 (the 2nd pass with T4) = $4.96h$. Since the J-PAS main camera has 4.7° , the survey speed is, therefore, $\sim 1^\circ h^{-1}$, and it will require ~ 9000 h on target to complete the full survey.

Of course, the total observing time will be higher when we include predictable overheads:

- *Readout time* We will take a total of $56 \times 4 + 14 \times 4 + 6 + 6 + 16 = 308$ exposures, which for a estimated readout time of $11s$, are equivalent to $3388s$ or $0.94h$.
- *Overlap* Our observations will overlap about 5%, to ensure an homogeneous photometric calibration across different pointings.
- *Visibility* Due to the inconvenient (from the point of view of Extragalactic Astronomy) presence of most of the Milky Way in the Northern Hemisphere, we will need an additional 10% of survey time, which will be used to repeatedly observe some areas in the sky (creating a J-PAS deep field in an area almost coincident with Stripe 82).

Therefore, combining all these effects, we would actually need a factor of $1.19 \times 1.05 \times 1.10 = 1.38$ more on-target time, or about $12400h$ of observations.

Taking into account the experience of similar observatories we conservatively expect to be able to observe on-target effectively for at least 1800 h/yr (this is equivalent to $\sim 48\%$ useful time, similar to the values at e.g. Calar Alto). Therefore, the full completion of J-PAS will require 6.88 yrs. The expected initial date for the survey is mid-2015, so the full survey will finish in 2021, around the start of other Stage IV projects like Euclid, LSST or DESI. As we will see below, the observing strategy of J-PAS is designed in such a way that it will obtain highly competitive cosmological constraints from its 2nd-3rd year of operation.

2.2.2. Limiting magnitudes

To generate mock observations we have written a python Exposure Time Calculator which is included in the BPZ 2.0 python distribution (Benítez 2014) As usual, it generates the expected S/N given a certain observational set-up and object magnitude. It takes as inputs the expected full filter transmission curve (assumed to take into account the CCD, optics and the atmosphere at the desired airmass), the pixel size, mirror area, sky background, total exposure and the number of readouts and the readout noise. Given an object area and magnitude, it calculates all the relevant parameters as the sky and readout noise within the aperture, S/N , etc. Included in the calculation is a further degradation of the theoretical results by factor of $0.1 - 0.25$, as measured empirically when working with real instruments (as the one used in the ING ETC <http://catserver.ing.iac.es/signal/>). Table 1 lists the global parameters used to generate the mock observations. Our NB imaging will be binned by a 2×2 factor into effective $(0.456'')$ ² pixels and we assume a readout noise of $6e^-$ for our mocks, despite the fact that the purported goal for JPCam is $4e^-$.

A crucial factor in the ETC is a realistic estimation of the sky background. The sky at the OAJ site at the Pico del Buitre was directly measured in 2009, during the last solar cycle minimum, and it is extremely

Table 1: ETC global parameters used for the synthetic observations

Mirror area	3.89m ²
Readout noise	6e ⁻
Min. Number of exposures	4
Binned pixel size	0.456 ² □''
Aperture area	7.07□''

Table 2: Assumed sky background per □'' for the mocks presented here, calculated by averaging over the solar (2015.5-2021) and moon cycles (26 darkest nights) and assuming an airmass of 1.2. For reference we have included the zenith measurements of the OAJ dark sky background at the solar minimum (Moles et al., 2010), without any correction for airmass. The magnitudes are Vega-based.

Band	<i>m_{mock}</i>	<i>m_{dark}</i>
U	20.82	
B	21.43	22.8
V	21.14	22.1
R	20.47	21.5
I	19.24	20.4

dark (Moles et al., 2010), clearly comparable (at similar altitudes) with other superb sites as Mauna Kea or La Silla. However since the former measurements only sample a small part of the solar cycle, we estimate the sky brightness for our mock observations using the Mauna Kea 2500m results of Krisciunas (1997), which cover a full solar cycle and are comparable to the OAJ measurements at solar minimum. We take the average of the 1992-1996 years, which approximately correspond to the same part of the solar cycle as the future 2015-2021 J-PAS observations; this is quite conservative because there is evidence that the current solar cycle will be much milder than the previous one (<http://solarscience.msfc.nasa.gov/SunspotCycle.shtml>). Since Krisciunas et al. (1997) only provide measurements for the B and V bands, we calculate the expected colors in other bands by using the average dark sky color of all the observatories listed in Patat et al. (2003). In addition we brightened the sky by 0.12 mags to take into account that we assume that the average airmass will be 1.2.

To account for the moon phase, we use Walker (1987) and calculate the proper average for each band within the 26 darkest nights in the moon cycle (the brightest two nights will be devoted to other projects). The resulting average sky brightness per broad band filter is listed in Table 2. We then use the sky spectrum of Puxley et al. (<http://www.gemini.edu>) and normalize it to the required value in each band. The normalized sky spectrum is plotted in Figure 2, together with the published measurements of Javalambre dark sky at the zenith. Note that this differs, in the sense of being much more conservative, from the sky spectrum in Benítez et al. (2009), where it was assumed that the timing of each filter observation would be adapted to the moon phase in an optimal way.

We have tested our ETC with the observations of Taniguchi et al. (2007), which are described in enough detail to simulate accurately and provide empirical *S/N* measurements. We find the agreement excellent, with an average offset of 0.04 and a scatter of 0.2.

The final limiting magnitudes and exposure times are plotted in Fig. 3 and listed in Tables 3., 4. and 5.

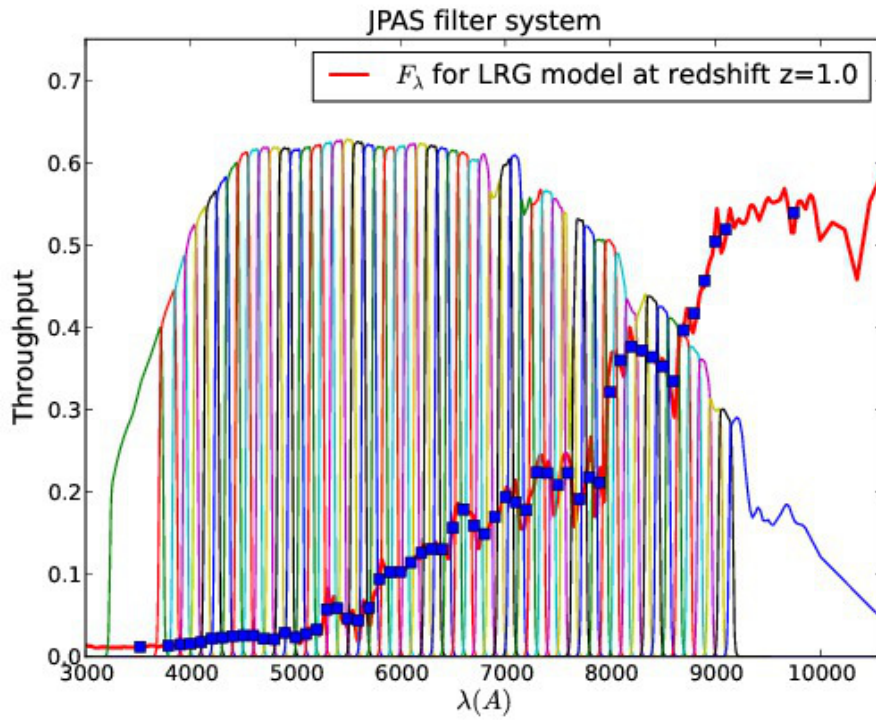


Figure 1: The J-PAS filter system. We have included the redshifted spectrum of an early type galaxy at $z=1.0$ from Polleta et al. 2007. The filters are spaced by about 100 \AA but have FWHM of 145 \AA , what produces a significant overlap among them. The blue squares represent the flux which would be observed through the filters. Note that many spectral features apart from the 4000 \AA break are resolved, that is why the precision in redshift is much larger than that which would be produced by a single break, $\Delta z/(1+z) \sim \Delta\lambda/\lambda \sim 0.02$

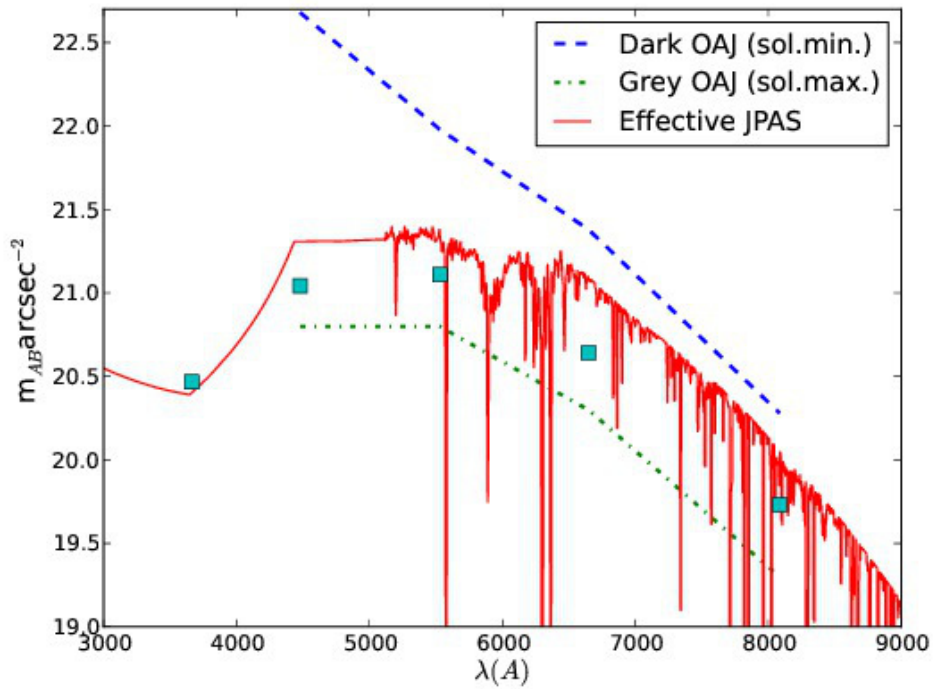


Figure 2: Sky background used to generate our mocks, calculated averaging over the solar (2015.5-2021) and moon cycles (26 darkest nights) for a 1.2 airmass. For reference we include the airmass-corrected measurement of the sky background at the OAJ (dashed line) and the sky that our model would predict at 7 nights from the dark moon at the solar maximum (dash-dot line)

Filter	λ_c	FWHM(\AA)	$m_{AB}^{5\sigma}(3''\text{D})$	$m_{AB}^{5\sigma}(/ \square'')$	$t_{exp}(s)$	Tray
J-PAS3785	3791	158	22.20	23.26	240	T1
J-PAS3900	3904	141	22.23	23.29	240	T1
J-PAS4000	4003	141	22.30	23.36	240	T1
J-PAS4100	4102	142	22.35	23.41	240	T2
J-PAS4200	4202	142	22.37	23.43	240	T2
J-PAS4300	4302	142	22.37	23.44	240	T2
J-PAS4400	4402	142	22.38	23.44	240	T2
J-PAS4500	4501	142	22.39	23.45	240	T1
J-PAS4600	4601	143	22.39	23.45	240	T1
J-PAS4700	4701	143	22.40	23.46	240	T1
J-PAS4800	4801	143	22.39	23.45	240	T1
J-PAS4900	4901	143	22.40	23.46	240	T1
J-PAS5000	5001	143	22.39	23.45	240	T1
J-PAS5100	5101	143	22.39	23.45	240	T1
J-PAS5200	5201	143	22.37	23.44	240	T1
J-PAS5300	5301	143	22.38	23.44	240	T1
J-PAS5400	5401	143	22.39	23.45	240	T1
J-PAS5500	5501	143	22.28	23.35	240	T2
J-PAS5600	5601	143	22.14	23.20	240	T2
J-PAS5700	5701	143	22.36	23.42	240	T2
J-PAS5800	5801	143	22.34	23.40	240	T2
J-PAS5900	5901	143	22.23	23.29	240	T3
J-PAS6000	6001	143	22.33	23.39	240	T3
J-PAS6100	6101	143	22.37	23.44	240	T3
J-PAS6200	6201	143	22.31	23.37	240	T3
J-PAS6300	6301	143	22.20	23.26	480	T4
J-PAS6400	6401	143	22.54	23.60	480	T4
J-PAS6500	6501	143	22.74	23.80	480	T4
J-PAS6600	6601	143	22.73	23.80	480	T4
J-PAS6700	6701	143	22.32	23.38	240	T2
J-PAS6800	6800	142	22.25	23.31	240	T2
J-PAS6900	6901	143	22.18	23.24	240	T2
J-PAS7000	7002	142	22.21	23.27	240	T2
J-PAS7100	7100	141	22.19	23.25	240	T2
J-PAS7200	7200	144	22.11	23.17	240	T2
J-PAS7300	7301	143	22.00	23.06	240	T3
J-PAS7400	7401	143	21.98	23.05	240	T3
J-PAS7500	7500	143	21.95	23.02	240	T3
J-PAS7600	7596	142	21.78	22.84	240	T3
J-PAS7700	7705	136	21.76	22.82	240	T3
J-PAS7800	7800	143	21.65	22.71	240	T3
J-PAS7900	7901	143	21.64	22.70	240	T3
J-PAS8000	8000	143	21.62	22.68	240	T3

Table 3: J-PAS Narrow Band observations. The central wavelengths λ_c and filter widths (FWHM) have been calculated taking into account the expected CCD Quantum Efficiency and the Javalambre expected atmosphere at 1.2 airmasses. We also list the $5 - \sigma$ detection magnitudes in a $3''$ diameter aperture and per \square'' .

Filter	λ_C	FWHM(\AA)	$\mathbf{m}_{AB}^{5\sigma}(3''\mathcal{D})$	$\mathbf{m}_{AB}^{5\sigma}(/ \square'')$	$t_{exp}(s)$	Tray
J-PAS8100	8099	142	21.62	22.68	240	T3
J-PAS8200	8200	143	21.55	22.61	240	T3
J-PAS8300	8302	142	21.77	22.83	480	T4
J-PAS8400	8400	143	21.85	22.91	480	T4
J-PAS8500	8500	143	21.82	22.89	480	T4
J-PAS8600	8600	143	21.68	22.74	480	T4
J-PAS8700	8700	143	21.58	22.64	480	T4
J-PAS8800	8800	143	21.36	22.42	480	T4
J-PAS8900	8898	141	21.36	22.42	480	T4
J-PAS9000	8999	143	21.34	22.41	480	T4
J-PAS9100	9100	142	21.22	22.28	480	T4

Table 4: J-PAS Narrow Band observations. The central wavelengths λ_c and filter widths (FWHM) have been calculated taking into account the expected CCD Quantum Efficiency and the Javalambre expected atmosphere at 1.2 airmasses. We also list the $5 - \sigma$ detection magnitudes in a $3''$ diameter aperture and per \square'' .

Filter	λ_C	FWHM(\AA)	$\mathbf{m}_{AB}^{5\sigma}(3''\mathcal{D})$	$\mathbf{m}_{AB}^{5\sigma}(/ \square'')$	$t_{exp}(s)$	Tray
J-PAS3518	3596	261	22.66	23.73	240	T1
u_{J-PAS}	3856	357	23.10	24.16	225	T5
g_{J-PAS}	4931	1441	23.75	24.81	225	T5
r_{J-PAS}	6301	1189	23.93	24.99	600	T5
J-PAS10069	9505	618	21.51	22.57	480	T4

Table 5: J-PAS Medium and Broad band observations. The central wavelengths λ_c and filter widths (FWHM) have been calculated taking into account the expected E2V CCD Quantum Efficiency and the Javalambre expected atmosphere at 1.2 airmasses. We also list the $5 - \sigma$ detection magnitudes in a $3''$ diameter aperture and per \square''^2 .

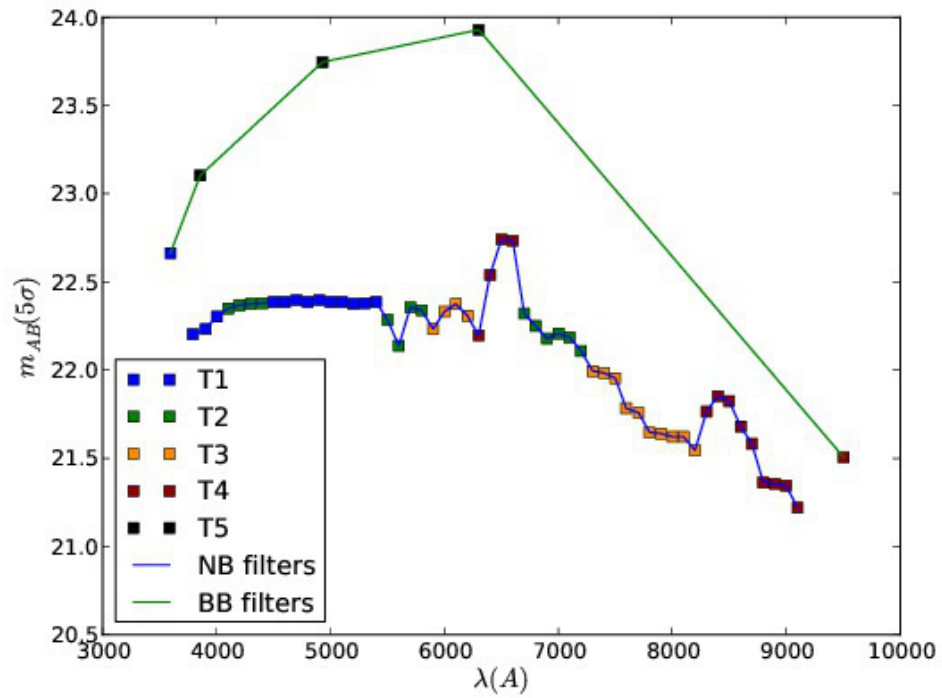


Figure 3: Limiting AB magnitudes (5σ , 3 arcsec aperture) for all the filters in the survey, color coded by their tray distribution

2.3. J-PAS Survey Area Definition

2.3.1. Area Selection

In this Section we describe the selection process for the area that will be covered by J-PAS. The survey definition based on the scientific objectives has fixed a minimum area of $8,000\text{ deg}^2$, selected on the basic criterion of low galactic extinction. Earlier discussions remarked on the necessity of dividing this area between the Northern and Southern galactic hemispheres, in order to share in an approximately homogeneous manner the area to be observed along the year—or, equivalently, along the different right ascensions. It is also necessary to ensure the compactness of the survey area, in order to optimize the exposure time.

2.3.2. Raw observability from Javalambre

The obvious first point that must be taken into account when selecting the sky area for J-PAS is that the area must be observable from the Javalambre Observatory site (OAJ), for a period of time as long as possible over a natural year. We have measured the total observability for each point in the celestial sphere, defined as the number of night hours³ when a given point is higher than 40° above the horizon, as seen from OAJ, in a year. The top panel in Figure 4 shows that information. We have also eliminated (as non-observable) two nights before and after each full Moon and a cone of 30° around the Moon in grey nights⁴. This induces a slight decrease in observability around the ecliptic.

Within these conditions, we see that the area that lies approximately at $\delta > 40^\circ$ is observable for more than 1000 hours per year (dark blue area in Figure 1), and everything at $\delta > 10^\circ$ is observable at least for 300 hours per year (cyan area).

2.3.3. Correction by dust column extinction

In principle one could use an *a priori* value of the galactic latitude to define a zone of avoidance in the survey, which has indeed been the method of choice in other surveys. However, because we want to define a large area and the best partition of it in the Northern and Southern galactic hemispheres (NGH and SGH), we decided to use a slightly more sophisticated approach. We have used the DIRBE dust maps published by Schlegel, Finkbeiner & Davies (1998) to estimate the dust extinction in each direction. The central panel in Figure 1 shows this map, in terms of the values of $E(B-V)$.

In order to combine the observability and the dust content in each direction we have defined a corrected observability. For each direction we calculate the extinction at 3800 Angstroms using the standard Milky Way extinction law and the value of $E(B-V)$ given by Schlegel et al. (1998), and estimate the increase in exposure time that would be necessary to reach the nominal depth at 3800 Angstroms taking that extinction into account. We then correct the available time according to that factor, which yields a smaller number of hours of observability in each direction. We must remark several things here. First, this is only a crude approximation, as we have used a very low-resolution dust map and a simple formula for the exposure times. Second, even if the corrections were accurate, they would only apply to the bluest filters in the J-PAS set, and we have applied them to correct all the exposure times. And finally, the use of this corrected visibility *does not mean that we will be correcting the exposure times in the survey*—it is only a convenient way to put together the information about visibility and dust.

Taking into account all of these caveats, the map showing the corrected visibility is shown in the bottom panel of Figure 1. As expected, we see the original visibility modulated by the presence of the Milky Way. It is important to point out that there is a relatively large area with visibility > 300 hours/year in the SGH.

The same data can also be represented in equatorial coordinates, both cartesian and projected, as shown in Figure 5.

³We define night time using the strict astronomical definition, i.e. time between astronomical twilights.

⁴Five nights around new Moon are considered dark, the above mentioned two nights around full Moon are completely eliminated, and the rest are considered grey.

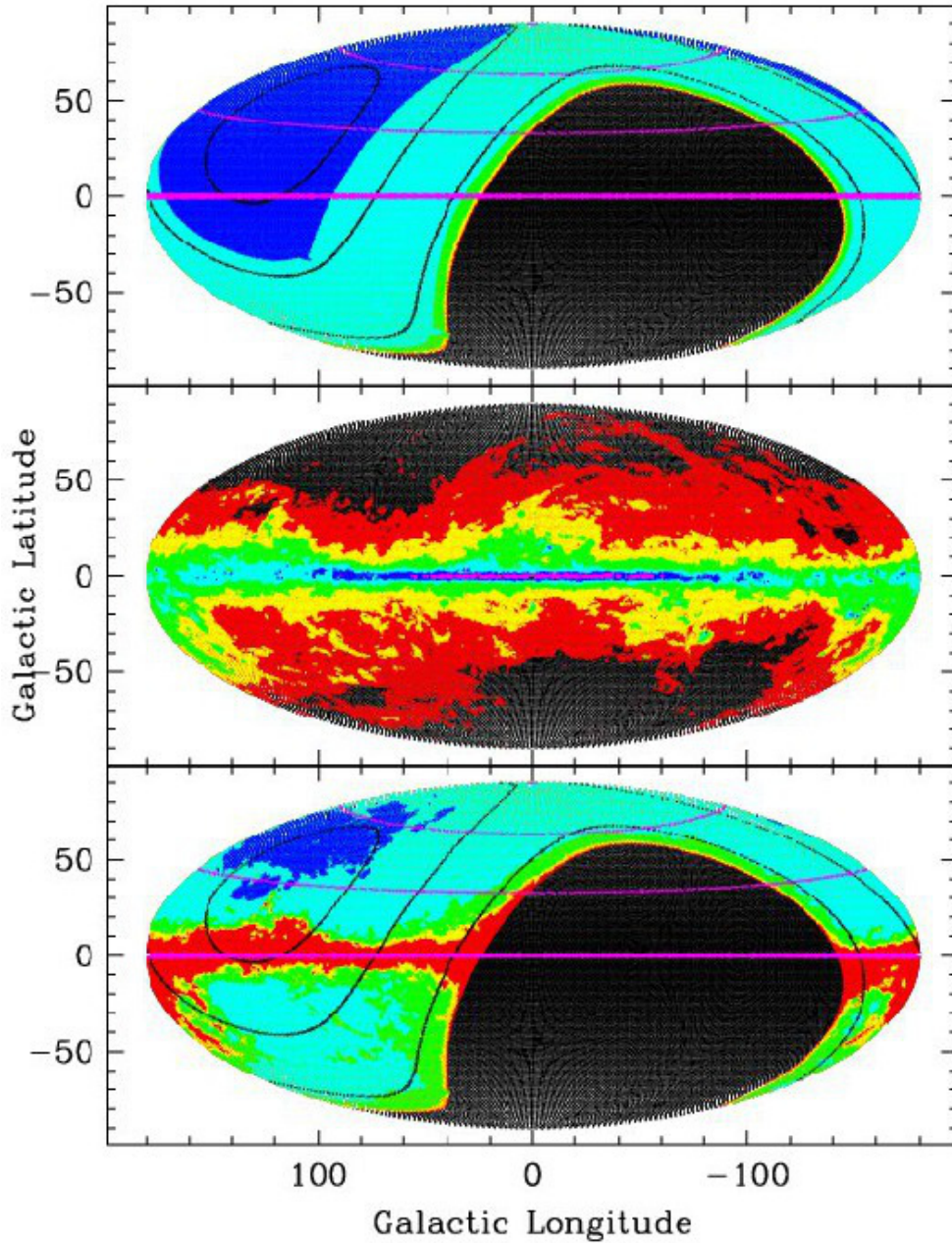


Figure 4: (Top) Visibility from OAJ. (Red, yellow, green, cyan, blue) correspond to visibilities greater than (0, 30, 100, 300, 1000) hours/year. Magenta lines represent galactic latitudes $b = (0^\circ, 30^\circ, 60^\circ)$, and black lines represent declinations $\delta = (0^\circ, 30^\circ, 60^\circ)$. (Middle) Dust column in each direction, as measured by Schlegel et al. (1998). The color scale (black, red, yellow, green, cyan, blue, magenta) corresponds to values of $E(B-V) > (0.00, 0.03, 0.10, 0.30, 1.00, 3.00, 10.00)$. (Bottom) Corrected visibility as described in the text. All colors and lines are the same as in the top panel.

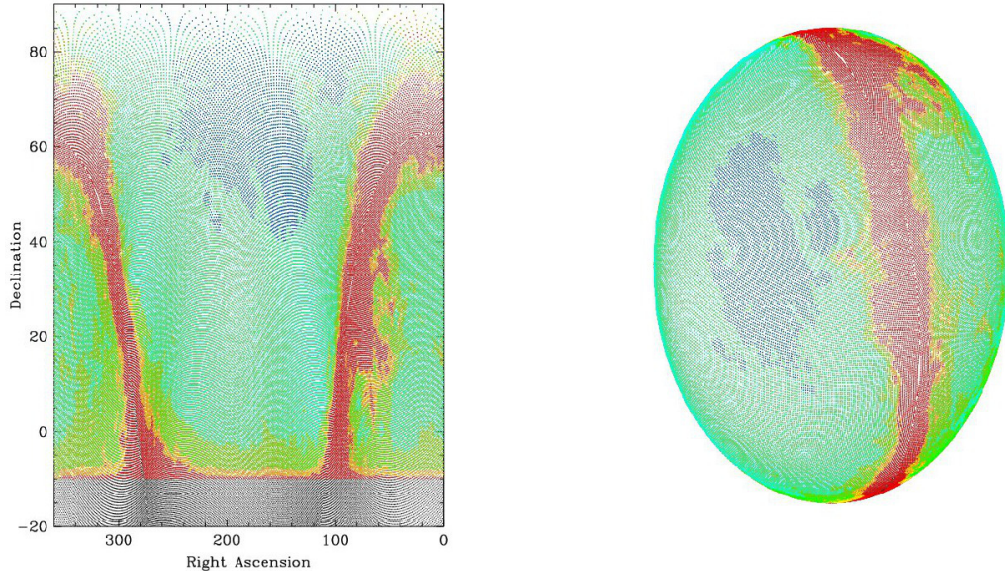


Figure 5: (Left) Corrected visibility plotted using equatorial coordinates. Colors are the same as those in Figure 4. (Right) Corrected visibility projected for the northern celestial hemisphere. Notice that this projection does not show the area below $\delta = 0^\circ$.

2.3.4. Definition of the survey area

Once both the information about visibility and dust are combined, it should not be complicated to select the area to be covered by the survey. In a first approximation, we could simply choose those areas with the highest value of corrected observability. In order to do this, and using this criterion, we choose the best (6000, 12000, 18000) square degrees in the sky and plot them in Figure 6 (left) as the (respectively) green, yellow, and red areas. One problem with this approach is that, by far, most of the best area is necessarily in the NGH, because of the much higher observability from OAJ. Choosing this area without any correction would lead us to a problem during autumn, when only a relatively small area of the NGH is visible, and we may find ourselves without any observable, but not already covered area. This is a well-known issue and, as shown in the left panel of Figure 6, we need to take it into account unless we want to end up with a survey that only covers the NGH.

In order to avoid this, we take a different approach. We define the best areas independently for the NGH and SGH, taking the best (3000, 6000, 9000) square degrees from the former, and the best (1000, 2000, 3000) square degrees from the latter. We use these figures because we have from the beginning devised an approximate partition of $6000 + 2000 \square^\circ$ as a reasonable compromise. The result of this exercise is shown in Figure 7 (left). We also show the distribution of those areas in terms of right ascension, to give an indication of the best month when each area can be observed. As a result of those tests, we can see that the transitions between NGH and SGH around June and December are less populated in terms of available area, but this should not pose a serious problem, and may be alleviated with an adequate choice of a deep field.

A possible, perhaps simpler, alternative approach would be to avoid combining both sky quality indicators (visibility and dust column) and just define some limits in each of them. One could, e.g., take the best $8000 \square^\circ$ in terms of lowest $E(B - V)$ within some well-defined visibility limit to ensure the feasibility of the observations, for example, areas of the sky with visibility > 200 hours. We have repeated all the tests previously described with this criterion, and the result is less satisfactory in terms of the final sample. In particular, when this method is used, the area chosen moves away from the Galaxy in both hemispheres (as it is unmodulated by the visibility), in such a way that the transition from NGH to SGH and back is extremely abrupt, leaving almost no observable area in between.

We have thus decided to use the corrected visibility, together with the separation in terms of a northern and

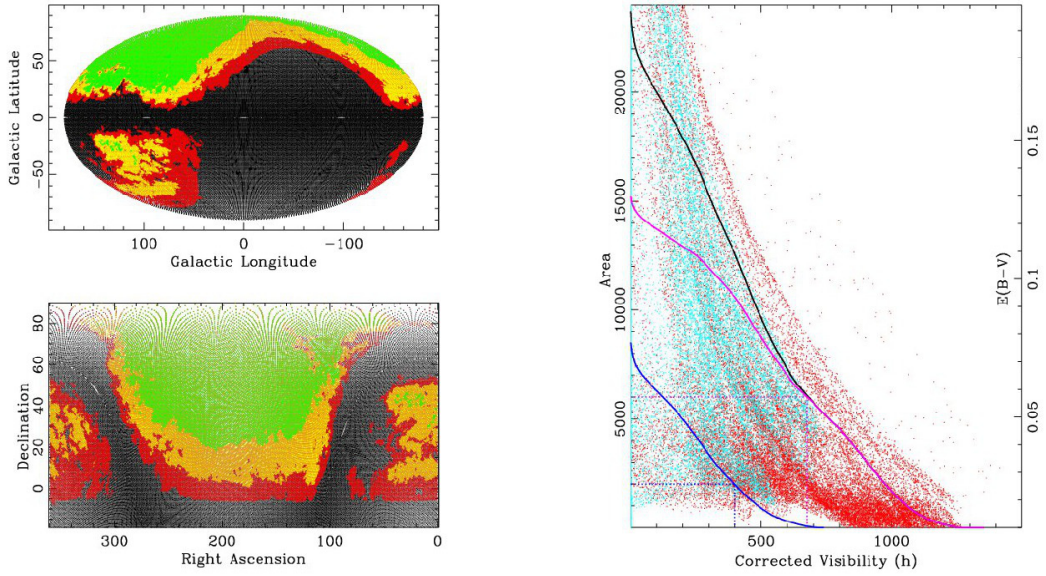


Figure 6: (Left) Sky areas with highest corrected visibilities. The (6000, 12000, 18000) square degrees with highest corrected visibilities are plotted as (green, yellow, red) areas. (Right) Cumulative plot of total area vs corrected visibility (black line), NGH-only (magenta line and red points) and SGH-only (blue line and cyan points). Dots correspond to values of $E(B-V)$ (see right side axis) for each different direction. For the best 6000sq° in the NGH the visibility is >675 hours/year, and >400 hours/year for the best 2000sq° in the SGH.

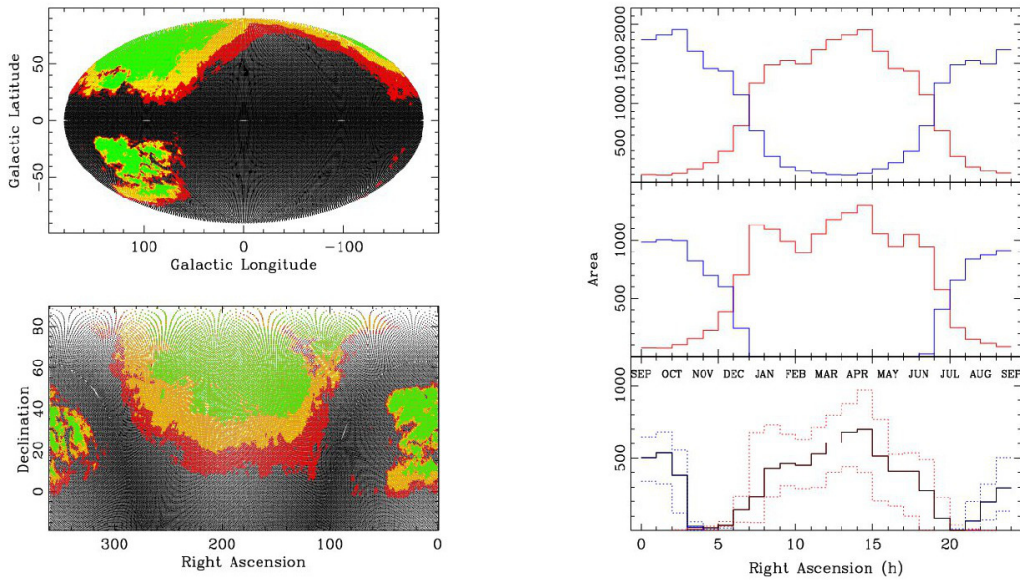


Figure 7: Sky areas with highest corrected visibilities, when chosen independently in both galactic hemispheres. The best (3000, 6000, 9000) square degrees are plotted as (green, yellow, red) areas in the NGH, and the best (1000, 2000, 3000) square degrees correspond to the same in the SGH. (Right) Histogram of sky area (red NGH, blue SGH) vs Right Ascension (in hours) for different samples: whole-sky in the top panel, corrected visibility > 0 h in the middle panel, and the three selected areas seen in the left, with the continuous lines corresponding to (6000 + 2000) square degrees, and the dotted lines corresponding to the other two cases. The optimal month for each RA is indicated in the lower panel.

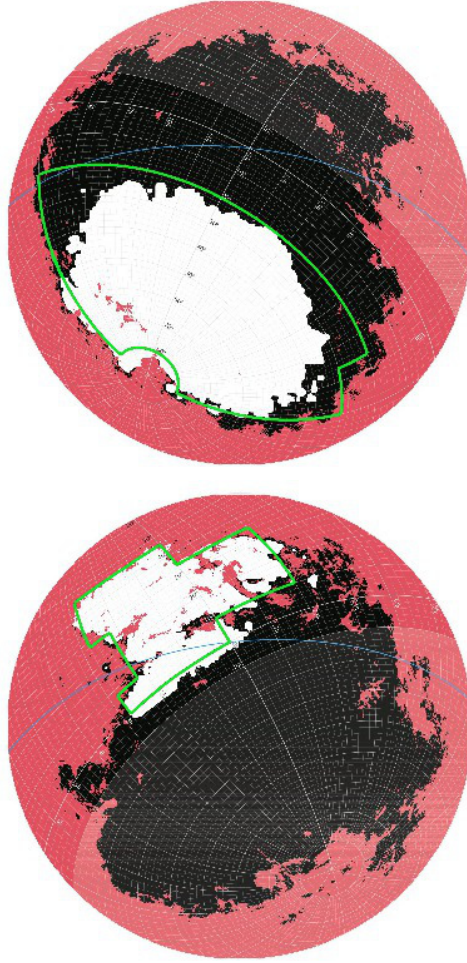


Figure 8: Representation in Lambert Projection of the Northern and Southern Galactic Hemispheres and the J-PAS selected areas. Each plot shows in pink the area with relatively high galactic extinction (as given by $E(B-V) > 0.1$ in the Schlegel et al. 1998 maps), and in white the area that is selected when taking the best (6000 + 2000) square degrees selected separately in both hemispheres and described in the text. The blue line is the ecliptic. We suggest the areas marked in green as compact versions of the white ones, that will define the J-PAS North and South areas. They cover approximately (6500 + 2250) square degrees.

southern area, as the main criterion to select the survey area. The characteristics of our survey have also been factored in: our strategy and observational set-up heavily penalizes the use of sparse or irregular areas. With this in mind, we present in Figure 8 a possible compact selection of both areas, that covers a total of $\sim 8650 \square^\circ$.

2.3.5. *Overlap with SDSS and SDSS Stripe 82*

Figure 9 shows the approximate fingerprint on the sky of both J-PAS and the Sloan Digital Sky Survey. Given that the coordinates of Apache Point are slightly further South than Javalambre, the SDSS coverage reaches further South than J-PAS will. However, we have explicitly included in the Southern Galactic area an equatorial strip that extends down to $\delta = -2.5^\circ$, in order to overlap with the deeper Sloan Digital Sky Survey Extension in the area known as Stripe 82.

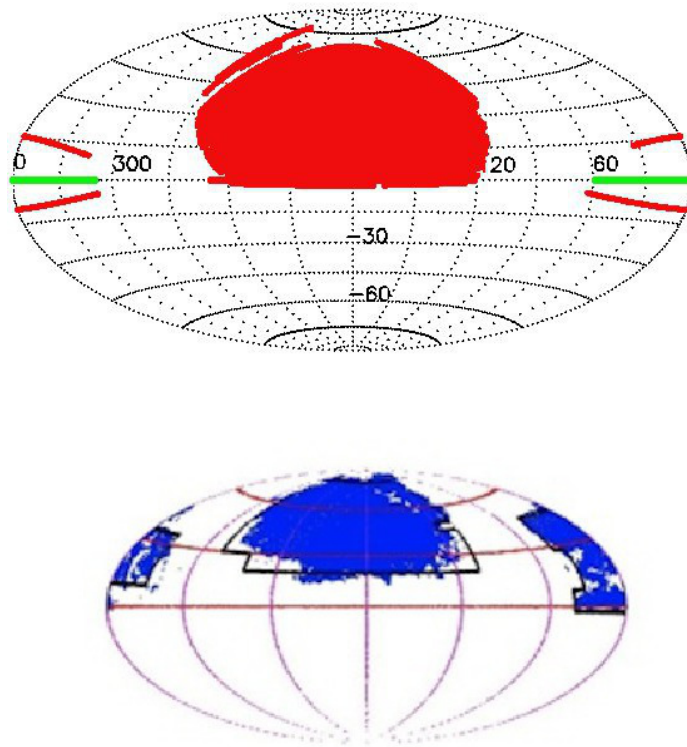


Figure 9: Aitoff projection of the full sky in equatorial coordinates, showing (left panel) the area covered by the Sloan Digital Sky Survey, with Stripe 82 highlighted in green. The right panel shows the best 6000+2000 square degrees selected in both galactic hemispheres as described in the text, as well as the J-PAS areas suggested in this document, that amount to 6500+2250 square degrees.

2.4. Expected performance

2.4.1. Inputs for the empirical mocks

To generate our mocks we use the prior galaxy distribution of Benítez (2014), which produces an accurate distribution of magnitudes, redshifts and spectral types as measured from the COSMOS (Ilbert et al., 2009), UDF (Coe et al., 2006), GOODS MUSIC (Grazian et al., 2006) and CFHTLS (Coupon et al., 2009) catalogs. The templates are plotted in Fig. 10, showing our divide between early type (LRG) templates and emission line galaxy templates (ELG). We repeatedly draw values of m , z and T from our prior distributions until we reach the equivalent of an area of 20''^2 , using a fractional step for T of 0.1. The resulting galaxy number counts for different spectral types are shown in Fig. 11 and its redshift distribution in Fig. 12.

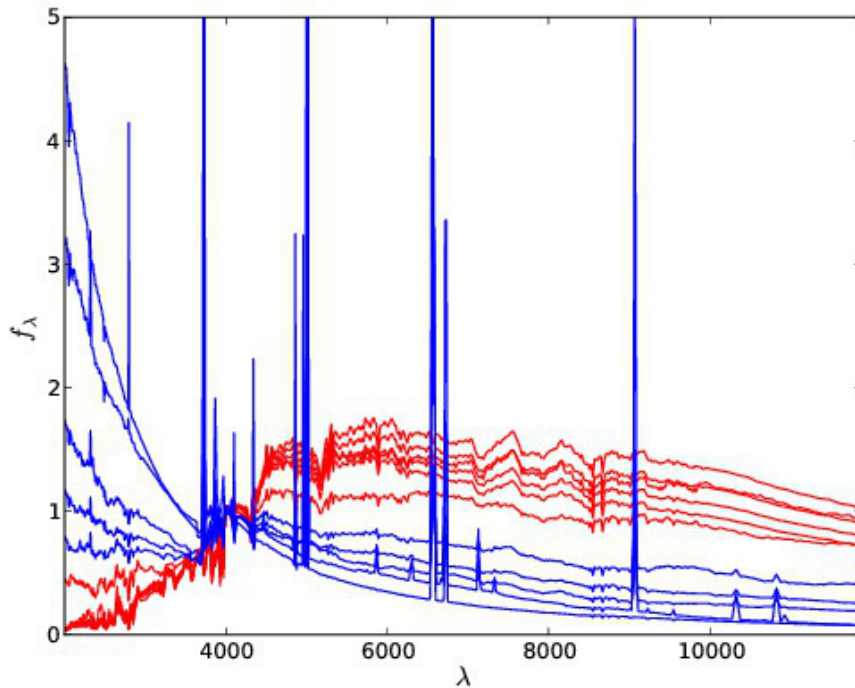


Figure 10: BPZ-2 templates, in red, Luminous Red Galaxies (RG), in blue, Emission Line Galaxies (ELG). We interpolate between contiguous templates

To generate the mocks, we use the ETC described above to calculate realistic instrumental noise within $3''$ diameter apertures. In addition we add a $0.06 - 0.08$ systematic noise to the photometry, similar to the one measured in other photometric catalogs with abundant spectroscopy. The addition of this noise, combined with the color “granularity” provided by the template interpolation reproduces very well the photometric redshift properties found in other real catalogs, both in precision and in number of outliers (see Benitez 2014).

2.4.2. Empirical mocks

J-PAS will be the first Stage IV project to start operations, and its observing strategy is designed to take advantage of this head-start to produce competitive constraints on dark energy as early as possible after the survey start. In Table 6. we show the expected schedule of observations.

For most cosmological applications which rely on a measurement of the Power Spectrum (P), a crucial quantity is the number density $N(z)$ of different galaxy types as a function of redshift. The effective volume V_{eff} for measuring P increases as $nP/(1+nP)^2$, where n is the galaxy number density. Table 6 lists the expected values of V_{eff} , the resulting values of nP are plotted in Fig. 13. We use the $P(k)$ of Tegmark et al. (2003).

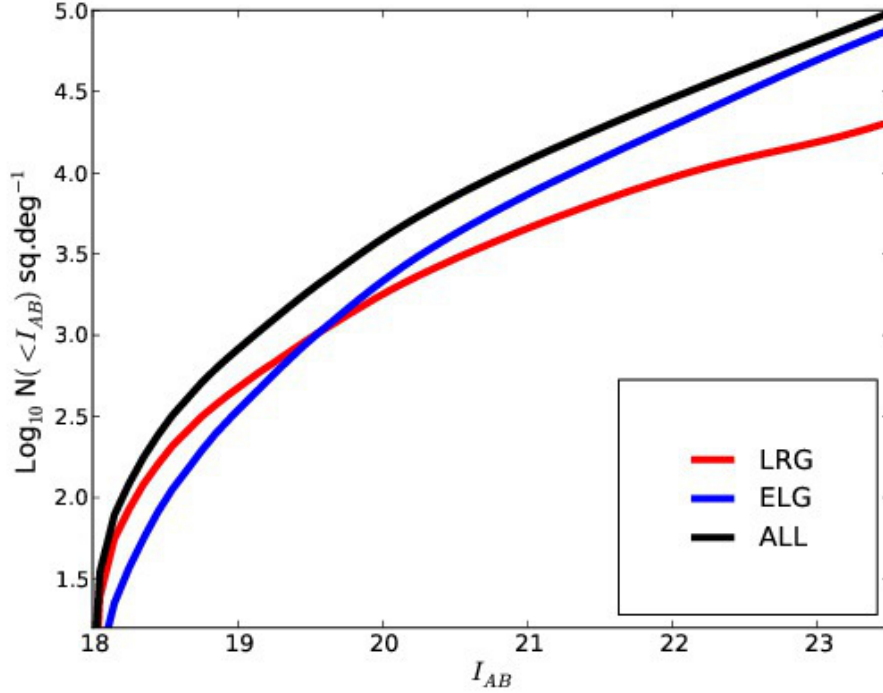


Figure 11: Number counts per square degree in our mock catalogs as a function of spectral types (LRG corresponds to early types, ELG to emission line galaxies)

Trays	Date	N_{RG}	N_{ELG}	V_{eff}	$N_{RG}^{z>0.7}$	$N_{ELG}^{z>0.7}$	$V_{eff}^{z>0.7}$
T543	Y3	4.6	33.9	9.5	0.7	9.4	5.8
All	Y6	17.6	73.1	13.9	3.7	19.7	9.9

Table 6: J-PAS Observational schedule. The first columns indicates how many trays are expected to be completed. The date indicates the number of years after we start. N_{RG} and N_{ELG} correspond to the total number of respectively, Red and Emission Line galaxies, in 10^6 units. V_{eff} is the effective volume for Power Spectrum measurements

J-PAS will also measure lower precision photometric redshifts for hundreds of millions of galaxies, which can be used for other scientific goals, both in Cosmology and Galaxy Evolution. Figures 14 and 15 show the expected surface density of galaxies with different photo-z precisions at Y3 (half the survey) and Y6 (end of the survey). Table 7. and 8. list the corresponding numbers.

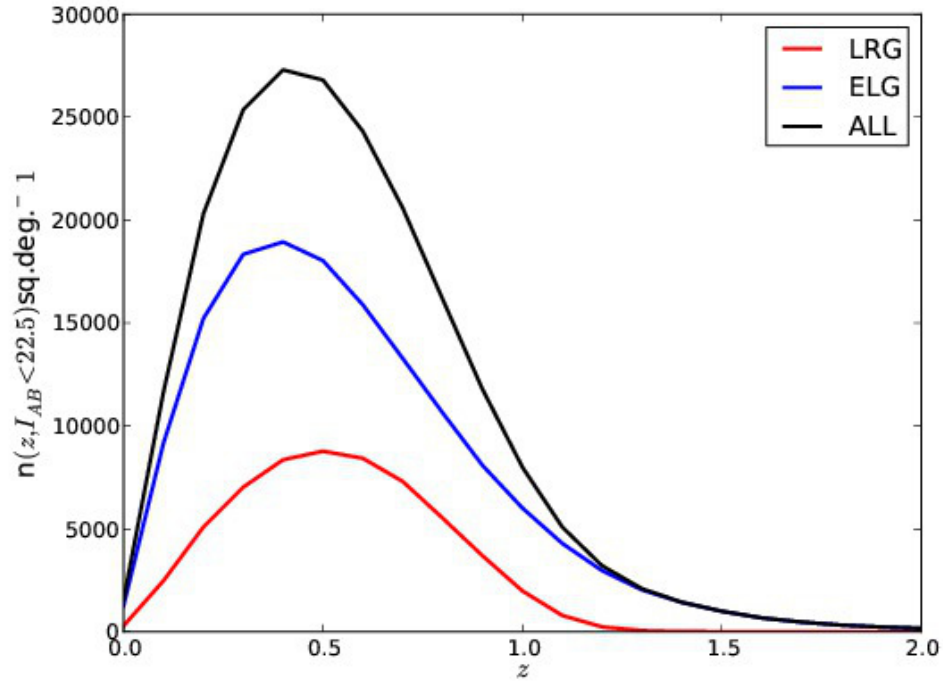


Figure 12: Redshift distribution of galaxies in our mock catalogs $I_{AB} < 23.5$

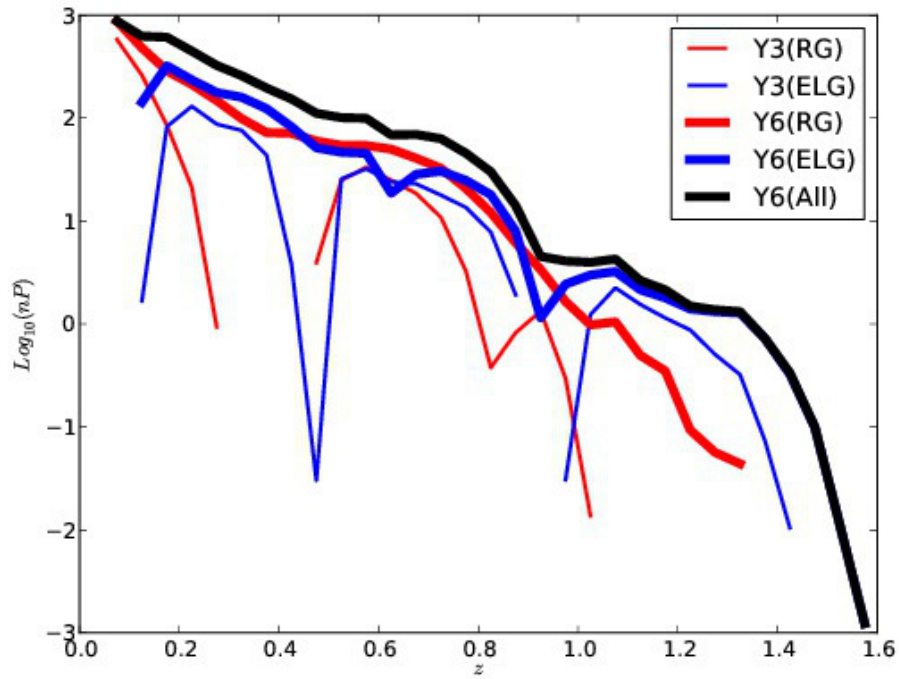


Figure 13: Product of the galaxy density for Red Galaxies (RG) and Emission Line galaxies (ELG) with $dz/(1+z) < 0.003$ by the power spectrum (taking into account the corresponding bias) for different stages of completion of J-PAS

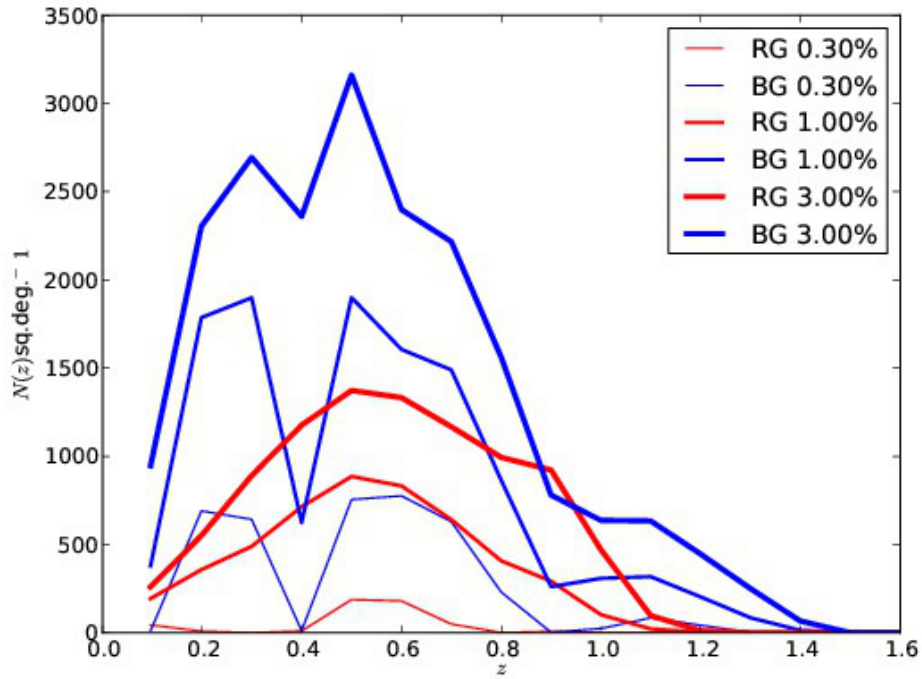


Figure 14: Expected surface density of galaxies for different photometric redshift errors at Y3 (half the survey)

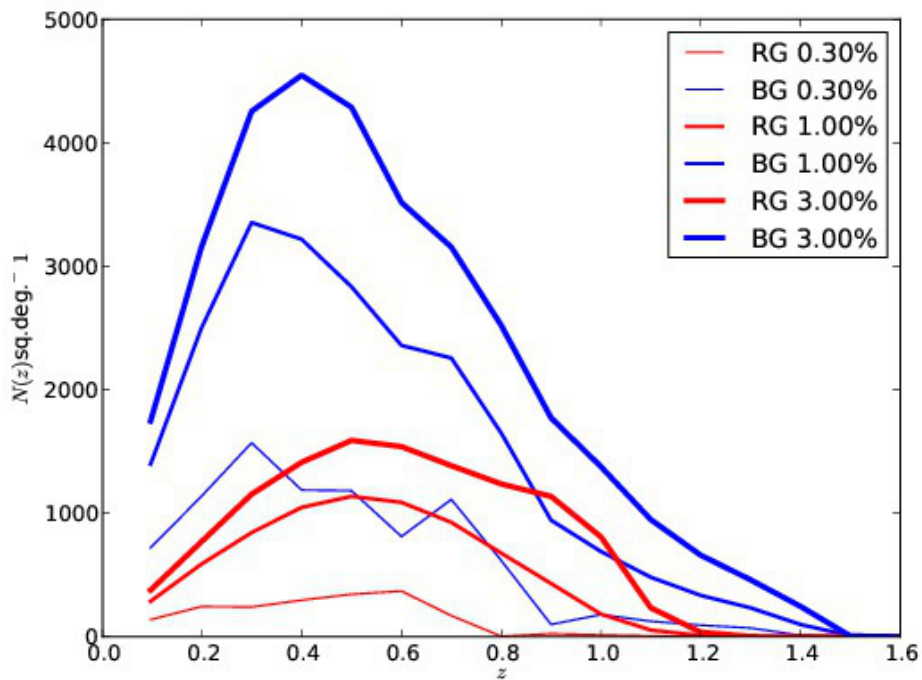


Figure 15: Expected surface density of galaxies for different photometric redshift errors at Y6

z	$N_{0.3\%}^{RG}$	$N_{0.3\%}^{ELG}$	$N_{1\%}^{RG}$	$N_{1\%}^{ELG}$	$N_{3\%}^{RG}$	$N_{3\%}^{ELG}$
0.10	43.75	10.45	193.65	379.25	260.50	946.80
0.20	8.80	690.45	357.45	1786.25	550.70	2303.90
0.30	0.00	642.95	489.15	1898.45	890.20	2693.80
0.40	9.80	11.35	713.95	624.15	1176.70	2359.50
0.50	188.00	755.05	885.90	1899.65	1373.10	3161.00
0.60	180.50	776.05	832.30	1605.90	1332.60	2398.10
0.70	49.45	629.80	641.50	1489.70	1167.30	2216.90
0.80	0.90	230.75	407.75	864.40	994.00	1561.50
0.90	7.55	2.20	292.40	261.15	922.20	780.20
1.00	0.10	23.80	102.55	308.45	470.80	637.40
1.10	0.00	84.40	21.90	318.05	97.00	633.80
1.20	0.00	42.50	2.05	203.35	11.50	445.90
1.30	0.00	0.95	0.20	85.20	0.50	250.50
1.40	0.00	0.00	0.00	13.75	0.00	66.70
1.50	0.00	0.00	0.05	0.60	0.00	0.00
1.60	0.00	0.00	0.00	0.05	0.00	0.00

Table 7: Expected Observed Galaxy Density at Y3: Expected surface density of galaxies with different photometric redshift errors at Y3 (half the survey)

z	$N_{0.3\%}^{RG}$	$N_{0.3\%}^{ELG}$	$N_{1\%}^{RG}$	$N_{1\%}^{ELG}$	$N_{3\%}^{RG}$	$N_{3\%}^{ELG}$
0.10	138.80	720.30	287.65	1397.25	378.20	1746.70
0.20	244.60	1136.95	588.05	2498.50	769.10	3154.60
0.30	240.90	1570.30	843.40	3353.65	1154.30	4254.60
0.40	296.45	1188.15	1047.20	3218.35	1412.60	4546.30
0.50	344.20	1182.45	1136.95	2833.15	1589.70	4286.00
0.60	370.15	811.70	1088.45	2359.25	1539.70	3516.60
0.70	170.90	1111.90	926.35	2256.85	1385.10	3155.00
0.80	3.80	617.55	677.20	1649.75	1237.20	2521.60
0.90	24.40	99.65	431.40	943.85	1136.70	1772.10
1.00	14.95	179.70	183.55	690.45	809.00	1377.30
1.10	6.90	125.55	54.10	482.05	234.30	948.90
1.20	1.35	94.00	10.00	335.55	37.30	660.80
1.30	0.40	71.10	1.50	234.20	1.70	461.40
1.40	0.10	11.80	0.10	99.85	0.00	246.80
1.50	0.00	0.20	0.00	8.30	0.00	6.80
1.60	0.00	0.00	0.00	0.05	0.00	0.00

Table 8: Expected surface density of galaxies with different photometric redshift errors at Y6 (end of survey)

3. Scientific Goals I: Cosmology

The J-PAS data are so versatile that the survey is, effectively, four different sub-surveys, each of which develops one of the main DETF Dark Energy probes.

Although J-PAS was initially designed to measure BAOs (Benítez et al., 2009), still one of the main goals of the Survey, an imaging instrument with narrow-band filters can do much more than that. By tuning the instrument, the filter system and the survey strategy, we have been able to construct a tool unique in its capability to detect galaxy groups and clusters. Furthermore, the excellent conditions at the site in Pico del Buitre (with seeing better than 0.7") have turned an initially modest effort on weak lensing into a promising new survey, where not only the shapes of several hundred millions of galaxies will be measured, but their redshifts will be known with high accuracy as well.

We will take full advantage of the fact that, by observing the same areas of the sky hundreds of times (at least three exposures in each one of the 56 filters), the survey can have valuable time-domain information. By tuning the cadence of the observations to coincide with the typical durations of supernova explosions, we will be able to sample their spectral surfaces (i.e., the flux as a function of wavelength and time) in such a way that spectroscopic follow-up is unnecessary for a large number of objects. This refined strategy will enable us to conduct one of the most prolific surveys of Type-Ia supernovas, with thousands of science-grade objects up to $z \sim 0.5$.

3.1. The J-PAS Redshift Survey

The main feature of J-PAS, that distinguishes it from other surveys, is that it will achieve very high completeness while still measuring redshifts with near-spectroscopic accuracies. As will be shown in this Section, by combining several tracers of large-scale structure such as luminous red galaxies (LRGs) up to $z \sim 1$, emission-line galaxies (ELGs) up to $z \sim 1.4$, and Ly- α emitters (LAEs) and quasars up to $z \sim 5$, we will be able to assemble a wide *and* deep 3D map of the Universe over 1/5 of the whole sky ($> 8500 \square^\circ$).

3.1.1. Cosmology with galaxy surveys

Galaxy surveys have evolved enormously since late 70's, when the first maps of the local Universe were laboriously compiled from extremely scarce resources (Yahil et al., 1980; Davis & Huchra, 1982). The move from "retail" to "wholesale" began with the IRAS Point Source Catalog Redshift Survey (Strauss et al., 1992), which, despite containing only a few thousands of galaxies, was one of the first surveys that enabled cosmological applications related to large-scale structure (Fisher et al., 1993).

It soon became clear that galaxy surveys could be optimized for cosmology in general (Heavens & Taylor, 1997), and in particular to obtain information about the cosmological constant (Ballinger et al., 1996; Efstathiou et al., 1990). The 90's saw the first large efforts to collect massive numbers of galaxies and other extragalactic objects, increasing previous numbers of objects with known redshifts by almost two orders of magnitude: APM (Maddox et al., 1990), the Two-degree Field survey (2dF) (Folkes et al., 1999; Colless et al., 2001) and the Sloan Digital Sky Survey (SDSS) (York et al., 2000). These precursor surveys were able to measure for the first time the clustering of structures over large scales (Peacock et al., 2001; Dodelson et al., 2002; Hawkins et al., 2003; Tegmark et al., 2004), and they allowed for the first measurement of BAOs (Eisenstein et al., 2005; Cole et al., 2005; Percival et al., 2010). However, these early surveys were unable to reach a sufficiently large volume of the cosmos in order to allow a measurement of the fine details of the distribution of large-scale structure. Hence, despite the ground-breaking checks on the standard cosmological model that these surveys provided, their constraints on dark energy (particularly its equation of state, w) were not very strong.

More recently, BOSS (Schlegel et al., 2007) and WiggleZ (Glazebrook et al., 2007; Blake et al., 2011) both achieved high enough densities of galaxies to allow unambiguous detections of the BAO features on the power spectrum (Blake et al., 2011; Anderson et al., 2012, 2013), as well as a vast array of other applications. The next

generation of surveys such as DES (The Dark Energy Survey Collaboration, 2005), HETDEX (Hill et al., 2008), PAU (Castander et al., 2012), PFS (Ellis et al., 2012), DESI (Levi et al., 2013), 4-MOST (De Jong et al., 2012), LSST (Ivezic et al., 2008), and Euclid (Laureijs et al., 2011; Amendola et al., 2012), promises to deliver further leaps in depth, image quality, photometric accuracy, as well as in the sheer numbers of detected objects. J-PAS, in particular, will deliver many millions of galaxies and other extragalactic objects with extremely accurate photometric redshifts, over a large fraction of the volume of the observable Universe.

The treasure trove of possible applications of these huge datasets is immense, and remains mostly untapped (Albrecht et al., 2006). However, a critical gap between the observations and the science applications is the optimal extraction of information from the catalog.

Given the practical limitations imposed by atmospheric conditions, instrument performance, surveyed area and galactic contamination, all instruments end up surveying the cosmos in an uneven way, with some regions better observed (and therefore better sampled) than others. Hence, when studying large-scale structure through the two-point correlation function or its Fourier transform, the power spectrum $P(k)$ (Peebles, 1980; Peacock, 1992), we must first overcome the angular and radial modulations in the density of galaxies that arise not from true fluctuations of the underlying density field, but from varying observational conditions and instrumental performance. Since galaxies can be regarded as (biased) tracers of peaks of the density field (Kaiser, 1984; Bardeen et al., 1986; Sheth & Tormen, 1999), their counts are realizations of random point processes subject to shot noise, hence a modulation in the average number of galaxies induces modulations in shot noise as well.

A more basic difficulty arises from the fact that one cannot determine the amplitude of the spectrum with arbitrary precision at all scales if observations are limited to a finite volume – this is known as volume sample variance, or cosmic variance. Finite volumes can also introduce covariances between power at different scales, and modulations in the survey’s galaxy selection function can generate further biases and covariances. When estimating either the two-point correlation function or the power spectrum from real data, these problems should be kept under control – see, e.g., Landy & Szalay (1993); Bernstein (1994); Vogeley & Szalay (1996); Szapudi & Colombi (1996); Hamilton (1997); Tegmark et al. (1998).

The main problem is how to balance shot noise in light of cosmic variance in a such a way that we are able to recover the maximal amount of information from our catalog – in other words, how to estimate the power spectrum while minimizing the total covariance.

A key step forward was obtained by Feldman et al. (1994) (henceforth FKP), who showed that, under the assumption of Gaussianity, there is an optimal weighted average which minimizes the variance of the amplitude of the power spectrum averaged over some volume in Fourier space. Given fiducial models for the matter power spectrum, $P(z; \mathbf{k})$, for the average number of galaxies in our catalog, $\bar{n}(z; \hat{x})$, and for the bias of the tracer of large-scale structure $b(z)$, the FKP weighted average results in an uncertainty for the power spectrum which can be expressed as:

$$\left[\frac{P}{\sigma_p} \right]^2 = \frac{V_{\mathbf{k}}}{2} \int d^3 \mathbf{x} \left[\frac{\bar{n}(z, \hat{x}) b^2(z) P(z; \mathbf{k})}{1 + \bar{n}(z, \hat{x}) b^2(z) P(z; \mathbf{k})} \right]^2, \quad (15)$$

where the radial direction $|\mathbf{x}| = r$ in the volume integral should be expressed in terms of z , using the fiducial model (e.g., a Λ CDM FRW model). In Eq. (15), the volume element in Fourier space around the bin \mathbf{k} is defined as $V_{\mathbf{k}} = \int_{\mathbf{k}} d^3 \mathbf{k} / (2\pi)^3$, and the integral over volume is known as V_{eff} , the *effective volume* of the survey (Tegmark, 1997; Tegmark et al., 1998). Since Eq. (15) expresses the inverse of a covariance, it is basically a Fisher information matrix (Tegmark et al., 1998).

Since the constraining power of a galaxy survey is proportional to the effective volume, the ideal scenario occurs when the product $\bar{n} b^2 P \gtrsim 1$ for the largest possible fraction of the survey’s volume. When this is the case, shot noise is subdominant, and it may become possible to reach the statistical limit set by cosmic variance – in the extreme situation of negligible shot noise, $\sigma_p / P \rightarrow \sqrt{2 / V_{\mathbf{k}} V_{\text{eff}}}$.

The formula above can be easily applied to a catalog of galaxies of a single type (like luminous red galaxies, LRGs), or to a catalog containing several different types of galaxies (LRGs, emission-line galaxies, quasars,

etc.) J-PAS is in a unique situation, in the sense that it will be able to detect galaxies of several different types (Benítez et al. (2009), see also this paper), as well as quasars (Abramo et al., 2012), in large enough numbers to make each one of these types of objects into suitable tracers of large-scale structure on their own rights.

However, it has long been observed that the several distinct types of galaxies, as well as quasars, cluster in a different way (Dressler, 1980), which means that they have different biases (Kaiser, 1984) with respect to the clustering of the underlying density field. This bias is a manifestation of point processes that randomly associate (Dekel & Lahav, 1999) peaks of the density contrast $\delta = \delta\rho/\rho$ with galaxies of one type or another (Bardeen et al., 1986; Sheth & Tormen, 1999), in such a way that more massive objects (with higher biases) tend to form in regions of higher density (Mo & White, 1996; Jing, 1998; Benson et al., 2000). Typically, the dependence of bias on mass and other environmental factors translates into a dependence on the morphology and/or luminosity of the galaxy (Davis & Geller, 1976; Norberg et al., 2002).

Given the mass- or luminosity-dependence of bias, it is clearly sub-optimal to simply assume that all galaxies (or quasars) cluster in the same way, and then take some averaged bias for the whole catalog – since this would imply a marginalization over the wide variations in bias, which would then lead to a degradation in the estimates of the power spectrum. When a catalog includes many types of tracers of large-scale structure, corresponding to halos with different biases, the FKP method can be generalized in such a way that each inequivalent type of tracer is taken into account in an optimal way Percival et al. (2004); Abramo (2012). By breaking the tracers into subgroups it is not only possible to measure the power spectrum and the bias of each individual species of tracers to better precision, but we can also obtain dramatic improvements on the measurements of redshift-space distortions and non-Gaussianities that extrapolate the limits imposed by cosmic variance (Seljak, 2009; McDonald & Seljak, 2009; Hamaus et al., 2010, 2011, 2012; Abramo & Leonard, 2013). However, in order to realize these gains it is necessary to measure these tracers in overlapping volumes, and in very high densities. J-PAS will in fact detect millions of different types of galaxies (distinguished not only by their types, but also by shapes, spectral types, etc.), as well as quasars, hence it will be in a unique position to take advantage of this exciting new technique.

3.1.2. The Fisher matrix approach

Since $\sigma(\log P) = \sigma_p/P$, it is easy to see that Eq. (15) gives the Fisher matrix in terms of the power spectrum averaged in some bin $V_{\mathbf{k}}$ around \mathbf{k} . The Fisher matrix for some parameters θ^i ($i = 1, \dots, N_p$) which we would like to infer from the power spectrum measured by a galaxy survey can then be written using the usual Jacobian for the transformation of a Fisher matrix, and the result after summing over all the bins in Fourier space, and over the volume of the survey, is:

$$F_{ij} = \frac{1}{2} \int \frac{d^3\mathbf{k} d^3\mathbf{x}}{(2\pi)^3} \frac{\partial \log P}{\partial \theta^i} \left[\frac{\bar{n} b^2 P}{1 + \bar{n} b^2 P} \right]^2 \frac{\partial \log P}{\partial \theta^j}. \quad (16)$$

It can in fact be shown that this result also follows directly from the statistics of counts-in-cells, i.e., from the Fisher matrix in “pixel space”, where each cell in position space is regarded as a pixel – even in the case of multiple species of tracers (Abramo, 2012).

It is important to notice that the measured power spectrum has both angular and redshift dependence. The power spectrum is the amplitude of the auto-correlation of the density contrast in Fourier space, which can be expressed as $\langle \delta(z; \mathbf{k}) \delta^*(z; \mathbf{k}') \rangle = (2\pi)^3 P(z; \mathbf{k}) \delta_D(\mathbf{k} - \mathbf{k}')$, where δ_D is the Dirac delta-function. However, galaxy surveys map our past light-cone in redshift space, so in order to infer anything from them we must be able to account for this redshift dependence.

The most obvious way in which redshift affects the power spectrum is through the matter growth function $D(z)$, where in linear perturbation theory $\delta_l(z; \mathbf{k}) = D(z)\delta_l(0; \mathbf{k})$, from which it follows that $P_l(z; \mathbf{k}) = D^2(z)P_l(0; \mathbf{k})$. Non-linear structure formation introduces a much more complex dependence of the spectrum with redshift, (Jain & Bertschinger, 1994; Peacock & Dodds, 1996; Heavens et al., 1998; Seljak, 2000; Ma & Fry, 2000; Bernardeau et al., 2002; Crocce & Scoccimarro, 2006; Angulo et al., 2008; Matsubara, 2008). The growth of matter fluctuations depends on the cosmological parameters, and it could even bear imprints of theories of modified gravity that attempt to explain cosmic acceleration (Dolgov & Kawasaki, 2003; Carroll et al., 2004; Chiba et al., 2007; Sotiriou & Faraoni, 2010), both in the linear (Linder & Jenkins, 2003; Linder, 2005; Bertschinger, 2006; Huterer & Linder, 2007; Hu & Sawicki, 2007) and non-linear regimes (Stabenau & Jain, 2006; Koyama & Silva, 2007; Laszlo & Bean, 2008; Oyaizu, 2008; Oyaizu et al., 2008).

Since there are considerable uncertainties in the exact form of the galaxy power spectrum when non-linearities are present, we will impose a phenomenological cut-off in the maximal wavenumbers that are taken into account for the purposes of forecasting constraints on cosmological parameter – typically, these non-linear scales are believed to lie near $k_{nl} \sim 0.1 h \text{ Mpc}^{-1}$ at $z = 0$. There is evidence that the non-linear scale is weakly dependent on redshift (since non-linear effects become more pronounced with time) and on halo bias as well (Smith et al., 2007), but we will take a more conservative approach and fix that scale to that which applies at $z = 0$. Hence, in order to protect our forecasts from the unknown effects of non-linear structure formation, we will damp the effective volume (and, therefore, the Fisher matrix) by an exponential factor, whose effect is to suppress the information coming from those modes (Seo & Eisenstein, 2007; Eisenstein et al., 2007).

Since one cannot separate, in principle, cosmological redshifts from peculiar velocities, the clustering of matter in redshift space introduces an anisotropy in the two-point correlation function, $\xi(r) \rightarrow \xi_s(r_\perp, r_\parallel)$, where r_\perp denotes angular distances – across the line of sight – and r_\parallel denotes distances along the line of sight \hat{x} – which are inferred from the redshifts. These anisotropies are also present in the power spectrum, $P(k) \rightarrow P_s(k, \mu)$ (Kaiser, 1987; Hamilton, 1998), where $\mu = \hat{k} \cdot \hat{x}$ is the cosine of the angle between the wavenumber and the line of sight. In the linear regime, the redshift-space power spectrum of some galaxy type g is given by:

$$P_{g,s}(z; k, \mu) = [b_g + f(z)\mu^2]^2 P(z; k), \quad (17)$$

where $f(z) = -d \log D(z) / d \log(1+z)$, and $P(z; k)$ is the real-space mass power spectrum, which is assumed isotropic. There are additional distortions arising from the quasi-linear and nonlinear regimes of structure formation, such as peculiar velocities of galaxies inside clusters. These can lead, e.g., to smearing of the clustering on intermediate scales (Kaiser, 1987; Scoccimarro, 2004; Eisenstein et al., 2007; Cabré & Gaztañaga, 2009). Finally, the statistics of density peaks of Gaussian fields can also lead to a smearing of the redshift-space clustering, even in linear perturbation theory (Desjacques & Sheth, 2010).

The effects of nonlinear structure formation on the power spectrum, especially at or near the BAO scale, can complicate the cosmological exploitation of the data, however, these effects can be mitigated by relating the velocity field to the gradient of the density field. Up to now, these “reconstruction” schemes have relied on spectroscopic redshifts (Eisenstein et al., 2007; Padmanabhan et al., 2012b; Xu et al., 2012; Mehta et al., 2012), and with the superb photo- z ’s of J-PAS, we should be able to exploit the benefits of this method.

Perturbation theory and N-body simulations can help to take into account, or even parametrize, most of these effects (Scoccimarro, 2004; Taruya et al., 2009), but despite recent progress in this area (Reid & White, 2011; Jennings et al., 2011), many questions about the proper modeling and interpretation of RSDs on small ($r \lesssim 5 \text{ Mpc}$) and even intermediate ($r \lesssim 50 \text{ Mpc}$) scales remain open. Here we assume that we will be able to model adequately the modes up to $k \gtrsim 0.1 h \text{ Mpc}^{-1}$.

Table 9: Fiducial values of basic cosmological parameters

Parameter	h	Ω_m	$\Omega_b h^2$	Ω_k	n_s	w_0	w_a
Value	0.7	0.27	0.0223	0	0.963	-1	0

We assume a flat Λ CDM FRW model consistent with the maximum likelihood set of parameters found by the joint analysis of WMAP and other datasets (Komatsu et al., 2011). For the fiducial model we also take the neutrino masses, the running (α) of the scalar spectral index, as well as the non-Gaussian parameter f_{NL} , to vanish.

Another factor that can erase information contained in the power spectrum is errors in photometric redshifts, which tend to smear information along the radial (line of sight) direction (Blake & Bridle, 2005). The narrow-band filter system of J-PAS was in fact designed to measure distances down to $\sim 20h^{-1}$ Mpc in the radial direction, and hence to detect features up to $k_{\parallel} \sim 0.2h$ Mpc $^{-1}$ at $z \sim 1$ – see also Benítez et al. (2009). Since the errors in the radial direction and in redshift are related by $\sigma_{r_{\parallel}} = cH^{-1}(z)\sigma_z$, we can factor these uncertainties into the Fisher matrix by damping the modes along the line of sight which are smaller than this uncertainty. In order to take these uncertainties into account, we multiply the effective volume by $\exp\left[-k_{\parallel}^2 c^2 H^{-2}(z)\sigma_{z,\alpha}^2\right]$ – and, as discussed in Sec. 2, the estimated redshift precision is $\sigma_{z,LRG} \simeq 0.003(1+z)$ for LRGs, $\sigma_{z,ELG} \simeq 0.0025(1+z)$ for ELGs, and $\sigma_{z,QSO} \simeq 0.0025(1+z)$ for quasars.

It should be noted that the Fisher matrix suffers from well-known limitations: first, it relies on a quadratic approximation to the likelihood function around its maximum, and on the hypothesis that the variables of interest obey a Gaussian random distribution. Under these assumptions, the Cramér-Rao theorem assures us that the set of constraints derived from the Fisher matrix are in fact an upper bound – a best-case scenario (Trotta et al., 2010). Although non-Gaussian features in the likelihood are probably subdominant for the sake of our analysis [at least if we manage to avoid the highly non-linear scales, see Takahashi et al. (2011)], the Fisher matrix is not the appropriate tool for assessing the skewness of joint probabilities. This can be particularly problematic for parameters which are not well constrained, such as the equation of state of dark energy and its time dependence (Albrecht et al., 2006). In extreme cases, the Fisher matrix may lead to a significant underestimation of the uncertainties (Wolz et al., 2012) compared to methods that are able to sample and to integrate the likelihood function directly, such as Markov Chain Monte Carlo (Metropolis et al., 1953; Lewis & Bridle, 2002). However, the influence of priors can have an even larger impact on forecasts, hence for the purposes of the constraints shown in this paper we have chosen to employ the Fisher matrix, but to be conservative about priors.

Whenever necessary, we have used a fiducial model specified in Table 9.

3.1.3. Baryonic Acoustic Oscillations

The dynamics of dark matter, baryons and photons in the early Universe are well understood: the theory (Dodelson, 2003; Mukhanov, 2005; Peter & Uzan, 2009) is described by a set of Einstein-Boltzmann equations well inside the linear regime, and observations of the CMB have overwhelmingly confirmed this picture (Smoot et al., 1992; Bennett et al., 2003; Spergel et al., 2003; Komatsu et al., 2011; *Planck* Collaboration et al., 2013e). Before recombination ($z \sim 1100$) atoms were still ionized, so photons were able to transfer some of their pressure to the baryon fluid through scatterings with the free electrons in the plasma. Dark matter, on the other hand, provided most of the gravitational drag which pulled matter into the over-dense regions, causing the baryons and radiation to heat up inside the gravitational wells. This competition between gravity and radiation pressure led to acoustic waves, which are manifested in the photons after decoupling as a series of peaks in the angular spectrum of CMB anisotropies (Spergel et al., 2003; Komatsu et al., 2011; *Planck* Collaboration et al., 2013e).

From the point of view of the baryonic matter, after recombination these waves freeze in, since baryons decouple from radiation at that time (in fact, decoupling takes place slightly after recombination). The characteristic scale of these baryonic waves is given by the sound horizon at decoupling (Dodelson, 2003), and after correcting for the damped peculiar velocities of baryons subsequent to decoupling, the scale of frozen baryon acoustic oscillations is predicted to be around 150 Mpc (comoving) for the concordance Λ CDM model (Komatsu et al., 2011). After decoupling, gravity takes care of propagating this correlation length in the baryonic matter to dark matter, and therefore to the full matter transfer function (Eisenstein & Hu, 1998; Eisenstein et al., 1998; Meiksin et al., 1999; Eisenstein et al., 2007). The predicted “wiggles” in the matter power spectrum are in excellent agreement with observations of large-scale structure (Scranton et al., 2005; Percival et al., 2010; Blake et al., 2011; Anderson et al., 2012).

The acoustic (BAO) scale is a soft feature in the two-point correlation function and the power spectrum: baryons are, after all, subdominant with respect to dark matter, which was only indirectly touched by the acoustic oscillations. Moreover, the BAO scale is broadened since recombination due to the velocity dispersion of baryons at the surface of last scattering, and more recently due to mode-coupling from non-linear structure formation, such that the dispersion (or intrinsic smearing) of that scale is around 6% at $z = 3$, and about 10% at $z = 1$ (Eisenstein et al., 2007). Even with these effects factored in, the baryon acoustic scale should still be a bump on the two-point correlation function at scales $80 - 120 h^{-1}$ Mpc – a feature strong enough that it can be measured to exquisite precision in the next few years.

BAOs are therefore manifested in the matter distribution as a signature correlation length that can be accurately and confidently predicted on the basis of known physics in the linear regime, and given parameters that are measured in a completely independent way, by, e.g. the CMB. This length scale constitutes a *statistical standard ruler* which can be directly measured by mapping galaxies in the Universe, and computing their two-point correlation function (Blake & Glazebrook, 2003; Seo & Eisenstein, 2003).

Distances between pairs of galaxies can occur in the radial direction (r_{\parallel}), or in the angular direction (r_{\perp}), and each one corresponds to a different cosmological distance. In the angular direction, two galaxies at a redshift z that are separated by an angle $\delta\theta$ are a distance $d_a(z)\delta\theta$ apart. On the radial (line-of-sight) direction, two galaxies at the same angular position in the sky, separated by a redshift δz , are a distance $cH^{-1}\delta z$ apart. In a flat FRW model where the equation of state of dark energy is parametrized as $w(z) = w_0 + w_a z/(1+z)$ (Chevallier & Polarski, 2001; Linder, 2003), the angular distances are given by:

$$d_a(z) = \frac{c}{1+z} \int_0^z \frac{dz'}{H(z')} . \quad (18)$$

where the Hubble parameter at any redshift is (neglecting the contribution from relativistic particles):

$$H(z) = H_0(1+z)^{3/2} \sqrt{\Omega_m + (1 - \Omega_m)(1+z)^{3(w_0+w_a)} e^{-3w_a z/(1+z)}} . \quad (19)$$

Clearly, this direct dependence of the radial and angular distances on the equation of state and its time variation implies that BAOs are a superb tool to study dark energy (Seo & Eisenstein, 2003). In fact, radial BAOs are slightly superior to angular BAOs, since the latter involve one further integration over redshift.

The scale of BAOs can be measured in the angular and radial directions, and that scale should be the same either way (in position space), hence a direct comparison of the two constitutes a cross-check that can lead to further constraints on the parameters (Alcock & Paczynski, 1979). We can easily include this additional information in our Fisher matrix, however, this presupposes that we can model RSDs accurately, without introducing systematic errors, biases, etc. (Hu & Haiman, 2003). N-body simulations seem to indicate that it is indeed possible to separate, at the level of the Fisher matrix, the measurements of the scale of BAOs from the information contained in the RSDs (Seo & Eisenstein, 2007). One could even use the consistency condition that the peculiar velocity field is determined by the gradient of the gravitational potential, and partially “reconstruct” the linear correlation function (Eisenstein et al., 2007). This reconstruction scheme can lead to better constraints not only on the BAO scale (Padmanabhan et al., 2012b; Xu et al., 2012; Mehta et al., 2012).

The concrete method that we employ to compute the Fisher matrix is that of Wang et al. (2010), which is itself an adaptation of the approach of Seo & Eisenstein (2003, 2007). The basic idea is to write the linear theory, redshift-space power spectrum explicitly in terms of the distances measured in the angular and radial directions, and then use the property that, for cosmologies near the fiducial one, the power spectrum transforms as the Jacobian between the volumes elements for the two cosmologies, $d\bar{V}/dV = (\bar{d}_a/d_a)^2 H/\bar{H}$, where we indicate quantities evaluated at their fiducial values with a bar. After including an extra shot noise term Seljak (2000), we have:

$$P_{obs}(z; k, \mu) = \left[\frac{d_a(z)}{\bar{d}_a(z)} \right]^2 \frac{\bar{H}(z)}{H(z)} P_g(z; k, \mu) + P_{shot}(z), \quad (20)$$

where:

$$\begin{aligned} P_g(z; k, \mu) &= D^2(z) [b_g(z) + f(z)\mu^2]^2 P_l(0; k) \\ &= [b_s(z) + f_s(z)\mu^2]^2 \frac{P_l(0; k)}{\sigma_8^2}. \end{aligned} \quad (21)$$

We have absorbed the growth factor, as well as the normalization of the spectrum (expressed through σ_8) into the effective bias, $b_s(z) = b_g(z)D(z)\sigma_8$, and into an effective RSD parameter, $f_s(z) = f(z)D(z)\sigma_8$. Here $P_l(0, k)$ denotes the linear theory, position space power spectrum at $z = 0$, which can be computed for almost any type of cosmological model with the help of the available CMB Einstein-Boltzmann codes (Seljak & Zaldarriaga, 1996; Lewis et al., 2000).

In Eq.s (20)-(21) the wavenumbers in the fiducial model are related to those in a general cosmology, by:

$$k_{\parallel} = \bar{k}_{\parallel} \frac{H(z)}{\bar{H}(z)}, \quad k_{\perp} = \bar{k}_{\perp} \frac{\bar{d}_a(z)}{d_a(z)}, \quad (22)$$

and the properties of k and μ under changes in the cosmological model follow from their definitions, $k = \sqrt{k_{\parallel}^2 + k_{\perp}^2}$, and $\mu^2 = k_{\parallel}^2/k^2$.

In order to take into account the smearing due to non-linear structure formation we adopt the procedure of Eisenstein et al. (2007), which distinguishes between the radial modes (which inherit additional non-linear effects through the redshift-space distortions) and the angular modes. The non-linear scales in the angular direction are given by $\Sigma_{\perp} = D(z)\Sigma_0$, and those on the radial direction by $\Sigma_{\parallel} = D(z)(1+f)\Sigma_0$, where Σ_0 is the baseline non-linear scale, which we assume to be $\Sigma_0 = 10 \text{ h}^{-1} \text{ Mpc}$. With these definitions, the Fisher matrix, Eq. (16), becomes:

$$\begin{aligned} F_{ij} &= \frac{1}{2} \int_{k_{min}} \frac{d^3 \mathbf{k}}{(2\pi)^3} \int d^3 \mathbf{x} \frac{\partial \log P_{obs}}{\partial \theta^i} \frac{\partial \log P_{obs}}{\partial \theta^j} \\ &\times \left[\frac{\bar{n} P_{obs}}{1 + \bar{n} P_{obs}} \right]^2 e^{-k^2 \Sigma_{\perp}^2 - k^2 \mu^2 (\Sigma_{\parallel}^2 - \Sigma_{\perp}^2)} e^{-k^2 \mu^2 c^2 H^{-2} \sigma_z^2}, \end{aligned} \quad (23)$$

where σ_z is the photometric redshift error. Notice that, to a good approximation, the smearing due to photometric redshift errors only affects the radial modes. The lower limit in the integration over k in Eq. (23) is defined as $k_{min} = (V_0)^{-1/3}$, where V_0 is the volume of the smallest redshift slice (see below), and its role is to ensure that we do not integrate over modes which correspond to scales larger than the typical size of our redshift slices.

In order to minimize the effects of systematic errors in the distance measurements, we adopt the procedure first suggested by Seo & Eisenstein (2003), and separate our survey into several redshift bins, where on each bin we regard d_a and H as free variables (to be determined from the data). Moreover, we also regard the bias, b , the redshift distortion parameter, f , and the unknown extra shot noise, P_{shot} , as independent parameters on each redshift slice. This means that, besides the ‘‘global’’ cosmological parameters such as Ω_k , h , etc., we have another $5N_{bin}$ free parameters, where N_{bin} is the number of redshift bins. Notice that, in the volume integration of Eq. (23), each slice only contributes to the slice-dependent parameters that belong to that same slice, since $d \log P_{obs}[z_n]/d\theta[z_{n'}] = 0$ when $n \neq n'$.

Table 10: First 10 redshift bins, their central redshifts, angular distances, values of the Hubble radius, and comoving volumes per unit area, for the fiducial cosmology (a flat Λ CDM model with $\Omega_m = 0.27$).

Bin	z	d_a (h^{-1} Gpc)	$\sigma(d_a)/d_a$ (ELGs)	cH^{-1} (h^{-1} Gpc)	$\sigma(H)/H$ (ELGs)	V (h^{-3} Gpc ³ /□°)
1	0.3	0.647	0.03	0.384	0.058	1.14×10^{-4}
2	0.5	0.891	0.019	0.427	0.035	2.55×10^{-4}
3	0.7	1.046	0.015	0.478	0.026	4.76×10^{-4}
4	0.9	1.144	0.016	0.540	0.025	5.37×10^{-4}
5	1.1	1.203	0.017	0.600	0.024	6.49×10^{-4}
6	1.3	1.236	0.021	0.668	0.03	7.37×10^{-4}
7	1.5	1.251	–	0.742	–	8.03×10^{-4}
8	1.7	1.253	–	0.820	–	8.51×10^{-4}
9	1.9	1.247	–	0.902	–	8.83×10^{-4}
10	2.1	1.234	–	0.988	–	9.04×10^{-4}

Our basic set of parameters is, therefore:

$$\theta = \{d_a^n, H^n, b^n, f^n, P_{shot}^n\} + \theta_g, \quad (24)$$

where the superscript n refers to the redshift bins, and θ_g represents the set of N_g global cosmological parameters which determine the shape of the power spectrum. In full generality, these global parameters include the physical densities of cold dark matter ($\omega_c = \Omega_c h^2$) and baryons ($\omega_b = \Omega_b h^2$), the Hubble parameter (h), the spatial curvature (Ω_k) scalar spectral index (n_s), the amplitude of the spectrum (A), the sum of neutrino masses (m_ν), and the non-Gaussianity parameter (f_{NL} , which enters as a scale-dependent bias):

$$\theta_g = \{h, \omega_c, \omega_b, \Omega_k, n_s, A, m_\nu, f_{NL}\}. \quad (25)$$

Hence, the total number of parameters is $5N_{bin} + 8$.

Notice that the parameters that describe the dark energy equation of state, w_0 and w_a , are conspicuously absent from this list – as are also missing any parameters which could hint at modified gravity models, like the phenomenological growth parameter γ in $f(z) \simeq \Omega_m^\gamma(z)$, with $\gamma \simeq 0.55$ in General Relativity (Peebles, 1980; Wang & Steinhardt, 1998; Linder & Cahn, 2007). This is because we are assuming that the equation of state and its time variation will be inferred only from the measurements of angular and radial distances (i.e., from the BAO scale measured at each redshift). Likewise, parameters such as γ will be measured only using information from the shape of RSDs and the BAOs.

We employ bins of $\Delta z = 0.2$, starting from $z = 0.2$, so the bin n -th is centered on the redshift $z_n = 0.1(2n + 1)$. Given the expected number of objects forecasted in Sec. 2, the last bin is $n = 5$ for the case of LRGs, $n = 6$ in the case of ELGs, and $n = 20$ in the case of quasars. Table 10 presents the redshift bins, and their corresponding physical dimensions for our fiducial model. It is clear that the typical length scales of each redshift bin are much larger than the BAO scale.

Our fiducial model for the bias is as follows: for luminous red galaxies (LRG), we adopt $b_{LRG} = 1.8$; for emission-line galaxies (ELG) we assume that $b_{ELG} = 0.9 + 0.4z$; and for quasars (QSO) we assume that $b_{QSO} = 0.5 + 0.3(1 + z)^2$ – see, e.g., Ross et al. (2009).

The series of steps leading to constraints which employ only information from BAOs, with or without including RSDs, has been described in detail by Seo & Eisenstein (2003) and by Wang (2006); Wang et al. (2010). In addition to the Fisher matrix above, we also include priors, such as the constraints forecasted for the *Planck* satellite arising from temperature anisotropies Mukherjee et al. (2008). In particular, the *Planck* Fisher matrix, $F_{ij}^{(Planck)}$, serves to calibrate the absolute scale of BAOs, as well as to limit the allowed ranges for the parameters that affect the shape of the power spectrum.

Our procedure is as follows:

1. Add *Planck* priors for the BAO scale to the full Fisher matrix of Eq. (23), to obtain the survey's Fisher matrix with priors, $F_{ij}^p = F_{ij} + F_{ij}^{(Planck)}$.
2. Marginalize⁵ the bias on each slice, b^n , the extra shot noise term, P_{shot}^n , as well as the global cosmological parameters, from the Fisher matrix F_{ij}^p . This intermediate marginalized Fisher matrix, F_{ij}^m , has $3N_{bin}$ parameters.
3. Project the marginalized Fisher matrix F_{ij}^m into the final set of cosmological parameters – which includes, naturally, the dark energy parameters w_0 and w_a .

For a more conservative approach, we can also marginalize against the RSD parameters f^n on each slice, which corresponds to assuming that the form and redshift dependence of these distortions are completely unknown. In that case, the final step is identical to (iii) above, except that now the marginalized Fisher matrix has $2N_{bin}$ parameters.

3.1.4. Forecasts for constraints from BAOs

The BAO scale provides a statistical standard ruler. This means that the power spectrum (or, equivalently, the 2-pt correlation function) have a characteristic scale. Eq. (20) shows that measurements of that scale in the power spectrum inferred from data on a particular redshift can be translated into estimates of the Hubble parameter, H and of the angular-diameter distance, d_a , for that redshift. In Fig. 16 we show how J-PAS can constrain the radial distance and the angular distance to a given redshift, using three different types of tracers: red galaxies (RG), emission-line galaxies (ELG), and quasars (QSO).

In Fig. 17 we present the expected RSD parameter for our fiducial model, as a function of redshift, and the uncertainties estimated for J-PAS. It is useful to employ a fit for the RSD that allows us to explore modified gravity models, and a popular parametrization is $f = \Omega_m^\gamma(z)$, where $\gamma = 0.55$ for General Relativity (GR).

Neutrinos. Since neutrinos are only weakly interacting, they can stream freely away from hot and dense regions much before the time of recombination, which means that they can carry away some of the structure on small scales. Since the effect of neutrinos is most pronounced on scales $k \gtrsim 0.02 h \text{ Mpc}^{-1}$, the constraints are particularly sensitive to non-linear effects and non-linear bias.

⁵By marginalization we mean, concretely: (a) invert the full Fisher matrix to obtain the covariance matrix; (b) eliminate the lines and columns from the covariance matrix that correspond to the marginalized parameters; (c) invert the reduced covariance matrix to obtain the marginalized Fisher matrix.

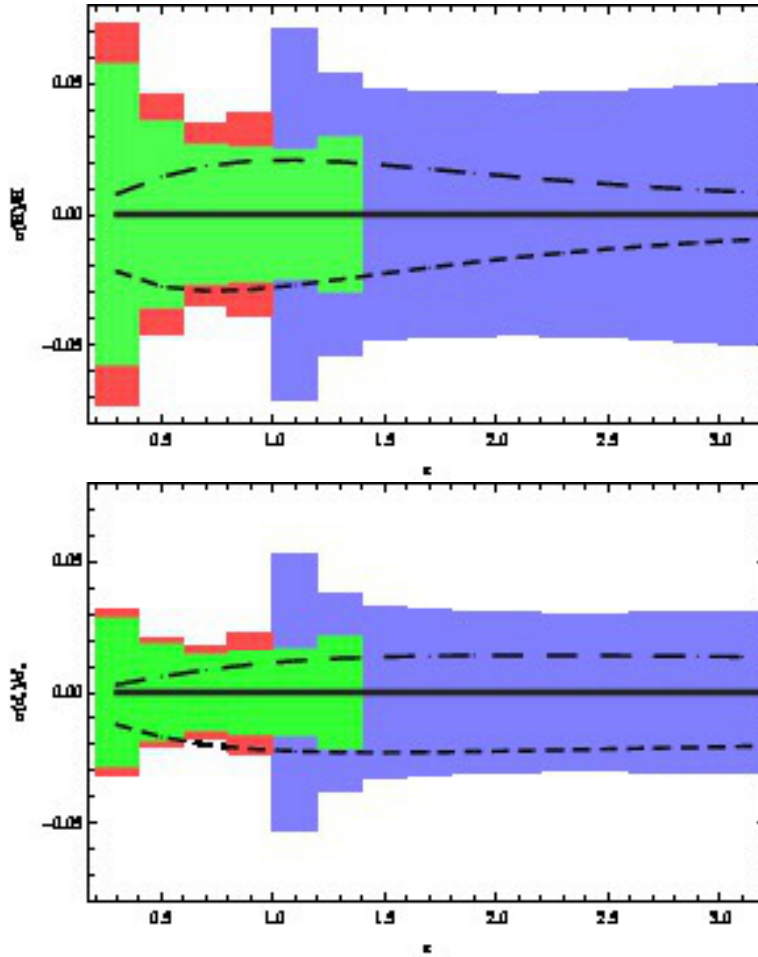


Figure 16: Relative uncertainties in the determination of the Hubble parameter $H(z)$ and angular-diameter distance $d_a(z)$ on each redshift slice, relative to our fiducial Λ CDM model. The red boxes (which reach up to $z \sim 1$) correspond to the constraints imposed by red galaxies alone; the green boxes, to the constraints from emission-line galaxies; and the blue boxes, which extend to higher redshifts, correspond to the constraints from quasars. Also indicated are two alternative dark energy models, one with $w_0 = -0.9$ and $w_a = 0$ (upper, long-dashed lines), and another with $w_0 = -1.0$ and $w_a = -0.3$ (lower, short-dashed lines)

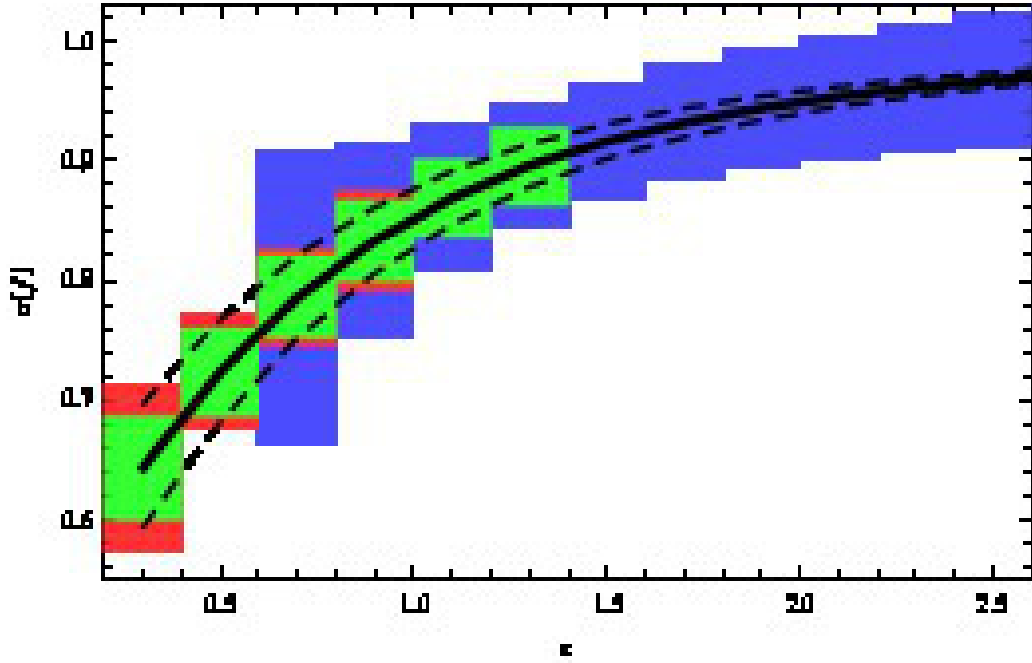


Figure 17: Redshift-distortion (RSD) parameter $f(z)$ for the fiducial Λ CDM + GR model, and uncertainties in its measurement on each redshift slice. For GR, the RSD parameter is very well fitted by $f = \Omega_m^\gamma(z)$, with $\gamma = 0.55$. Also indicated are two hypothetical modified gravity models, with $\gamma_0 = 0.45$ (lower dashed line) and with $\gamma = 0.65$ (upper dashed line). Legends are the same as for Fig. 16

Assuming that these uncertainties from non-linear effects only spoil the scales $k > 0.1 h \text{ Mpc}^{-1}$, we forecast that J-PAS will be able to constrain the total neutrino mass, $M_\nu = \sum m_\nu$, at the level of $M_\nu \lesssim 0.3 \text{ eV}$ (1σ) with ELGs alone. This result was obtained using a fiducial value of $M_\nu \lesssim 0.05 \text{ eV}$. By combining information from RGs and QSOs as well, we estimate that J-PAS will be able to improve upon these constraints by $\sim 30\%$.

Spatial curvature. *Planck* can already constrain the spatial curvature of the Universe to better than 1%. However, J-PAS will be able to limit the spatial curvature independently from CMB data, to a precision of a few percent. This comes basically from comparing clustering in the radial and in the angular directions: whereas the radial distances are barely influenced by spatial curvature, the angular distances are strongly affected by the geometry, and comparing the two allows us to extract the spatial curvature. In Fig. 18 we show how the constraint on Ω_k evolves as we include more redshift slices. The information from high-redshift quasars is particularly important to break low-redshift degeneracies, and improve the constraint to a level of $\sim 5\%$.

Figure of merit. The distance measurements can be converted into constraints on the cosmological parameters. This is achieved by projecting the Fisher information matrix from all redshift slices, with parameters $\theta^i = \{H(z), d_a(z)\}$, into the set of cosmological parameters, which in our case is $\tilde{\theta}^a = \{\omega_0, \omega_a, \Omega_k, \Omega_\lambda\}$. The Fisher matrix for this final set of parameters is then:

$$F_{ab} = \sum_{ij} \frac{\partial \theta^i}{\partial \tilde{\theta}^a} F_{ij} \frac{\partial \theta^j}{\partial \tilde{\theta}^b}, \quad (26)$$

where the summation above includes all redshift slices which have any information about distances.

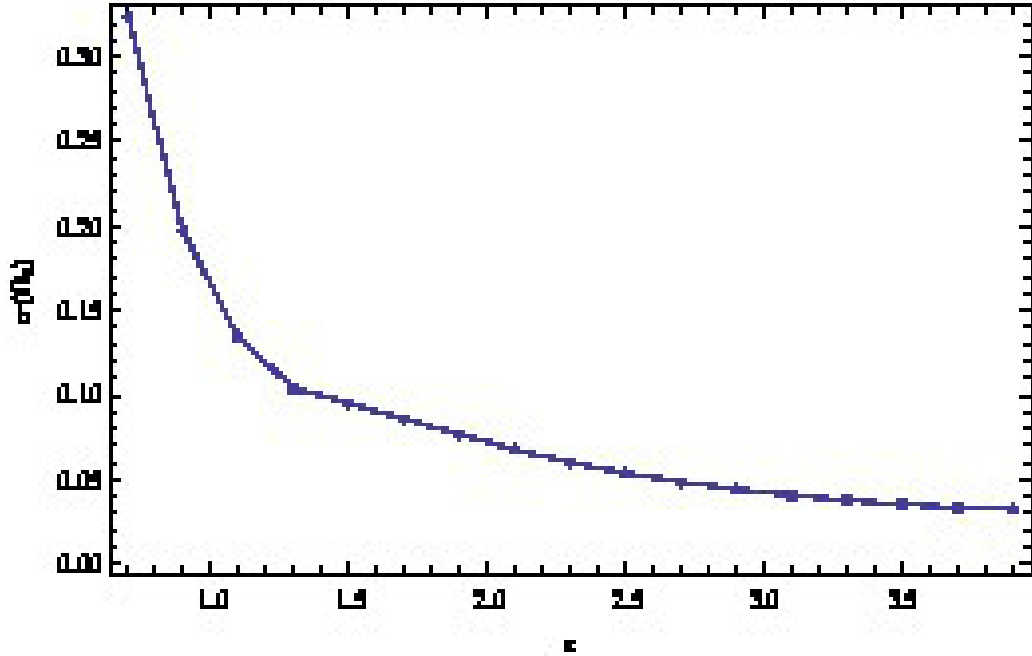


Figure 18: Cumulative constraints on the spatial curvature, as expressed by the parameter Ω_k .

Since w_0 , the value of the equation of state at $z = 0$, is highly correlated with the value w_a of its time derivative in the CPL parametrization, it is useful to find the redshift for which the value of the equation of state is independent of its time derivative. The error in the pivot, w_p , is therefore independent of the error in w_a . In Table 11 we present the uncertainties in the equation of state expressed in terms of the pivot, its time derivative, and, for completeness, that of w_0 as well. In order to help break some degeneracies, we have also used *Planck*priors and Stage-II priors, as defined in Albrecht et al. (2006). In the last column the dark energy figure of merit, defined as $\text{FoM} = \sigma^{-1}(w_p)\sigma^{-1}(w_a) = \det^{-1}F(w_0, w_a)$. As a comparison, the latest constraints from BOSS/CMASS (Sánchez et al., 2013), and including information from CMB, supernovas and other existing BAO surveys, has a $\text{FoM} \simeq 25$. J-PAS is the only survey which has the capability to deliver a $\text{FoM} \simeq 100 - 200$ over the next 5-8 years.

Table 11: Summary of constraints

Tracer	LRGs	ELGs	QSOs	All
$\sigma(w_p)$	0.030	0.026	0.027	0.023
$\sigma(w_a)$	0.38	0.31	0.37	0.26
$\sigma(w_0)$	0.08	0.07	0.09	0.06
FoM	87	121	100	164
$\sigma(M_V)$	0.39	0.28	0.29	0.2
$\sigma(f_{NL})$	6.9	10.3	3.1	1.9
$\sigma(\gamma)$	0.1	0.06	0.11	0.05
$\sigma(\Omega_k)$	0.28	0.12	0.05	0.03

3.1.5. Field reconstructions from the redshift survey

Reconstructions of the underlying smooth matter field, such as, e.g., techniques based on efficient Bayesian inference methods (Jasche & Kitaura, 2010; Kitaura et al., 2012), are useful for a variety of reasons. (1) It has recently been shown that the linearized cosmic density field recovers information about the primordial fluctuations, leading to better constraints on cosmological parameters (see e. g. Neyrinck et al., 2009; Joachimi et al., 2011; Kitaura & Angulo, 2012). (2) It can be used to obtain estimates of the primordial fluctuations by undoing the effects of gravity, by such methods as inverting the Lagrangian to Eulerian mapping, can be effective in order to reduce the errors in the measurements of the location of the BAO peak from spectroscopic redshift surveys (see e. g. Eisenstein et al., 2007; Seo et al., 2010; Padmanabhan et al., 2012a; Mehta et al., 2012). (3) These approaches also allow us to find the cosmic web corresponding to a distribution of matter tracers down to an accuracy of a few Mpc (see Kitaura et al., 2012a; Heß et al., 2013). (4) Another interesting application is to perform constrained simulations of the observed Universe (see e. g. Heß et al., 2013; Wang et al., 2013; Dolag et al., 2005; Klypin et al., 2003; Mathis et al., 2002). (5) Finally, under certain assumptions, these methods can be used to reduce the impact of photometric redshift uncertainties in the estimation of galaxy clustering (Kitaura & Enßlin, 2008; Jasche & Wandelt, 2012). J-PAS, with its high density of tracers, should be an ideal dataset where these methods could be applied.

The number of studies one can perform with the new level of precision in the reconstruction of both Eulerian and Lagrangian space go beyond BAO measurements and cosmological parameter estimation. One can generate templates for the detection of weak signals, such as the WHIM (see e. g. Suarez-Velázquez et al., 2013), the ISW effect (see e. g. Granett et al., 2009), the kSZ effect (see e. g. DeDeo et al., 2005; Ho et al., 2009), the cosmic ray signal (Dolag et al., 2005) or the dark matter annihilation signal (Cuesta et al., 2011).

The reconstruction of the cosmic web can help to understand the process of structure formation and the importance of the environment in the formation of clusters and galaxies (see e. g. Aragón-Calvo et al., 2007; Hahn et al., 2007; Forero-Romero et al., 2009; Libeskind et al., 2011; Tempel et al., 2011,?; Benítez-Llambay et al., 2013).

3.1.6. Morphology of the Cosmic Web

The redshift space distribution of galaxies reveals that galaxies are preferentially distributed in a network frequently referred to as the cosmic web. Ever since the discovery of the CfA wall it had been acknowledged that sheets, filaments and voids are the key components of the cosmic web. This point of view has been supported by the discovery of the Great Wall at $z \simeq 0.08$ in the SDSS survey. The Great Wall is the largest contiguous distribution of matter in the currently observable universe and its discovery leads to the tantalizing issue of whether the wall is the densest large structure in the universe, or whether similar-size structures would be abundant in larger galaxy surveys. The issue of whether or not the Great Wall is an unusual object is important for cosmology, since models of a highly inhomogeneous universe have been advanced arguing that, since the dimming of high redshift supernovae can be explained in such models, the presence of a smooth DE component may be rendered unnecessary Celerier et al. (2000); Tomita (2001); Hunt & Sarkar (2010); Foreman et al. (2010); Nadathur & Sarkar (2011).

A large and deep redshift survey such as J-PAS should be able to shed some useful light on this issue by allowing one to compile an enormous data base of superclusters and voids, which would supplement the one currently available from SDSS. This would help quantify a key property of the supercluster-void network: its morphology. It is well known that standard statistical tools such as the two-point correlation function cannot reveal information about the connectedness of large-scale structure and must therefore be supplemented by geometrical indicators such as percolation analysis, the genus curve, minimal spanning trees and Minkowski functionals Sahni & Coles (1995). Ratios of Minkowski functionals, known as Shapefinders, can enable one to answer the question as to whether a given supercluster or void is filamentary, planar or spherical Sahni et al. (1998). Two recent papers have applied the Shapefinders to a catalogue of superclusters and voids in the SDSS survey including a detailed analysis of the morphology of the Great Wall Einasto et al. (2011). In addition, extreme value statistics has been used to ask whether the Sloan Great Wall is an unusual object – the answer to which seems to be in the affirmative Sheth & Diaferio (2011). Clearly improved deeper datasets are needed to resolve these important issues and the J-PAS survey could play a key role in quantifying supercluster-voids morphology.

3.1.7. *N*-body Mocks

The complexity of the data processing and scientific exploitation of J-PAS will demand realistic synthetic observations. We will construct mock universes that will help in the testing and development of analysis codes, data reduction pipelines, and in the verification of the forecasts presented in this document. In addition, the mock observations will assist the science analysis through comparison with theoretical models, but also these theoretical models will be constrained by J-PAS observations.

We plan to create these mock universes in a three-step process. First, the nonlinear mass content of the universe will be given by following the gravitational interaction of particles in *N*-body simulations (see the recent review of Kuhlen et al., 2012). Second, the properties of galaxies inside dark matter haloes will be predicted by using i) semi-analytic models of galaxy formation (e.g. Lagos et al., 2012; Henriques et al., 2013), ii) sub-halo abundance matching (e.g. Vale & Ostriker, 2004; Zehavi et al., 2011), or iii) empirical rules based on local background density (e.g. White et al., 1987; Cole et al., 1998). Of particular importance for J-PAS will be addition realistic photometric redshift estimates for each galaxy in the simulations, which will help to improve and calibrate the relevant algorithms. Finally, the J-PAS footprint, selection function, redshift completeness, flux limit, gravitational lensing effects, among other, will be added in post-processing to the simulated galaxy population. As a result, we will deliver a fake but realistic J-PAS survey prior to the arrival of data.

The characteristics of J-PAS requires to simulations covering a few tens of cubic Gigaparsecs in volume, and with a mass resolution sufficient to robustly identify haloes of at least $M \sim 10^{10} M_{\odot}$. In addition, an adequate temporal resolution is needed in order to resolve the mass accretion and merger history of dark matter structures. These specifications are very demanding in terms of computational resources, and are not met by any of the state-of-the-art simulations (e.g. Angulo et al., 2012; Watson et al., 2013). Therefore, we plan carry out a dedicated simulation program targeting the desired features, and also spanning the range of cosmological parameter space currently allowed by cosmological datasets, and with varying assumptions about the physical processes affecting simulated galaxies.

Another important aspect of the J-PAS simulation program will be the construction of accurate covariance matrices for the cosmological interpretation of data, in particular of the galaxy clustering, abundance of clusters and gravitational lensing signal. These goals require thousands of realizations of the cosmological observation. Since carrying out a large number of direct *N*-body simulation is beyond current computational capabilities, we plan the use of approximate methods (Angulo et al., 2013; Kitaura, 2013; White et al., 2013), which are built on top of an ensemble of low-resolution *N*-body simulation. All the aspects discussed will contribute towards the accuracy and correctness of analyses of J-PAS data.

The comparison between the observations from J-PAS and cosmological predictions from N -body simulations and semi-analytic models will be extended by creating simulated data products that more directly correspond to the actual observations, namely synthetic images and extracted source catalogues. We will use the Millennium Run Observatory (MRObs Overzier et al., 2013a) to produce physically-motivated, synthetic images of the night sky by adding the various observational effects to predictions from cosmological simulations. Halo merger trees based on the Millennium Run dark matter simulations in WMAP1 and WMAP7 cosmologies form the backbone for the semi-analytic modeling of galaxies inside haloes. This modeling is based on simple recipes for, e.g., gas cooling, star formation, supernova and AGN heating, gas stripping, and merging between galaxies. At each time step of the simulation, the physical properties of galaxies are translated into theoretical stellar populations in order to predict the spectra of galaxies. Light-cones are constructed that arrange the simulated galaxies on the sky in a way that is similar to how galaxies would appear in a galaxy redshift survey. Next, multi-band apparent magnitudes are calculated, including the effects of absorption by the intergalactic medium. The light-cone is then projected onto a virtual sky, and the positions, shapes, sizes and observed-frame apparent magnitudes of the galaxies are used to build a ‘perfect or ‘pre-observation image. The perfect image is fed into the MRObs telescope simulator that applies models for the T250+JPCAM system (e.g., pixel scale, readout noise, dark current, sensitivity and gain), the OAJ site conditions (e.g., sky background, extinction, point spread function), and the J-PAS observation strategy (e.g., exposures). The result is a synthetic J-PAS image of a simulated universe. In Fig. 19 we show an example of a simulated J-PAS image in the direction of a distant galaxy cluster observed in the filters g (blue), r (green), and z (red).

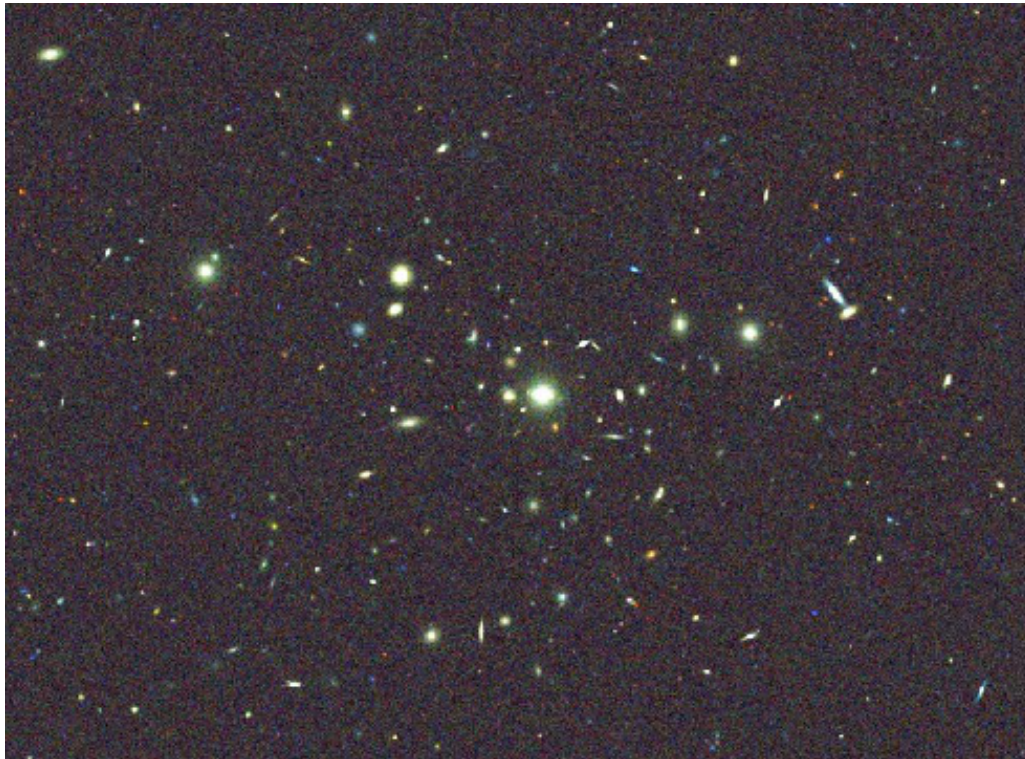


Figure 19: A simulated J-PAS image in the filters g (blue), r (green), and z (red), produced using the Millennium Run Observatory (see text for details).

The simulated J-PAS data set can be used, for example, for testing the data reduction pipeline, but also for testing many of the J-PAS science projects. For example, source extraction algorithms are applied to the simulated image, resulting in a catalogue of the apparent properties of all objects detected in the image. Then, photometric redshifts, SEDs or morphologies can be determined, and the results can be tested against the actual physical properties given for each object by the simulations. The object catalogues can also be cross-matched with higher level data available from the simulations to find, for example, the halo masses, the dark matter density field, or to look up progenitors and descendants.

3.2. *The J-PAS Cluster Survey*

The number density of galaxy clusters as a function of mass and redshift can be used to constrain cosmological parameters by measuring the growth of structure in the universe Borgani et al. (2001); Henry (2000); Gladders et al. (2007); Henry et al. (2009); Vikhlinin et al. (2009); Mantz et al. (2010); Rozo et al. (2010). The cluster mass function $N(M, z)$ probes both the growth factor and the evolution of cosmic volume, and hence can distinguish, a priori, between a cosmological constant and possible deviations from General Relativity. In particular, it depends jointly on the matter density, Ω_m , and on the amplitude of the primordial power spectrum through σ_8 . The evolution of the cluster mass function also provides sensitive constraints on the dark energy parameters (w_0, w_a). J-PAS, with its unprecedented volume coverage and redshift accuracy, will be able to map clusters and groups up to very early epochs ($z \sim 1$), and down to relatively small masses. Its capability to accurately measure the redshifts of line-emitting galaxies up to $z \sim 1.3$ will help avoiding biases in the determination of the galaxy content of each cluster. Finally, we will be able to calibrate optical richness or stellar mass content for the group and cluster candidates with dark matter mass haloes estimated from lensing with a very high precision due to the expected large number of clusters. As a result, J-PAS will produce the most complete and mass-sensitive cluster catalog available for cosmological and galaxy evolution studies.

Detecting galaxy clusters. The detection of galaxy systems and the completeness of the samples as a function of redshift are crucial for a cluster counting probe. There is a wide range of optical cluster finding algorithms that can be used in the J-PAS data, from methods using positional information of galaxies to detect over-densities to those which include observational properties of the potential member galaxies, like colors and magnitudes. Some of the most relevant methods in the literature are the cluster red sequence methods (Gladders & Yee, 2000; López-Cruz et al., 2004; Gladders & Yee, 2005; Wilson et al., 2008; Gilbank et al., 2011), the MaxBCG (Koester et al., 2007), the new Gaussian Mixture Brightest Cluster Galaxy (GMBCG) algorithm (Hao et al., 2010), the cut-and-enhance algorithm (Goto et al., 2002), the C4 cluster-finding algorithm (Miller et al., 2005), the counts in cells method (Couch et al., 1991; Lidman & Peterson, 1996), the Percolation Algorithms (Dalton et al., 1997; Botzler et al., 2004), the Voronoi Tessellation algorithm (Ramella et al., 2001; Kim et al., 2002; Lopes et al., 2004) or the Friends of Friends Algorithm (Huchra & Geller, 1982; Ramella et al., 2002; Botzler et al., 2004; Van Breukelen & Clewle, 2009) and adapted modifications to photo-z surveys Zandivarez et al. (2014), the Matched Filter technique (Postman et al., 1996, 2002) and later modifications: the Adaptive Matched Filter (Kepner et al., 1999), the Hybrid Matched Filter (Kim et al., 2002), the Simple Smoothing Kernels (Shectman, 1985), the Adaptive Kernel method (Gal et al., 2000, 2003) the 3D-Matched Filter (Milkeraitis et al., 2010) or the Bayesian Cluster Finder (Ascaso et al., 2012). For a review on cluster finder techniques, see Ascaso (2013) and references herein.

Accurate mass estimates are of utmost importance for studies of galaxy systems, and are absolutely necessary to do precision cosmology. Cluster masses, however, are not trivial to measure precisely. Triaxiality and projection effects can bias the dynamical masses determined by assuming virial relations; masses estimated through gravitational lensing are sensitive to assumptions about the isotropy of the mass distribution; masses estimated via the Sunyaev-Zel'dovich thermal effect are prone to blending and assymetrizing, potentially biasing the mass function (e.g. (Allen et al., 2011)); X-ray-derived masses are sensitive to places where hydrostatic equilibrium breaks down (either near the central AGN activity or even at large scales due to ongoing merging and or residual non-thermal pressure – (Dupke & Bregman, 2001), (Dupke & Bregman, 2001), (Nagai et al., 2007)), or because of gas clumping ((Nagai, & Lau, 2011)). Therefore, masses found using these techniques often disagree at a level that is insufficient to achieve the precision that is desired for maximal cosmological discriminatory power. These are particularly critical issues for photometric surveys, where redshift precision is limited and complementary corroborative data is unevenly found.

In order to circumvent this deficiency a significant amount of effort has been placed into determining the so-called mass proxies, i.e., indicators of the mass of clusters devised by inspecting the least important mass component of clusters – i.e., galaxies (often of only one Hubble type). These efforts have brought us impressive results, with sophisticated techniques for improving the scatter of the optical mass proxies (Andreon & Bergé, 2012; Munari et al., 2013; Rozo et al., 2009, 2011). With its excellent photo-z precision, J-PAS will be able to reduce significantly the galaxy membership noise for clusters and groups of galaxies. This, combined with weak lensing measurements, will provide much better grounds for richness (of various types) and mass relations.

The Probability Friend-of-friends (PFoF) cluster set. By using a mock galaxy catalogue tailored to the J-PAS depth and magnitude limit, a modified version of the Friends-of-Friends algorithm has been used by Zandivarez et al. (2014) to detect galaxy groups and to assess the reliability of the algorithm.

In that work, they built a light-cone mock catalogue using synthetic galaxies constructed from the Millennium Run Simulation I Springel (2005) combined with a semi-analytical model of galaxy formation developed by Guo et al. 2011. The mock catalogue comprises ~ 800000 galaxies down to an observer frame apparent magnitude of 23 in the SDSS i-band, with a median redshift of 0.72 and a maximum of 1.5 within a solid angle of $17.6deg^2$. The solid angle was chosen to avoid repetition of structures down to redshift 1 caused by the limited size of the simulation box. Photometric redshifts were assigned to each galaxy in the mock catalogue in a realistic way by using a technique described in Ascaso et al. 2014 (in prep.) and Arnalte-Mur et al. (2013).

The identification of groups in the mock catalogue was performed by using the adaptation of the original FoF algorithm to work with photometric redshifts developed by Liu et al. (2009). The redshift probability distribution functions for the galaxies were adopted as Lorentzian functions. The sample of photometric groups comprises 15512 groups with four or more members.

The reliability of the finder algorithm as a function of redshift was tested by computing the purity and completeness of the resulting sample. The purity and completeness were defined by a member-to-member comparison of the identified sample to a reference sample. The reference sample was adopted as the sample of groups that have four or more members with $i_{SDSS} < 23$, where the groups were previously identified in volume-limited catalogue in real space.

The reference sample of groups was obtained from a subsample of the J-PAS mock catalogue defined without introducing any flux limit or redshift space distortions (Zandiverez et al., 2014). They used the Friend of Friends (FoF, Huchra & Geller 1982) algorithm to detect groups on this ideal subsample, obtaining a sample of 201,032 groups with 4 or more galaxy members, within a solid angle of 17.6 deg^2 up to redshift 1.5. This will be considered also the reference sample in this work, in order to compare the detections with other methods. Additionally, we selected from the reference groups those that have 4 or more members with observed-frame magnitude $i_{SDSS} < 23$, which refer to those groups that could be identified in the flux limited catalogue. This will be called the restricted-reference sample, and it comprises 11294 groups.

Considering the fraction of photometric groups that are also in the reference sample and the sample of reference groups that can be recovered with this algorithm, they found that it is possible to identify a sample of photometric groups with less than 40% of completely false groups, while 60% of the underlying true groups are recovered. The purity of the photometric groups can be highly improved if only groups with more than ten members are considered (purity $> 90\%$ in the whole redshift range).

By applying this algorithm to the future J-PAS, it is expected to find around 700000 photometric groups with more than ten members, among which more than 90% would be related to real groups.

The Bayesian Cluster Finder (BCF) cluster set. Additionally, we used the mock galaxy catalogues from (Merson et al., 2013), which were built from a semi-analytical model of galaxy formation, applied to the halo merger trees extracted from a cosmological N-body simulation. The semi-analytical model that they use is the Durham semi-analytical galaxy formation model, GALFORM (Cole et al., 2000), which models the star formation and merger history for a galaxy. Among other physical processes, this model includes feedback as a result of SNe, active galactic nuclei (AGN) and photo-ionization of the intergalactic medium. The model predicts the star formation history of the galaxy and therefore the spectral energy distribution (SED). The population of dark matter (DM) haloes for the mock catalogue is extracted from the Millennium Simulation (Springel et al., 2005), a 2160^3 particle N-body simulation of the Λ Cold Dark Matter cosmology starting at $z = 127$ and hierarchical growing to the present day. The halo merger trees are constructed using particle and halo data stored at 64 fixed epoch snapshots spaced logarithmically. The minimum halo resolution is 20 particles, corresponding to $1.72 \times 10^{10} h^{-1} M_{\odot}$. Finally, the light-cone was constructed from this simulation by replicating the simulation box and choosing an orientation resulting into a 226.56 deg^2 light-cone. In addition, a flux cut in ~ 24 AB was applied to mimic the condition of the J-PAS survey. All the details can be found in (Merson et al., 2013).

In order to obtain realistic J-PAS-like photometric redshifts for this mock catalogue, we follow a similar approach to obtain photometry and photometric redshift as for the ALHAMBRA as in Ascaso et al. 2014 (in prep) and Arnalte-Mur et al. (2013). We first obtained spectral types from the original rest-frame photometry and spectroscopic redshifts in the mock by running the Bayesian Photometric Redshift package (BPZ, Benitez (2000); Benitez (2014)) with the ONLY_TYPE yes option. Then, we obtained consistent J-PAS photometry for these spectral types by using the J-PAS filter curve response and adding realistic noise. Finally, we obtained the photometric redshift estimations, together with spectral types and absolute magnitudes associated to the previous photometry by running again BPZ in normal mode. In previous work where we applied this technique (the ALHAMBRA survey), the photometric redshifts that we obtain are found to be very realistic as their performance is very similar to those obtained for real data (Molino et al, 2014).

In the next step, we detected galaxy clusters and groups in the J-PAS-like mock catalogue by using the Bayesian Cluster Finder (BCF, Ascaso et al. 2012, 2014). We performed a search in twenty-four redshift slices from $z = 0.1$ to $z = 1.2$, with redshift bins of $z = 0.05$. The core radius was selected as 1.5 Mpc, and the Luminosity Function has been chosen to have a value of $M^*(0) = -21.44$ and $\alpha = -1.05$ (Blanton et al. 2003). We calculated the expected $g - i$ and $i - z$ colors from synthetic spectra, and we artificially created these bands by calculating the contribution of each of the J-PAS narrow bands to the new synthetic band (see Molino et al 2014 for details). We also calculated the expected BCG magnitude-redshift relation for the given bands by performing a color transformation to the expected K-band. We merged the galaxy clusters following the same prescription as in Ascaso et al. 2014. The expected number of galaxy clusters and groups per square degree range between ~ 46 down to $5 \times 10^{13} M_\odot$ and ~ 75 down to $3 \times 10^{13} M_\odot$, obtaining an expected total number of structures between ~ 400.000 and 650.000 for the whole J-PAS down to $5 \times 10^{13} M_\odot$ and $3 \times 10^{13} M_\odot$ respectively.

The selection function. In order to assess the completeness and purity of our results, we compared with the initial set of clusters in the simulation. In Fig. 20, we show the completeness and purity results versus Dark Matter halo and its respective stellar mass interval respectively for the output results. According to this results, we are able to detect galaxy clusters with purity and completeness rates $> 80\%$ for clusters and groups down to $M \geq 3 \times 10^1 3M_\odot$ up to redshift 0.8 and down to $M \geq 5 \times 10^1 3M_\odot$ up to redshift 1.2. The extremely good quality of the photometric redshifts in the J-PAS survey make these results comparable to what we would expect for a low-resolution spectroscopic survey. In fact, the photometric redshift resolution becomes directly proportional to the inferior mass limit we can resolve according to our simulations.

3.2.1. Self-contained mass calibration

The superb seeing conditions ($< 0.7''$) of which the r -band filter is planned to be conducted will allow to estimate the masses of the clusters using the weak lensing technique, the only one sensitive to both dark and baryonic matter.

Since many observational properties of clusters correlate well with mass, we will be able to self-calibrate mass-observable relations. J-PAS will explore the relation between the mass of galaxy clusters obtained with weak gravitational lensing and the optical properties like number of member galaxies, stellar light or total stellar mass ($N_{\text{gal}}, L_{\text{tot}}, M_*^{\text{tot}}$). The latter showed to be a robust proxy of cluster mass at the same level of the best X-ray proxies (i.e. Y_X , the product of X-ray temperature, and gas mass) (Andreon & Bergé, 2012).

The scatter of the mass-observable relation is also an important issue when using it with cosmological purposes. To bring the errors of the scatter down to a few percent, J-PAS will adopt a self-calibration method, binning clusters using mass proxies and the redshift information to then stack the weak lensing signal of the clusters belonging to the same bin and measuring averaged masses. Detailed simulations have proven that averaging out over large number of clusters/groups is the most robust way to reduce the effects caused by triaxial of the halos and uncorrelated large scale structure along the line-of-sight, thus recovering the true value of the averaged mass within the bin (Spinelli et al., 2012) and decreasing the scatter of the scaling relations.

3.2.2. Figure of Merit

Here we assume the same fiducial cosmology as in previous Sections, i.e.: $h = 0.71$, $\Omega_m = 0.27$, $\Omega_L = 0.73$, $\Omega_b = 0.024$, $w_0 = -1.0$, $w_a = 0.$, $\sigma_8 = 0.8$, $n_s = 1.0$, $\tau = 0.09$, and $\Omega_K = 0$. Based on our previous predictions, we assume that the cluster catalog will reach down to a mass threshold of 5×10^{13} , up to $z = 1.2$, with a photometric redshift precision of $\sigma_z/(1+z) = 0.003$ and a mass-richness calibration dispersion of $\sigma_{\ln M} = 0.25$.

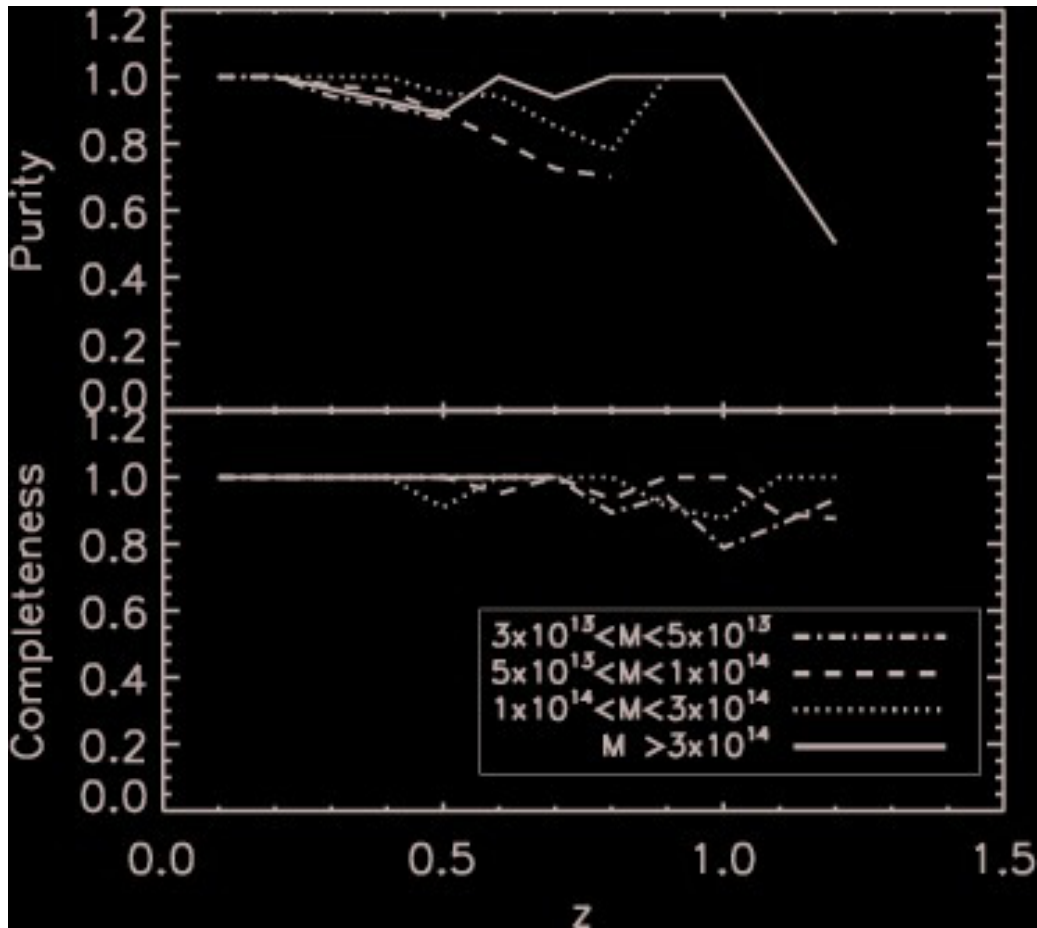


Figure 20: Completeness and purity rates as a function of redshift for different dark matter halo masses for the J-PAS survey. We see that the purity rates remains constant as a function of redshift as $\sim 80\%$, whereas the completeness rates is always higher than 80% and it starts to decrease at $z \sim 0.8$.

The covariance matrix then, can be expressed as (Wang et al., 2004; Lima & Hu, 2004; Cunha et al., 2010):

$$C = \langle (m_{i\mu} - \bar{m}_{i\mu})(m_{j\nu} - \bar{m}_{j\nu}) \rangle = \bar{m}_{i\mu} \bar{m}_{j\nu} b_{i\mu} b_{j\nu} \int \frac{d^3k}{(2\pi)^3} W_i^*(k) W_j(k) P(k, z_{ij}), \quad (27)$$

where i, j refer to bins in redshift and μ, ν bins in mass,

$$m_{i\mu} = \bar{m}_{i\mu} (1 + b_{i\mu} \delta_i), \quad \delta(x) = \frac{\rho(x) - \bar{\rho}}{\bar{\rho}},$$

where $\delta(x)$ is the dimensionless density perturbation of the underlying matter distribution.

For a detailed window treatment depending on the survey, see Hu & Kravtsov (2003). According to their Eq. (6), the windows can be divided up into slices in redshift. If we consider a series of slices in redshift at comoving distances r_i and widths δr_i , with a field of radius Θ_s in radians and a flat spatial geometry, then the window function are written as:

$$W_i(k) = 2 \exp^{ik_{\parallel} r_i} \frac{\sin(k_{\parallel} \delta r_i / 2)}{k_{\parallel} \delta r_i / 2} \frac{J_1(k_{\perp} r_i \Theta_s)}{k_{\perp} r_i \Theta_s},$$

where $k^2 = k_{\perp}^2 + k_{\parallel}^2$.

Now, following Wang et al. (2004); Cunha et al. (2010), we compute the mean number of counts and the bias term as:

$$\bar{m}_{i\mu} = \Delta\Omega \int \frac{dV(z_i)}{dz} p_i(z_i^p | z) dz \int_{M_{obs}^{\mu}}^{M_{obs}^{\mu+1}} \frac{dM_{obs}}{M_{obs}} \int d \ln M p_{i\mu}(M_{obs} | M) \frac{dn}{d \ln M}, \quad (28)$$

$$b_{i\mu} = \frac{1}{\bar{m}_{i\mu}} \Delta\Omega \int \frac{dV(z_i)}{dz} p_i(z_i^p | z) dz \int_{M_{obs}^{\mu}}^{M_{obs}^{\mu+1}} \frac{dM_{obs}}{M_{obs}} \int d \ln M p_{i\mu}(M_{obs} | M) b(M) \frac{dn}{d \ln M}, \quad (29)$$

where $\Delta\Omega$ is the solid angle of the survey, and $\frac{dV}{dz}$ is the comoving volume unit at redshift z_i :

$$\frac{d^2V}{d\Omega dz} = D_H \frac{(1+z)^2 D_A^2}{E(z)},$$

Here, $p_i(z_i^p | z)$ and $p_{i\mu}(M_{obs} | M)$ are the probabilities of measuring a photometric redshift z_i^p , given the true cluster redshift z and M_{obs} , or given the true mass M respectively. $\frac{dn}{d \ln M}$ is the halo density distribution and $b(M)$ is the bias function. The two latter ones are extracted from simulations. The bias parameter of halos of a fixed mass M is assumed to be scale independent (Sheth & Tormen, 1999):

$$b(M) = 1 + \frac{(a\delta_c^2/\sigma^2) - 1}{\delta_c} + \frac{2p}{\delta_c(1 + (a\delta_c^2/\sigma^2)^p)}, \quad (30)$$

where $a = 0.75$, $p = 0.3$ and $\delta_c = 1.686$ is the threshold linear overdensity corresponding to spherical collapse in an Einstein-de Sitter universe.

The differential comoving number density of clusters is given by Jenkins et al. (2001) (although there are other models that one could use for this purpose, such as Tinker et al. (2008)):

$$\frac{dn}{d \ln M} = 0.3 \frac{\rho_m}{M} \frac{d \ln \sigma^{-1}}{d \ln M} \exp(-|\ln \sigma^{-1} + 0.64|^{3.82}), \quad (31)$$

where $\rho_m = \rho_0 \Omega_m$ is the mean matter density, with $\rho_0 = 3H_0^2/(8\pi G)$. The variance σ is the rms amplitude of mass fluctuation inside a particular spherically symmetric window, defined as:

$$\sigma^2 = \int \frac{d^3 k}{(2\pi)^2} k^2 P(k) |W(kR)|^2.$$

$P(k)$ is the linear power spectrum, and $W(kR)$ is the Fourier transform of the real-space window function $W(x)$, which we have assumed, as usual, to be given by real-space spherical top hat of radius R , so:

$$\tilde{W}_R(k) = \frac{3}{(kR)^3} (\sin(kR) - kR \cos(kR)),$$

where M is the mass included in the window:

$$M = \frac{4\pi\rho_m R^3}{3}.$$

Finally, the total covariance matrix is given by (Lima & Hu, 2005; Cunha et al., 2010):

$$C_{ij} := C_{ij} + m_i \delta_{ij},$$

where the last term refers to the (shot) noise matrix, and m_i are the cluster counts in each bin. In order to make a realistic forecast of the optical cluster constraints, one must marginalize over nuisance parameters which are introduced to account for the mass and redshift uncertainties.

The Mass-Observable relation. The mass selection function can be written as (Lima & Hu, 2007; Cunha et al., 2010):

$$p(M_{obs}|M) = \frac{1}{\sqrt{2\pi}\sigma_{\ln M}} \exp(-\chi^2(M_{obs})), \quad (32)$$

where:

$$\chi(M_{obs}) = \frac{\ln M_{obs} - \ln M - \ln M^{bias}(M_{obs}, z)}{\sqrt{2}\sigma_{\ln M}}. \quad (33)$$

Then, we introduce a series of nuisance parameters as in Lima & Hu (2007), although more complicated forms can also be modified to be dependent also on mass as in Cunha et al. (2010):

$$\ln M^{bias}(M_{obs}, z) = \ln M_0^{bias} + a_1 \ln(1+z), \quad (34)$$

and

$$\sigma_{\ln M}^2 = \sigma_0^2 + \sum_{i=1}^3 b_i z^i, \quad (35)$$

Hence, we have six nuisance parameters whose fiducial values can be chosen, according to Lima & Hu (2007), as $(\ln M_0^{bias} = 0, a_1 = 0, \sigma_0 = 0.25, b_1 = 0, b_2 = 0, b_3 = 0)$.

Photometric redshift true cluster redshift relation. The probability of measuring a photometric redshift, z^p given the true cluster redshift z , can be parametrized as (Lima & Hu, 2007; Cunha et al., 2010):

$$p(z^p|z) = \frac{1}{\sqrt{2\pi}\sigma_z} \exp(-y^2(z^p)), \quad (36)$$

where:

$$y(z^p) = \frac{z^p - z - z^{bias}}{\sqrt{2}\sigma_z}. \quad (37)$$

Here z^{bias} is the photometric redshift bias, and σ_z is the scatter in the photo- z 's. We add two more nuisance parameters as ($z_0^{bias} = 0.$, $\sigma_z = 0.003$), accounting for a total of eight nuisance parameters to marginalize over before we can say anything about cosmological parameters.

Fisher matrices and priors. Finally, we compute the Fisher matrix as:

$$F_{lm} = \sum_{ij\mu\nu} \frac{\partial \bar{m}_{i\mu}}{\partial p_l} (C^{-1})_{ij\mu\nu} \frac{\partial \bar{m}_{j\nu}}{\partial p_m} \quad (38)$$

where l, m run over the cosmological parameters. This Fisher matrix can be combined with any other Fisher matrix – as long as the two datasets are uncorrelated. As usual, marginalized constraints for any parameter (or subsets of parameters) are obtained by summing all the relevant Fisher matrices, then inverting the total Fisher matrix.

With regard to the dark energy equation of state, we forecast that J-PAS will be able to reach a Figure of Merit (FoM; see the previous Subsection) of approximately 170, when we combine cluster counts with *Planck* and Stage-II experiments, as described in Albrecht et al. (2006). We would like to stress the key role of the nuisance parameters (of which we have eight, as described above), which parametrize our ignorance about the mass calibration, redshift bias and other uncertainties.

3.3. Joint constraints on Dark Energy from BAOs and cluster counts

We can combine the constraints obtained through the measurements of BAOs, and those coming from cluster counts. Since the information about the clustering of halos was not used in the derivation of cosmological constraints from counting the numbers of clusters (see Sec. 3.2), we can simply add the Fisher matrices for the two datasets.

In Fig. 21 we show the constraints for the equation of state of dark energy for cluster counts alone (outer, red contour), for BAOs alone (blue contour), and BAOs combined with cluster counts (inner, black contour). In all cases *Planck* and Stage-II priors were employed (Albrecht et al., 2006). We can see that the constraints from BAOs and cluster counts are comparable, but there is a substantial complementarity between the two.

The combined power of cluster counts and BAOs can be gleaned from the DETF Figure of Merit (FoM). The FoM of cluster counts, combined with *Planck* and Stage-II priors, is approximately 175. In Table 12 we show the forecasted FoMs for several combinations of the datasets.

Table 12: Figure of merit.

Test	LRGs	ELGs	QSOs	All
BAOs + <i>Planck</i> + Stage II	87	121	100	163
BAOs + Clusters + <i>Planck</i> + Stage II	195	222	201	256

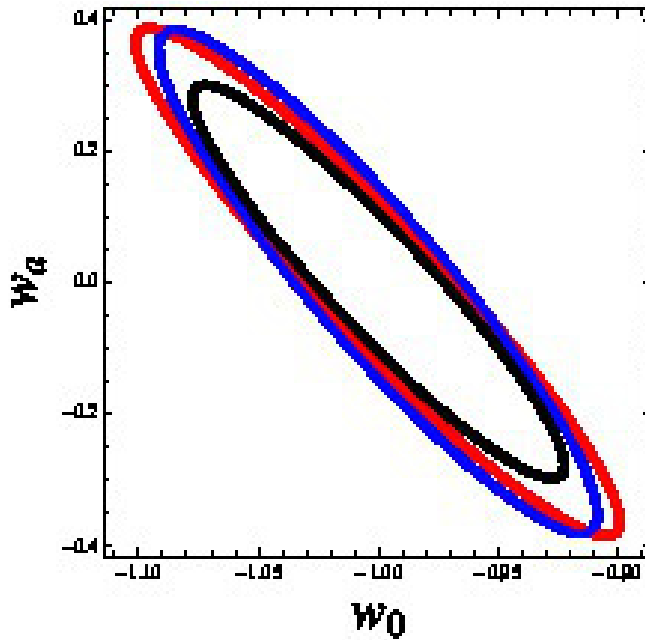


Figure 21: Constraints for the dark energy equation of state parameters w_0 and w_a from cluster counts alone (outer, red contour), from BAOs alone (blue contour), and BAOs combined with cluster counts (inner, black contour). We used *Planck* and Stage-II priors.

3.4. The J-PAS SN Cosmological Survey

Type-Ia supernovae (SNeIa) comprise one of the four main observables that will be the keys to understand the origin of the recent acceleration in the expansion of the Universe. However, there are many aspects of SNeIa properties and their relation to their environments that remain poorly understood (Conley et al., 2011; Smith et al., 2012; Kessler et al., 2013). For instance, recent studies have pointed out that passive galaxies host faster-declining SNeIa that follow a different color-luminosity relation and that are more luminous after corrections based on light-curve stretch and color (Sullivan et al., 2006; Lampeitl et al., 2010). Moreover, older passive galaxies – as those found in galaxy clusters – tend to host dimmer and even briefer SNeIa (Gallagher et al., 2008; Xavier et al., 2013). Some of these characteristics were already shown to introduce more scatter and also systematic biases to SNeIa distance determinations and to the cosmological parameters derived from them (Kelly et al., 2010; Lampeitl et al., 2010; Sullivan et al., 2010), but these effects and relations are still not fully understood. This is in part due to the coarse characterization of the supernovae host galaxies, to the sizes of SNe Ia sub-samples in each environment and to the small number of low-redshift SNeIa that have been studied. The J-PAS Supernova Survey will be a massive, low and intermediate redshift ($z < 0.4$) supernova survey (the only one, to our knowledge, being planned at the moment) that will serve to fill that gap.

Future SNeIa experiments will no longer be sample-size limited. In order to achieve a precision of $\sim 1\%$ in the dark energy equation of state parameter $w = P/\rho$, it will be crucial to control systematic uncertainties. Many of these uncertainties – like dust extinction, rest-frame ultraviolet variability, intrinsic color variations and correlations between SNe and environment properties – will need large samples of well observed SNe and host galaxies. A large sample of low redshift ($z < 0.1$) objects, with which we can study the properties of SNeIa and their hosts in a cosmology-independent way, is also important.

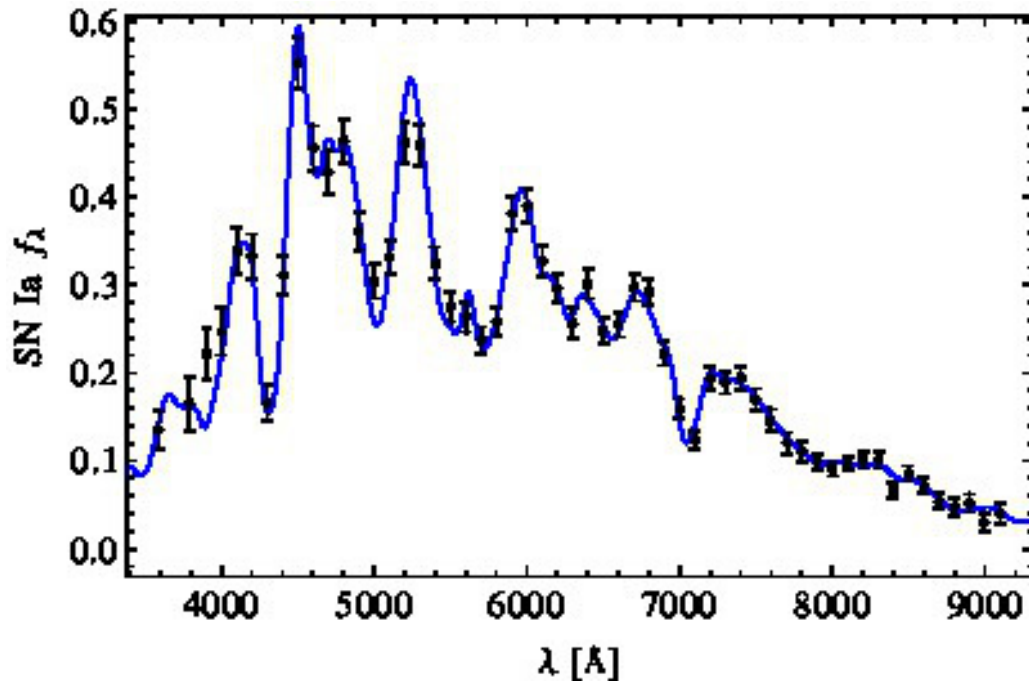


Figure 22: Expected J-PAS photometry (black dots) for a SNe Ia at $z = 0.148$, seven days after its luminosity peak, and its true spectrum in arbitrary units (blue line). SNe spectral features are broad enough to be detected. To be concise we present the measurements of the whole spectrum on the same day. The reader should keep in mind that, in a given epoch, J-PAS will image the SNe in 14 filters.

Due to the broad features of the spectra of SNeIa, the filter system of J-PAS makes it an ideal instrument not only to discover them, but also to measure their light curves (albeit often using different filters), to characterize their types (SN Ia/Ib/Ic/II etc.) and to photometrically estimate their redshifts. For a glimpse of J-PAS SNe photometry, see Fig. 22. Due to the imaging nature of the survey, the local environments of the supernovae will also be fully characterized – something that has never been done before in a systematic, massive way. Finally, due to the large area of the survey, the number of SNeIa will be large enough that we can separate them (and their environments) into different subtypes without running into problems related to low statistics.

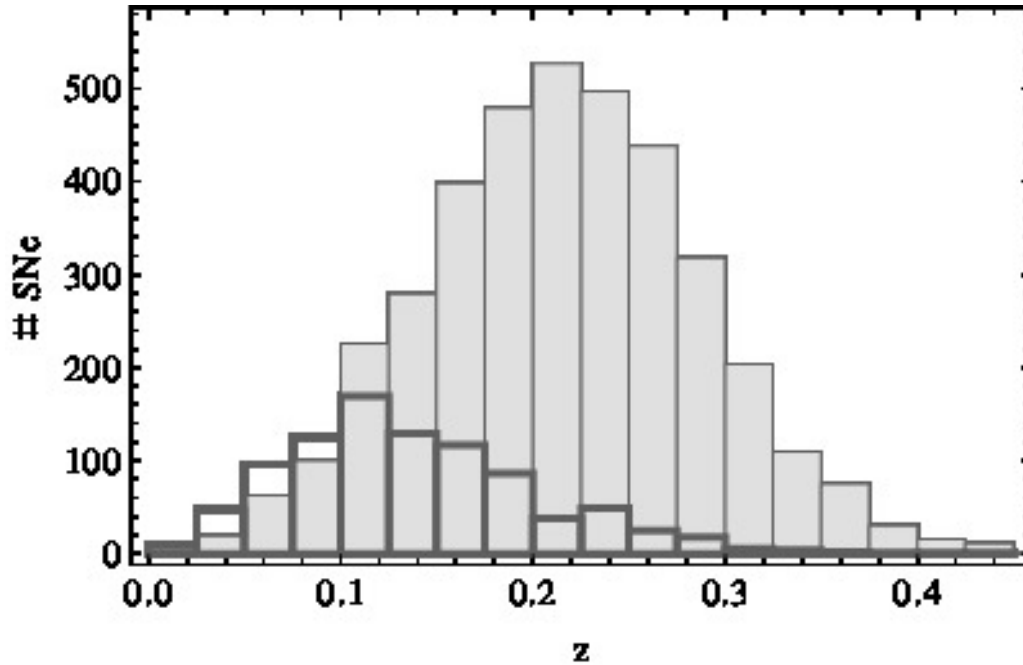


Figure 23: Expected SNe Ia (gray filling, thin contours) and CCSNe (no filling, thick contours) redshift distribution for J-PAS. The total number of objects are ~ 3800 SNeIa and ~ 900 CCSNe. The contamination between these samples should be less than 4%.

Optical surveys are deemed to miss a fraction of exploding supernovae due to host galaxy extinction. This effect is particularly relevant in LIRGs (Luminous Infrared Galaxies) and ULIRGs (Ultraluminous Infrared Galaxies), whose contribution to the SN rate increase with redshift (Mannucci et al., 2007; Mattila et al., 2012). Since J-PAS will be sensitive to SNe up to $z \sim 0.4$, we will be able to estimate the fraction of missing SNe with unprecedented accuracy (current estimates are between 5% up to 40% (Mannucci et al., 2007; Mattila et al., 2012)).

To estimate the J-PAS Supernova Survey performance, we ran detailed simulations with the SNANA software package (Kessler et al., 2009), Peter Nugent’s Core Collapse Supernovae (CCSNe) templates⁶ and the SALT2 SNeIa light-curve model (Guy et al., 2007), assuming that the relation between the distance modulus and the SNe Ia observables, $\mu = m_B - M + \alpha x_1 - \beta c$, has an intrinsic scatter of $\sigma_{\text{int}} = 0.14$. We set the SNe redshifts to their host galaxies *photo-z*s, which we assumed to have an uncertainty of $\sigma_z = 0.005(1 + z)$. The SNe typing was performed with the *psnid* software (Sako et al., 2011) in the SNANA package. Although the results depend on the exact observation schedule which can be affected by other circumstances, our simulations show that, for a conservative scenario, J-PAS will be able to detect and characterize around 3,800 SNeIa and 900 CCSNe up to $z \sim 0.4$ and approximately 190 SNeIa and 280 CCSNe at low redshifts ($z < 0.1$). Their redshift distributions are shown in Fig. 23.

Survey	σ_{m_B}	σ_{x_1}	σ_c	σ_{T_0}	σ_{μ}^*	σ_{μ}
<i>photo-z</i> SDSS	0.074	0.72	0.066	0.87	0.21	0.25
<i>spec-z</i> SDSS	0.069	0.69	0.043	0.77	0.13	0.19
J-PAS	0.078	0.54	0.046	0.95	0.12	0.18

Table 13: Average errors in the SNeIa SALT2 light-curve parameters (apparent magnitude m_B , light-curve width x_1 , color c , epoch of maximum luminosity in days T_0 and the distance modulus μ ignoring and including the intrinsic scatter σ_{int}) for J-PAS and for simulations of the SDSS Supernova Survey, both with photometry only (*photo-z* SDSS) and with spectroscopy of all SNe hosts (*spec-z* SDSS). J-PAS have similar data quality to photometric surveys backed up by spectroscopy and much better quality than purely photometric surveys.

To classify a particular simulated light-curve as a ‘‘SN type X’’, we required that its fit by a type X template should have a χ^2 p -value of at least 0.01. Also, the probability P_X that the light-curve belongs to the type X SNe, calculated by `psnid`, should be higher than 0.90. Our simulations show that J-PAS can achieve low contamination rates (less than 4%) for both SNeIa and CCSNe samples. For SNeIa studies that require a higher purity, further data cuts on the x_1 – c SALT2 parameters plane like the one described by (Campbell et al., 2013) can lead to samples with ~ 4000 objects and less than 1% contamination.

To evaluate the SNeIa data quality, we analyzed the average errors on the SALT2 light-curve parameters by calculating the root mean square (rms) of the difference between their fitted and their true values. While purely photometric broad band surveys can detect and measure light-curves of many thousands of SNe, the lack of a good redshift prior undermines its SNe data quality. The use of spectroscopy for constraining the SNe host galaxy’s redshift significantly improves the data quality but presents a bottleneck for sample sizes. Table 13 shows the average errors for J-PAS and, as reference points, for simulations of the SDSS Supernova Survey (Frieman et al., 2008), which have a similar redshift distribution. With the help of its excellent host galaxy *photo-z*, J-PAS can perform as well as broad band surveys backed up by spectroscopy and much better than purely photometric broad band surveys. This advantage (and the full characterization of the SNe’s host galaxies) will be beneficial not only for supernovae discovered by J-PAS but for all past and future SNe from other surveys, provided they overlap with J-PAS footprint. For J-PAS in particular, its narrow band filters will allow for the study of correlations between SNe spectral features and broadband properties like light-curve width and color.

3.5. The J-PAS Lensing Survey

The combination of two superb characteristics of the OAJ, namely the quality and the time stability of its median 0.71’’ seeing (Moles et al. 2010, PASP, 122, 363), with a broad band filter in JPCam, should yield an extremely high quality image of the whole northern sky at a very reasonable cost of observing time and effort. Together with our redshift information, the lensing measurements would produce an outstanding dataset for cosmic lensing studies many years before the arrival of Euclid.

3.5.1. Cosmic shear

The most obvious application is cosmic-shear tomography that probes both expansion of the universe and the growth of structures by the variation of the lensing strength between lens and source slices at different redshifts. With the precision of the photometric redshift estimates, we should be able to establish ~ 10 non-overlapping slices which will not only be powerful on its own, but enable thorough systematics tests, crucial for any reliable weak-lensing analysis. We refer to the extensive literature on this topic (see e.g. Weinberg et al. (2013) for a recent review).

⁶http://supernova.lbl.gov/~nugent/nugent_templates.html

Another promising application is the shear-ratio test (Jain & Taylor, 2003; Bernstein & Jain, 2004), which probes the geometry of the universe from the scaling of the lensing signal with redshift. Because this application does favor deeper surveys to get a long lever arm, a larger number of non-overlapping slices at redshifts below 0.5 can only yield a significant measurement if the lensing data is truly exquisite. As an alternative route, one could attempt to construct a high-significance lensing analysis by performing the shape measurement simultaneously across several of the narrow-band filters and the broad-band filter. Modern model-fitting codes (e.g. Miller et al., 2013; Zuntz et al., 2013) can in principle work in this mode, provided an accurate PSF model can be constructed in each of the filters and that the filters cover a similar wavelength range so that changes to the morphology remain minor.

This approach would have several advantages: First, it limits the negative influence of pixel noise, which constitutes the most prominent systematic bias in weak-lensing measurements today (Massey et al., 2007; Kitching et al., 2012; Melchior & Viola, 2012). Second, it would allow us to extend the magnitude and redshift range, for which we can get reliable shape measurements, critical to both cosmological applications as pointed out above. Third, it would virtually eliminate the chromatic mismatch between the stars, which are used to build the PSF models, and the galaxies (Cypriano et al., 2010).

The survey design is advantageous also for treating the most relevant astrophysical systematic: intrinsic alignments. Precise photo-zs will enable us to exclude pairs of galaxies at the same redshift, whose ellipticities are intrinsically coupled. It will furthermore allow a good discrimination of early-type galaxies, for which intrinsic alignments have been confirmed already (Mandelbaum et al., 2006), from late-type galaxies, for which the current upper limits indicate a much smaller amount of alignment (Hirata et al., 2007; Mandelbaum et al., 2011).

3.5.2. *Galaxy-galaxy lensing*

Given the relatively shallow depth of J-PAS (at least when using only the broad-band filter), galaxy-galaxy lensing is statistically even more powerful than cosmic-shear measurements. It can be utilized for several kinds of analyses, most prominently constraining the galaxy bias. Because of its multitude of filters, J-PAS will be able to discern several different lens populations, which in turn should allow us to constrain more complex halo-occupation models. This also presents a much faster and scalable approach compared to previous work that mostly relied on spectroscopic follow-up to define the lens samples (e.g. Seljan et al., 2005; Hirata et al., 2007; Reyes et al., 2011). A straightforward extension is the incorporation of galaxy clustering information. For the substantial advantages of this combination, we refer to Yoo & Seljak (2012).

3.5.3. *Cluster Weak Lensing*

Substantial progress has been made through numerical simulations in understanding the formation and structure of collisionless dark-matter (DM) halos in quasi gravitational equilibrium, governed by nonlinear growth of cosmic density perturbations. In the standard Λ CDM paradigm of hierarchical structure formation, galaxy-cluster sized halos form through successive mergers of smaller halos, as well as through smooth accretion of matter along surrounding filamentary structures (Colberg et al., 2000). Cluster halos are located at dense nodes where the large-scale filaments intersect, generally triaxial reflecting the collisionless nature of DM, and elongated in the preferential infall direction of subhalos, namely, along surrounding filaments.

The internal structure of DM halos constitutes one of the most distinct predictions of the CDM paradigm. N-body simulations of collisionless CDM established a nearly self-similar form for the spherically-averaged density profile $\rho(r)$ of DM halos (Navarro et al, 1997, hereafter Navarro-Frenk-White, NFW) over a wide range of halo masses, with some intrinsic variance associated with mass assembly histories and dynamical structure of individual halos (Jing & Suto, 2000; Tasitsiomi et al., 2004; Navarro et al., 2010). The degree of mass concentration, $c_{200} = r_{200}/r_s$, is predicted to correlate with halo mass, since DM halos that are more massive collapse later on average, when the mean background density of the universe is correspondingly lower (Bullock et al., 2001; Neto et al., 2007). Accordingly, cluster-sized halos are predicted to be less concentrated than less massive systems, and to have concentrations of $c_{200} \sim 3 - 4$ (Duffy et al., 2008; Bhattacharya et al., 2013).

Massive clusters serve as powerful gravitational lenses, producing various detectable effects, including deflection, magnifying and shearing of the images of distant background sources (Bartelmann & Schneider, 2001). Importantly, there is a weak-lensing regime where lensing effects can be linearly related to the mass distribution, which allows us to reconstruct the cluster mass distribution in a model-independent way. Weak-lensing shear offers a direct means of probing the total matter distribution of clusters (Kaiser & Squires, 1993) irrespective of the physical nature, composition, and state of lensing matter (Okabe & Umetsu, 2008), providing a direct probe for testing well-defined predictions (Oguri & Takada, 2011).

Lensing magnification provides complementary observational alternatives to gravitational shear (Broadhurst et al., 1995; Umetsu & Broadhurst, 2008; Umetsu et al., 2011; Hildebrandt et al., 2011; Ford et al., 2012; Umetsu, 2013; Coupon et al., 2013). Magnification can influence the observed surface density of background sources, expanding the area of sky, and enhancing the observed flux of background sources (Broadhurst et al., 1995). The former effect reduces the effective observing area in the source plane, decreasing the source counts per solid angle. The latter effect increases the number of sources above the limiting flux because the limiting luminosity at any background redshift lies effectively at a fainter limit. The net effect is known as magnification bias and depends on the steepness of the source number counts.

Magnification bias can be combined with shear to obtain a model-free determination of the projected mass profiles of clusters (Schneider et al., 2000; Umetsu & Broadhurst, 2008; Umetsu et al., 2011; Umetsu, 2013), effectively breaking the mass-sheet degeneracy inherent in a standard weak-lensing analysis based on shape information alone (Schneider & Seitz, 1995). Recent Subaru weak-lensing work established that deep multicolor imaging allows us to simultaneously detect the observationally independent shear and magnification signals. The combination of shear and magnification allows us not only to perform consistency tests of observational systematics but also to significantly enhance the precision and accuracy of cluster mass estimates (Rozo & Schmidt, 2010; Umetsu et al., 2012; Umetsu, 2013).

Unlike the shearing effect, magnification is sensitive to the sheet-like structure, so that making accurate magnification measurements is crucial for a robust statistical detection of the two-halo term contribution due to large-scale structure associated with the central clusters (Umetsu et al. 2014, in preparation).

In the J-PAS survey, we will couple our high-precision multi-band photometry and deep broadband imaging with cluster weak gravitational lensing to test fundamental predictions from structure formation models with unprecedented precision.

The J-PAS survey will allow us to measure simultaneously the weak-lensing shear and magnification effects from well-defined samples of background galaxies, free from significant contamination of unlensed cluster member and foreground galaxies. Specifically, the main scientific objectives that we will address are the following:

1. Halo density profile and mass-concentration relation: The stacked tangential-shear signal $\Delta\Sigma(R) = \Sigma(<R) - \Sigma(R)$ around a statistical sample of clusters is a sensitive probe of the internal structure of halos within the virial region, where the predicted two-halo contribution $\Delta\Sigma_{2h}$ is one-order smaller than that of the one-halo component $\Delta\Sigma_{1h}$ (e.g., Oguri & Hamana, 2011). With the J-PAS survey, we will define homogeneous samples of groups and clusters, and obtain the ensemble-averaged halo mass profiles, to compare with a family of standard density profiles, such as the NFW, truncated variant of NFW, and Einasto profiles, predicted for CDM halos in gravitational equilibrium. We will establish the halo c - M relation as a function of halo mass and redshift, which can be self-consistently obtained from J-PAS data alone. We will also constrain the mass dependence of the Einasto shape parameter to compare with predictions from numerical simulations (Gao et al., 2008).
2. Halo mass-bias relation, $b_h(M, z)$: The stacked weak-lensing signals on sufficiently large scales R can be used to determine the clustering strength of the halos, which is proportional to $b_h\sigma_8^2$ (Johnston et al., 2007; Covone et al., 2014). We will measure this clustering strength as a function of halo mass and redshift, by combining the observationally-independent shear and magnification effects for greater sensitivity.
3. Shear-ratio geometric tests: The amplitude of weak lensing should increase with source distance, rising steeply behind a lens and saturating at high redshift (Taylor et al., 2007; Medezinski et al., 2011). Such a characteristic geometric dependence of the lensing strength can be examined in a model-independent manner by using unbiased shape and photo- z measurements from the J-PAS survey. We will measure the relative lensing strength of source galaxies behind cluster samples as a function of redshift, for providing model-free constraints on the cosmological parameters.

3.5.4. Cluster strong lensing

In the center of the cluster (up to few hundred kpc), where the surface mass density is high enough, often multiple images of background sources are seen (e.g. Kneib et al. 1993; Broadhurst et al. 2005; Zitrin et al. 2012(b); Richard et al. 2010; Limousin et al. 2010, see also a review by Kneib & Natarajan 2011). As multiple images should be mapped back to the same single source, these are used then to place tighter (and high-resolution) constraints on the inner mass distribution, which can then be importantly combined with the independent WL measurements. We plan to incorporate well-tested and commonly-used methods for SL analyses and mass modeling, in various different parametrizations (e.g. Broadhurst et al. 2005; Coe et al. 2008; Zitrin et al. 2012(b); Jullo et al. 2007).

The identification of multiple images, however, is usually a very time consuming task, and often requires very high resolution space imaging. As a response, we had developed and implemented in recent years a unique modeling method which is guided primarily by the cluster member luminosity distribution in the cluster. The success of this method is remarkable - so that unprecedented numbers of multiple images can be in fact be found automatically by the luminosity-guided model itself without using any images a priori as constraints (e.g. Broadhurst et al. 2005; Zitrin et al. 2009a,(b), 2013b,a). Following the success of this "Light-Traces-Mass" method in identifying multiple-images simply by following the light distribution, we have generalized it to *automatically* map the matter in galaxy cluster cores, particularly useful for large sky surveys, by scaling their light distribution using extrapolations from clusters where multiple images are already known. The success of this method and its implementation in 10,000 SDSS clusters were shown in Zitrin et al. (2012a). In addition, this method can help traces cosmic or structure evolution, as we showed in the works mentioned above. We plan to perform the same automated procedure also here, so that cluster maps can be reproduced rapidly and automatically.

In addition, recent efforts have proven larger success in identifying arcs in large sky surveys (e.g. Maturi et al. 2013; Bayliss et al. 2011). Combined with our automated lens model, this will reveal giant arcs (highly stretched and distorted multiply imaged galaxies), which can then be used to refine the lens model. Independently, the number counts of giant arcs was claimed to add constraints on cosmology (e.g. Bartelmann et al 1998; Horesh et al. 2011).

3.5.5. Cross-correlation with *Herschel*

The magnification bias due to weak lensing modifies the galaxy angular correlation function because the observed images do not coincide with true source locations (Gunn, 1967; Kaiser, 1992; Moessner et al., 1998; Loverde et al., 2008), but the effect is generally minor and difficult to single out. A unambiguous manifestation of weak lensing is the cross-correlation between two source samples with non-overlapping redshift distributions. The occurrence of such correlations has been tested and established in several contexts (see, e.g. Scranton et al., 2005; Ménard et al., 2010; Bartelmann & Schneider, 2001, and references therein).

Since the gravitational magnification decreases the effective detection limit it is obvious that the amplitude of the magnification bias increases with increasing steepness of the number counts of background sources and is then particularly large at sub-mm wavelengths where the counts are extremely steep (Clements et al., 2010; Oliver et al., 2010). At the same time, for a survey covering a sufficiently large area the counteractive effect on the solid angle is small (Jain & Lima, 2011). A substantial fraction of galaxies detected by deep large area *Herschel* surveys at 250, 350 and 500 μm with the Spectral and Photometric Imaging Receiver (SPIRE; Griffin et al., 2010) reside at $z \gtrsim 1.5$ (Amblard et al., 2010; Lapi et al., 2011) and therefore constitute an excellent background sample for the J-PAS galaxies, which are located at $z \lesssim 1.4$ (with a peak in the redshift distribution at $z \ll 1$). In particular, two of the largest area extragalactic surveys carried out by the *Herschel* space observatory (Pilbratt et al., 2010), the *Herschel* Multitiered Extragalactic Survey (HerMES; Oliver et al., 2012) and the *Herschel* Astrophysical Terahertz Large Area Survey (H-ATLAS; Eales et al., 2010) cover $\gtrsim 200 \text{ deg}^2$ in common with the J-PAS survey.

A first attempt at measuring lensing-induced cross-correlations between *Herschel*/SPIRE galaxies and low- z galaxies was carried out by Wang et al. (2011). Later on, González-Nuevo et al. (2014) report a highly significant spatial correlation between galaxies with $S_{350\mu\text{m}} \geq 30 \text{ mJy}$ detected in the equatorial fields of H-ATLAS ($\simeq 161 \text{ deg}^2$) with estimated redshift $\gtrsim 1.5$ (26,630 sources) and SDSS galaxies at $0.2 \leq z \leq 0.6$ (686,333 sources). The significance of the measured cross-correlation is much higher than those reported so far for samples with non-overlapping redshift distributions selected in other wavebands.

These works demonstrated that it possible to achieve similar, or even better, measured cross-correlation signal significance, compared with the QSO case, with a reduce number of foreground sources. These results open the possibility to extend the analysis on the cross-correlation function to different redshift bins and therefore, to study the evolution of quantities as the typical halo mass, the number of halo satellites or the lensing optical depth. On this respect J-PAS will provide the required large foreground sample with accurate enough photometric redshifts in order to split the cross-correlation analysis in at least $\sim 3 - 4$ redshift bins between $z = 0.2 - 1.0$.

3.6. Correlations with the Cosmic Microwave Background Anisotropies (CMB)

Apart from the blue/red-shift on CMB photons induced by the ISW in over/under-dense regions, the cross-correlation of a J-PAS like survey with observations in the millimeter like those from WMAP⁷, *Planck*⁸, ACT⁹ or SPT¹⁰ offer a wealth of cosmological tests, related to the physics of galaxy formation, the motion of matter and bulk flows, lensing of the CMB and the search for the missing baryons. In this section we will briefly address foreseen ISW analyses together with all those new approaches, leaving detailed forecasts for future studies.

3.6.1. Integrated Sachs Wolfe effect

The late integrated Sachs-Wolfe effect (ISW) describes the gravitational blue/red-shift imprinted on photons of the Cosmic Microwave Background (CMB) radiation as they travel through large scale, time dependent gravitational potentials at low redshifts ($z < 2$). In an accelerating universe, large scale gravitational potentials shrink and CMB photons leave wells that have become *shallower*, hence experiencing a gravitational blue-shift. The opposite mechanism works for large scale voids. This mechanism of gravitational blue/red-shift of CMB photons was first described by (Sachs & Wolfe, 1967), referring to either non-linear structures (like galaxy clusters, aka *Rees-Sciama* effect) or at very early times, during the epoch of recombination (Sachs-Wolfe effect or early Sachs-Wolfe effect).

The late ISW arises at late epochs and is a distinct signature of DE on the CMB. Since it arises at late epochs and gravitational potentials involve large scale interactions, the ISW contribution is more important on the largest angular scales, which are however dominated by the intrinsic Sachs-Wolfe anisotropies generated at the surface of Last Scattering, ($z \sim 1,050$).

Correlation with the LSS fluctuations. In order to distinguish late ISW fluctuations introduced in the low redshift universe from those Sachs-Wolfe anisotropies generated during recombination, it was first suggested by (Crittenden & Turok, 1996) to use galaxies as probes of potential fields in order to detect the presence of ISW via a cross-correlation analysis. Galaxies at the appropriate redshift range should spatially sample the same large scale gravitational potential wells giving rise to the ISW, and hence the large scale galaxy angular distribution should be correlated to the ISW component that is embedded in the CMB temperature anisotropy field.

After the first attempts on COBE CMB data (Boughn & Crittenden, 2002), analysis with the higher quality CMB data from WMAP were conducted right after temperature maps were publicly released (Boughn & Crittenden, 2004; Fosalba et al., 2003; Vielva et al., 2006; Pietrobon et al., 2006; Ho et al., 2008; Giannantonio et al., 2008; McEwen et al., 2008; Dupé et al., 2011; Schiavon et al., 2012). Those works claimed detections of the ISW in the $2 - 4.5 \sigma$ range, although a number of other works either found lower statistically significant results and/or warned about the presence of systematics associated to point source emission and abnormal power on the large scales (Hernández-Monteagudo et al., 2006; Rassat et al., 2007; Bielby et al., 2010; López-Corredoira et al., 2010; Hernández-Monteagudo, 2010; Francis & Peacock, 2010; Sawangwit et al., 2010; Hernandez-Monteagudo et al., 2013). Recent results from the *Planck* collaboration, with better control of foregrounds and systematics, larger sky coverage and lensing information, provide evidence for the ISW at the $\sim 2-3 \sigma$ level (*Planck* Collaboration et al., 2013c).

⁷URL site: <http://map.gsfc.nasa.gov>

⁸URL site <http://www.rssd.esa.int/index.php?project=planck>

⁹URL site: <http://act.princeton.edu>

¹⁰URL site: <http://pole.uchicago.edu>

There are several estimators to determine the cross-correlation between the ISW fluctuations and a galaxy density field. The most used one is the cross-correlation function (Giannantonio et al., 2008), which, although it is suitable for analysis of partial/small sky coverage surveys, it is a relatively slow technique. Alternatives to this estimator are the covariance of the wavelet coefficients (CWC; e.g., Vielva et al., 2006) or the cross-angular power spectrum (CAPS; e.g., Hernández-Monteagudo, 2008). These two approaches are typically faster than the CCF, although their handling of incomplete skies is less intuitive. There exist also optimal implementations of the cross-angular power spectrum Schiavon et al. (2012) working on the base of a quadratic maximum-likelihood estimator (e.g., Tegmark, 1997). These methods, on the one hand, provide an optimal handling of the statistical problem but, on the other hand, are the most CPU expensive (and hence slowest) of the statistical approaches considered so far. In practice, when dealing with a real data set, it is important to check the results with all the approaches, since systematics typically affect the cross-correlation estimators in different manners. For forecast purposes, working with the harmonic space is the most natural option, since, at a first approach, the CAPS can be seen as a quantity of uncorrelated components.

Both the sky coverage and the redshift depth are critical aspects of a galaxy survey to serve as a dark matter tracer to detect the ISW effect (e.g., Hernández-Monteagudo, 2008; Douspis et al., 2008). At this respect, J-PAS offers an excellent opportunity to alternatively probe DE through the ISW effect. In Figure 24 we display the signal-to-noise to be obtained, below a given multipole ℓ , after cross-correlating the angular distribution of LRGs, ELGs and QSOs from J-PAS with CMB maps. The LRGs should provide ISW evidence at the $\sim 2.1\sigma$ level, higher than ELGs ($\sim 1.8\sigma$) and QSOs ($\sim 1.4\sigma$). When combining these three different probes and after accounting for their correlation, the total foreseen statistical significance for the ISW detection (in the standard Λ CDM scenario) amounts to 2.6σ . This remains at the same level of evidence claimed by the *Planck* team, *Planck* Collaboration et al. (2013c).

Constraints on cosmological parameters. Although the ISW signal is subdominant with respect to the intrinsic anisotropies in the CMB, it is a complementary probe for the dark energy properties. In particular, the ISW can help to constrain the time evolution of the equation of state of the dark energy fluid.

In Figure 25 a forecast for the a model of Dark Energy with constant equation of state $w_0 \neq 1$ ($p = w_0\rho$) is given. The blue area represents the 2σ confidence level imposed by the CMB angular power spectra (from *Planck*), whereas the red ones correspond to including the ISW effect into the likelihood function (assumed Gaussian in this forecast). The underlying fiducial model is the WMAP 7yr best-fit (Komatsu et al., 2011). Similarly, in Figure 26 we present the forecast for a $w(z)$ dark energy model ($w(z) = w_0 + w_a(1 + a)$, being a the scale factor).

Recovery of the ISW fluctuations. One of the most novel analyses related to the ISW effect is the recovery of the actual ISW fluctuations produced by the gravitational potentials. One can distinguish two different types of approaches in this problem. (Barreiro et al., 2008, 2012) propose using 2D information of the CMB and projected galaxy density field in order to yield a minimum variance ISW map estimate. On the other hand, provided the exquisite redshift information to be provided by J-PAS, it is also possible to produce 3D density and gravitational potential maps, which can be then projected along the line of sight to generate ISW shells centered at any arbitrary redshift probed by J-PAS (e.g., Jasche et al., 2010).

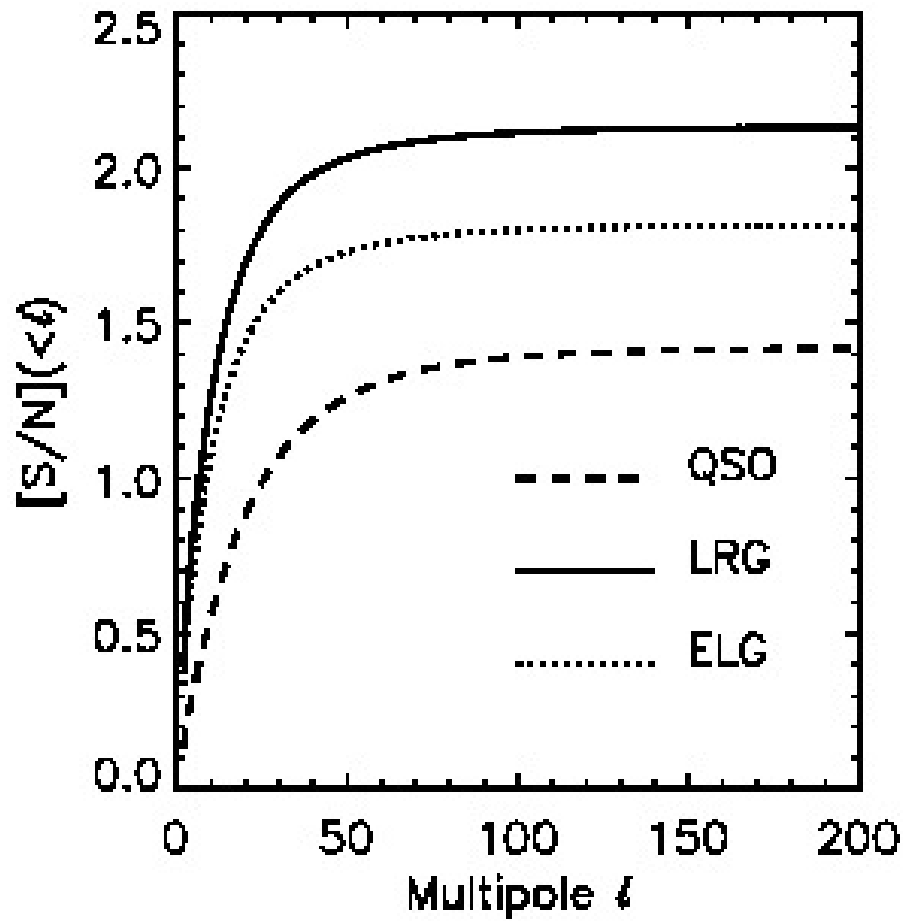


Figure 24: Signal-to-noise ratio for the ISW effect, as a function of the maximum multipole considered in the analysis, for three different probes of J-PAS: LRGs (solid line), ELGs (dotted line) and QSOs (dashed line). After adding the signal from all these probes, we foresee a statistical significance of the ISW via a cross-correlation analysis at the level of 2.6σ .

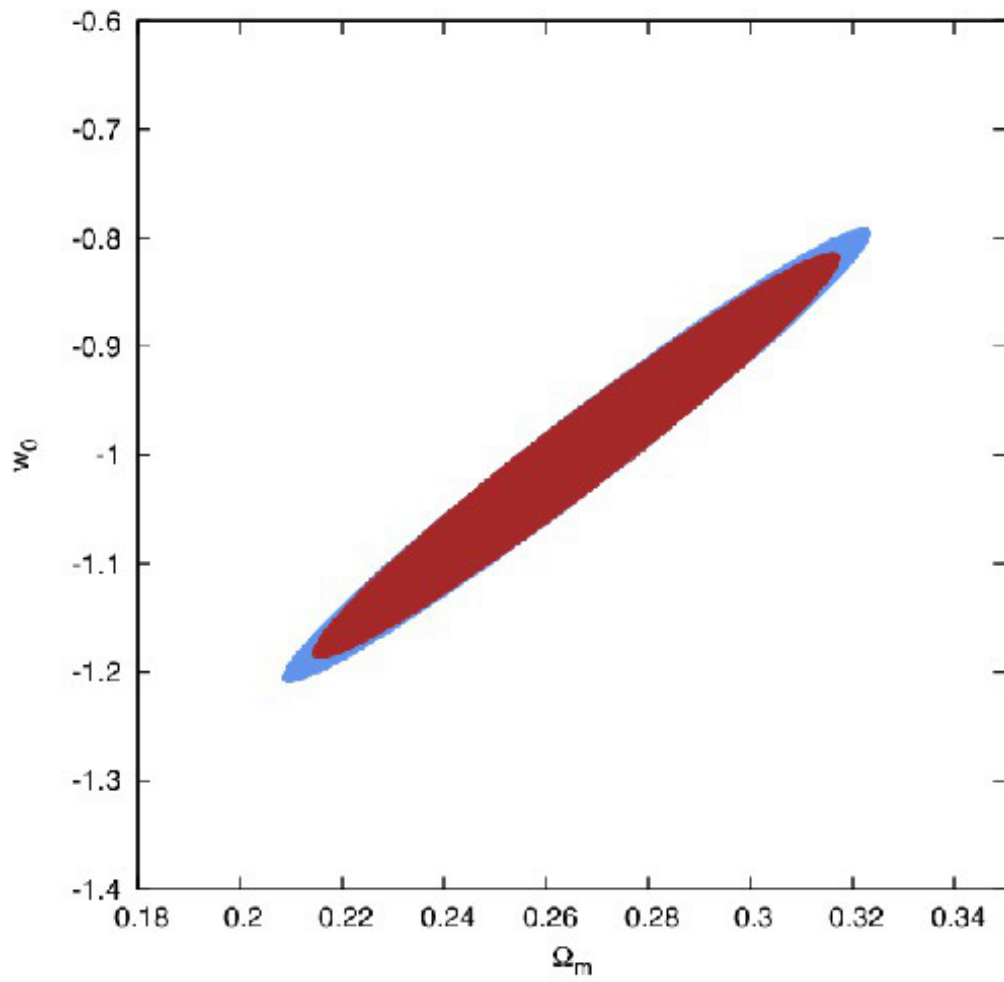


Figure 25: Constraints of Ω_m and w_0 from CMB *Planck* alone (blue) and CMB *Planck* + ISW (red) at 2σ CL, for a $w_0 \neq 1$ dark energy model ($p = w_0\rho$).

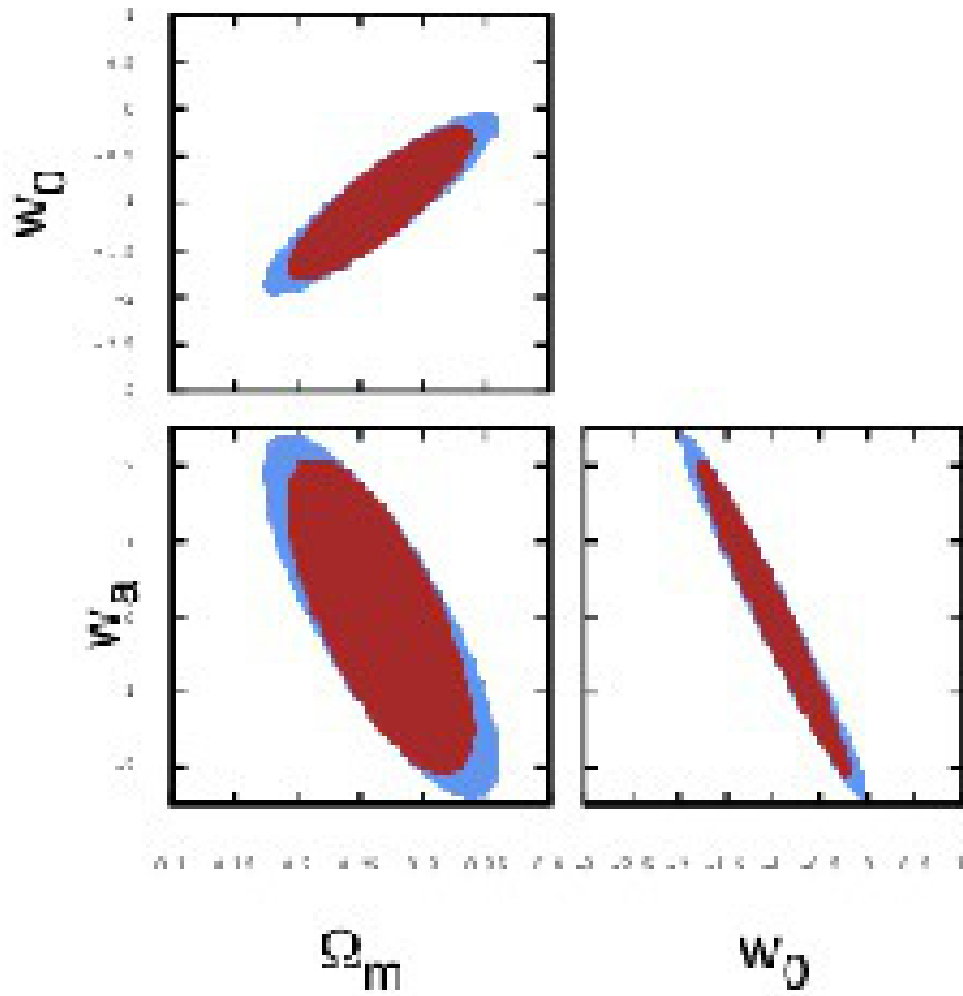


Figure 26: Constraints of Ω_m , w_0 and w_a from CMB *Planck* alone (blue) and CMB *Planck* + ISW (red) at 2σ CL, for a $w(z)$ dark energy model ($w(z) = w_0 + w_a(1+z)$, being a the scale factor).

These analysis would probe the large angle domain of the CMB, where discussion about possible anomalies challenging the Λ CDM scenario are ongoing, (e.g., Bennett et al., 2011; *Planck* Collaboration et al., 2013d). Consequently, tests of the Cosmological Principle and universal homogeneity would naturally follow.

3.6.2. *The thermal history of the Universe*

The common understanding of the process of galaxy formation pictures baryons cooling down after falling in potential wells seeded by dark matter. In order to avoid the over-cooling problem by which too massive galaxies are generated (Lin and Mohr, 2004), additional gas heating mechanisms must be invoked, e.g., (Borgani et al., 2004; McNamara & Nulsen, 2007) and references therein. How exactly this process proceeds is a matter of active investigation currently. Measurements of the thermal Sunyaev-Zel'dovich effect (hereafter tSZ, Sunyaev & Zeldovich, 1972) have recently been used to shed additional light on this problem. The tSZ describes the distortion that the black body spectrum of the CMB undergoes when it Compton scatters off hot electrons in collapsed structures like galaxies and groups and clusters of galaxies. Measurements from CMB experiments like ACT (Hand et al., 2012) and *Planck* (*Planck* Collaboration et al., 2011, 2012) have shown that by looking at the amplitude of the tSZ in halos it is possible to put constraints on the amount of baryonic mass residing in halos of different total mass, and hence gain insight on the feedback processes involving baryonic physics in those structures.

The unprecedented depth and volume of group and cluster catalogs to be obtained from J-PAS will constitute a very important contribution to these studies. The photometric depth of J-PAS should allow to identify $\sim 5 \times 10^5$ groups down to $\sim 5 \times 10^{13} M_{\odot}$ in the local universe, improving enormously current statistics. Likewise, and by first time, J-PAS should enable extend this study to earlier cosmological epochs and provide alternative constraints of the history of galaxy formation.

3.6.3. *Bulk flows, missing baryons and redshift space distortions*

About half the baryons in the local universe remain hidden to direct observations, (Cen & Ostriker, 1999, 2006). These *missing* baryons are expected to be in an ionized, diffuse phase also known as *Warm-Hot Intergalactic Medium* (WHIM). These baryons should be part of comoving flows of matter (also known as *bulk flows*) triggered by gravity. It turns out that the moving baryons also leave an imprint on the CMB by means of the kinetic Sunyaev-Zel'dovich effect (Sunyaev & Zeldovich, 1980)(hereafter kSZ). The kSZ describes the brightness anisotropies induced on the CMB by moving electrons by means of Thomson scattering: it is sensitive to radial component of the electron peculiar velocity with respect to the CMB, and its spectral dependence is identical to that of the intrinsic CMB anisotropies, making its detection difficult.

With the advent of last generation CMB experiments, the levels of angular resolution and sensitivity are approaching the ballpark required by the kSZ. Indeed, the ACT experiment provided recently a promising claim of kSZ detection (Hand et al., 2012), while the *Planck* surveyor has used the limits on the kSZ to set strong constraints on the homogeneity of the universe on Gpc scales, (*Planck* Collaboration et al., 2013a). J-PAS will provide an exquisite mapping of the large scale structure up to $z \sim 1$, with very accurate photo- z 's for groups and clusters. By inverting the galaxy density field into the underlying dark matter density and peculiar velocity fields (Ho et al., 2009; Kitaura et al., 2012a), it is possible to search for kSZ signatures in CMB maps by means of cross-correlation studies. This combination of J-PAS data with CMB observations would hence provide the first view of the evolution of peculiar velocity fields at different cosmological epochs.

3.6.4. CMB lensing maps

J-PAS will map hundreds of thousands of Quasi Stellar Objects (QSOs) in the redshift range $z \in [1.5, 3]$ (see Sect.3.1), hence providing an estimate of the density map of the universe at those epochs. It is roughly in this redshift range where CMB photons are more efficiently deflected by gravitational lensing following the inhomogeneities in the distribution of matter. The presence of lensing in CMB maps has been first detected in terms of the convergence field, (Das et al., 2011; Van Engelen et al., 2012), although the highest signal-to-noise ratio of the detection is owed to *Planck* (*Planck* Collaboration et al., 2013b). A further confirmation of this effect can be obtained by cross-correlating tracers of the matter distribution at those epochs with CMB lensing convergence maps, (Sherwin et al., 2012; *Planck* Collaboration et al., 2013b).

The J-PAS will allow to explore this CMB convergence – matter correlation by combining its QSO catalog with lensing measurements provided by the all sky *Planck* mission. The huge common cosmological volume sampled in this analysis should further improve our constraints on the QSO bias evolution, and will test the model predictions on lensing on scales practically unexplored yet. As shown by, e.g., (Acquaviva et al., 2008), it is on these larger scales where one can look at a scale dependence of the density linear growth factor to set constraints on alternative gravity theories (like $f(R)$) and further test General Relativity. For that, it is required combining RSD measurements on the larger scales with CMB lensing cross correlations, so that the bias degeneracy may be avoided with CMB data and direct constraints on the growth factor history may be set.

3.7. Alternative Cosmologies and Theories of gravity

The absence of guidance from fundamental physics about the mechanism behind cosmic acceleration has given rise to a number of non-standard cosmologies. These are based either on the existence of new fields in Nature, the role of large-scale inhomogeneities or on modifications of general relativistic gravitation theory on large scales. Combining the expansion history measured geometrically with growth of structure data from J-PAS, it will be possible to distinguish among several of these scenarios. In what follows, we briefly discuss some of the most popular alternative models.

3.7.1. Quintessence

The simplest approach toward constructing a model for an accelerating universe is to work with the idea that the unknown, un-clumped dark energy component is due exclusively to a minimally coupled scalar field ϕ (quintessence field) which has not yet reached its ground state and whose current dynamics is basically determined by its potential energy $V(\phi)$ Peebles & Ratra (1988). The dynamics of quintessence in the presence of non-relativistic matter has been studied in detail for many different potentials (see, e.g., Tsujikawa (2013)) and can be broadly classed into three groups: thawing, freezing and hybrid models Caldwell & Linder 2005; Alcaniz et al. (2009).

The dynamics of quintessence or ϕ CDM models is obtained by solving the equations

$$3M_{Pl}^2 H^2 = \frac{\dot{\phi}^2}{2} + V(\phi) + \rho_m, \quad (39)$$

$$2M_{Pl}^2 \dot{H} = -(\dot{\phi}^2 + \rho_m) \quad (40)$$

where the pressure and the energy density of the quintessence field are given, respectively, by $p_\phi = \dot{\phi}^2/2 - V(\phi)$ and $\rho_\phi = \dot{\phi}^2/2 + V(\phi)$ and a dot represents a derivative with respect to t . The scalar field satisfies the continuity equation $\dot{\rho}_\phi + 3H\rho_\phi(1+w) = 0$, i.e.,

$$\ddot{\phi} + 3H\dot{\phi} + dV(\phi)/d\phi = 0. \quad (41)$$

where $w = p_\phi/\rho_\phi$ is the equation-of-state parameter of the dark energy.

In order to realize current cosmic acceleration, the mass of the quintessence field, $m_\phi = \sqrt{d^2V(\phi)/d\phi^2}$ should be extremely small, i.e., $|m_\phi| \lesssim H_0 \simeq 10^{-33}$ eV. Although being difficult to reconcile such a ultra light mass with the energy scales appearing in particle physics, there has been some attempts to construct realistic quintessence models in the framework of fundamental physics Frieman et al. (1995). From the observational viewpoint, tight constraints can be placed on the equation-of-state parameter combining geometric probes with the growth rate of matter perturbations δ_m , which depends explicitly on w .

3.7.2. Interaction in the dark sector

Unless some unknown symmetry in Nature prevents or suppresses a non-minimal coupling in the dark sector, the dark energy field may interact with the pressureless component of dark matter. In recent papers, cosmological models with interaction in the dark sector were shown to be a possible alternative to the standard cosmology (Carvalho et al., 1992; Overduin & Cooperstock, 1998; Amendola, 2000; Zimdahl & Pavon, 2001; Alcaniz and Lima, 2005(@; Costa & Alcaniz, 2010). Among some possibilities, a model with constant-rate particle creation from the vacuum has the same number of parameters as the spatially flat standard model and seems to be able to alleviate some observational/theoretical tensions appearing in the latter scenario (Borges & Carneiro, 2005; Alcaniz et al., 2012).

In this class of models, the dimensionless Hubble function is given by (Borges & Carneiro, 2005)

$$E_I(z) \equiv \frac{H(z)}{H_0} = 1 - \Omega_{m0} + \Omega_{m0}(1+z)^{\frac{3}{2}}, \quad (42)$$

whereas for the spatially flat Λ CDM scenario the well-known expression is written as

$$E_{\Lambda\text{CDM}}(z) = (1 - \Omega_{m0} + \Omega_{m0}(1+z)^3)^{\frac{1}{2}}. \quad (43)$$

Although at low- z , the difference between the predicted expansion rate from both models is very small, at higher z , e.g., $z = 1$, they provide very distinct results. Assuming $\Omega_{m0} = 0.45$ in Eq. (42), as the best-fit concordance value for the present matter density¹¹, and $\Omega_{m0} = 0.3$ in Eq. (43), we find $E_I(1) = 1.82$ and $E_{\Lambda\text{CDM}}(1) = 1.76$. This amounts to say that the relative difference is

$$\frac{E_I(1) - E_{\Lambda\text{CDM}}(1)}{E_{\Lambda\text{CDM}}(1)} = 3.4\%, \quad (44)$$

which is slightly larger than the expected uncertainties in J-PAS BAO data at this redshift (see Sec. 3.2). For the interaction models described in Wang et al. (2007) the relative differences are even higher, above 6% for $z = 1$.

¹¹If the creation of particles from vacuum is important during the late times of universe expansion, the present matter density is higher than in the standard model, provided it has the standard value at early times Pigozzo et al. (2011).

Besides the phenomenological models, interacting models based on field theory have also been discussed in the literature Micheletti et al. (2012). In the particular case of an interaction described by a coupling ξ , such that He et al. (2010)

$$\dot{\rho} + H \left[\left(2 - \frac{\xi}{3} \right) \rho_K + \left(1 - \frac{\xi}{3} \right) \rho_W \right] = 0, \quad (45)$$

constraints on the interacting parameter ξ can be investigated from different sets of observations Feng et al. (2008). In this regard, an interesting possibility comes from galaxy clusters measurements since close to balance ($\dot{\rho} = 0$) the virial ratio should be approximated by

$$\frac{\rho_K}{\rho_W} \simeq -\frac{1 - \frac{\xi}{3}}{2 - \frac{\xi}{3}}. \quad (46)$$

Clusters, therefore, turn out to be good probes for these models. Indeed, the very possibility of an interaction of clumping matter with an external object, here dark energy, leads to consequences for the virial condition. Thus, the virial condition is a good test for the dynamics of the dark sector. This has been performed with a small sample of clusters Abdalla et al. (2009); Abdalla, Abramo & Souza (2010) and a wider set should provide further restrictions.

3.7.3. Unified models of dark matter and dark energy

From the cosmological viewpoint, the main distinction between pressureless CDM and dark energy is that the former agglomerates at small length scales whereas the latter is a smooth component on these scales. Recently, the idea of a unified description for CDM and dark energy has received much attention (Watterich, 2002; Kasuya, 2001; Padmanabhan & Choudhury, 2002; Dev et al., 2003; Alcaniz et al., 2003; Makler et al., 2003; Colistete et al., 2004; Bertolami et al., 2004; Alcaniz et al., 2005). An interesting attempt in this direction was suggested in Kamenshik et al. (2001) and further developed in Bilić et al. (2002). It uses to an exotic fluid, the so-called Chaplygin gas (Cg), whose equation of state is given by

$$p_{Cg} = -\frac{A}{\rho_{Cg}^\alpha}. \quad (47)$$

Inserting the above equation into the energy conservation equation gives the expression for the Cg energy density

$$\rho_{Cg} = \rho_{Cg,0} \left[A_s + (1 + A_s)(1 + z)^{3(1+\alpha)} \right]^{1/1+\alpha}, \quad (48)$$

where $A_s = A/\rho_{Cg,0}^{1+\alpha}$ is a quantity related to the sound speed of the Chaplygin gas today. From the above equations, it is clear that the Chaplygin gas interpolates between epochs dominated by non-relativistic matter [$\rho_{Cg}(z \gg 1) \propto z^3$] and by a negative-pressure time-independent dark energy [$\rho_{Cg}(z \sim 0) = \text{const.}$]. Observationally, one of the major difficulties of these models concern the predicted oscillations or instabilities in the matter power spectrum. In this regard, J-PAS data can tightly constrain the idea of unified models of the dark sector and verify if it may or not constitute a viable alternative to the standard model.

3.7.4. The Lemaître-Tolman-Bondi Models

Recently, inhomogeneous cosmologies have gathered considerable interest as a possible explanation for current cosmological observations without invoking a dark energy field. In the simplest class of such models our location is close to the center of a large, spherically symmetric void described by the Lemaître-Tolman-Bondi (LTB) metric Alnes et al. (2006)

$$ds^2 = dt^2 - \frac{A'^2(r,t)}{1-k(r)} dr^2 - A(r,t)d\Omega^2, \quad (49)$$

where $d\Omega^2 = d\theta^2 + \sin^2\theta d\phi^2$, $k(r)$ is the radial position-dependent curvature function and $A(r,t)/r$ a position-dependent scale factor. Plugging Eq. (49) into the Einstein equations, one finds that the two independent equations are

$$\frac{\dot{A} + k(r)}{A^2} + \frac{2\dot{A}A' + k'(r)}{AA'} = 8\pi G(\rho_m + \rho_\Lambda), \quad (50)$$

$$\dot{A}^2 + 2A\ddot{A} + k(r) = 8\pi G\rho_\Lambda A^2, \quad (51)$$

which provide the following generalized acceleration equation

$$\frac{2\ddot{A}}{3A} + \frac{1\ddot{A}'}{3A'} = -\frac{4\pi G}{3}(\rho_m - 2\rho_\Lambda). \quad (52)$$

Clearly, cosmic acceleration is possible in these models even for $\rho_\Lambda = 0$ if the angular or radial scale factor is decelerating fast enough. Since the LTB metric allows for different rates of expansion in the longitudinal and transverse directions, the combination of data constraining the transverse Hubble rate (e.g., SNe Ia observations), together with J-PAS measurements of the radial BAO scale in many redshift slices, will be able to constrain this class of models as well as the hypothesis of large-scale homogeneity and isotropy (see, e.g. García-Bellido & Haugboelle (2009)).

3.7.5. Most general scalar-tensor theories

Modified theories of gravity have recently been applied to cosmology as a realistic alternative approach to the late-time cosmic acceleration. There are many modified gravitational theories proposed in literature. Most of them, however, belong to a general class of scalar-tensor theories dubbed Horndeski theories Horndeski (1974). The Horndeski theories are constructed to keep the space-time derivatives of the field equations of motion up to second order, whose Lagrangian is given by Deffayet et al. (2011)

$$\mathcal{L} = \sum_{i=2}^5 \mathcal{L}_i, \quad (53)$$

where

$$\mathcal{L}_2 = K(\phi, X), \quad (54)$$

$$\mathcal{L}_3 = -G_3(\phi, X)\square\phi, \quad (55)$$

$$\mathcal{L}_4 = G_4(\phi, X)R + G_{4,X}[(\square\phi)^2 - (\nabla_\mu\nabla_\nu\phi)(\nabla^\mu\nabla^\nu\phi)], \quad (56)$$

$$\begin{aligned} \mathcal{L}_5 = & G_5(\phi, X)G_{\mu\nu}(\nabla^\mu\nabla^\nu\phi) \\ & - \frac{1}{6}G_{5,X}[(\square\phi)^3 - 3(\square\phi)(\nabla_\mu\nabla_\nu\phi)(\nabla^\mu\nabla^\nu\phi) + 2(\nabla^\mu\nabla_\alpha\phi)(\nabla^\alpha\nabla_\beta\phi)(\nabla^\beta\nabla_\mu\phi)]. \end{aligned} \quad (57)$$

K and G_i ($i = 3, 4, 5$) are functions in terms of a scalar field ϕ and its kinetic energy $X = -\partial^\mu \phi \partial_\mu \phi / 2$ with the partial derivatives $G_{i,X} \equiv \partial G_i / \partial X$, R is the Ricci scalar, and $G_{\mu\nu}$ is the Einstein tensor. The Lagrangian (53) involves only one scalar degree of freedom.

Quintessence and k-essence are described by the functions $G_3 = 0$, $G_4 = M_{\text{pl}}^2/2$, and $G_5 = 0$, where M_{pl} is the reduced Planck mass whereas the Brans-Dicke (BD) theory Brans & Dicke (1961) corresponds to $K = \omega_{\text{BD}} X / \phi - V(\phi)$, $G_3 = 0$, $G_4 = \phi/2$, and $G_5 = 0$, where ω_{BD} is a constant. The $f(R)$ -gravity in the metric and Palatini formalisms are the special cases of BD theory with $\omega_{\text{BD}} = 0$ and $\omega_{\text{BD}} = -3/2$, respectively FR (1972). The covariant Galileon Nicolis et al. (2009) corresponds to the choice $K = X - c_2 \phi$, $G_3 = c_3 X$, $G_4 = M_{\text{pl}}^2/2 + c_4 X^2$, and $G_5 = c_5 X^2$, where c_i 's are constants.

In the following we also take into account a barotropic perfect fluid of non-relativistic matter (cold dark matter and baryons) minimally coupled to the field ϕ . Then the total 4-dimensional action is given by

$$S = \int d^4x \sqrt{-g} (\mathcal{L} + \mathcal{L}_m), \quad (58)$$

where g is a determinant of the metric $g_{\mu\nu}$, and \mathcal{L}_m is the Lagrangian of non-relativistic matter with the energy density ρ_m .

Background equations. Assuming a flat FLRW space-time, the background equations of motion following from the action (58) read De Felice et al. (2011)

$$3H^2 M_{\text{pl}}^2 = \rho_{\text{DE}} + \rho_m, \quad (59)$$

$$2\dot{H} M_{\text{pl}}^2 = -(\rho_{\text{DE}} + P_{\text{DE}}) - \rho_m, \quad (60)$$

$$\dot{\rho}_m + 3H\rho_m = 0, \quad (61)$$

where $H = \dot{a}/a$ is the Hubble parameter, a dot represents a derivative with respect to the cosmic time t , and the energy density and pressure, written in terms of derivatives of the scalar field ϕ (see, e.g., De Felice et al. (2011)) satisfy the usual continuity equation. From the above equations, we can also define the equation-of-state parameter, $w_{\text{DE}} = P_{\text{DE}}/\rho_{\text{DE}}$. For a given model, the evolution of w_{DE} is known by solving Eqs. (59)-(61).

Cosmological perturbations. We consider the scalar metric perturbations Ψ and Φ in the longitudinal gauge about the flat FLRW background. The perturbed line element is then given by

$$ds^2 = -(1 + 2\Psi) dt^2 + a^2(t)(1 + 2\Phi) d\mathbf{x}^2. \quad (62)$$

We decompose the scalar field and the non-relativistic matter density into the background and inhomogeneous parts, as $\phi(t) + \delta\phi(t, \mathbf{x})$ and $\rho_m(t) + \delta\rho_m(t, \mathbf{x})$, respectively. The four velocity of non-relativistic matter can be written in the form $u^\mu = (1 - \Psi, \nabla^i v)$, where v is the rotational-free velocity potential. We also introduce the following quantities

$$\delta \equiv \delta\rho_m/\rho_m, \quad \theta \equiv \nabla^2 v. \quad (63)$$

In Fourier space the matter perturbation obeys the following equations of motion

$$\dot{\delta} + \theta/a + 3\dot{\Phi} = 0, \quad \dot{\theta} + H\theta - (k^2/a)\Psi = 0, \quad (64)$$

where k is a comoving wavenumber. Introducing the gauge-invariant density contrast $\delta_m \equiv \delta + (3aH/k^2)\theta$, it follows that

$$\ddot{\delta}_m + 2H\dot{\delta}_m + (k^2/a^2)\Psi = 3(\dot{I} + 2HI), \quad \text{where} \quad I \equiv (aH/k^2)\theta - \Phi. \quad (65)$$

The full linear perturbation equations for the action (58) have been derived in Ref. De Felice et al. (2011). For the scales relevant to the large-scale structure one can employ the quasi-static approximation on sub-horizon scales, under which the dominant contributions to the perturbation equations are those including the terms k^2/a^2 , δ , and the mass M of a scalar degree of freedom. Under this approximation we obtain the modified Poisson equation De Felice et al. (2011)

$$\frac{k^2}{a^2}\Psi \simeq -4\pi G_{\text{eff}}\rho_m\delta, \quad (66)$$

where G_{eff} is the effective gravitational coupling defined by

$$G_{\text{eff}} = \frac{2M_{\text{pl}}^2[(\mathcal{C}_2\mathcal{C}_5 - \mathcal{C}_3^2)(k/a)^2 - \mathcal{C}_2M^2]}{(\mathcal{C}_1^2\mathcal{C}_2 + \mathcal{C}_4^2\mathcal{C}_5 - 2\mathcal{C}_1\mathcal{C}_3\mathcal{C}_4)(k/a)^2 - \mathcal{C}_4^2M^2}G. \quad (67)$$

Here G is the bare gravitational constant related to M_{pl} via $G = 1/(8\pi M_{\text{pl}}^2)$. The coefficients \mathcal{C}_i ($i = 1, \dots, 5$) are

$$\begin{aligned} \mathcal{C}_1 \equiv & -2XG_{3,X} - 4H(G_{4,X} + 2XG_{4,XX})\dot{\phi} + 2G_{4,\phi} + 4XG_{4,\phi X} \\ & + 4H(G_{5,\phi} + XG_{5,\phi X})\dot{\phi} - 2H^2X(3G_{5,X} + 2XG_{5,XX}), \end{aligned} \quad (68)$$

$$\mathcal{C}_2 \equiv 4[G_4 - X(\ddot{\phi}G_{5,X} + G_{5,\phi})], \quad (69)$$

$$\begin{aligned} \mathcal{C}_3 \equiv & -4G_{4,X}H\dot{\phi} - 4(G_{4,X} + 2XG_{4,XX})\ddot{\phi} + 4G_{4,\phi} - 8XG_{4,\phi X} \\ & + 4(G_{5,\phi} + XG_{5,\phi X})\ddot{\phi} - 4H[(G_{5,X} + XG_{5,XX})\ddot{\phi} - G_{5,\phi} + XG_{5,\phi X}]\dot{\phi} \\ & + 4X[G_{5,\phi\phi} - (H^2 + \dot{H})G_{5,X}], \end{aligned} \quad (70)$$

$$\mathcal{C}_4 \equiv 4[G_4 - 2XG_{4,X} - X(H\dot{\phi}G_{5,X} - G_{5,\phi})], \quad (71)$$

$$\begin{aligned} \mathcal{C}_5 \equiv & -K_{,X} - 2(G_{3,X} + XG_{3,XX})\ddot{\phi} - 4HG_{3,X}\dot{\phi} + 2G_{3,\phi} - 2XG_{3,\phi X} \\ & + [-4H(3G_{4,XX} + 2XG_{4,XXX})\ddot{\phi} + 4H(3G_{4,\phi X} - 2XG_{4,\phi XX})]\dot{\phi} + (6G_{4,\phi X} + 4XG_{4,\phi XX})\ddot{\phi} \\ & - 20H^2XG_{4,XX} + 4XG_{4,\phi\phi X} - 4\dot{H}(G_{4,X} + 2XG_{4,XX}) - 6H^2G_{4,X} \\ & + \{4H(2G_{5,\phi X} + XG_{5,\phi XX})\ddot{\phi} - 4H[(H^2 + \dot{H})(G_{5,X} + XG_{5,XX}) - XG_{5,\phi\phi X}]\}\dot{\phi} - 4H^2X^2G_{5,\phi XX} \\ & - 2H^2(G_{5,X} + 5XG_{5,XX} + 2X^2G_{5,XXX})\ddot{\phi} + 2(3H^2 + 2\dot{H})G_{5,\phi} + 4\dot{H}XG_{5,\phi X} + 10H^2XG_{5,\phi X}. \end{aligned} \quad (72)$$

The explicit form of the mass term M can be found in Refs. De Felice et al. (2011).

Under the quasi-static approximation on sub-horizon scales the r.h.s. of Eq. (65) can be neglected relative to the l.h.s. of it. Since $\delta_m \simeq \delta$, the matter perturbation obeys the following equation

$$\delta_m'' + \left(2 + \frac{H'}{H}\right) \delta_m' - \frac{3}{2} \frac{G_{\text{eff}}}{G} \Omega_m \delta_m \simeq 0, \quad (73)$$

where $\Omega_m \equiv \rho_m / (3M_{\text{pl}}^2 H^2)$, and a prime represents a derivative with respect to $N = \ln a$. In order to quantify the difference between the two gravitational potentials we introduce the following anisotropic parameter

$$\eta \equiv -\Phi/\Psi. \quad (74)$$

On sub-horizon scales this is approximately given by

$$\eta \simeq \frac{(\mathcal{C}_4 \mathcal{C}_5 - \mathcal{C}_1 \mathcal{C}_3)(k/a)^2 - \mathcal{C}_4 M^2}{(\mathcal{C}_2 \mathcal{C}_5 - \mathcal{C}_3^2)(k/a)^2 - \mathcal{C}_2 M^2}. \quad (75)$$

We introduce the effective gravitational potential Φ_{eff} associated with the deviation of the light rays in CMB and weak lensing observations, $\Phi_{\text{eff}} \equiv (\Psi - \Phi)/2$ Amendola et al. (2008). Using Eqs. (66) and (74), we obtain

$$\Phi_{\text{eff}} \simeq -\frac{3}{2} \frac{G_{\text{eff}}}{G} \frac{1 + \eta}{2} \left(\frac{aH}{k}\right)^2 \Omega_m \delta_m. \quad (76)$$

We also define

$$f_m \equiv \frac{\dot{\delta}_m}{H \delta_m} = \frac{\delta_m'}{\delta_m}. \quad (77)$$

The galaxy perturbation δ_g is related with δ_m via the bias factor b , i.e. $\delta_g = b \delta_m$. The galaxy power spectrum $\mathcal{P}_g^s(\mathbf{k})$ in the redshift space can be modeled as Kaiser (1987) (see also Sec. 3.1.1)

$$\mathcal{P}_g^s(\mathbf{k}) = \mathcal{P}_{gg}(\mathbf{k}) + 2\mu^2 \mathcal{P}_{g\theta}(\mathbf{k}) + \mu^4 \mathcal{P}_{\theta\theta}(\mathbf{k}), \quad (78)$$

where $\mu = \mathbf{k} \cdot \mathbf{r} / (kr)$ is the cosine of the angle of the \mathbf{k} vector to the line of sight (vector \mathbf{r}). $\mathcal{P}_{gg}(\mathbf{k})$ and $\mathcal{P}_{\theta\theta}(\mathbf{k})$ are the real space power spectra of galaxies and θ , respectively, and $\mathcal{P}_{g\theta}(\mathbf{k})$ is the cross power spectrum of galaxy- θ fluctuations in real space. In Eq. (78) we have not taken into account the non-linear effect coming from the velocity distribution of galaxies in collapsed structures.

For the linearly evolving perturbations, the first of Eq. (64) shows that θ is related with the growth rate of matter perturbations, i.e.

$$\theta / (aH) \simeq -f_m \delta_m, \quad (79)$$

where we neglected the $\dot{\Phi}$ term. In this case the three power spectra on the r.h.s. of Eq. (78) have the same shape, leading to Kaiser (1987)

$$\mathcal{P}_g^s(\mathbf{k}) = \mathcal{P}_g(\mathbf{k}) (1 + 2\mu^2 \beta + \mu^4 \beta^2), \quad (80)$$

where $\beta = f_m/b$ and $\mathcal{P}_g(\mathbf{k})$ is the real space galaxy spectrum. Using Eq. (80), one can constrain β and $b\sigma_8$ from observations. Provided that the continuity equation (79) holds, the normalizations of \mathcal{P}_{gg} , $\mathcal{P}_{g\theta}$, and $\mathcal{P}_{\theta\theta}$ in Eq. (78) depend on $(b\sigma_8)^2$, $(b\sigma_8)(f_m\sigma_8)$, and $(f_m\sigma_8)^2$, respectively. Then the redshift space distortions (RSD) can be also modeled as an additive component by observing $b\sigma_8$ and $f_m\sigma_8$ Song & Percival (2009). The quantity $f_m\sigma_8$ has an advantage over β in that it can be measured without knowing the bias factor b .

3.7.6. $f(R)$ – Gravity

Among several possibilities (see, e.g., Caldwell & Kamionkowski (2009)), the simplest extension of Einstein’s general relativity is the so-called $f(R)$ -gravity De Felice & Tsujikawa (2010). In the metric formalism, this theory is characterized by the functions $K = -(M_{\text{pl}}^2/2)(Rf_{,R} - f)$, $G_3 = 0$, $G_4 = M_{\text{pl}}\phi/2$, and $G_5 = 0$ with $\phi = M_{\text{pl}}f_{,R}$ in the Horndeski action. The field equations are given by

$$f_{,R}R_{\mu\nu}(g) - \frac{1}{2}f(R)g_{\mu\nu} - \nabla_{\mu}\nabla_{\nu}f_{,R} + g_{\mu\nu}\square f_{,R} = \kappa^2 T_{\mu\nu}, \quad (81)$$

whose trace is written as

$$3\square f_{,R} + f_{,R}R - 2f(R) = \kappa^2 T, \quad (82)$$

where $f_{,R}$ denotes partial derivative with respect to R and $T_{\mu\nu}$ is the usual energy-momentum tensor of matter fields.

In what follows, we consider a metric $f(R)$ -gravity model described by the Lagrangian $\mathcal{L} = (M_{\text{pl}}^2/2)f(R)$ with Hu & Sawicki (2007)

$$f(R) = R - \lambda R_c \frac{(R/R_c)^{2n}}{(R/R_c)^{2n} + 1}, \quad (83)$$

where n , λ , and R_c are positive constants. In the early cosmological epoch ($R \gg R_c$) the model is close to the Λ CDM model ($f(R) \simeq R - \lambda R_c$), but there is the deviation from the standard scenario at late times. Substituting these functions into Eqs. (59)-(61) and solving them numerically, the dark energy equation of state w_{DE} for the model (83) starts to evolve from the value -1 and then it typically enters the phantom region $w_{\text{DE}} < -1$ by today Hu & Sawicki (2007).

In $f(R)$ gravity the scalar mass M is approximately given by $M^2 \simeq 1/(3f_{,RR})$ for $M^2 \gg H^2$ Starobinsky (2007). When $M^2 \gg k^2/a^2$ the perturbations are in the GR regime where $G_{\text{eff}} \simeq G$ and $\eta \simeq 1$. At late times there is the transition to the “scalar-tensor” regime ($M^2 \ll k^2/a^2$) in which $G_{\text{eff}} \simeq 4G/3$ and $\eta \simeq 1/2$. For larger k the transition from the GR regime to the scalar-tensor regime occurs earlier Starobinsky (2007). The epoch of transition also depends on the model parameters n and λ . If all the perturbation modes relevant to large-scale structures are in the scalar-tensor regime today, they show at present a γ index in the range $[0.40, 0.43]$ Tsujikawa et al. (2009). If some of the modes are in the GR regime today, the γ values at $z = 0$ should range from 0.40 up to 0.55. Furthermore, in the scenario where all modes are in the scalar-tensor regime, then at higher redshifts the growth index should generally decrease with increasing redshift, reaching values as low as $\gamma \simeq 0.1$ at $z \sim 1$ Tsujikawa et al. (2009).

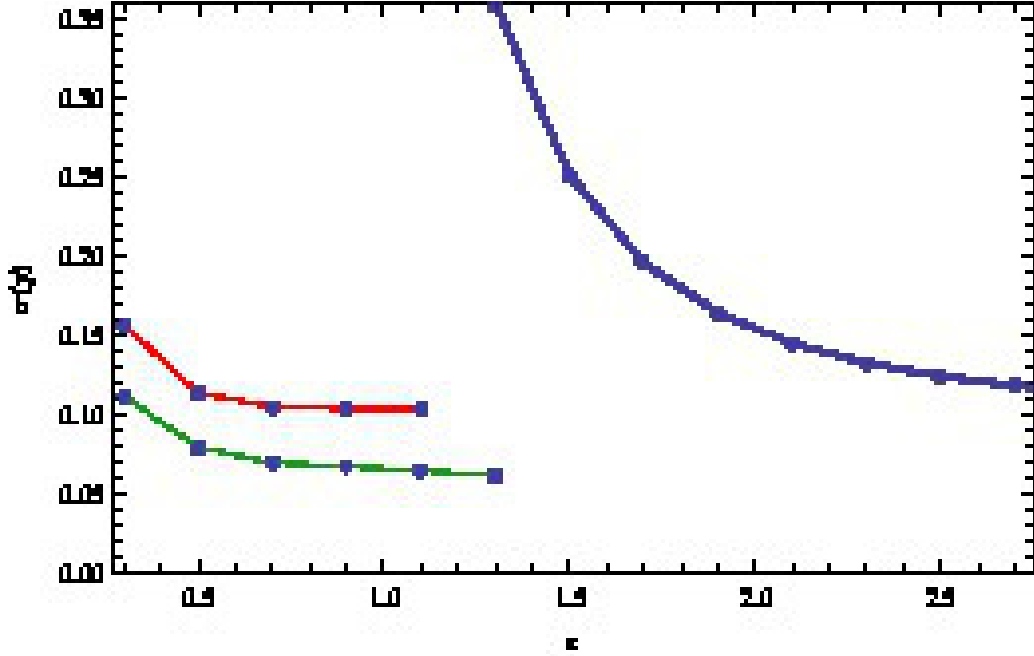


Figure 27: Cumulative constraints on the modified gravity parameter γ , as a function of redshift. This plot shows how the constraints improve as we include each additional redshift slice. The red line, leading up to $z = 1.1$, denotes the constraints from RGs; the green line, up to $z = 1.3$, denotes the constraints from ELGs; and the blue line, which extends to $z > 2.7$, denotes the constraints from QSOs.

In Fig. 27 we show the aggregate uncertainties on γ from each type of tracer detected by J-PAS, as a function of z . The uncertainties in γ displayed in this figure should also allow discerning among different modified gravity models for which the growth index γ depends on the wave number k and the redshift z , as motivated by the discussion above. Provided the foreseen errors on γ shown in this figure are roughly at the level of $\sigma_\gamma \simeq 0.07\text{--}0.12$ for LRGs and ELGs, respectively, such scenarios should be easily distinguishable from GR.

We also note that, in the so-called covariant Galileon model De Felice et al. (2011), the growth rate of matter perturbations and the variation of γ are generally larger than those in $f(R)$ gravity. Therefore, we expect this kind of modified theory to be even more tightly constrained by the J-PAS data.

3.7.7. Vector-tensor theories of gravity

Modified gravities involving new vector degrees of freedom have received much attention in recent years motivated in part by the problem of the large angle anomalies observed in the CMB temperature maps which could suggest the existence of preferred spatial directions. Thus, the most general action for a vector-tensor theory without any restriction but having linear second order equations of motion reads:

$$S = \int d^4x \sqrt{-g} \left(-\frac{R}{16\pi G} + \omega R A_\mu A^\mu + \sigma R_{\mu\nu} A^\mu A^\nu + \lambda (\nabla_\mu A^\mu)^2 + \epsilon F_{\mu\nu} F^{\mu\nu} - V(A_\mu A^\mu) \right). \quad (84)$$

In the so-called Einstein-Aether theories Zlosnik et al. (2007), the norm of the field is fixed by means of a Lagrange multiplier $\lambda(A_\mu A^\mu \pm m^2)$ so that A_μ can be constrained to be either time-like or space-like. In the time-like case, it has been shown that this kind of fields can act as dark matter. As a matter of fact this kind of Einstein-Aether theories can be understood as relativistic versions of the MODified Newtonian Dynamics (MOND) theory Milgrom (1983) proposed to explain galactic rotation curves from a modification of Newton second law at low accelerations. This kind of theories can mimic some of the properties of cosmological dark matter but the predictions are in tension with CMB and LSS observations. Further developments of this kind of theories are the Tensor-Vector-Scalar (TeVeS) Bekenstein (2004) theories which could provide accelerated expansion solutions Diaz-Rivera et al. (2006).

In the general case in which the norm is not fixed, it is possible to construct dark energy models by choosing appropriate potential terms Armendariz (2004); Kiselev (2004). Nevertheless, one of the most appealing properties of vector-tensor theories is that unlike scalar ones, they can generically give rise to periods of acceleration even in the absence of potential terms Beltran-Jimenez & Maroto (2009). Thus, it is possible to show that in the $V = 0$ case, there are six models whose PPN parameters are exactly the same as in General Relativity and therefore do not suffer from inconsistencies with local gravity tests Beltran-Jimenez & Maroto (2009), namely: $\sigma = -4\lambda = -4\varepsilon$, $\sigma = -3\lambda = -2\varepsilon$, $\sigma = 0$ and $\sigma = m\varepsilon$ with $m = 0, -2, -4$, all of them with $\omega = 0$. However, in general these models exhibit classical or quantum instabilities in certain regions of the parameter space. There is however a particular case which is stable both at the classical and at the quantum level corresponding to $\sigma = \omega = 0$ Beltran-Jimenez & Maroto (2009), and behaves at the background level exactly as Λ CDM. The corresponding perturbations have speed of sound $c_s^2 = 1$ and vanishing anisotropic stress $\pi = 0$ i.e. $\Phi = -\Psi$ and therefore the model behaves as a quintessence theory without potential term. Notice that unlike Λ CDM or scalar-tensor theories, this model does not include dimensional parameters in the action apart from Newton constant.

This is an example of one of the main difficulties when trying to determine the nature of dark energy from observations which is the degeneracy problem Kunz (2012), i.e. different dark energy models or modified gravities can give rise to the same background evolution. This degeneracy can be broken in certain cases at the level of perturbations. Thus for example, modified gravity theories involving geometric degrees of freedom generically predict non-vanishing anisotropic stress $\pi \neq 0$ unlike standard dark energy models.

3.7.8. Higher dimensions and massive gravity

Modifications of gravity resorting to extra dimensions were proposed by Dvali-Gabadadze-Porrati (DGP) Dvali et al. (2000). In these models our universe is understood as a 3-brane embedded in a five-dimensional bulk space. The corresponding gravitational action reads:

$$S = -\frac{M_5^3}{2} \int d^5x \sqrt{-g} R_5 - \frac{M_p^2}{2} \int d^4x \sqrt{-h} R_4 + S_{GH} \quad (85)$$

with M_5 the 5-dimensional Planck scale, R_5 is the Ricci scalar in five dimensions and S_{GH} a boundary term. In this model, gravity behaves as ordinary four-dimensional General Relativity on small scales, whereas on large scales the gravitational interaction leaks into the bulk. The corresponding cross-over scale is: $r_c = M_p^2 / (2M_5^3)$. In a flat Robertson-Walker background, the DGP model predicts a modified Friedmann equation given by:

$$\left(1 - \frac{\varepsilon}{Hr_c}\right) H^2 = \frac{8\pi G}{3} \rho \quad (86)$$

with $\varepsilon = \pm 1$. When $Hr_c \gg 1$, i.e. the Hubble radius is much smaller than the cross-over scale, we recover the standard Friedmann equation. However at late times, the modification implies that in a matter dominated universe in the so-called self-accelerating branch $\varepsilon = +1$, the scale factor accelerates towards a de Sitter regime. Unfortunately this branch has a ghost-like instability. Despite this fact, the DGP model provides the first example of degravitation, i.e. the possibility of modifying General Relativity in the infrared in such a way that gravity weakens on large scales. This is a generic feature of massive gravity theories and has been proposed as a way to weaken the effects of vacuum energy on the geometry.

In massive gravities, the graviton contains five degrees of freedom, namely the two standard helicity-2 modes, two additional helicity-1 mode and one helicity-0. The standard Fierz-Pauli Lagrangian for massive gravity is known to exhibit certain ghosts instabilities associated to non-linearities containing higher derivatives in the helicity-0 sector. Recently a new massive gravity theory has been proposed De Rham (2010) in which all the nonlinearities containing higher than second derivatives are eliminated. This model has been shown De Rham et al. (2011) to exhibit self-accelerated solutions without the instability problems of the original DGP model.

3.8. Inflation

Inflation represents a period of accelerated expansion of the universe at very early times that provides the appropriate conditions to give rise to some of the present properties of the universe such as homogeneity, isotropy and flatness. In addition, quantum fluctuations of the inflaton field that dominates the dynamics of the universe at those early times are the seeds that evolved via gravitational instability to the present large-scale structure of the universe.

The simplest models of inflation produce a nearly scale invariant primordial power spectrum with a spectral index n_s close to one. Beyond the power spectrum, inflation also predicts density perturbations with a distribution very close to that of a homogeneous and isotropic Gaussian random field. The degree of deviation from Gaussianity depends on the specific model and is characterized by the so-called non-linear coupling parameter f_{NL} (Verde et al., 2000; Sefusatti & Komatsu, 2007; Dalal et al., 2008).

Large-scale galaxy surveys are among the best cosmological observations to provide information about the physics of inflation. J-PAS will be able to measure with high sensitivity the parameters characterizing the primordial power spectrum, n_s and its *running*, as well as possible departures from Gaussianity, f_{NL} . This information, in combination with CMB measurements, will help in understanding the properties of the inflationary potential.

Beyond these parameters, J-PAS will also serve to probe fundamental implications of standard inflation as homogeneity, isotropy and Gaussianity. The large-scale anomalies recently confirmed by Planck *Planck* Collaboration et al. (2013g), indicates some hints of statistical anisotropy at scales above several degrees. Although the sky coverage of J-PAS is not wide enough to study in detail these anomalies, it is sufficient to explore whether homogeneity and isotropy are hold.

The capabilities of J-PAS to constrain deviations from Gaussianity are much higher. In particular, primordial non-Gaussianity produces a non-linear bias in the galaxy clustering that will be measured by J-PAS, providing constraints on the local shape of $f_{NL} < 8.2, 4.7, 1.8$ for ELGs, RGs, QSOs, respectively. The expected combined sensitivity is $f_{NL} < 1$.

The initial perturbations generated during the inflationary epoch leave their imprint in the galaxy formation process. In particular, the halo two-point correlation function contains information about all the higher moments of the matter distribution (Matarrese 1986). The halo bias is modified in the presence of primordial non-Gaussianity that could be originated in different ways in the context of the inflationary theory. J-PAS represents an excellent survey to study primordial non-Gaussianity due to its depth and area of sky to be covered.

The Bardeen potential $\Phi(\mathbf{x})$ in the case of local non-Gaussianity is

$$\Phi(\mathbf{x}) = \phi(\mathbf{x}) + f_{NL} (\phi^2(\mathbf{x}) - \langle \phi^2 \rangle) , \quad (87)$$

where $\phi(\mathbf{x})$ is a Gaussian random field and f_{NL} is the non-linear coupling parameter. It is possible to relate the matter overdensity field δ_R , smoothed on a scale R , with the potential through the Poisson equation. In Fourier space this gives the expression

$$\delta_R(k) = \mathcal{M}_R(k)\Phi(k) , \quad (88)$$

where

$$\mathcal{M}_R(k) = \frac{2c^2 k^2 T(k)}{3\Omega_m H_0^2} W_R(k) . \quad (89)$$

Here, $T(k)$ is the matter transfer function and $W_R(k)$ is the Fourier transform of the window function with characteristic radius R . Usually a spherically symmetric top-hat function is assumed for $W_R(k)$. Primordial non-Gaussianity present in the initial perturbations modify the bias relation in the following way

$$b_R(k, z) = b_g(z) + 2(b_g(z) - 1)\delta_c(z) \frac{\mathcal{F}_R(k)}{\mathcal{M}_R(k)} , \quad (90)$$

where $b_g(z)$ is the usual Gaussian bias and

$$\mathcal{F}_R(k) = \frac{f_{NL}}{8\pi^2 \sigma_R^2} \int_0^\infty dk_1 k_1^2 \mathcal{M}_R(k_1) P_\phi(k_1) \int_{-1}^1 d\mu \mathcal{M}_R(k_2) \left(\frac{P_\phi(k_2)}{P_\phi(k)} + 2 \right) . \quad (91)$$

In this expression $k_2 = \sqrt{k^2 + k_1^2 + 2kk_1\mu}$ and $P_\phi(k)$ is the power spectrum of the gaussian field ϕ . In the large scale limit we have that $\mathcal{F}_R(k) \simeq f_{NL}$ and the correction to the non-Gaussian bias becomes as in Dalal et al. (2008).

Equation (90) depends on the mass M (or equivalent the radius R) of the halo whose distribution is given by the mass function $n(M, z)$. The total effective bias is a weighted sum of equation (90):

$$b(k, z) = \frac{\int_{M_{min}}^\infty dM b_M(k, z) n(M, z)}{\int_{M_{min}}^\infty dM n(M, z)} . \quad (92)$$

The lower limit M_{min} in the integral corresponds to the minimum mass of the halos present in the survey. The mass M_{min} is a free parameter depending on the characteristics of the survey. We will assumed a value of $10^{12-13} M_\odot$.

Among the catalogues of J-PAS the best to constrain the primordial non-Gaussianity is the QSO sample. The reason is that this population has a large bias and also it is deeper in redshift, given a stronger signal of non-gaussianity (see equation (90)).

	QSO	LRG
$f_{NL} = 0$	1.46	3.34
$f_{NL} = 10$	1.52	6.51
$f_{NL} = 30$	1.67	7.46

Table 14: The $1-\sigma$ errors on f_{NL} obtained from QSO and LRG catalogues derived from J-PAS. Different fiducials for f_{NL} are considered.

	QSO	LRG
$f_{NL}(k_p) = 10$	3.25	15.4
$f_{NL}(k_p) = 30$	1.13	5.56

Table 15: Errors on the index n_f for different values of the amplitude $f_{NL}(k_p)$. The fiducial value of n_f is assumed to be zero which corresponds to a scale invariant case.

The conditional constraints on f_{NL} obtained from J-PAS are given in Table 14. The error increases as the fiducial value of f_{NL} is higher. This increment is more pronounced in the case of the LRG sample. For the QSO catalogue the error in f_{NL} remains almost unaltered at a value of $\Delta(f_{NL}) \approx 1.5$. By combining all the tracers detected by J-PAS, in the sense of Abramo & Leonard (2013), we expect to achieve a limit $f_{NL} < 1$.

Scale-dependent Non-Gaussianity

In the case of scale-dependent non-Gaussianity the non-linear coupling parameter f_{NL} depends on the wavevector k . This leads to a non-local coupling of the fields. The k -dependence of f_{NL} can be parametrized by

$$f_{NL}(k) = f_{NL}(k_p) \left(\frac{k}{k_p} \right)^{n_f}, \quad (93)$$

where k_p is the pivot wave vector. This quantity has no physical meaning and it can be chosen such that the two parameters $f_{NL}(k_p)$ and n_f have negligible correlation. The index n_f represents the derivative

$$n_f = \left(\frac{d \log f_{NL}(k)}{d \log k} \right)_{k=k_p}. \quad (94)$$

The modification to the $\mathcal{F}_R(k)$ function when scale-dependent f_{NL} is taken into account is

$$\mathcal{F}_R(k) = \frac{1}{8\pi^2 \sigma_R^2} \int_0^\infty dk_1 k_1^2 \mathcal{M}_R(k_1) P_\phi(k_1) \int_{-1}^1 d\mu \mathcal{M}_R(k_2) \left(f_{NL}(k) \frac{P_\phi(k_2)}{P_\phi(k)} + 2f_{NL}(k_2) \right). \quad (95)$$

The constraints on non-Gaussianity when f_{NL} is assumed scale-dependent are given in Table 15. In this scenario with scale-dependent non-Gaussianity we have a two-dimensional parameter space given by the amplitude $f_{NL}(k_p)$ and an index n_f . The pivot point is chosen around $k_p = 0.27 h \text{ Mpc}^{-1}$ in order to cancel the correlation between them. The fiducial value of the index n_f is zero. Since the correlation between the amplitude and the index vanishes and the fiducial model is $n_f = 0$, then the error in the amplitude $f_{NL}(k_p)$ for this particular pivot scale is the same as for a model with constant f_{NL} (Table 14). On other hand the errors in n_f are in the Table 15. When the amplitude is $f_{NL}(k_p) = 0$ there is no information on n_f in the model and then it is not possible to constrain the index. As the amplitude is increased the error in n_f decreases because the model is more sensitive to the tilt.

4. Scientific Goals II: the J-PAS Galaxy Evolution Survey

J-PAS will build a formidable legacy data set by delivering low resolution spectroscopy ($R \sim 50$) for every pixel over an SDSS-like area of the sky. A unique characteristic of this type of data is the fact that photo-spectra based on narrow-band imaging, unlike standard spectroscopy, does not suffer from systematic uncertainties in the flux calibration. Every data point of the photo-spectrum -i.e. every filter- is observationally independent, so the resulting SED is not affected by low frequency systematics in the relative flux calibration (or color terms) that can lead to biases in the derived physical properties. Multi-filter spectrophotometry thus provides accurate (low-resolution) SEDs over a wide range in wavelengths and spatial scales. The four main features of J-PAS that are relevant to the study of galaxy evolution are as follows:

- (1) a narrow-band filter system providing low resolution spectra ($R \sim 50$) that will result in very high quality photometric redshifts and adequate sampling of galaxy SEDs,
- (2) a uniform and non-biased spatial sampling allowing environmental studies at small scales, unlike spectroscopic surveys that depend on target selection and are sometimes affected by fiber collision problems,
- (3) an IFU-like character, allowing a pixel-by-pixel investigation of extended galaxies, and
- (4) a large survey area and volume which will sample hundreds of millions of galaxies.

With these specific capabilities in mind, we have identified five key extra-galactic science drivers for J-PAS. These are the following:

1. The Nearby Universe: We will take advantage of the IFU-like capabilities of the J-PAS survey to determine the properties of the spatially resolved components of galaxies in the nearby universe, studying the evolution of galactic disks and spiral structure, bars, satellites, and spheroidal components.

2. Evolution of the galaxy population since $z \sim 1$: Using accurate photometric redshifts and the low-resolution spectra based on the narrow-band filter system we will determine the evolution of the galaxy population from the present-day up to $z \sim 1$ when the star formation rate density was an order of magnitude larger, and when most massive galaxies had formed the bulk of their mass. We will study the build-up of the stellar mass function, the evolution of the mass and SFR density, spectral types, and the bimodality of galaxy populations and the transition region (the “green valley”). Stellar populations will be studied from analysis of the continuum through spectral fitting techniques, spectral indices and emission lines (individual objects and stacked samples).

3. The High Redshift Universe: By exploiting data from GALEX in the observed near-ultraviolet as well as several real and synthesized J-PAS broad-band filters we will furthermore be able to select galaxies at $z \approx 1 - 4$ using the Lyman break technique. At $z \sim 3$ we will construct the largest sample of LBGs probing the bright end of the UV luminosity function, allowing unprecedented studies of, e.g., their stellar populations and clustering. We will also be able to detect luminous Ly α emitters in the redshift range $z = 2.1 - 2.5$ using the narrow-band selection technique, and search for giant extended Ly α (and other) emission line nebulae.

4. The Growth of the Large-Scale Structure: J-PAS will allow us to study the build-up of groups and clusters of galaxies, the evolution of the intra-group and intra-cluster light, and the role of environment on galaxy evolution based on an accurate reconstruction of the cosmic density field.

5. The Build-up of Supermassive Black Holes: J-PAS will collect large samples of AGN such as Seyfert galaxies, quasars, blazars, and radio galaxies over a very wide redshift range, allowing large statistical studies of the clustering, environments, triggering mechanisms, morphologies of the various AGN populations, and their role in galaxy evolution during the downsizing epoch.

In Section 4.1 below we will describe some of the measurement techniques that will be applied to the J-PAS data. Section 4.2 will describe each of the five key science drivers listed above in more detail. We conclude with a brief overview of other multi-wavelength data that will be available in the J-PAS area in Section 4.3.

4.1. Measurement Techniques

4.1.1. Redshifts and Sample size

The J-PAS narrow-band system will deliver photometric redshifts with a projected accuracy of $\sigma_z < 0.003(1+z)$, which is set by the goal of measuring the BAO signal along the line of sight. These photometric redshifts have been estimated for the subset of red $L > L^*$ galaxies at $z < 0.9$ with good Bayesian redshift “odds” using the well-tested Bayesian photometric redshift technique (Benítez, 2000; Benítez et al., 2004; Coe et al., 2006; Benítez et al., 2009).

Summarizing from the data presented in Section 2.4, by year 6 J-PAS will have detected respectively 18 and 73 million red and blue galaxies with 0.3% redshift errors. About 20% of these objects will lie at $z > 0.7$. If we relax the 0.3% redshift accuracy that is required by the cosmology experiment to $\gtrsim 1\%$ errors which are more than acceptable for typical measurements of galaxy evolution, J-PAS will detect 64M of red and 200M of blue galaxies with 1% redshift error (100M and 286M for 3% redshift error). The redshift distributions peak around $z \sim 0.5$, and contain several tens of millions of objects at $z > 1$ (primarily blue galaxies).

4.1.2. Stellar Population Modeling and Emission Line Measurements

Spectral Fitting Diagnostics for Old Stellar Populations. The use of multi-filter photometric surveys to determine SEDs and redshifts with high enough level of accuracy (like SDSS, see also COMBO-17: Wolf et al. (2008); COSMOS: Ilbert et al. (2009); ALHAMBRA: Moles et al. (2008)) has opened a new way to analyze the stellar populations of galaxies at different redshifts and in different environments, allowing accurate studies of the evolution of galaxies and cosmology based on very large samples. The combination of the number of filters, the sky coverage and the depth of the survey will make J-PAS an unprecedented experiment for stellar population studies.

One of the major advantages of a survey like J-PAS is the fact that it provides low resolution spectroscopy for every pixel of the sky. We define the term “J-spectra” as the low resolution spectra constructed from the 54 contiguous optical J-PAS NB filters. With low resolution spectrophotometric data, spectral fitting techniques over the full spectral range will allow the maximal exploitation of the information in the data. A unique characteristic of J-PAS is the fact that the J-spectra do not suffer from systematic uncertainties in the flux calibration, unlike standard spectroscopy. Every single point of the J-spectrum – i.e., every filter – is observationally independent from the other J-spectrum data points, so the resulting SED is not affected by large scale (low frequency) systematics in the relative flux calibration (hence in the SED colors). This means that the absolute shape of the J-spectrum continuum and its colors have a larger degree of reliability for conducting stellar population studies. Standard spectroscopy, which is affected by well-known flux calibration issues, is better suited for detailed studies of particular spectral features or line strength indices.

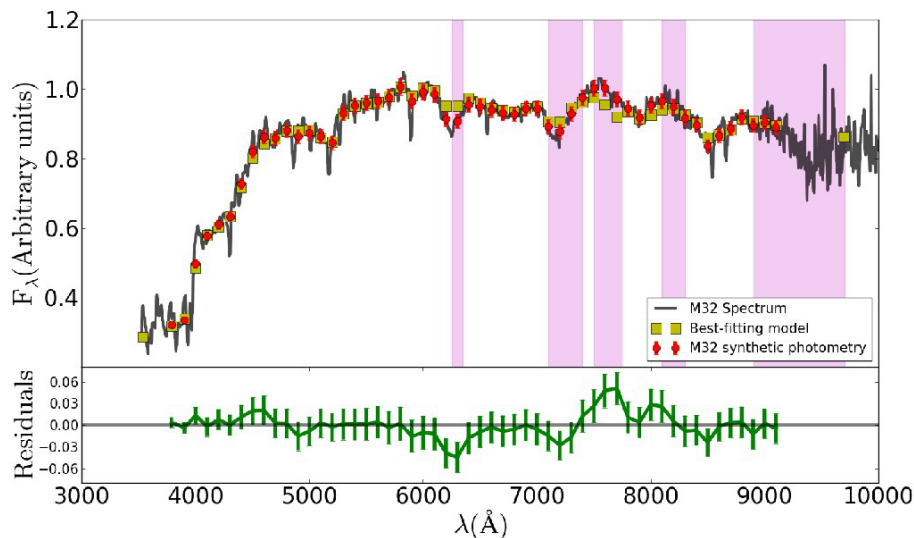


Figure 28: Spectral fitting of M32 as seen by J-PAS using the MIUSCAT SSP SEDs as template models. The spectrum of M32 at the nominal spectral resolution is illustrated by the black solid line, whereas the same spectrum at the J-PAS resolution is plotted with red dots. The best fit of a mixture of SSPs to the spectrum of M32, as derived from a standard χ^2 minimization technique, is shown with yellow squares. The residuals are shown in the lower panel in the same scale. Purple bands indicate the locations of potential telluric lines. See the text for more details.

For the proper analysis of the J-spectra of galaxies and stars in terms of their physical properties it is crucial to use template stellar libraries with extremely accurate flux calibration, such as MIUSCAT (Vazdekis et al., 2010; Ricciardelli et al., 2012). The MIUSCAT SSP models are perfectly suited for the analysis and interpretation of optical spectrophotometric data, provided that the flux calibration of the library stars is accurate over the full optical spectral coverage. Another important characteristic of the template stellar libraries required for J-PAS is the spectral coverage. Since J-PAS will sample the rest frame UV and optical regions of sources up to $z \sim 1$, we need synthetic libraries which adequately cover this range.

Reliability of Stellar Population Studies with J-spectra. Much of the recent progress in our understanding of galaxy evolution has come from the so called fossil-methods, which model the mixture of SSPs of different ages and metallicities to infer the main star formation episodes of galaxies out of medium resolution spectra (Walcher et al., 2011, and references therein). Besides the redshift, stellar masses and the luminosity/mass weighted ages and metallicities of the galaxies, these analysis techniques can recover the mass assembly and even chemical evolution histories, at least in a statistical sense (i.e., when applied to large samples). The evolutionary information decoded by these methods resides in the continuum shape and stellar absorption features. While the optical SED will be adequately sampled by J-PAS, most absorption features will be very heavily smoothed. This limitation poses the question: what can be learnt about stellar populations from J-spectra alone? From a purely academic perspective, the spectral resolution of the J-spectra ($R \sim 50$) is sufficient for identifying and measuring the strongest spectral features of quiescent stellar populations. For instance, the $\lambda 4000\text{\AA}$ break, the G-band at $\lambda 4300\text{\AA}$, the region around the Mgb doublet and the Fe lines at $\sim \lambda 5200\text{\AA}$, and the strongest TiO bands redwards of $\sim \lambda 6000\text{\AA}$, are distinguishable in the J-spectra, as illustrated below. It is important to note that the effective resolving power of absorption features is ultimately linked to the S/N ratio of the J-spectra.

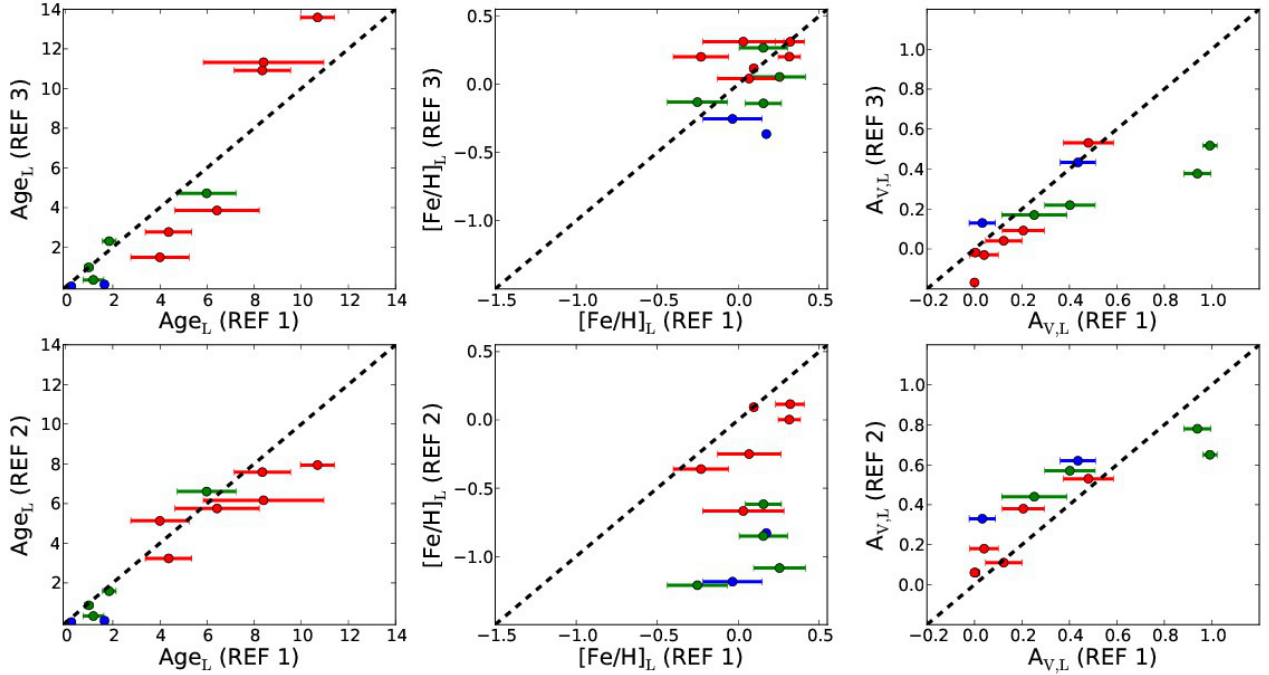
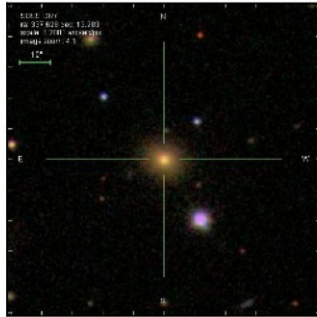
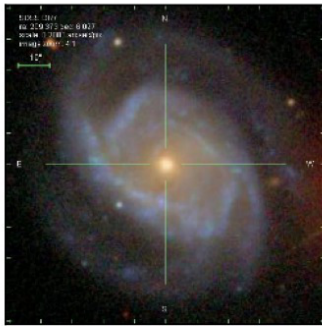


Figure 29: Summary of results of the “J-PAS Stellar Population Challenge” (see text for details). The figure presents a comparison between the luminosity weighted mean ages, metallicities and extinctions (A_V) obtained for 12 SDSS galaxies using three different analysis techniques, namely REF1, REF2 and REF3. Different colours correspond to galaxies with no emission lines and strong stellar continuum (red), weak emission lines and mild stellar continuum (green) and strong emission lines and weak stellar continuum (blue).

The case of M32. To illustrate this, let us focus on a classic test case of a quiescent stellar population: M32. Figure 28 presents the best fit SED derived from the integrated spectrum of M32 from Bica et al. (1990), taken from the compilation of Santos et al. (2002), and using the MIUSCAT SSP models as input templates. The M32 spectrum and the template spectra have been convolved with the J-PAS filters to simulate a realistic scenario. Errors have been set to 0.025 mag in each filter, which corresponds to a $S/N \sim 43$ in flux units. It is clear from the figure that the best fit, derived from a standard χ^2 minimization technique (Díaz-García et al., in prep.), reproduces well the observed spectrum at both short and long wavelengths. The residuals are shown in the lower panel. Note the telluric absorption features still present in the spectroscopic data redwards $\lambda 6000\text{\AA}$. Also, it is worth noting that the MIUSCAT models do not account for different α -element abundance ratios. The best fit solution to a single SSP corresponds to a MIUSCAT model of 3.2 ± 0.8 Gyr and a metallicity of around solar (0.11 ± 0.11 dex). When a more complex mixture of SSPs is allowed, a luminosity weighted age of 6.5 ± 1.5 Gyr and solar metallicity (0.05 ± 0.08 dex) is obtained. In both cases, the results are overall in good agreement with those based on much higher resolution spectroscopic data (e.g. Vazdekis & Arimoto, 1999; Schiavon et al., 2004; Coelho et al., 2009), hence illustrating the power of the low resolution data provided by J-PAS for stellar population studies.



Info
 =====
 (RA , DEC) = (337.628 , 13.983)
 $S_z = 172.85$ [65.96-232.22]
 $\chi^2 = 9.235 \rightarrow 9.235$
 $N_{Ok} = 44$
 $N_{SSP} = 2$
 E.L. = 0 - 0



Info
 =====
 (RA , DEC) = (209.373 , 6.097)
 $S_z = 272.26$ [173.25-339.57]
 $\chi^2 = 20.733 \rightarrow 20.733$
 $N_{Ok} = 45$
 $N_{SSP} = 2$
 E.L. = 4 - 011011

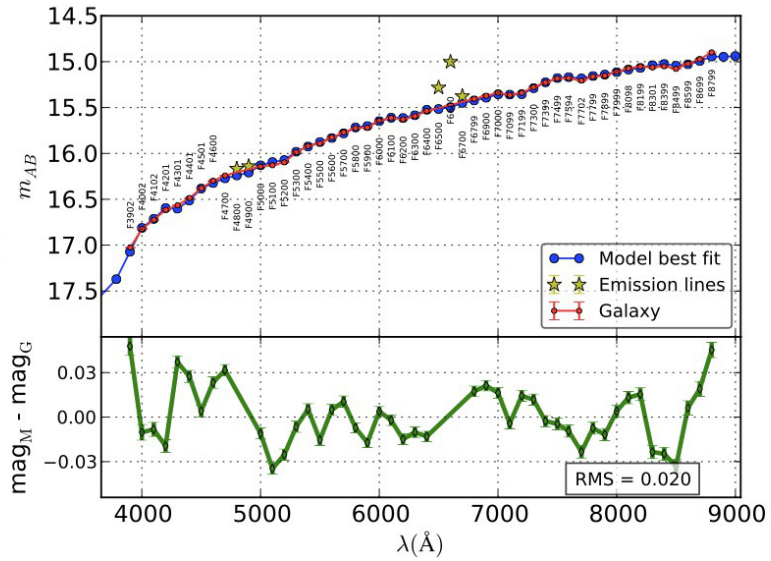
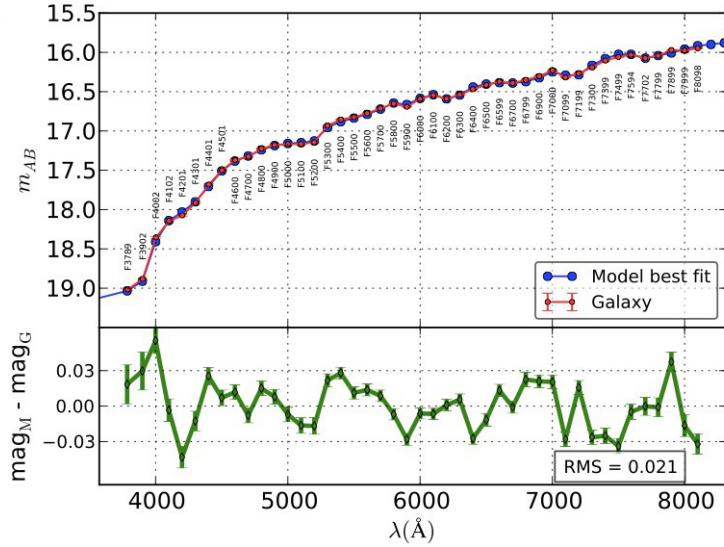


Figure 30: Two examples of SDSS galaxies taken from the “J-PAS Stellar Population Challenge” (see text for details). The SDSS images are shown on the left. On the right, the constructed J-spectrum (red) and the best fit (blue) are illustrated. Bottom panels show the residuals of the fits. In this particular case, emission lines (yellow stars) are detected but ignored in the overall fit.

The J-PAS Stellar Population Challenge. The reliability of the stellar population parameters derived from the J-spectra depends not only on resolution, quality and spectral type, but also on the analysis technique employed. To account for this, we have set up an internal test within the J-PAS collaboration: the “J-PAS Stellar Population Challenge”. A dozen galaxies of various types were retrieved from the SDSS and their spectra were convolved with the J-PAS filters. The corresponding J-spectra were then distributed to the participants, who analyzed them using a common set of ingredients. This is necessary for homogenizing the results and allow for fair comparisons. Input SSP models were set to Bruzual and Charlot (2003), with the STELIB library, Padova (1994) evolutionary tracks and a Chabrier initial mass function (IMF). Also, a simple foreground dust screen with a Cardelli et al. (1989) reddening law was assumed. The participants were asked to provide estimates of the luminosity and mass weighted mean ages and metallicities, the V -band extinction, the stellar mass. In some cases, filters were masked out because of possible contamination by line emission. Figure 29 presents a comparative view of the luminosity weighted mean ages, metallicities and extinctions retrieved by the three different participants (“REF1”, “REF2”, and “REF3”). Suffice it to say that the analysis techniques employed in each case constitute a representative sample of methods employed in the current literature, ranging from full spectral fits, mixed populations fits, as well as a novel technique involving matching with SDSS galaxies. The important point is that the results derived by these different methods show a satisfactory degree of consistency, except for one particular technique that seems to underestimate the metallicities of, mainly, galaxies with emission lines. It is equally important to note that the results agree well with those obtained from full spectral fits of the original SDSS spectra analyzed with the same ingredients and the Starlight code (Cid Fernandes et al., 2005). This test demonstrates that, at least for the global properties analyzed here, the J-spectra do not lead to a substantial loss of information with respect to conventional medium resolution spectroscopy.

For illustration, Figure 30 provides two examples of SDSS galaxies employed in the test. Since the SDSS spectra do not cover the whole spectral range of J-PAS and because in some cases certain spectral windows are unusable, these tests used less data (typically 45 out of the 54+5 J-PAS filters) than will actually be available. Notice also that these experiments were carried out in the rest-frame (i.e., at $z = 0$), but the overall conclusion should remain valid up to at least $z \sim 0.5$. As the redshift increases, more UV light will be sampled, forcing analysis methods to deal with a spectral range not as well consolidated as the optical. On the other hand, the reduced age range should help alleviating some of the main degeneracies which affect population synthesis. In addition to that, the fact that the width of the narrow-band J-PAS filters (defined to be constant with λ) effectively decreases with redshift by a factor of $(1+z)$, leads to a significant improvement in the overall spectral resolution of the J-spectra at high redshift. In fact, as presented later, the higher effective spectral resolution toward higher redshifts helps to reduce the intrinsic uncertainties in the determination of stellar population parameters.

The different techniques employed in this test can (and will) be improved and fine-tuned to retrieve more robust determinations, making use of large spectroscopic datasets in the literature as training sets. On the other hand, by no means we try to convince the reader that the J-PAS data provide the same information that high resolution spectroscopy can provide. J-spectra will not be sensitive to weak absorption lines and will not allow detailed studies of element abundance ratios based on individual line strengths. What we hope to illustrate here is that J-spectra, even though they are of much lower resolution, provide meaningful information for stellar population studies. The lack of spectral resolution is partially compensated for by a much more reliable continuum determination (as compared to standard spectroscopy), so that spectral fitting techniques over the full spectral coverage can provide reliable information on, e.g., ages, metallicities, extinction, unlike standard spectroscopy. In fact, the definition of line strength indices in the 80’s and 90’s (e.g. those in the Lick system Gorgas et al., 1993; Worthey et al., 1994) was motivated by the need to overcome the intrinsic uncertainties of flux calibration in standard spectroscopy.

J-PAS will thus offer a new and fresh approach to stellar population studies. It is important to note that the state-of-the-art SSP models aim to provide accurate predictions for the observed SEDs, not only for different ages and metallicities, but also for different α -element abundance ratios. Different parameters in the models do not only affect predictions for the individual line strengths of Mg, Na, Ti, etc., but also the overall shape of the continuum (see, e.g. Sansom et al., 2013). Therefore, when the proper set of SSP models is employed, the J-spectra may be sufficient for distinguishing between different abundance ratios from the full spectral fitting.

Random Uncertainties in Stellar Population Determinations. To have a first estimate of the minimum random uncertainties that we may expect when measuring ages, metallicities and extinctions from the J-spectra, we have performed a Monte Carlo simulation with galaxy templates covering the expected parameter space of age, metallicity, extinction, redshift and S/N. Overabundances or varying IMFs were not considered in this test. The procedure can be summarized as follows:

- A set of 9 MIUSCAT SSPs with ages of 0.5, 3, and 10 Gyr, and metallicities of 0.0, -0.4 , -0.7 dex were selected as the model target galaxies. The chosen values are representative of the typical ages and metallicities of red sequence galaxies over a range in mass and up to redshift ~ 1 that J-PAS is expected to observe.
- The 9 target SSPs were modified to match three different extinction values ($A_V = 0.0, 0.3$ and 0.6), six different redshifts ($z = 0.0, 0.2, 0.4, 0.6, 0.8$ and 1.0), and four different values of the average S/N per filter (10, 20, 50 and 100). Overall, this translates into 648 target SSPs.
- For each target SSP, one thousand simulations were created according to the assumed S/N per filter. For each simulation, a χ^2 minimization fitting technique that mixes two (younger + older) SSPs (see details in Díaz-García et al. in prep.) was performed, resulting in a best fit with its corresponding redshift, luminosity weighted mean age, metallicity and extinction. The whole set of SSPs ($0.06 \leq \text{age} \leq 14.1$ Gyr; 48 steps; $-2.3 \leq [\text{Fe}/\text{H}] \leq +0.2$ dex; 7 steps) of the MIUSCAT database has been employed to perform the fits.
- With all the best solutions for each target SSP, the mean values of age and metallicity and the root mean square (rms) of the obtained solutions (σ_{Age} and $\sigma_{[\text{Fe}/\text{H}]}$) were computed. These values can be considered as a first order estimate of the best-case uncertainties in the parameter estimation.

The results of this test are presented in Table 16. It is worth noting that the uncertainties presented here illustrate the typical random errors that we may expect just due to the noise in the J-PAS photometry. Systematic effects coming from differences in the spectrophotometric system of real J-spectra and SSP templates, or intrinsic differences between simple template models and more complex real galaxies will add additional uncertainty to the derived values, certainly dominating the final errors for high S/N data. In this sense, the numbers in Table 16 must be considered as a lower limit (best case) to the final errors expected in luminosity-weighted SSP-equivalent ages and metallicities. As expected, the uncertainties in age and metallicity decrease as the S/N per filter increases, also depending on the parameter space region (Age-[Fe/H]). For instance, at $z = 0$, σ_{Age} and $\sigma_{[\text{Fe}/\text{H}]}$ vary from ~ 3 Gyr and ~ 0.2 dex for S/N= 10 down to ~ 0.6 Gyr and ~ 0.02 dex for S/N= 100. Interestingly, we also see a trend of smaller errors obtained at higher redshift. This is probably due to the fact that the effective spectral resolution increases with redshift as $(1 + z)$, which improves the power to disentangle the age-metallicity degeneracy. This is an interesting result that, to some extent, helps to alleviate the effects of a decreasing S/N with increasing redshift when determining the stellar population parameters.

Table 16: Typical uncertainties in the determination of ages and metallicities (σ_{Age} in Gyr and $\sigma_{[Fe/H]}$ in dex) for old stellar populations using standard spectral fitting techniques applied to J-spectra. According to the photometric errors in the J-PAS filters given by the different S/N per filter (10, 20, 50 and 100), Monte Carlo simulations have been performed for different redshifts ($z = 0.0, 0.2, 0.4, 0.6, 0.8$ and 1.0), extinction ($A_v = 0.0, 0.3$ and 0.6), age (0.5, 3 and 10 Gyr) and metallicity ($[Fe/H] = -0.7, -0.4$ and 0.0 dex). In each case, σ_{Age} and $\sigma_{[Fe/H]}$ represent the rms standard deviation of the 3×1000 best solutions obtained around the nominal age and metallicity input values for the 3 different extinction values. See the text for more details on the procedure.

S/N	Age	z=0.0			z=0.2			z=0.4			z=0.6			z=0.8			z=1.0			
		[Fe/H] (dex)																		
		-0.7	-0.4	0.0	-0.7	-0.4	0.0	-0.7	-0.4	0.0	-0.7	-0.4	0.0	-0.7	-0.4	0.0	-0.7	-0.4	0.0	
10	0.5 Gyr	σ_{Age}	0.98	1.04	1.04	0.84	0.93	0.69	0.70	0.79	0.56	0.68	0.61	0.57	0.52	0.48	0.49	0.43	0.47	0.55
		$\sigma_{[Fe/H]}$	0.35	0.26	0.23	0.31	0.19	0.15	0.35	0.27	0.15	0.35	0.29	0.17	0.39	0.31	0.18	0.48	0.34	0.17
	3 Gyr	σ_{Age}	2.55	2.69	2.75	2.57	2.68	2.71	2.44	2.16	1.95	2.20	1.90	1.31	2.01	1.86	0.91	1.76	1.75	0.73
		$\sigma_{[Fe/H]}$	0.29	0.32	0.26	0.26	0.24	0.23	0.28	0.25	0.13	0.27	0.20	0.06	0.24	0.16	0.04	0.22	0.16	0.02
	10 Gyr	σ_{Age}	2.97	2.86	2.62	2.73	2.72	2.43	2.80	2.63	1.50	2.60	2.31	1.47	2.47	1.84	1.41	2.33	1.61	1.06
		$\sigma_{[Fe/H]}$	0.26	0.22	0.14	0.23	0.18	0.13	0.22	0.20	0.06	0.18	0.18	0.04	0.15	0.13	0.01	0.13	0.13	0.01
20	0.5 Gyr	σ_{Age}	0.85	0.70	0.65	0.63	0.39	0.50	0.67	0.57	0.35	0.53	0.38	0.26	0.38	0.31	0.27	0.35	0.32	0.33
		$\sigma_{[Fe/H]}$	0.25	0.13	0.13	0.20	0.11	0.10	0.25	0.26	0.12	0.29	0.25	0.12	0.31	0.26	0.11	0.38	0.26	0.12
	3 Gyr	σ_{Age}	1.90	1.96	1.93	2.00	1.79	2.11	1.79	1.51	1.02	1.42	1.05	0.65	1.21	1.17	0.62	1.10	0.94	0.58
		$\sigma_{[Fe/H]}$	0.19	0.16	0.15	0.17	0.14	0.14	0.19	0.14	0.05	0.16	0.09	0.02	0.14	0.08	0.02	0.13	0.08	0.01
	10 Gyr	σ_{Age}	2.09	1.97	2.17	2.19	2.10	1.99	1.98	1.98	0.96	1.75	1.54	0.83	1.62	1.41	0.75	1.64	1.12	0.49
		$\sigma_{[Fe/H]}$	0.13	0.11	0.11	0.12	0.12	0.09	0.13	0.13	0.03	0.11	0.10	0.01	0.09	0.08	0.01	0.09	0.07	0.01
50	0.5 Gyr	σ_{Age}	0.37	0.30	0.25	0.39	0.13	0.22	0.43	0.29	0.09	0.24	0.17	0.05	0.26	0.04	0.04	0.23	0.06	0.05
		$\sigma_{[Fe/H]}$	0.13	0.03	0.05	0.12	0.02	0.05	0.18	0.15	0.07	0.18	0.13	0.05	0.17	0.09	0.05	0.10	0.05	0.04
	3 Gyr	σ_{Age}	1.05	1.30	1.16	1.01	1.20	1.40	0.97	0.72	0.53	0.81	0.46	0.48	0.70	0.27	0.47	0.73	0.27	0.38
		$\sigma_{[Fe/H]}$	0.07	0.08	0.08	0.07	0.07	0.08	0.09	0.06	0.02	0.07	0.04	0.01	0.04	0.03	0.00	0.04	0.03	0.01
	10 Gyr	σ_{Age}	1.28	1.33	1.35	1.26	1.37	1.17	1.05	1.18	0.43	0.58	0.86	0.30	0.53	0.58	0.27	0.42	0.47	0.15
		$\sigma_{[Fe/H]}$	0.06	0.05	0.05	0.06	0.06	0.04	0.06	0.06	0.01	0.04	0.04	0.01	0.03	0.03	0.01	0.02	0.03	0.01
100	0.5 Gyr	σ_{Age}	0.20	0.19	0.16	0.30	0.07	0.05	0.17	0.03	0.03	0.12	0.02	0.04	0.11	0.03	0.03	0.14	0.02	0.03
		$\sigma_{[Fe/H]}$	0.02	0.01	0.01	0.06	0.01	0.01	0.08	0.01	0.02	0.07	0.01	0.02	0.07	0.01	0.02	0.05	0.02	0.01
	3 Gyr	σ_{Age}	0.45	0.69	0.92	0.49	0.70	0.83	0.44	0.25	0.40	0.41	0.14	0.37	0.50	0.07	0.29	0.52	0.06	0.20
		$\sigma_{[Fe/H]}$	0.03	0.04	0.04	0.04	0.03	0.03	0.04	0.02	0.01	0.03	0.01	0.00	0.02	0.01	0.01	0.01	0.01	0.01
	10 Gyr	σ_{Age}	0.65	0.74	0.54	0.65	0.65	0.42	0.36	0.65	0.11	0.17	0.52	0.02	0.15	0.04	0.01	0.11	0.06	0.01
		$\sigma_{[Fe/H]}$	0.02	0.02	0.03	0.03	0.03	0.02	0.02	0.02	0.01	0.01	0.01	0.01	0.01	0.01	0.01	0.01	0.01	0.01

Pseudo Line-Strength Indices for Old Stellar Populations. Spectroscopic absorption line indices, as for instance the Lick system (Worthey et al., 1994), have been widely used to build diagnostic diagrams, where an age-sensitive index and a metallicity indicator are used to disentangle the age/metallicity degeneracy. Although this approach can give accurate estimates of age and metallicity, it is very expensive in terms of telescope time, since it requires high S/N spectra. A similar approach can be applied to narrow-band photometric surveys such as J-PAS, where the galaxy SED sampled at regular and small intervals in wavelength can be considered as a low-resolution spectrum.

We model photometric absorption indices on the basis of the MILES stellar population models (Vazdekis et al., 2010), and using the J-PAS filter definitions. We focus on two age-sensitive features (D4000 and H_β) and one metallicity indicator (Mg). To measure the photometric indices (H_β and Mg), we consider three J-PAS filters: one filter containing the feature of interest, and two filters directly on the red and blue side of the feature to measure the continuum. Hence, the index is given by the difference in magnitude between feature and continuum. The 4000Å spectral break is defined by adopting the classical definition of Bruzual A. (1983), which uses the magnitude difference between the bands at [4050, 4250] and [3750, 3950]Å.

Figure 31 shows the potential of this approach for disentangling age and metallicity in J-PAS. The orthogonality of the diagram is appreciable mainly when H_β is used as age indicator. On the other hand, the D4000 diagnostic is not independent of metallicity, but it is also more sensitive to age variation, showing a higher dynamical range. We have verified that the accuracy of the J-PAS photometric redshifts is not sufficient for the purpose of measuring indices, as it is large enough to move the filter containing the index by almost one filter-width, hence compromising the measurement. Thus, we plan to apply this approach to objects with known spectroscopic redshift. By assuming a redshift error of $\pm 150 \text{ km s}^{-1}$, taken as a conservative upper limit for the uncertainty on the galaxy rotational velocity, we obtain the index error indicated in Figure 31 by the thick red bar. The resulting uncertainties in the stellar population parameters are $< 1 \text{ Gyr}$ for the age and $\sim 0.2 \text{ dex}$ for the metallicity. The thin black bars in the same figure indicate an error in the index of 0.01 mag, which we consider to be the minimum photometric error obtainable. Photometric errors smaller than this will be hard to achieve because of zero-point errors. Such an error in the index translates into a S/N requirement of ~ 150 for each filter. For nearby galaxies, we aim to reach such a S/N ratio by azimuthal integration over rings of increasing radius. With such an approach we will be able to obtain spatially resolved stellar population analysis for a large number of nearby galaxies, for which spectroscopic redshifts are already available in the SDSS database.

Spectral Diagnostics for Emission Line Galaxies. Emission lines carry information about the excitation mechanism (AGN, young or old stars, shocks), the chemical abundance of the warm gas, and its dust content. In star-forming systems, the $H\alpha$ luminosity is a well-known tracer of the current star formation rate (Kennicutt, 1998), while for AGN [OIII] λ 5007 is a useful proxy for the accretion power of their super-massive black holes (Heckman et al., 2004).

Due to the low spectral resolution of J-spectra, direct measurements of emission line fluxes will be a challenge when using J-PAS data alone. A line of equivalent width W increases the flux in a filter of width $\Delta\lambda$ by a factor $(1 + W/\Delta\lambda)$. For $\Delta\lambda = 100\text{Å}$ and a photometric accuracy of 2%, lines stronger than $W \sim 7\text{Å}$ should be detected with a $S/N > 3$ assuming the adjacent filters trace the continuum appropriately and that no other strong line is present within the filter. Even in the most favorable situation, J-PAS data will not be able to separate $H\alpha$ from [NII] $\lambda\lambda$ 6548,6584Å precluding the application of traditional SF and AGN classification schemes (Baldwin et al., 1981). In short, direct emission line flux estimates from J-PAS will be of very limited use, except for the most extreme cases.

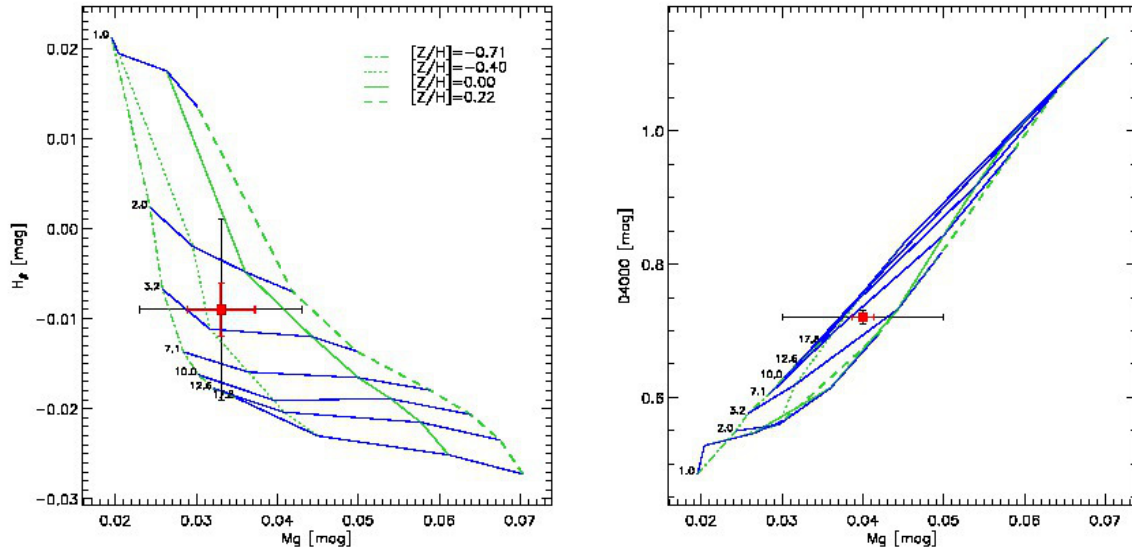


Figure 31: Index-index diagrams for age-sensitive indicators ($H\beta$ in the left-hand panel and D4000 in the right-hand one) versus the metallicity-sensitive index Mg. The model grids are shown for ages ranging from 1 to 17.8 Gyr and for metallicities ranging from -0.71 up to 0.22 dex. The thin black bar shows an index error of 0.01 mag, equivalent to a S/N ratio of ~ 150 per filter. The thick red bar indicates the uncertainty assuming a redshift error of 150 km s^{-1} .

A way to circumvent these problems was devised within our collaboration (Schoenell, 2010). The idea is to “borrow” emission line measurements from galaxies in the SDSS (or any other reference spectroscopic data set) that have approximately (say, in a χ^2 sense) the same J-spectrum as the J-PAS target. The underlying premise is that galaxies which are similar in so many filters should also be similar if observed under higher resolution. Experiments with this spectral matching scheme produced encouraging results. The method is able to recover the $[\text{NII}]/\text{H}\alpha$ and $\text{H}\alpha/\text{H}\beta$ ratios to within 0.16 dex. Other emission line indices (line ratios and equivalent widths) can be recovered with a similar accuracy. Figure 32 and Table 17 illustrate the application of this method to simulate J-PAS data out of actual SDSS spectra. As shown by Schoenell (2010); Schoenell et al. (2013), this method can be easily cast into a fully Bayesian framework, producing posterior probability distributions for any observed quantity. Conceivably, and in analogy with photo- z methods, even better results could be obtained by using the appropriate priors.

This technique opens up the possibility to use J-PAS to study emission lines at a level of detail much beyond initial expectations, substantially enlarging the scope of the project. In fact, this indirect (but very efficient) spectral matching trick can be applied to *any* observed or physical property derived from a SDSS spectrum. For instance, stellar population properties such as mean ages, stellar extinction, mass-to-light ratios and velocity dispersion derived from a full spectral analysis, such as those obtained by STARLIGHT¹² fits (Cid Fernandes et al., 2005), can be estimated through exactly the same formalism. More details on this method are presented in Schoenell et al. (2013)

¹²<http://www.starlight.ufsc.br>

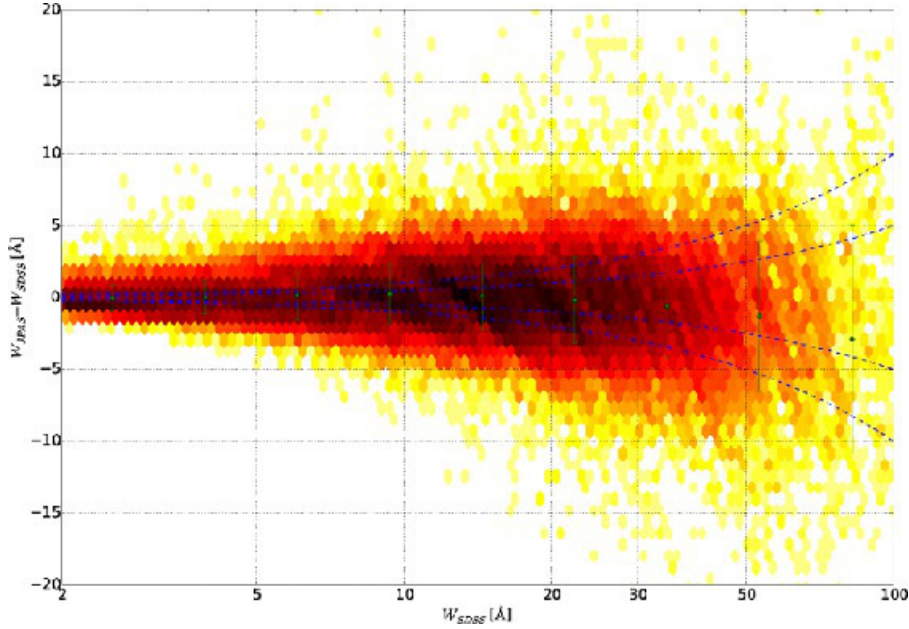


Figure 32: Tests of the spectral matching method. On the x axis we have the $H\alpha$ equivalent width measured on the SDSS spectra (W_{SDSS}) and, on the y axis, we have the difference between the value measured by the method explained in the text and the spectroscopic one ($W_{JPAS} - W_{SDSS}$). The color-scale is logarithmic. The two pairs of dotted lines indicate the $\Delta W = 5$ and 10% of W_{SDSS} .

Confronting the Models. One key aspect that has per force been excluded from the considerations above is the uncertainty in the stellar population models to which the J-PAS data are to be compared. These models are provided as sets of estimates of the spectral energy distributions (SEDs) of populations of stars of fixed age, metallicity and, in some cases, α -element abundance ratios, which are referred to as “single stellar populations” (SSPs). It is well known that the various stellar libraries, isochrones and other modeling constituents used in the competing model sets result in significant differences in the flux levels of the SEDs derived. These can be at the 5% level, and often vary systematically with wavelength. However, while this presents a challenge to the analysis of J-PAS data, it also presents an opportunity. The large quantity of data for nearby galaxies that will be obtained by the J-PAS survey, particularly those for which high resolution spectroscopy is available, will allow the comparison of the results from various model sets. By comparing the best fitting SSPs from both high resolution absorption-line analysis and the low resolution J-spectra in each of the competing model sets, for the first time an analysis of the consistency and quality of fits of the modeling will be possible. This will allow feedback to the stellar synthesis community, hopefully resulting in insights into the wavelength dependent differences between models.

4.1.3. Density Field Construction

The estimation of the cosmic density field is of capital importance for large area surveys which are able to cover a wide range of environments, from the low density voids to the high density cores of clusters. In practice, the reconstruction of the galaxy density field reduces to the (weighted) count of objects within some aperture around a set of positions where the density field is to be evaluated. In the general case, the density at an observationally defined position $\mathbf{r} = (RA, DEC, z)$ can be estimated as in Kovač et al. (2010):

$$\rho(\mathbf{r}) = \sum_i m_i W(|\mathbf{r} - \mathbf{r}_i|; R), \quad (96)$$

Table 17: Emission line accuracy simulation. For each property (which can be an emission line equivalent width or an emission line ratio) we measured the average Δp , median Δp and standard deviation $\sigma(\Delta p)$ of the difference between our estimation and the value given by the STARLIGHT-SDSS database, which is based on the actual spectra.

Property	Δp	Δp	$\sigma(\Delta p)$
$\log W_{[OII]}$	0.051	0.065	0.223
$\log W_{H\beta}$	0.024	0.020	0.145
$\log W_{[OIII]}$	0.046	0.048	0.245
$\log W_{H\alpha}$	0.010	0.008	0.160
$\log W_{[NII]}$	-0.028	-0.024	0.159
$\log[NII]/H\alpha$	-0.045	-0.042	0.141
$\log[OIII]/H\beta$	0.026	0.027	0.250
$\log H\alpha/H\beta$	-0.011	-0.013	0.107
$\log[SII]/H\alpha$	-0.006	0.019	0.172
$\log[OII]/H\beta$	0.036	0.049	0.202
$\log[OIII]/[NII]$	0.075	0.063	0.265

where the summation is over those galaxies in the sample that have been chosen to define the density field, which we refer to as *tracer galaxies*, m_i is the astrophysical weight of the tracer galaxy, and the function $W(|\mathbf{r} - \mathbf{r}_i|; R)$ is the kernel used to weight the tracer galaxies, which is a spatial smoothing function, and R is the smoothing length. The W function is typically chosen such that it weights tracer galaxies depending on their distance $|\mathbf{r} - \mathbf{r}_i|$ from the position where the density field is being reconstructed. Kovač et al. (2010) show that photometric redshifts can be used in the estimation of the density field by using the probability distribution function (PDF) of the z_{phot} . It is common to express the resulting measurement of density as a dimensionless density contrast $\delta(\mathbf{r})$ defined as $\delta(\mathbf{r}) = [\rho(\mathbf{r}) - \bar{\rho}(z)]/\bar{\rho}(z)$, where $\bar{\rho}(z)$ is the mean density at a given redshift. We will test our methodology using *mock catalogues* derived from cosmological simulations available to the J-PAS collaboration. These mock catalogues mimic the J-PAS observational strategy, and are essential to assess the reliability and accuracy of the recovered density field.

Note that we can measure the density field from the galaxy distribution (δ^g), while we are ultimately interested in the underlying dark matter (DM) density field (δ^m), which defines the structures in the Universe. Both distributions are linked through the bias parameter b , with $\delta^g = b \times \delta^m$. The bias could be a complicated function of redshift, galaxy population, etc. The astrophysical weights m_i in Eq. (96) can be used to give less importance to more biased populations, thus improving the relation between the measured galaxy density field and δ^m . For example, the bias of red massive galaxies is higher than that of blue galaxies. Therefore, the optimum combination of different galaxy populations will enhance the precision and the reliability of our δ^g measurements. To reach this goal, instead of using as the weight some galaxy property, such as luminosity or mass, we can use the real bias of each population, estimated directly through clustering or weak lensing analysis.

J-PAS will allow us to compare and combine numerous estimators of density and environment. For example, the distance to the n th nearest neighbor is also a widely used density field estimator (see Haas et al., 2012). In this case the aperture R varies with the local density, from short lengths in dense environments to large ones in voids. Finally, decomposition of the density field into the main virialised structures such as clusters, groups, filaments, and voids can provide an alternative approach to quantifying the environment. J-PAS will allow us to search for differences between galaxies that are situated in similar local density but in different topological structures, and vice versa. This will allow important tests designed to understand the precise role of environment in galaxy evolution.

4.1.4. Morphological measurements

Since the first discovery of galaxies, classifications of their morphologies have been proposed. Hubble established a classification in which galaxies were divided in two main classes according to their global shape: ellipticals (E) and spirals (S). E galaxies were sub-divided in seven groups according to their ellipticity from E0 (round Es) to E7 (the most flattened Es). S galaxies were ordered into three groups depending on the relationship between the bulge and spiral arms (Sa, Sb, and Sc). Hubble established a sequence of shapes from E0 to Sc, with lenticular galaxies forming the bridge between E7 and Sa galaxies. Almost a hundred years after this classification there are still many open questions related to our understanding of the physics behind the formation and evolution of these different morphological types.

Large-scale imaging surveys such as the SDSS, Pan-STARRS, DES and J-PAS present us with a greatly increased number of galaxies to classify. Moreover, multi-wavelength, spatially-resolved datasets require us to also investigate the galaxy colors and the colours of many different components within those galaxies (i.e. thin and thick disk, bulge, bar, arms). These large data sets make any classification scheme based on visual classifications an enormous challenge, unless a large number of classifiers is involved (see the Galaxy Zoo project; Lintott et al., 2008). In most instances, therefore, automatic algorithms for galaxy classification are needed. Automatic methods for the classification of galaxies can be divided into two broad groups: parametric and non-parametric methods. Parametric methods measure a set of physical parameters by fitting some parametric laws to the light distribution of galaxies, and attempt to classify them accordingly. In contrast, non-parametric techniques characterize the morphological types of galaxies by translating them into a different mathematical or physical representation and then identify the most significant components.

In J-PAS different methods will be used for the morphological classification. The first two methods are based on the modeling of the surface brightness distribution of the galaxies. In the first one, a parametric method, we will model the galaxy surface brightness distribution by fitting the traditional parametric laws (see e.g., Prieto et al., 2001; Aguerri et al., 2004, and references therein). We will use standard codes like GASPH2D (Méndez-Abreu et al., 2008) or GALFIT (Peng et al., 2002). The modelization will provide us with an effective radius and surface brightness profile of the main galaxy components (see e.g., Aguerri et al., 2004; Méndez-Abreu et al., 2008, and references therein). These can then be used to evaluate the main scaling relations of galaxies and their evolution with time. This modeling will also allow us to perform a broad galaxy classification (early- versus late-type) based on the bulge-to-disc ratio or the Sersic shape parameter. Exploiting more fully the multi-band nature of J-PAS, we will also apply a recently developed multi-wavelength version of GALFIT named MegaMorph (Häußler et al., 2013). MegaMorph enables the automated measurement of wavelength-dependent structural parameters for very large samples of galaxies. In fact, fitting galaxy light profiles with multi-wavelength data increases the stability and accuracy of the measured parameters, and hence produces more complete and meaningful multi-wavelength photometry than has been available previously. We will recover the color and the color gradient of each galaxy component and we will study how it varies for different Hubble types. We will be able to understand how many components galaxies have, which components formed first, and if it has been rejuvenated by star formation due to recent mergers, or perhaps quenched.

In the second method, a non-parametric one, the modelization of the galaxy surface brightness distribution will be performed by fitting Chebyshev polynomials (CHEFs, Jiménez-Teja & Benítez, 2012). The CHEF method will not be directly performed on all objects to be classified, but on a visually, well classified, and complete set of galaxies (e.g., the EFIGI catalog; Baillard et al., 2011). In this way, we will project the CHEF mathematical basis onto a physically meaningful basis composed by the CHEF models of these EFIGI galaxies (after scaling, rotating, and flux normalizing them). Then, we will decompose the J-PAS galaxies using this physical basis providing us with a probability for each source to belong to a certain morphological type (according to the EFIGI precise classification).

Other non-parametric classifications will be achieved by using the codes GALSVN and MORPHOT. These two algorithms classify galaxies using a multi-dimensional set of galaxy parameters. The approach of the MORPHOT tool is fully empirical. In particular, MORPHOT exploits 21 morphological diagnostics, directly and easily computable from the galaxy image, to provide two independent classifications: one based on a Maximum Likelihood, semi-analytical technique, the other one using a Neural Network. The technique has been tested on a sample of ~ 1000 visually classified WINGS galaxies, proving to be almost as effective as 'eyeball' estimates. In particular, at variance with most existing tools for automatic morphological classification of galaxies, MORPHOT has been shown to be able to distinguish between ellipticals and S0 galaxies with unprecedented accuracy (see Figure 33). This morphological classification scheme is expected to be most efficient for those galaxies with an area larger than 200 pixels (see Fasano et al., 2012).

The second non-parametric algorithm that we will use for the morphological galaxy classification will be GALSVN. This code was developed by Huertas-Company et al. (2008) and has been applied to several samples of galaxies at different redshifts including galaxies from the ALHAMBRA survey (see Pović et al., 2013, and references therein). The ALHAMBRA images are of similar quality as the expected J-PAS data. The algorithm is a generalization of the non-parametric classifications by using an unlimited number of dimensions. The classification provided by this algorithm is probabilistic following a Bayesian approach (Huertas-Company et al., 2008). The algorithm is trained with a set of galaxies visually classified. These galaxies are inserted into the real scientific images according to the observed redshift distribution of the galaxies that we wish to classify. For each classified galaxy the algorithm then provides a probability for it to belong to each of the considered morphological classes. For example, the ALHAMBRA galaxies were classified in two groups (early and late types). Thus, each classified galaxy has a probability to belong to these two classes. Due to the similarities between the J-PAS and ALHAMBRA images, we expect to be able to classify all J-PAS galaxies down to 22 AB mag in the r' -band filter in at least in two broad groups (early and late). For the ALHAMBRA galaxy survey ($4^\circ \times 4^\circ$) we have obtained a sample of 22 051 well-classified objects at $z < 1.5$ having $F613W < 22$ mag (Pović et al., 2013). This means that we expect to classify several millions of galaxies in the full J-PAS survey. Large galaxies (larger than 200 pixels) will be classified using a finer classification in which all the Hubble galaxy types will be considered.

In summary, J-PAS will deliver the largest sample of galaxies with morphological classifications, bulge-to-disk ratios, and integrated and component colors in the literature, which will be useful for a wide variety of studies of galaxy evolution.

4.2. Science Themes

4.2.1. Theme I. The Nearby Universe

What can J-PAS do for improving our understanding of the formation of galaxies across the local Hubble sequence in general, and for galaxies like our own Milky Way in particular? Although the general picture of disk galaxy formation has more or less been established, the relative importance of the various secular and accretion-driven processes is an ongoing topic of investigation. Fortunately, galaxies possess a long memory in terms of the fossil record in their stars which we can use to trace their evolutionary history. Since the seminal work of Eggen et al. (1962) the importance of the study of ages and chemical abundances has been recognized. Of particular relevance is the problem of radial migrations of gas and stars within the disk. The realization that stars in galactic disks can migrate radially across significant distances has, in recent years, completely changed the discourse on spiral galaxy evolution. The subject of disk migration has received particular attention in the last few years in light of new astro-archaeology surveys of the Milky Way (e.g., APOGEE, HERMES, and Gaia). Radial migration in the Milky Way brings stars from the inner and the outer disk, where the mean abundances are different, into the solar neighborhood. The result is a change in the age-metallicity relation, and in the relations between ages and metallicities on one hand and velocity dispersion on the other. However, radial mixing is very much a theoretical concept, and its relative importance to the evolution of the Galactic disk is still unknown. We also do not know what the main mechanism is that produces the radial migration. Sellwood & Binney (2002) postulated that resonant scattering of disk stars off of successive, transient spiral density waves can produce significant displacements (>4 kpc). Minchev & Famaey (2010) further argued that an overlap of bar and spiral arms resonances could drastically enhance the migration efficiency within disks. Lastly, Quillen et al. (2009) showed that radial migrations of stars to the outskirts of disk galaxies could arise via tidal perturbations during the peri-center passages of dwarf satellites. These different mechanisms are furthermore expected to have different efficiencies in galaxies of different masses, different bar strengths, and different environments. Therefore, studying the properties of the spatially resolved stellar populations in large samples of galaxies covering a large range of masses, structural properties and environments should allow us to constrain the importance of secular evolution/radial migrations and the main physical mechanisms responsible.

Another problem that has received considerable attention in the last few years relates to the formation of the thick disk. Because of its old age and because it constitutes a kinematically and chemically recognizable relic of the early Galaxy, the thick disk is a highly significant component for the study of galaxy formation. How did the thick disk form? Several mechanisms have been proposed, including (i) gas rich mergers at high redshift (e.g., Brook et al., 2004), (ii) accretion debris (Abadi et al., 2003), (iii) heating of the thin disk via disruption of its early massive clusters (e.g., Kroupa, 2002), (iv) heating of the thin disk by accretion events, and (v) migration of more energetic orbits from the inner galaxy to larger radii where the potential gradient is weaker (Schönrich & Binney, 2009). To test these formation models, detailed comparison of thin and thick disk properties are required across a range of galaxy masses. In particular, the relative ages and chemical enrichment patterns of the thin and thick disks are expected to differ among these different formation models. If the thick disk results from a gradual kinematical heating of the thin disk, there should be a smooth age and enrichment gradient between the two. In contrast, if the thick disk is formed from accreted stars we should expect the ages and metallicities of the thin and thick disk to be only weakly correlated. We may also expect to see variations with the mass of the galaxies, with less massive galaxies being more susceptible to external heating and more massive galaxies being better able to tidally disrupt satellites. Measuring the ages and metallicities of thick disks outside the local group has proved to be challenging (see Yoachim & Dalcanton, 2008, for an early attempt).

Large spectroscopic studies of stellar populations across the disks of spiral galaxies have been very scarce (Yoachim & Dalcanton, 2008; Yoachim et al., 2012; MacArthur et al., 2009; Sánchez-Blázquez et al., 2009). In total, less than ~ 30 galaxies have been studied and these studies were mostly limited to the inner disk. Furthermore, disk galaxies are intrinsically complex, with multiple structural components (e.g., disks, bulges, bars, and halos). Long-slit spectroscopic studies therefore often lose valuable information or introduce confusion bias. Spectroscopic surveys such as CALIFA (Sánchez et al., 2012), VENGA (Blanc et al., 2013), and SAMI (Croom et al., 2012) are using integral field units to perform spatially resolved studies of the stellar populations in nearby disk galaxies. Although these surveys will allow a major step forward, the number of galaxies that they reach is still fairly limited. J-PAS will offer a number of benefits over other studies. First, the large survey area and corresponding large sample size will allow us to isolate statistically the influence of parameters such as mass, morphological type, and environment, on the spatially resolved stellar populations and population gradients across the disks. Second, J-PAS will be able to trace the low surface brightness external parts of disks beyond 3 scale-lengths, which are very difficult to reach for the spectroscopic surveys mentioned above. The spatial resolution offered by J-PAS will allow us to resolve the stellar populations in the different components of galaxies, such as arms, inter-arms, bars, rings, and central components.

Dwarf Galaxies. Dwarf elliptical galaxies (dEs) are small, low-luminosity galaxies which constitute the dominant population of nearby galaxy clusters. Indeed, dEs alone outnumber high luminosity galaxies by a factor of 6 in the Local Group (Mateo, 1998), and they represent more than 50% of the galaxies in the Virgo cluster (Sandage et al., 1985). As potential building blocks of massive galaxies in hierarchical frameworks of galaxy formation, dwarf elliptical galaxies may provide important clues on the main processes involved in galaxy assembly and evolution.

With the advent of larger telescopes and more sophisticated instrumentation, we now know that dEs display a much wider range of properties than originally thought, opening again the debate about their origin. The three most widely adopted scenarios are: (1) They might be primordial objects which expelled their gas in early stages of their evolution because of supernova explosions (e.g. Mori et al., 1999), (2) dEs could be the by-product of late-type disk galaxies that entered clusters ~ 5 Gyr ago and evolved into a hot spheroid because of internal dynamical processes (Conselice et al., 2001). (3) Tidal harassment within the cluster. Dwarf ellipticals are mostly found in clusters and groups of galaxies, while star forming dwarfs are predominantly found in the field (Dressler, 1980). This very pronounced morphology density-relation for dwarfs shows that indeed the environment plays a very important role in their evolution.

In recent years, a growing number of studies has shown that they are a surprisingly inhomogenous class: photometric studies of large samples of Virgo dwarf early-types have revealed the presence of disks, bars, spiral arms, and nuclei (e.g. Lisker et al., 2007; Janz et al., 2012). A diversity of properties has also been found through the analysis of dE stellar populations, such as their ages, metallicities, and the gradients thereof (e.g. Chilingarian, 2009; Koleva et al., 2011). Kinematic studies confirm and add to the variety: the degree of rotation is not correlated with the (projected) flattening, and kinematically-decoupled components are found in some early-type field dwarfs (Toloba et al., 2011; Ryś et al., 2013). This diversity has made it challenging to both relate the different subtypes to each other, as well as to place the whole class in the larger context of galaxy assembly and (trans)formation processes.

Despite their large numbers and paramount importance in our understanding of galaxy evolution, the low-luminosity character of these systems has always prevented extensive studies of similar quality as those performed on normal galaxies. On one hand, major photometric surveys (e.g. SDSS), while a good source for identifying candidates, are often too shallow to map the properties of these galaxies far out in radius. Spectroscopic studies, on the other hand, are based on a rather limited number of dwarf galaxies and are typically restricted to a single aperture measurement or a short long-slit profile. Today, integral-field spectroscopic studies, while providing a wealth of detailed spectral information, are still scarce (e.g. Ryś et al., 2013). None of the upcoming major integral-field surveys (e.g. CALIFA, SAMI, ManGA) will change this picture in the foreseeable future.

The J-PAS Galaxy Evolution Survey presented here opens up a new and important window in this field. Not only will it allow the identification of many dwarf galaxies in different environments over the surveyed area of 8500Mpc^2 , but, most importantly, it will be deep enough to probe regions well beyond where the surface brightness profiles of these galaxies are no longer described well by a single exponential profile. The multi-band observing strategy of the J-PAS survey will allow us, for the first time, to produce a very detailed study of the stellar populations of dwarf galaxies well into their outskirts. The analysis of their star formation histories at different radii will reveal whether star formation takes place in an inside-out fashion (i.e. as most ordinary galaxies exhibit) or if on the contrary secular evolutionary processes dominate their evolution. It will also reveal the importance of environmental processes in those dwarfs living in clusters. Combined with the results obtained for ordinary galaxies, the J-PAS survey has the potential to become the absolute reference in the field of stellar populations by providing the complete picture of galaxy evolution as a function of mass, luminosity, and galacto-centric radius for the largest set of galaxies ever observed.

Extragalactic Globular Clusters. The formation of globular clusters (GCs) is thought to be linked to major episodes of star formation in galaxies (Larson, 1996; Elmegreen & Efremov, 1997; Ashman & Zepf, 2001). A key observational result on this topic is the existence of a bimodal color distributions in the GC systems of most galaxies, including our Milky Way. This fact has been widely interpreted as evidence for two distinct GC subpopulations – metal rich (red) and metal poor (blue) – and this has been confirmed in many cases by conducting detailed spectroscopic studies of extragalactic GC systems in nearby galaxies. Different galaxy formation scenarios are proposed to explain the existence of the GC subpopulations, involving mergers, in situ formation or accretion processes. In this sense, GCs are relics that provide valuable information on how the main star formation episodes of their host galaxies took place. An interesting review on extragalactic GCS and their capability to shed light on galaxy formation can be found in Brodie & Strader (2006).

How can J-PAS contribute to our understanding of GC systems and, therefore, galaxy formation and evolution? Extragalactic GCs appear as point-like sources in the outskirts of galaxies. A good characterization of GC subpopulations in terms of ages and metallicities in all kind of galaxies is essential to have robust statistics and put constraints on the complex process of GC and galaxy formation. Detailed studies have been limited to spectroscopic work on 8 – 10 m class telescopes, and are therefore scarce and time-consuming (e.g. Strader et al., 2005; Cenarro et al., 2007). As a low resolution IFU, J-PAS will constitute a revolution in this topic by providing a massive census of extragalactic GCs for thousands of nearby galaxies in the 8500Mpc^2 survey area. The multi-filter approach will allow not only to detect GC candidates but also to characterize their stellar populations in the same way as explained in Section 4.1.2.

It is well known that the number of GCs scales with the galaxy luminosity (Harris & Racine, 1979). This introduces the definition of the so called *specific frequency* of GCs, S_N , which can be considered approximately as the number of GCs per unit luminosity (Harris & van den Bergh, 1981; Harris, 1991) normalized to $M_V = -15$. The specific frequency varies in the range 0.3 – 1 for spiral galaxies, 1 – 15 for giant ellipticals and 1 – 30 for dwarf elliptical galaxies. For instance, the Milky Way has $S_N \sim 0.6$ (~ 150 GCs), whereas the giant elliptical M87 has a S_N of 14.1 ± 1.6 (Harris et al., 1998), with more than 1000 GCs. Interestingly, GCs are also considered as standard rulers for inferring cosmological distances. GC systems follow a roughly universal, Gaussian-like luminosity function (LF) that peaks at $M_V \sim -7.5$ (e.g. Harris, 2001; Cezario et al., 2013). Therefore the number of GCs that J-PAS will detect depends on the distance to the galaxy and the galaxy type and luminosity.

To get an idea of the impact that J-PAS will have in this field, let us consider the galaxies in the Virgo Cluster. Assuming a distance of ~ 17 Mpc ($m-M \sim 31.15$) the globular cluster LF peaks at $V \sim 23.65$, or $g \sim 24$ (depending on the GC color). The J-PAS magnitude limit in g band reaches down to 23.75 ($S/N=5$; 3 arcsec aperture). This means that J-PAS will be able to detect nearly all GCs in the bright half of the globular cluster LF, which amounts to several hundreds of GCs in a typical massive elliptical galaxy. The brightest GCs in Virgo galaxies have $g \sim 20 - 20.5$, depending on the colour. So, making use of the survey broad-band filters, J-PAS will detect all the GCs 2.5 – 3 mag fainter than this value. More interestingly, if we focus on the J-PAS narrow-band filters, at the Virgo cluster distance J-PAS will detect all the GCs down to 2 – 2.5 mag fainter than the brightest GCs. This amounts to from around one hundred GCs per giant elliptical in Virgo to a few (0 – 5) GCs in dwarf ellipticals, as the number of GCs scales with the galaxy luminosity.

Putting all the above numbers in context: integrated over the $8500 \square^\circ$ area that J-PAS will cover, it is expected to observe tens of thousands of GCs in nearby galaxies (say < 20 Mpc), with a J-spectrum for each GC. This will provide a first estimate of the GC metallicity and age, allowing to split between metal rich and metal poor GCs, as well as to study the ages of the GCs and infer new clues on the formation epoch depending on the host galaxy type.

Tidal Disruption Events in Globular Clusters. J-PAS will also provide a highly efficient means of detecting the aftermath of tidal disruption events within extragalactic GCs caused by stars being torn apart by tidal forces from intermediate-mass black holes (IMBHs, masses in the 100–10,000 M_\odot range) within the cluster. The possibility that globular clusters harbor IMBHs has been a bone of contention for more than 30 years. Demonstrating whether or not IMBHs exist in globular clusters has important ramifications on our understanding of not only black hole formation, but also of the postulated feedback mechanism linking the growth of black holes and galaxy formation that is believed to cause the well-known $M_{BH} - \sigma$ relation in massive galaxies. If IMBHs exist in the centers of globular clusters, they should occasionally disrupt passing stars (Rees, 1988; Baumgardt et al., 2004). It is predicted that the debris from the disrupted star forms a precessing, self-interacting stream, which ultimately forms an accretion disk, an optically-thick envelope, and a quasi-spherical $\sim 10^4$ K diffuse photosphere around the black hole.

This envelope of stellar debris is expected to intercept X-rays from matter in the accretion disk around the black hole and reprocess it in the optical/UV part of the spectrum in the form of emission lines superimposed on the stellar continuum of the stars within the GC. This emission should be detectable for a few hundred years after the disruption event (Clausen & Eracleous, 2011; Strubbe & Quataert, 2009). Such a post-tidal disruption event by a GC black hole is believed to have been observed in a GC near the Fornax Cluster elliptical galaxy NGC 1399 that harbors the luminous X-ray source CXO J033831.8–352604. Irwin et al. (2010) detected strong [N II] and [O III] emission lines in the optical spectrum of this GC, and Clausen et al. (2012) argued that the X-ray and optical properties of this cluster are consistent with the tidal disruption of a star by a 100–200 M_{\odot} black hole 100–200 years ago. The tens of thousands of extragalactic GCs that J-PAS will observe within 20 Mpc will provide fertile hunting grounds for further examples of tidal disruption aftermaths. The J-spectra of the brighter ($m_g \sim 20 - 20.5$ mag) systems should be sufficient for detecting the strong emission lines such as those found in CXO J033831.8–352604.

4.2.2. Theme II. Evolution of the Galaxy Population since $z \sim 1$

Over the past decade, large-area sky surveys of the relatively nearby universe, such as SDSS (York et al., 2000), 2MASS (Skrutskie et al., 1997), and GALEX (Martin et al., 2005), have proven the power of large data sets for answering fundamental questions on extragalactic astronomy. These data, combined with the much deeper multi-wavelength pencil-beam surveys of the high-redshift universe (e.g. AEGIS, COMBO-17, GEMS, CANDELS), have improved significantly our understanding of the evolution of galaxies and stellar populations in galaxies over the last 9 billion years and more. Systematic studies of, for example, morphologies, number densities, luminosity and stellar mass functions, stellar populations, and the effect of the environment over a wide range in redshift are required to construct a detailed picture of galaxy evolution. In the relatively nearby universe, the SDSS has been instrumental in constraining many of the relevant parameters through a combination of large-area imaging with targeted medium-resolution spectroscopic follow-up. Large “value-added” data sets based on the combination of SDSS optical samples with samples in the UV from GALEX, in the near-infrared from 2MASS and WISE, and in the radio from FIRST have greatly extended the range of extragalactic science questions that can be addressed with these data. At higher redshifts, multi-filter photometric surveys such as COMBO-17 (Wolf et al., 2008), COSMOS (Ilbert et al., 2009), and ALHAMBRA (Moles et al., 2008) have allowed to determine photometric redshifts while at the same time sample the SEDs of galaxies with an accuracy sufficient for evaluating stellar populations as a function of, e.g., redshift and environment.

For the majority of galaxies that will be unresolved, J-PAS will be used to determine, e.g., the stellar masses, luminosity/mass-weighted ages, dust content, some line-strength indices suited for low-resolution data, current star-formation rates, past star-formation histories, and the presence of AGNs. All these parameters will be studied as a function of, e.g., redshift and environment thereby constraining the main mechanisms responsible for galaxy evolution over the crucial redshift range $0 \lesssim z \lesssim 1.5$, which can be compared to data from deeper surveys probing higher redshifts.

In Fig. 34 we present an overview of many of the main past and present galaxy surveys in terms of their sky coverage and limiting magnitude. The largest spectroscopic surveys do not typically reach very deep, while the deepest photometric surveys are typically limited in sky coverage. J-PAS will populate a “sweet-spot” in the area–depth plane. The sky coverage is comparable to that of the SDSS photometric survey. Its main power however lies in the fact that it achieves a similar or greater depth compared to SDSS in each of its many narrow-band filters. This adds great leverage to the study of galaxy evolution when spectra are not feasible and a small set of broad band filters offer a spectral characterization that is too coarse for most detailed diagnostic studies. The J-PAS broad-band filters will reach ~ 2 mag deeper than those of the SDSS, allowing the detection of lower-mass galaxies, higher redshift galaxies, and more low surface brightness details in nearby systems compared to SDSS. Other large optical surveys, such as KIDS and DES will observe $> 1500\text{ deg}^2$ of sky, and will go several magnitudes fainter than J-PAS in the optical broad-bands, but will not have the great leverage in photometric redshifts and spectral classifications achieved by the 56 filters of J-PAS. It is therefore expected that these surveys will be highly complementary, rather than repetitive.

What kind of galaxies will J-PAS be able to detect? In Fig. 35 we show a recent simulation of galaxies in an area of about 2 square degrees as a function of redshift and R -band magnitude, colour-coded according to their stellar mass. The J-PAS detection limit in the R -band is about 24 mag (5σ , AB) measured inside a $3''$ diameter circular aperture (horizontal line). In principle, J-PAS will thus be able to detect large numbers of galaxies down to $M_* \approx 10^9 M_\odot$ up to $z \sim 0.4$ and $M_* \approx 10^{10} M_\odot$ up to $z \sim 1.5$. Although the exact amount of information that we will be able to extract from these galaxies based on the 56 J-PAS bands will depend on, for example, the achieved S/N in each filter, the redshift and the spectral type of each galaxy, Fig. 35 illustrates the enormous leverage power in stellar mass and redshift that J-PAS will bring to the field of galaxy evolution. This will allow us to open (or re-open) a large number of parallel investigations in this field. It would be cumbersome to discuss all the possibilities here, but we will list a few.

In a colour-magnitude diagram (CMD) the distribution of galaxies appears bimodal, and this is true at both low and high redshift. Quiescent early-type galaxies (ETGs) and star-forming late-type galaxies (SFGs) populate preferentially the red sequence and the blue cloud, respectively. The colors of non-star-forming galaxies in the red sequence change with redshift as expected for passively aging stellar populations. In the blue cloud, galaxy colors are determined by recently born stars and vary little with redshift. The cosmic star formation rate (SFR) density evolved strongly with time, achieving a peak when the universe had about half of its current age, at $z \sim 1.5 - 2$. Galaxies in the blue cloud that see their star formation quenched should move quickly toward the red sequence, traversing the so-called “green valley” in the interim. Even though the details are not yet fully understood, the triggering of star formation by post-merger starbursts in blue cloud galaxies, the quenching of star formation by AGN feedback, and the amounts of neutral gas available, are all crucial for regulating the evolution of galaxies. Understanding how and why galaxies traverse the CMD and evolve with time will be one of the main goals pursued by J-PAS.

If we look at galaxy assembly in detail, the evolutionary scheme is more complicated. The stellar mass in red galaxies increases by a factor of two since $z = 1$ (Bell et al., 2004; Faber et al., 2007; Cristóbal-Hornillos et al., 2009), in agreement with hierarchical models of galaxy formation and evolution. However, red sequence galaxies as massive as $3 \times 10^{11} M_{\odot}$ were already in place at $z \sim 2$ (Nicol et al., 2011), and many of these galaxies are very compact (Daddi et al., 2005; Trujillo et al., 2006). The fact that such massive, dense systems ($M \simeq 10^{11} M_{\odot}$, $R_e \sim 1.5$ kpc) appear to be scarce in the nearby universe (Trujillo et al. (2009) find $< 0.03\%$ based on the SDSS, see also Taylor et al. (2010)) implies that the structural properties of these massive objects have evolved strongly between $z \sim 2$ and the present (Trujillo et al., 2007; Buitrago et al., 2008). J-PAS will be able to contribute to this problem in at least two ways. First, it will be possible to sample the evolution from massive galaxies at high redshift to massive galaxies at low redshift in various redshift bins from $z \sim 1$ to $z = 0$ with unprecedented statistics. The statistics of this evolving population could then shed light on the main mechanisms that transform the structural properties of these galaxies over time. Second, J-PAS will allow us to search for rare local galaxies that are in a stage analogous to the dense and compact stage as those at high redshift, thereby shedding light on the formation mechanisms of these systems (e.g. Overzier et al., 2009). It is believed that the formation of (compact) spheroids at high redshift is related to the core–cusp dichotomy observed in local early-type galaxies (Kormendy et al., 2009), in which the most massive early-types tend to have a deficit of light in their inner regions with respect to their outer Sersic profile, and lower mass early-types tend to have an excess of light in their inner regions. These observations are consistent with the latter being the result of so-called “wet” or dissipative mergers at high redshift that form dense mass concentrations in the core, while the former are the result of “dry” mergers that lead to a “cored” inner profile. Examples of this process can be seen in various classes of nearby galaxies that are good analogues of the compact spheroids at high redshift in various stages of their evolution (e.g. see Overzier et al., 2009; Trujillo et al., 2012; Jiang et al., 2012).

Another area in which J-PAS data could excel is that of the population of intensely star-forming (starbursting) galaxy population. In the very nearby universe, the relatively rare class of starburst galaxies are the only set of galaxies in which we can directly observe the interplay between (massive) star formation and the interstellar medium at high spatial and spectral resolution. Though interesting by itself, these studies are important for providing insight into similar processes that were much more common in galaxies at much earlier times. Despite detailed observations of star-forming populations at high redshift observed with for example the Hubble Space Telescope, we still rely largely on locally determined calibrations and diagnostics when determining their physical properties. J-PAS will allow us to not only establish new large “training sets” to aid in the determination of galaxy properties at higher redshifts, it will also allow us to directly compare the main properties of the heavily star-forming population as a function of redshift. At $z \gtrsim 1$, the far-UV is directly accessible in the U -band, while at lower redshifts a combination between GALEX and J-PAS will allow us to select large numbers of UV-luminous starburst systems that share many similarities with the typical star-forming population at $z \gtrsim 2 - 4$ (Heckman et al., 2005).

A related area of research will involve studying the effects of galactic outflows and their importance in galaxy evolution. For systems at $z \gtrsim 0.3$, the Fe II $\lambda\lambda 2586, 2600$ and Mg II $\lambda\lambda 2796, 2803$ absorption line doublets, which are sensitive probes of the cool galaxy-wide ionized winds, are accessible in the observed optical. J-PAS should deliver the largest sample to date of systems covering a wide range of redshift, stellar mass, and SFR (density) that are well-suited for detailed follow-up spectroscopy of such wind features. This will allow an unprecedented survey of the interplay between gas and stars that is crucial to constrain the importance of stellar winds feedback in galaxy evolution (e.g. Tremonti et al., 2007; Rubin et al., 2010; Heckman et al., 2011; Diamond-Stanic et al., 2012; Rubin et al., 2013).

4.2.3. Theme III. The Growth of Large-scale Structure and Environment

Galaxy evolution as a function of environment. Dressler (1980) showed that the fraction of elliptical and lenticular galaxies increases towards denser regions, while the fraction of spiral galaxies shows the opposite behavior. This so-called morphology – density relation motivated many studies of the relation between galaxy properties and local density, and its evolution with redshift. Some of the main properties that have been found to correlate with local density are the fraction of red or early-type galaxies (e.g., Dressler et al., 1997; Postman et al., 2005; Cucciati et al., 2006; Tasca et al., 2009; Iovino et al., 2010; Cappellari et al., 2011), the galaxy luminosity and stellar mass functions (e.g., Bolzonella et al., 2010; Pozzetti et al., 2010; Vulcani et al., 2011), and the merger fraction (Lin et al., 2010; De Ravel et al., 2011; Kampczyk et al., 2013). We have since learnt that the stellar mass of galaxies is one of the primary drivers responsible for the observed correlations, in the sense that, for example, the red/early-type fraction is higher for more massive galaxies. However, the local density or the environment must still play an important role, particularly in the transformation of low-mass, blue galaxies into red galaxies (Cucciati et al., 2010; Peng et al., 2010). However, the precise scale lengths on which the various environmental effects operate on galaxies are still a matter of debate. For example, it has been shown that the colors of galaxies, H α equivalent widths, and D_{4000A} depend on environment on small scales ($\lesssim 1h^{-1}$ Mpc), but that the environmental dependence of these quantities is significantly weaker on larger scales (e.g., Kauffmann et al., 2004; Blanton et al., 2006; Cucciati et al., 2010). Therefore, a robust computation of both the density field as well as the main galaxy properties such as color, morphology, and metallicity are needed in order to better constrain the interplay between galaxies and their environment.

With J-PAS, we will be able to combine detailed studies of the density field or environment with those of the properties of the galaxies that they contain. For example, we plan to extend the calculation of the cross-correlation function between early and late type galaxies to shorter distances over a wide redshift range. The ALHAMBRA survey has provided reliable results for the projected correlation function w_p (Davis & Peebles, 1983) over the range $r_p \in [0.03, 10]h^{-1}$ Mpc (Hurtado-Gil et al. in prep.), showing new distinctive features in the clustering of various galaxy populations that are typically not seen on scales above $0.1 h^{-1}$ Mpc. These results suggest an increase of the galaxy clustering among late-type galaxies for short distances, breaking its power law pattern. This effect is due to interactions between early and late type galaxies with their direct environment.

With the density field, several projects and synergies will be explored in the J-PAS collaboration, such as (i) the dependence of the red fraction/SFR/age/metallicity on the local density, (ii) the study of the luminosity/mass function in different environments, and (iii) state which environment is more important for galaxy evolution: the large-scale environment (groups, clusters, filaments), or the very small-scale environment. All these studies will provide fundamental clues about the dominant environmental effects involved in galaxy evolution as a function of redshift, and with their corresponding time-scales and the spatial extent of their reach.

Astrophysics of Groups and Clusters of Galaxies. Clusters of galaxies are not only important cosmological probes (see the discussion in Sect. 3.2 in this document), but they also offer a unique view on many important astrophysical processes that are highly pronounced and sometimes exclusively found in these dense environments. Galaxies in groups and clusters are under the influence of a number of environmental processes (e.g., harassment, strangulation, ram-pressure stripping, dynamical friction, cannibalism) that can have a strong impact on, e.g., their stellar and gas components, morphology, and star formation rate, as well as their spatial distribution within the cluster. However, the specific contribution of each process as a function of environment and redshift is still a matter of great debate. J-PAS, being complete for clusters of mass $> 5 \times 10^{13} M_{\odot}$ up to $z \sim 0.8$ – a wider extent in both redshift and mass compared to other surveys – will have the potential to revolutionize this particular area of research. The power of J-PAS for the study of galaxy properties in groups and clusters resides in its wide-area coverage together with its precise photo- z 's, which will yield a map of the (3D) large-scale structure. This allows not only the identification of the most likely members of groups/clusters in and outside the virial radius from $0 < z < 0.8$, but also yields coarse spectral information on a pixel-to-pixel basis. This will allow us to link internal galaxy properties to the overall cluster/group properties, at least in a large number of relatively nearby groups and clusters in which the galaxies are resolved. We will also study the evolution of the galaxy populations in groups and clusters by determining how the different properties, e.g., the sizes, morphologies, colors, stellar masses, M/L , SFRs, SEDs, ages, and metallicities have evolved with redshift.

In addition to the study of galaxy properties as a function of local environment with 'cleaner' samples (i.e., less background contamination) than have so far been available, the real novelty of J-PAS will lie in the fact that we can study the properties of galaxies in the outskirts ($R \gtrsim R_{vir}$) of groups/clusters. We will be able to scrutinize the environments of groups and clusters and the filamentary structure around them. It may be possible to witness the large numbers of groups and individual galaxies in the process of accretion onto clusters (e.g., see González et al., 2005; Berrier et al., 2009; Chiang et al., 2013). This will allow us to address the importance of the “pre-processing” of galaxy properties inside these sub-clumps, and to investigate how these infalling groups relate to the structure of the cosmic web on larger scales. J-PAS will thus also offer important topological information about the cosmic web up to $z \sim 1$.

We will be able to check if the so called fossil groups (massive groups formed by one dominant isolated elliptical galaxy) are at the junctions of filaments. We will be able to map the space around the groups and clusters quite accurately, as well as determine the alignment of galaxies with each other as well as other structures on small and large scales. We will be able to study how the magnitude gap between the BCG and the second brightest member, and the luminosity and stellar mass of the BCG change with the density of the environment. The relatively high precision in photometric redshifts will reduce significantly the uncertainties related to halo membership of galaxies of various types, allowing a substantial improvement in the dark matter halo mass determination through the mass-optical richness relation for both groups and clusters. We will use self-calibration based on weak lensing estimates and with cluster catalogs based on other frequencies such as the X-rays.

We will systematically investigate the deficit of low-mass galaxies in the center of groups and clusters as compared to the outskirts (mass segregation) and correlate the deficit with other parameters of the host groups and clusters. We will study the distributions of dwarf galaxies in clusters and groups and compare with the expectations from simulations (e.g. Weinmann et al., 2011). We will investigate in which cases the dwarf galaxies are associated with the group/cluster as a whole, around a common halo, or to specific galaxies within the groups and clusters, and if this is somehow related to the dynamical stage of the system.

At the extremely massive end of the galaxy mass function, the large J-PAS cluster sample will be ideal for the study of the first-ranked galaxies in groups and clusters, the BCGs and BGGs. The present-day structure of these galaxies and their evolution with redshift sets strong constraints on important components of our galaxy evolution models (De Lucia & Blaizot, 2007; Conroy et al., 2007; Hopkins et al., 2010; Dubois et al., 2013; Shankar et al., 2013), such as merging processes (Bernardi et al., 2007; Von der Linden et al., 2007; Liu et al., 2009, 2013; Burke & Collins, 2013; Ascaso et al., 2013), AGN feedback (Fan et al., 2008; Collins et al., 2009; Stott et al., 2011; Ascaso et al., 2011), the formation of the most massive black holes (McConnell et al., 2011; Hlavacek-Larrondo et al., 2012; Postman et al., 2012; Volonteri & Ciotti, 2013), and the gaseous and stellar components of the intra-cluster medium Gonzalez et al. 2007; Conroy et al. 2007; Murante et al. 2007; Rudick et al. 2011.

Given the large area covered by J-PAS, the survey will also be an exquisite tool to find rare objects. For example, the J-PAS sample of clusters and groups may yield the largest sample of AGNs in dense environments. We also hope to improve our knowledge about shocks in the intracluster/intragroup medium (traced by broad emission line systems), as seen, for example, in Stephan's quintet. Cluster-scale feedback from AGN versus central star formation will be studied in order to determine the important role of feedback in clusters. The low surface brightness limits of J-PAS will furthermore allow an unprecedented study of the intra-group and intra-cluster light components. Similarly, the study of mergers, shell galaxies, and tidal dwarf galaxies in structures ranging from small groups to dense environments will benefit greatly from the large area covered by the survey and the possibility to determine spatially-resolved properties at the low spectral resolution offered by J-PAS.

In summary, the J-PAS sample of groups and clusters will allow us to investigate in detail the formation of the cluster and cluster galaxy population since $z \sim 1.5$, where the results can be connected to dedicated observations of high redshift clusters based on optical-IR detections, X-ray, Sunyaev-Zel'dovich, and lensing techniques that are all sensitive to $z \sim 2$ (e.g. Blakeslee et al., 2003; Mei et al., 2006; Andreon, 2008; Rettura et al., 2010, 2011; Fassbender et al., 2011; Foley et al., 2011; Menanteau et al., 2012), and to the progenitors of clusters (the so-called "proto-clusters") based on the identification of large-scale galaxy overdensities detected in galaxy redshift surveys at $z \gtrsim 2$ (e.g. Chiang et al., 2013).

Close Pairs and Minor/Major Mergers. In their pioneering study, Toomre & Toomre (1972) were able to explain the tails and the distortions of four peculiar galaxies as the intermediate stage of a merger event between two spiral galaxies. Since then, the role of mergers in galaxy evolution has been recognized and studied systematically, both observationally and theoretically. To constrain the role of mergers in galaxy evolution two observational approaches are needed: (i) understand precisely how interactions modify the properties of galaxies and what is the fate of the merger remnants, and (ii) measure the merger history of different populations over cosmic time to estimate the integrated effect of mergers.

Regarding the first approach, it is well-known that “major mergers” (i.e., the merger of two galaxies with similar masses, $\mu \equiv M_2/M_1 \geq 1/4$) of two spiral galaxies is an efficient mechanism to create new red sequence galaxies (RSGs; Naab et al., 2006; Rothberg & Joseph, 2006a,b; Hopkins et al., 2008b; Rothberg & Fischer, 2010; Bournaud et al., 2011), while both major and minor mergers have been proposed in order to explain the observed mass and size evolution for massive RSGs since $z \sim 1$. When the separation r_p between two galaxies in a close pair decreases, the star formation rate (SFR) is enhanced (Barton et al., 2000; Lambas et al., 2003; Robaina et al., 2009; Knapen & James, 2009; Patton et al., 2011), the metallicity decreases (Kewley et al., 2006; Ellison et al., 2008; Scudder et al., 2012) and the AGN fraction increases (Ellison et al., 2011). The 2D photo-spectra provided by J-PAS will allow us to explore how the SFR in the central and in the external parts of galaxies in close pairs depend on r_p . We will also be able to study how other geometrical parameters of the pair, e.g., the angle between the semi-major axis of the galaxies or their inclination, affect the spatial distribution of the star formation. In relation to galaxy groups and clusters, we will be able to study the role of mergers in the size evolution of BCGs that appear to have evolved strongly since $z = 1$, in contrast to their stellar masses.

Regarding the second approach, the merger history of a given galaxy population can be characterized by estimating its merger fraction f_m , i.e., the fraction of galaxies in a sample undergoing merging. This can be determined either on the basis of morphological information (highly distorted galaxies are merger remnants (e.g. Conselice, 2003; Conselice et al., 2008; Cassata et al., 2005; Lotz et al., 2008; López-Sanjuan et al., 2009a; López-Sanjuan et al., 2009b; Jogee et al., 2009; Bridge et al., 2010)) or based on close-pair statistics (two galaxies close in the sky plane, $r_p \leq r_p^{\max}$, and in redshift space, $\Delta v \leq 500 \text{ km s}^{-1}$, are likely to merge, (e.g. Le Fèvre et al., 2000; Patton et al., 2000; Patton & Atfield, 2008; Lin et al., 2004, 2008; De Ravel et al., 2009; De Ravel et al., 2011; López-Sanjuan et al., 2010; López-Sanjuan et al., 2013)). With a parametrization of the merger fraction evolution following $f_m \propto (1+z)^m$, the *major merger* fraction evolution has been shown to depend on the luminosity and the stellar mass of the galaxies. Massive galaxies with $M_* > 10^{11} M_\odot$ have a higher merger fraction, but with little redshift evolution ($m \sim 0 - 2$), while lower mass galaxies ($M_* = 10^9 - 10^{11} M_\odot$) have a lower merging fraction but with stronger redshift evolution ($m \sim 3 - 4$). Regarding *minor mergers* with $\mu < 1/4$, the observations show a nearly constant evolution ($m \sim 0$) up to $z \sim 2$ (López-Sanjuan et al., 2011; López-Sanjuan et al., 2012; Lotz et al., 2011; Williams et al., 2011; Mármol-Queraltó et al., 2012).

Reliable merger fractions and rates can be determined based on photometric redshift surveys like J-PAS, by following the methodology of López-Sanjuan et al. (2010). This methodology uses the Probability Distribution Functions (PDF) of the photometric redshifts, z_{phot} , to estimate the probability that a galaxy pair with a projected separation $r_p \leq r_p^{\max}$ measured in the sky plane is also a close pair in redshift space (relative velocity $\Delta v \leq 500 \text{ km s}^{-1}$). This methodology has been tested in the Millennium Galaxy Catalogue (MGC, Liske et al. (2003)) at $z \sim 0.1$ and in the zCOSMOS spectroscopic survey (Lilly et al., 2009) up to $z \sim 1$. The results show that we can recover reliable merger fractions from photometric redshift surveys. We have also applied this methodology to measure successfully the merger fraction in GOODS-South (López-Sanjuan et al., 2010), COSMOS (López-Sanjuan et al., 2012) and ALHAMBRA (López-Sanjuan 2013b, in prep.). Thanks to the high accuracy of J-PAS photometric redshifts ($\Delta z/(1+z) \sim 0.3\%$) we will be able to estimate the major merger fraction from close pairs up to $z \sim 1$, and the minor merger fraction up to $z \sim 0.5$. In addition, we will characterize with unprecedented detail the dependence of the merger fraction on stellar mass, color, environment, etc. The methodology developed by López-Sanjuan et al. (2010) assumes that the PDFs are Gaussian in redshift space, and we are upgrading their methodology to use the more general PDFs (i.e., asymmetric and with multiple peaks) that are expected to be provided by the J-PAS photometric redshift techniques (see Fig. 36).

In summary, J-PAS will greatly improve our knowledge about the impact of interactions on galaxy properties and the role played by mergers in the evolution of the red sequence and the blue cloud since $z \sim 1$.

4.2.4. Theme IV. The High Redshift Universe

The two methods that have proved most effective in recent years for identifying high redshift galaxies are the so called Lyman-break and $\text{Ly}\alpha$ selection techniques. Both of these selections are based on the ultraviolet properties of the galaxy spectrum - redshifted into the optical/IR window at high redshifts - and are hence selecting only the galaxies which are young enough to produce copious amounts of ultraviolet light, and are sufficiently dust-free for a fair amount of this light to escape the galaxy.

The identification of galaxies through the Lyman-break technique is mainly based on two ultraviolet spectral features introduced by the blanketing effect of neutral hydrogen both within the galaxy itself, and by intervening clouds along the observers line-of-sight: the Lyman break at 912\AA and the Lyman forest between 912\AA and 1216\AA . Traditionally, these galaxies are discovered based on their broad-band colors measuring the drop in brightness due to the Lyman break and/or Lyman forest, and the galaxies hence selected are called Lyman Break Galaxies (LBGs). The second method selects galaxies which are $\text{Ly}\alpha$ emitters. The $\text{Ly}\alpha$ emission line is produced in the interstellar medium of the galaxy where the hydrogen atoms have been excited by the ultraviolet light from young stars. The traditional selection technique involves comparing images taken through a narrow-band filter with that taken through a broad-band (or another narrow-band) at comparable wavelengths. The galaxies selected using this method are generally called Lyman- α Emitters (LAEs).

The differences and similarities between the properties of LBGs and LAEs have been widely discussed in the recent literature. Most likely, however, the reported differences are a consequence of the different selection techniques (e.g. see Dunlop, 2013). The main reason why LAEs are often not detected by LBG selections is because they are typically very faint in the UV continuum, beyond the reach of a broad-band selection technique, despite them having similar UV continuum breaks as LBGs. The reason why not all LBGs are detected as LAEs is that while interstellar extinction peaks at the UV range, $\text{Ly}\alpha$ photons are affected by the resonant scattering, being easily scattered and destroyed by the neutral gas in the local and intergalactic medium. This characteristic permits the LBG/LAE ratio to be used to trace the neutral hydrogen fraction of the Universe, giving information about the last epochs of reionization.

We aim at studying this early galaxy population in the huge J-PAS volume avoiding biases due to the cosmic variance, a general problem in most LBG/LAE studies performed to date. Based on the J-PAS SEDs, we will be able to detect the brightest (in the continuum) LBGs in the redshift range $z \sim 2 - 3$. The J-PAS narrow-band filters will also permit us to identify which of these objects are luminous LAEs, thus avoiding the selection biases mentioned above. Combining J-PAS data with the GALEX UV data, we will also be able to identify and study LBGs at redshifts of $z \sim 1$. Finally, using the traditional narrow-band selection, we will be able to identify LAEs reaching objects too faint in their continuum to be identified by their SEDs. In addition, as a by-product of this LAE selection, we will also be able to detect the separate rare class of $\text{Ly}\alpha$ blobs. These approaches will be detailed below.

Lyman-Alpha Emitters. $\text{Ly}\alpha$ emitters (LAEs) are within the more distant baryonic structures so far detected in the universe. As most high-redshift objects, they are classified according to their selection method, the so-called narrow-band technique. It employs a combination of narrow and broad band filters to isolate the $\text{Ly}\alpha$ emission and characterize its energy distribution in the continuum. Although due to the resonant nature of the $\text{Ly}\alpha$ line, a huge fraction ($\sim 90\%$) of star-forming galaxies emit insufficient $\text{Ly}\alpha$ photons to be detected by narrow-band surveys (Hayes et al., 2010), LAEs can be found at almost any redshift from local (Östlin et al., 2009; Deharveng et al., 2008; Cowie et al., 2010, 2011) up to $z \sim 7$ (Iye et al., 2006) and beyond (Sobral et al., 2009). However, some low-redshift LAEs show quite different properties from those at $z > 2$ (Finkelstein et al., 2009,?; Oteo et al., 2011, 2012a,b). Thus, LAEs are representative of different effects related to galaxy evolution and to the complex resonant scattering mechanisms of the Lyman- α line.

At the highest redshifts, LAEs are indicative of the stage of reionization of the universe. Early reionization models claim that reionization is nearly complete at $z \sim 8$ and ends at around $z \sim 6.6$ (Choudhury & Ferrara, 2006). This is supported by the number density evolution of LAEs, that seems to decrease beyond $z \sim 6$ (Kobayashi et al., 2007). Analyzing samples of LAEs between $z \sim 3.1$ and $z \sim 5.7$, Ouchi et al. (2008) found that LAEs were more common at earlier epochs. Kovač et al. (2007) measured the spatial correlation function of a LAE sample at $z \sim 4.5$, finding a significant clustering strength consistent with those of the halos of Lyman break galaxies, albeit with a lower occupation number. In contrast, the relatively scarce number of LAEs detected at $z \sim 3$ could be consistent with them being the progenitors of present day L^* galaxies (Gawiser et al., 2007; Guaita et al., 2010). These authors did not find evidence for strong obscuration or a substantial AGN fraction ($\sim 1\%$), indicating that the LAEs are young, low stellar mass objects. In contrast, in a large sample at $z \sim 2.3$, Nilsson & Møller (2009) detect a significant AGN contribution and red spectral energy distributions (SEDs), implying a contribution from more massive, dustier and older sources than among the LAEs observed at $z > 3$ (see also Bongiovanni et al., 2010; Oteo et al., 2012a,b).

Most of the above results were obtained from sky areas no larger than $\sim 1\text{arcmin}^2$ and, consequently, the cosmic variance is a significant handicap of these surveys. The substantial area surveyed by J-PAS will allow us to address some unanswered problems. By taking advantage of the current design of the J-PAS filter set, we will perform a systematic search for LAEs at $2 \lesssim z \lesssim 2.4$ on a (proposed) J-PAS Deep Field (JDF), using the well-known narrow band technique employed to find high-redshift galaxies (e.g., Cowie & Hu, 1998; Gronwall et al., 2007; Ouchi et al., 2008), but combining the 4 bluest filters of J-PAS centered at 360, 379, 390 and 400 nm, alternatively for separated detection and continuum subtraction.

A similar approach, but using intermediate-band filters of the ALHAMBRA Survey (Moles et al., 2008) was successfully used in Bongiovanni et al. (2010), searching for LAEs at $z \sim 2.2$ in the GOODS-North field. Nevertheless, in this case, the medium-band filters employed favored the finding of large equivalent width (EW) objects. A JDF would be sensitive to LAEs with a minimum rest-frame $EW_{Ly\alpha}$ of $40 \pm 10\text{\AA}$ for a $m_{OFF}-m_{ON}$ color > 0.3 mag. For all J-PAS filters involved in the LAE detection, we performed several simulations by convolving their total transmission with real, conveniently redshifted spectra. The rest-frame EW threshold is similar for these filters.

Down to a magnitude limit of $i_{AB} = 23$ ($i_{AB} = 24$), we estimate a mean of 7 ± 2 (37 ± 4) LAEs / arcmin^2 with an $EW_{Ly\alpha} > 35\text{\AA}$ at a median redshift of $z \sim 2.25$ (Bongiovanni et al., 2010; Nilsson & Møller, 2009). The AGN fraction among this sample is expected to be about 40%. Despite the fact that we will only be able to detect the brightest LAEs at this mean redshift (i.e. between 6 and 23% of the total), the J-PAS data set will allow us to characterize some of the fundamental properties (stellar mass, metallicity, age, SFR, AGN fraction and dust content) by modeling the stellar populations from the low-resolution SED. The large number of LAEs detected over a wide range of spatial scales will furthermore allow an unprecedented study of the clustering of bright LAEs. We will search for signs of density evolution and test whether LAEs at $2 < z < 3$ are progenitors of local L^* galaxies.

Furthermore, the wide area covered by J-PAS allows us to search for the most extreme LAEs that are missed by typical deep pencil-beam surveys (e.g., Matsuda et al., 2004, 2011; Yang et al., 2009; Bridge et al., 2013). In particular, we will be able to perform a systematic search for the highly rare population of bright and extended Ly α nebulae or “Ly α blobs” (LABs). This will be the subject of the next section.

Ly α Blobs and Other Extended Emission Line Objects. A particularly rare subset of objects at high redshift that is also selected through their high equivalent width Ly α emission involves the population of giant, luminous Ly α nebulae. These nebulae, also referred to as “Ly α blobs” (LABs), have sizes ranging from a few tens to a few hundreds kpc and Ly α line luminosities ranging from a few times 10^{43} to 10^{45} erg s $^{-1}$ (e.g. Francis et al., 1996; Steidel et al., 2000; Overzier et al., 2001; Matsuda et al., 2004; Venemans et al., 2007). Luminous extended Ly α nebulae have been known to exist around low and high redshift AGN such as radio galaxies, quasars, and Seyfert galaxies for over three decades (e.g. McCarthy et al., 1990; Heckman et al., 1991; Fu & Stockton, 2009). The primary energy source powering the Ly α emission in these type of sources is the ionizing radiation from a central AGN, sometimes with contributions from star formation or radio jet-cloud interactions. The main mechanisms responsible for the spatially extended neutral gas are however still largely unknown. If the gas originates from within the source itself, it could have been driven out by radio jets (in the case of radio galaxies) or quasar and/or starburst superwinds. The gas may also originate externally to the galaxy, perhaps related to the same processes that provide fuel to the central black hole and power the AGN. At high redshifts, the gas could also be related to cold, dense gas recently accreted from the intergalactic medium during structure formation (Dijkstra & Loeb, 2009) or from a reservoir of previously expelled gas.

More recently, LABs have also been found serendipitously in Ly α surveys (e.g. Francis et al., 1996; Steidel et al., 2000; Matsuda et al., 2004, 2009, 2011; Prescott et al., 2013). Although they are similar in size and luminosity, these LABs are typically not associated with any known radio galaxies or Type I (i.e. unobscured) quasars. Multi-wavelength follow-up observations of these systems have shown that they frequently host Type II (i.e. obscured) AGN, starbursts, and/or outflowing superwinds (e.g. Bower et al., 2004; Dey et al., 2005; Geach et al., 2005; Overzier et al., 2013b). Nebular line metallicity measurements further show evidence that the gas is usually not pristine, indicating that it has previously been processed (e.g. Overzier et al., 2001, 2013b). Furthermore, numerous observations show that the LABs tend to occur predominantly in overdense environments, as evidenced by the fact that they frequently sit in local maxima in the distributions of LAEs or LBGs (e.g. Steidel et al., 2000; Francis et al., 2001; Overzier et al., 2008; Venemans et al., 2007; Erb et al., 2011). Recently, Overzier et al. (2013b) presented an analysis of a complete sample of LABs having Ly α luminosities in excess of 5×10^{43} erg s $^{-1}$ and sizes of $\gtrsim 50$ kpc, showing that essentially all of the luminous LABs harbor obscured AGN. Because AGN typically have short duty-cycles (10-100 Myr), the fact that we know of almost no LABs without an AGN suggests that they must be a direct consequence of the AGN activity. In the AGN scenario, the ionizing luminosity required to power the Ly α emission out to ~ 100 kpc is provided by the AGN, which can be obscured (e.g. for radio galaxies and other LABs) or unobscured (e.g. for quasars) along the line of sight.

This scenario also explains the empirical relation between LABs and environment, because at high redshift the most luminous AGN are also preferentially found in overdense regions. Alternative energy sources for the LABs have been suggested by invoking massive starbursts (of order $1000 M_{\odot} \text{ yr}^{-1}$) or gravitational cooling radiation related to structure formation. Although these processes appear capable of producing a sufficient number of ionizing photons, the observational evidence appears weak, at least for the brightest LABs. It is possible that cooling radiation and/or star formation play a greater role in $\text{Ly}\alpha$ sources of much more modest sizes and luminosities, such as the population of LAEs. It has been pointed out that LABs become rarer, less luminous, and smaller with decreasing redshift (Keel et al., 2009; Zirm et al., 2009; Overzier et al., 2013b). It is not yet clear whether this effect, if real, is related to the fact that the most luminous AGN and starbursts have died out following the decline in the cosmic star formation rate density and AGN activity, or whether it reflects the lack of extended reservoirs of dense neutral gas around galaxies at $z \lesssim 2$. However, the volumes of existing narrow-band surveys have been quite small, with essentially no constraints at $z < 1.6$ where $\text{Ly}\alpha$ is inaccessible from the ground.

While J-PAS does not reach the depths achieved by narrow band surveys performed with 4-8m range telescopes, this is compensated for by its unprecedented combination of survey area and number of narrow band filters. J-PAS will be able to make a significant contribution to the study of LABs. In order to assess the sensitivity to LABs, the left panel of Fig. 37 shows the J-PAS surface brightness limits as a function of wavelength. We compare these with some expected surface brightnesses for LABs that fall within each narrow-band filter. Assuming circular LABs with a flat surface brightness distribution and no detectable continuum, J-PAS can detect an LAB with a luminosity of $10^{45} \text{ erg s}^{-1}$ and a radius of 30 kpc at $z \simeq 2 - 3$ at 5σ . A more typical LAB with a luminosity of a few times $10^{44} \text{ erg s}^{-1}$ could easily be detected out to $z \sim 4$, provided that the bulk of the emission comes from a relatively compact region ($R \sim 10 \text{ kpc}$). In reality, the LABs will likely have rather clumpy morphologies of low and high surface brightness regions, as well as varying levels of continuum. At the very least, J-PAS will generate large numbers of candidates that could be followed up to confirm the redshifts, total sizes, and luminosities.

Furthermore, analogous to the extended emission line regions (EELRs) observed around radio galaxies and quasars, LABs often have luminous extended line emission in lines other than $\text{Ly}\alpha$, the brightest of which are $[\text{OII}]$, $[\text{OIII}]$, and $\text{H}\alpha$. At a luminosity of $\gtrsim 10^{44} \text{ erg s}^{-1}$ and sizes of a few tens of kpc, there is little chance of confusing these EELRs with the less luminous and more compact line emission from more typical star-forming galaxies and AGN. Although these lines are redshifted into the NIR at $z > 2$, at lower redshifts they offer a chance to study LAB-like objects at redshifts inaccessible by $\text{Ly}\alpha$ (e.g. Yuma et al., 2013; Brammer et al., 2013). J-PAS will be able to perform for the very first time a general census of the population of luminous emission line halos at a wide redshift range. In the right panel of Fig. 37, we show the expected surface brightnesses for EELRs with a line luminosity of $10^{44} \text{ erg s}^{-1}$ and a radius of 50 kpc. J-PAS will be able to detect such EELRs as traced by $\text{H}\alpha$ at $z \simeq 0 - 0.4$, by $[\text{OIII}]\lambda 5008$ at $z \simeq 0 - 0.8$, and by $[\text{OII}]\lambda 3727$ at $z \simeq 0 - 1.4$. Because J-PAS is a blind, low-resolution survey we will detect all EELRs above the surface brightness limits of the survey, allowing us to study in detail to which classes of objects they belong and to determine their evolution as a function of redshift.

How many LABs at $z \gtrsim 2$ will J-PAS find? We can get a sense of the numbers involved by looking at the different classes of luminous, extended Ly α emitting objects involved. The first category is that of LABs associated with quasars. With an area of $8650 \square^\circ$ J-PAS will detect about two million quasars down to $g_{AB} = 24$ in the comoving volume of 100 Gpc^3 at $2 < z < 3$ (Abramo et al., 2012). We do not currently have good statistics on the fraction of quasars that host Ly α halos, but there is good evidence that a significant fraction does (Heckman et al., 1991; Christensen et al., 2006). The second category is that of the LABs associated with radio galaxies and radio-loud quasars. The number density of radio sources at $z > 2$ having a luminosity $L_{2.7\text{GHz}} > 10^{33} \text{ erg s}^{-1} \text{ Hz}^{-1} \text{ ster}^{-1}$ at $2 < z < 5$ that is known to host extremely luminous Ly α halos, is about $4 \times 10^{-8} \text{ Mpc}^{-3}$ (Willott et al., 2001). This implies at least 400 potential radio source halos in J-PAS, but these numbers will increase as $n \propto L_{\text{radio}}^{-2}$ as we go down the radio luminosity function. Potentially, J-PAS will thus probe the extended emission line gas around thousands of radio sources at high redshift. The third category is that of LABs hosted by sources that are not quasars or radio galaxies (e.g., Type 2 AGN, starbursts, and other Ly α emitting sources). The numbers in this category are much harder to estimate. We currently know about 15 luminous LABs of this type, selected from a handful of surveys with different redshifts, different selection techniques, and different survey volumes. Most useful for estimating a number density for these LABs is perhaps the recent study of Prescott et al. (2013) who found two LABs of $L_{\text{Ly}\alpha} > 10^{44} \text{ erg s}^{-1}$ at $2 < z < 3$ within the $8.5 \square^\circ$ NOAO Wide-Field Survey Boötes field, corresponding to a number density of $2 \times 10^{-8} \text{ Mpc}^{-3}$. J-PAS should therefore discover hundreds of these kinds of LABs.

In terms of number statistics, J-PAS thus has the potential of being one of the most powerful surveys of LABs to date. With this in mind, we will be able to focus on the following key questions: (1) What fraction of LABs are associated with radio galaxies, quasars, and other sources? (2) What is the main powering mechanism of the luminous line emission? (3) What determines the kinematics of the gas? (4) What is the origin of the line-emitting gas? (5) What is the fate of the extended gas? (6) What drives their strong number density evolution with redshift? (7) What is the role of environment? (8) What is the nature and evolution of the related class of luminous extended emission line blobs at lower redshifts as traced by, e.g., H α , [OIII] and [OII]?

Lyman-Break Galaxies. Lyman-break galaxies (LBGs) constitute the dominant star-forming population at high-redshift (Steidel et al. 1995), and are a popular choice for estimating the star formation rate (SFR) density in the early universe (Madau et al. 1998). At $z \gtrsim 2$, the Lyman break redshifts into the optical domain where it is accessible with ground-based telescopes, using the so-called dropout technique (see for example Steidel et al. 2003). At lower redshifts of $z \sim 1$, LBGs can be selected by applying the dropout technique to deep optical data combined with data in the observed ultraviolet obtained by the Galaxy Evolution Explorer (GALEX). The enormous area of the J-PAS main survey will be exploited to probe the bright end of the LBG luminosity function at $z \approx 1 - 3$ to unprecedented detail.

LBGs at $z \sim 1$: Taking advantage of the around $700 \square^\circ$ of area in common between the footprints of the J-PAS Main Survey and the GALEX-Medium Imaging Survey (MIS), we will generate by far the largest known and most robust sample of bright LBGs at $0.8 < z < 1.2$. Using the 56-band SED sampling, we will then be able to obtain accurate photometric redshifts. Possible contaminants (AGNs and stars) will be ruled out based on SED diagnostics. Based on a preliminary study using GALEX-MIS and SDSS optical data in a $\sim 125 \square^\circ$ region we can recover ~ 30 robust LBG candidates at $0.8 < z_{\text{phot}} < 1.2$ per \square° (Fig. 1, left panel) after enforcing a limiting magnitude of 22.4 in r band. The LBG mean UV luminosity distribution obtained is shown in Fig. 1 (right panel) and it is complete above $L_{\text{NUV}} = 2 \times 10^{10} L_\odot$ (i.e. corresponding to $\sim 0.5 L_{\text{UV}, z=3}^*$ and the lower limit to define UV luminous galaxies in the nearby universe; see Heckman et al. (2005)), and accounts for the $\sim 50\%$ of the total LBG NUV luminosity contribution in the LBG LF (Burgarella et al., 2007). Therefore, we estimate it will be possible to detect up to $\sim 24,000$ LBG candidates in the GALEX-MIS/J-PAS common area above $\delta = -10 \text{ deg}$.

LBGs at $z \sim 2 - 3$: At redshifts $z \gtrsim 2$, the Lyman forest is shifted to the wavelength range covered by J-PAS filters. This permits us to select LBGs/LAEs based directly on their J-PAS SEDs and spectral fitting of model templates, including theoretical LBG spectra, and spectra of other types of galaxies and stars. The spectral fitting also provides us with information about the newly selected objects and permits ruling out contaminants, as mentioned above. In addition, by selecting candidates using spectral fitting instead of color cuts, we will equally select LBGs and LAEs up to the limiting continuum magnitude set up by the bluest J-PAS filters ($m_{AB} \sim 22.3$). This will permit us to study the LBG-LAE connection in a sample free of selection biases. An example of how J-PAS would see a LBG/LAE spectrum at $z \sim 3$ is shown in Fig. 40, where we have plotted the original, and J-PAS filter convolved, composite spectrum of 811 LBGs of Shapley et al. (2003).

Fig. 41 shows the LBG luminosity function (LF) at $z \sim 2$ and $z \sim 3$ (Ly et al., 2011). It is clear that both LFs are badly defined at their brightest ends. Considering the J-PAS limiting magnitude in the bluest filters and the survey area, we estimate we will discover $> 10^6$ LBGs/LAEs at $z \sim 2$ and $> 10^5$ at $z \sim 3$. This would significantly contribute in constraining the bright end of the LFs at these redshifts. Discovering and studying the brightest LBGs/LAEs is also interesting in their own right to understand the nature and properties of these UV ultraluminous galaxies (see, e.g. Bian et al., 2012).

The resulting catalogues of $z \sim 1$ and $z \sim 2 - 3$ LBGs will be used in the following science:

- Building the largest sample of LBGs at their corresponding redshifts - virtually free from cosmic variance effects - that represents the bright end of the UV luminosity function of this kind of galaxies.
- A characterization of fundamental properties (redshift, stellar mass, mean age, SFR, and dust content) of these bright LBGs, using stellar population modeling resources under Maximum Likelihood (ML) or Bayesian approaches. An example of a ML-template fitting and derived parameters for a LBG in the COSMOS field using data from ALHAMBRA survey is given in Fig. 39 from Oteo et al. (2012b).
- Cross-correlating the LBG data to be obtained with the QSO sample of J-PAS (see Section 4.2.5), we will be able to perform an unprecedented analysis of the LBG-AGN spatial correlation.

Damped Ly α systems (DLAs). Damped Lyman Alpha systems (DLAs) are high column density neutral hydrogen systems, observed through their characteristic signature (damped Ly α absorption) in the spectra of high redshift quasars. They are probably a consequence of the gas-rich outer regions of young, forming galaxies along the line of sight of the quasars, and are of significant interest for probing the early stages of galaxy formation at high redshift (see, Wolfe et al., 2005, for a review). Here we will evaluate the detectability of a DLA based on the J-PAS spectra of quasars. For a DLA to be observable, it must cause an absorption trough at a wavelength that is both redwards of the Lyman break of the quasar and the blue limit of the J-PAS filter transmission system. This translates into $\max(1.9; 912/1215(1 + z_{\text{quasar}})) < z_{\text{DLA}} < z_{\text{quasar}}$. Even though it is clear that very broad DLAs will be easily detected by J-PAS – see for an example the DLA recently published by Kulkarni et al. (2012) which has $\sim 200\text{\AA}$ (FWHM) – these systems tend to be very rare. To what extent will J-PAS be able to detect the more common DLAs that have typical widths that are just a fraction of a single J-PAS narrow-band filter? In order to evaluate this more quantitatively, we built a toy simulator which creates observed quasar spectra with intervening DLAs.

We construct a simple quasar model spectrum consisting of a flat continuum and three broad emission lines, Ly α at 1215Å, CIV at 1549Å, and CIII] at 1908Å. These emission lines ensure that we will be able to detect and identify the quasar as well as measure its redshift. We choose relevant parameters for these lines, which need not be detailed here, and simply note that the model quasar spectrum is realistic. The luminosity of the quasar is set by M_B , its absolute magnitude in the B filter. A realistic luminosity range for quasars spans from $M_B = -23$ to $M_B = -26$. From the value of M_B , we set the flux density value of the continuum in the Ly α region assuming that νL_ν is constant over the relevant wavelength range. An artificial and randomly distributed Ly α forest is added to the spectrum. We use the VLT/UVES spectrum of a $z = 2.4$ quasar¹³ to choose realistic parameters for the FWHM and equivalent width (EW) of the “trees” populating this forest. The DLA is modeled by a Voigt absorption profile. The rest-frame FWHM is the input parameter, while the EW is set to twice the FWHM (to reproduce the saturation of the line) and the α parameter of the Voigt profile is set to 2.5. The transformation from luminosity to the local flux density is computed using the luminosity distance D_L for the familiar cosmological parameter values $\Omega_m = 0.3$ and $\Omega_\Lambda = 0.7$. For the resulting spectrum, a J-PAS set of measurements (54 flux densities and their associated uncertainties) is then evaluated. The result is shown in Fig. 42, for a quasar of $M_B = -23$ at $z = 3.5$. For the DLA, we chose $z_{DLA} = 2.98$, a FWHM of 5Å and an EW of 10Å. For this case, the imprint of the DLA on the low-resolution quasar spectrum can be seen quite clearly. We are currently modeling the detectability of DLAs in J-PAS based on a wide range of parameters. A possibly complication in these kind of measurements may be the variability of the quasars. However, quasar variability will only be a source of uncertainty when observations through the different filters will be spread over long periods.

4.2.5. Theme V. Active Galactic Nuclei

The spatially resolved properties of nearby AGN. For nearby AGN, J-PAS will be able to spatially resolve the stellar populations. While stellar populations in nearby AGN host galaxies have been mapped in detail with CALIFA, J-PAS will allow a far greater number of galaxies to be observed. The resulting low resolution spectra will then be interpreted using spectral synthesis methods. Together with a properly constructed control sample, this will allow us to investigate the differences between the stellar populations of active and non-active galaxies, as well as the differences in the stellar populations of Type 1 and Type 2 AGN (Storchi-Bergmann et al., 2001), and between more luminous and less luminous classes of AGN (e.g. LINERs).

J-PAS will furthermore allow us to map the nebular emission over the AGN host galaxies in the strongest emission lines, by using filters containing emission lines and adjacent filters to obtain the continuum to be subtracted and isolate the gas emission (see Sect. 4.1.2). Line ratio maps between two emission line images can be used to map also the excitation of the gas. Again, comparisons between the extended emission of different AGN types can be investigated, such as the spatial extent of the emission and the gas excitation. Other properties that can be investigated are the presence of star-formation across the host galaxy, and the frequency of star formation in the disk for different types of AGNs (e.g., Storchi-Bergmann et al., 1995, 2012).

Optically selected AGN. Active galactic nuclei (AGN) play an important role in galaxy formation and evolution. The growth of central supermassive black holes (SMBHs) is suggested to be related to the formation of the bulge of the host galaxy. This scenario is supported by the Magorrian relation (Magorrian et al., 1998), and by the fact that both star formation and AGN activity show similar evolutions from $z \sim 1$ to the current epoch (e.g. Silverman et al., 2008).

¹³<http://www.eso.org/public/images/eso0013f/>

Quasars are the most luminous sources to redshifts of at least $z \simeq 6.5$, and have been key cosmological probes. Observations of high-redshift QSOs have revealed a marked increase in the optical depth to neutral hydrogen (HI) at redshifts $z \geq 5.7$, which signal the end of cosmological reionization. Measurements of the the quasar luminosity function (QLF) at high redshifts also constrain the growth of structures and the early formation of super-massive black holes in the first billion years of the Universe. QSOs have been used as tracers of large-scale structure (Porciani et al., 2004; Da Ângela et al., 2005; Shen et al., 2007; Ross et al., 2009), and they can even be employed to measure baryon acoustic oscillations (BAOs) at high redshifts (Abramo et al., 2012).

We have explored the feasibility of identifying type-I and type-II AGNs by simulating how these objects will be observed with J-PAS. Since type-I AGNs have broad, high equivalent width emission lines (with relative width $\lambda/\Delta\lambda \sim 30$), they should be easily detected even with the low spectral resolution of the J-PAS survey ($\lambda/\Delta\lambda \sim 40 - 80$). We illustrate how such detections can be made by taking the spectra of two SDSS AGNs, and simulating the low-resolution spectra as they would be observed through the J-PAS narrow-band filter system. In Fig. 43 we show the results for a type-I QSO at $z \sim 3$, and a Seyfert 2 at $z \sim 2.6$. Although type-II AGNs have much narrower spectral features than type-I, it will still be possible to detect those with high equivalent width (see also Bongiovanni et al., 2010). Assuming $\Delta\lambda \sim 100\text{\AA}$, the EW_{min} that could be measured in the rest frame for narrow-line sources is $\sim 140\text{\AA}$.

We estimated the number of QSOs that will be detected in the J-PAS survey using both the LFs and the surface densities of small-area but fairly complete surveys. A first crude estimate can be made using QSO surface density determinations made by Beck-Winchatz & Anderson (2007) on high-latitude HST fields. At a limiting magnitude of 23 we obtain, for an area of 8500 square degrees, $\sim 2.1 \times 10^6$ QSOs. For type-I quasars, the luminosity function is reasonably well-known for luminous objects ($M_I < -22$) and redshifts $\lesssim 2.5$ (e.g. Hopkins et al., 2007; Croom et al, 2009). Based on these luminosity functions, the number of QSOs that we expect to identify with J-PAS is around 2.5×10^6 objects up to $z = 2.5$. For higher redshifts we used the luminosity function by Willott et al. (2010) and estimate, in the range $4 < z < 7$, around 2.1×10^4 QSOs.

Given the broad spectral features of type-I quasars, the vast majority of these objects will have very accurate photometric redshifts ($\sigma_z \sim 0.0015(1+z)$) and a low rate of outliers (Abramo et al., 2012). The purity of the J-PAS dataset and the astrometric accuracy imply that this will be, by far, the largest and most complete sample of quasars and AGNs at the time of completion. With such a large sample of AGNs many astrophysical problems can be addressed with unprecedented detail and accuracy.

The luminosity function of QSOs and AGNs as a function of redshift constrains the evolution of AGN populations and their effects on their environment. The shape of the quasar LF at high redshifts, particularly its faint end, represents a critical observational constraint on the early formation history of massive black holes, on their contribution to the reionization, and on feedback processes which affect the formation of their hosts galaxies (Glikman et al., 2010). The true shape of the quasar LF is not well known at $z \gtrsim 4$ due to flux limits of large-area surveys. The J-PAS survey will allow us to determine the LF at high redshift.

Depending on the cadence of the J-PAS survey, it can also provide variability information on a large sample of AGNs, which, through reverberation mapping, may allow us to determine the size of the broad line region (BLR) for thousands of objects. Variability is also an important tool to cross-check contamination of quasars by blue stars (a potential problem mainly at $z \lesssim 1$).

QSOs can be competitive tracers of large-scale structure (Abramo et al., 2012; Sawangwit et al., 2011). Large quasar groups (LQG) and QSO pairs are also indicators of the underlying galaxy overdensity (Haberzettl et al., 2009; Sodr e et al., 2009) up to $z \sim 1 - 2$. These observations can probe the interplay between the environment at halo and super-halo scales, the galaxy stellar populations, and the QSO/AGN phase of galaxy evolution.

During the past two decades, a sample of >100 strongly lensed QSOs (SLQSOs) and binary QSOs (e.g. CASTLeS¹⁴) has been harvested from different surveys, either in the optical (e.g. SDSS, SLACS) or radio (e.g. CLASS). It is expected that this catalog will increase by about 2 orders of magnitude with ongoing and planned wide-field surveys. A large enough sample of SLQSOs can be used to constrain the CDM power spectrum on small scales, as well as to test different dark matter candidates (Macciò et al., 2008). On the other hand, follow-up measurements of time delays (e.g. COSMOGRAIL) of a large sample of multiple-image SLQSOs can allow a direct measurement of H_0 (see Jackson, 2007, for a review), yielding strong and independent constraints on cosmic expansion, the dark energy equation of state parameter w , and the flatness of the universe Ω_k despite the limitations of this method (see Falco et al., 1985; Wucknitz, 2002). Following the predictions of Oguri & Marshall (2010), J-PAS should be able to detect about 1000 SLQSO up to $z \sim 5$. By time-monitoring this sample, a $< 1\%$ level precision in the Hubble constant could be reached (Coe & Moustakas, 2009).

Radio-galaxies and radio-loud quasars. Radio continuum surveys such as the Faint Images of the Radio Sky at Twenty centimeters (FIRST) survey (Becker et al., 1995), the National Radio Astronomy Observatory (NRAO) Very Large Array (VLA) Sky Survey (NVSS Condon et al., 1998), and the Westerbork Northern Sky Survey (WENSS Rengelink et al., 1997) cover large fractions of the sky while probing the extra-galactic radio source population out to significant cosmological distances ($z \sim 6$; De Breuck et al., 2000). The clustering of radio sources, such as radio galaxies and radio-loud quasars, is an important probe for both cosmology and the evolution of galaxies and the large-scale structure. Radio continuum surveys, however, do not provide redshift information on the detected radio sources. Redshifts must be obtained by spectroscopic follow-up or by cross-correlating the radio-selected sample with surveys performed at other wavelengths and with known redshifts. Historically, radio source redshift distributions have been obtained statistically based either on an extrapolation of the redshift distribution determined for much smaller subsamples selected at relatively high flux densities (e.g. Dunlop & Peacock, 1990), or by observing a complete sample down to low flux densities in a small area (typically a few square degrees) of the sky (Waddington et al., 2001; Best, 2004; Brookes et al., 2008).

More recently, large-area sky surveys in the optical such as the SDSS and 2dF surveys have enabled the identification of large samples of radio sources from NVSS and FIRST through the cross-correlation with objects with known spectroscopic or photometric redshifts (e.g. Magliocchetti et al., 2004; Best et al., 2005; Donoso et al., 2009; Passmoor et al., 2013). Such cross-correlations have allowed us to study the properties and clustering of primarily the low redshift end of the radio source redshift distribution. For example, Best et al. (2005); Best & Heckman (2012) used the SDSS spectroscopic sample to study the properties of radio sources at a median redshift of $z \sim 0.1 - 0.2$. Donoso et al. (2009, 2010) was able to study the clustering properties of 14,000 radio sources at $0.4 < z < 0.8$ identified with luminous red galaxies (LRGs) from the SDSS, finding that the radio sources are more strongly clustered on scales of less than 1 Mpc compared to the parent LRG sample. They also found that the excess clustering scales with radio power, and that radio galaxies and radio-loud quasars are similar only at the highest radio luminosities. This suggests that the AGN triggering mechanism may be linked to environment. Chen et al. (2013) compared optical spectra of massive radio loud AGN at $z \sim 0.2$ and $z \sim 0.6$, also from SDSS, finding evidence that the history of the gas accretion, star formation and black hole growth is regulated by feedback from the radio-jets. Fine et al. (2011) compare the clustering of NVSS and FIRST radio sources in three samples at $z \sim 0.35$, $z \sim 0.55$ and $z \sim 0.68$, finding that the halo mass of radio AGN hosts must be constant over this redshift range, similar to that found for QSOs albeit at a much higher clustering amplitude (indicating that radio AGN have much more massive hosts than optical QSOs). Overzier et al. (2003) measured strong clustering of NVSS/FIRST radio sources at an (inferred) median redshift of $z \sim 1$, finding that radio galaxies trace the most massive structures in the universe, possibly the progenitors of rich Abell-type clusters.

¹⁴<http://www.cfa.harvard.edu/castles/>

It has been observed that the optical spectra of radio galaxies either show strong high-excitation emission lines, or low-excitation emission lines (Laing et al., 1994; Jackson & Rawlings, 1997; Tadhunter et al., 1998). These two classes of radio galaxies, high-excitation galaxies (HEGs) and low-excitation galaxies (LEGs), are, according to the current paradigm, interpreted as being powered respectively by cold gas on a high rate and radiatively efficient accretion process, and by radiatively inefficient accretion flows of hot gas at low accretion rates (e.g. Buttiglione et al., 2010; Best & Heckman, 2012; Janssen et al., 2012). Alternatively, or in addition to, the energy released through black hole spin is also a strong candidate to explain this class separation (e.g. McNamara et al., 2011; Martínez-Sansigre & Rawlings, 2011). Given that the jet launching mechanism in radio galaxies is conjectured to be strongly associated with the accretion disk emission (e.g. Rawlings & Saunders, 1991), the HEGs and LEGs radio and disk-related emission can pose important constraints and insights on the link between jets and accretion, which remains an important issue in AGN models.

Moreover, ‘standard’ radiatively efficient accretion, and advection-dominated radiatively inefficient accretion are associated with different AGN activity modes, and thus with different AGN feedback mechanisms. Whereas the standard accretion mode is associated with quasar activity, the radiatively inefficient mode leads to little radiated energy, but it can produce highly energetic jets, also known as the ‘radio mode’ (e.g. Hine & Longair, 1979; Hardcastle et al., 2007). ‘Radio mode’ activity is taken as the main mechanism to switch off star formation in the most massive galaxies, thereby explaining the shape of the observed luminosity function. This mode of AGN feedback is an important ingredient in semi-analytic models of galaxy formation, although its physical implementation is not exactly clear (e.g. Bower et al., 2006). The current procedure is therefore to adjust the feedback parameters in order to match observed luminosity functions. LEGs, being powered by this mode of AGN activity, are the perfect laboratory to study the ‘radio accretion mode’ and to quantify its physical parameters. A statistically significant study of LEGs is thus utterly compelling. Analytic models also predict that whereas the ‘radio mode’ of AGN activity should dominate over a wide range of luminosities at $z = 0$, the ‘standard mode’ is expected to have a much more significant weight at $z \sim 1$ (Hopkins & Hernquist, 2006). Being a strongly evolutionary population, the study of the space densities of HEG and LEG radio galaxies provides important clues as to how and when the two forms of accretion are triggered and their evolution with redshift. Best & Heckman (2012) presented a sample of ~ 7300 SDSS classified sources, with a median redshift of $z = 0.16$. Fernandes et al. (2014) have performed the highest redshift study of HEGs and LEGs at $z \sim 1$ with a sample of 27 galaxies. J-PAS should be able to robustly identify large numbers of these sources up to a redshift of $z \lesssim 0.8$.

By probing to much fainter magnitudes with very accurate photometric redshift information for individual sources, J-PAS will be used to identify much larger and less biased samples of radio sources, and out to much higher redshifts, than allowed by the existing data sets. The more accurate redshift distribution resulting from J-PAS will also allow a better assessment of the integrated Sachs-Wolfe effect through cross-correlation of the clustering signal detected on large angular scales in the NVSS (Overzier et al., 2003) with the CMB (Hernández-Monteagudo, 2010), and may even be employed toward constraining dark energy (Camera et al., 2012). At high redshifts, radio sources can be used as probes of cluster environments (Best et al., 2003; Venemans et al., 2007), and evolution observed in their typical environments as a function of redshift and radio power offers insight into the typical feeding and feedback mechanisms of radio-loud AGN (Hill & Lilly, 1991; Hart et al., 2011). In the relatively nearby universe, we will be able to focus on the properties and environment of the large number of faint radio sources in which the radio continuum emission may arise also from starbursts rather than (or besides) an AGN.

The NVSS survey has a source density of 15 and 1.5 / \square° at limiting flux densities of 10 and 100 mJy, respectively. The deeper FIRST survey reaches a source density of 35/ \square° at 3 mJy. The median redshifts probed by these surveys is $z \sim 1$. J-PAS will thus cover up to $\sim 300,000$ radio sources, allowing a great many studies related to the population of radio-loud AGN over the redshift range $z = 0 - 1.5$. J-PAS will be able to constrain fluxes and equivalent widths of the brightest lines (e.g. [OII], H β , [OIII], [SII], [NII], [OI], H α ; Buttiglione et al., 2010), which can be used to determine the main emission line diagnostic ratios for thousands of galaxies up to a redshift of $z \sim 1.5$, while at the same time providing insights into the stellar populations, morphologies, and environment and the evolution with redshift.

4.3. Synergy with other surveys

Naturally, J-PAS will be able to offer a wealth of information to studies performed at other wavelengths, and vice-versa. Here we will present a brief overview of a selection of other extra-galactic surveys from X-ray to radio wavelengths that will be cross-matched with J-PAS.

Synergy between J-PAS and X-ray surveys will allow us to probe the galaxy-AGN connection, star formation, and calibrate group and cluster masses. Apart from continuing targeted observations by the *Chandra* and *XMM-Newton* X-ray observatories, eROSITA will perform the first imaging all-sky survey in the medium energy X-ray range up to 10 keV with an unprecedented spectral and angular resolution, as a part of the Russian *Spectrum-Röntgen-Gamma satellite* (SRG, Kolodzig et al., 2013,?).

The *Galaxy Evolution Explorer* (GALEX, Martin et al., 2005) has performed imaging surveys in the Far UV (FUV) 1350 – 1780Å and Near UV (NUV) 1770 – 2730Å at a resolution of $\sim 5''$ (FWHM), allowing an unprecedented view on the history of star formation from $z \sim 1.5$ to the present. The GALEX All-Sky Imaging Survey (AIS) covers an area of 26,300/ \square° down to a NUV depth of 21 (AB) mag (40 million sources). The Medium Imaging Survey (MIS) covers an area of 5,000/ \square° to a NUV depth of 23 mag (22 million sources). The Deep Imaging Survey (DIS) covers about 100/ \square° down to ~ 25 mag. The GALEX surveys have been crucial for extending the wavelength range of the SDSS into the UV, where the youngest stellar populations dominate. Likewise, GALEX will be an invaluable resource for the J-PAS galaxy evolution survey.

In the near-infrared domain, the J-PAS galaxy survey will benefit from the on-going, UKIDSS Large Area Survey (LAS, Lawrence et al., 2007), that covers an area of 4000 square degrees at high Galactic latitudes, in the four bands *Y*, *J*, *H* and *K* to a depth of $K_{AB} = 18.4$. Going significantly deeper, a patch of ~ 750 square degrees will be observed to 5σ limiting depths of $z \approx 22.4$, $Y \approx 21.4$, $J \approx 20.9$, $H \approx 19.9$ and $K_s \approx 19.3$ (all in the Vega system) by the VISTA Kilo-degree Infrared Galaxy Survey (VIKING, Sutherland, 2012). An additional contribution, especially in the photometric *Y* band (up to ≈ 21.9 AB mag), could come from the Pan-STARRS PS-1¹⁵ 3π Steradian Survey (see Tonry et al., 2012). At longer wavelengths, the *Wide-field Infrared Survey Explorer* (WISE) has mapped the sky at 3.4, 4.6, 12, and 22 μm with an angular resolution of 6.1, 6.4, 6.5, and 12.0'', probing dust-enshrouded star-forming and starburst galaxies and AGN (Wright et al., 2010).

In the sub-mm domain, the SCUBA-2 “All-Sky” Survey (SaSSy: ~ 4800 square degrees, rms sensitivity of ~ 30 mJy beam $^{-1}$ at 850 μm) offers a new-generation survey approach. SCUBA-2 (Holland et al., 2013) is a 100–150 times faster instrument than the previous one, and will offer interesting possibilities for the analysis of different sub-types of luminous infrared galaxies (see MacKenzie et al., 2011, for a pilot study).

¹⁵From <http://www.ps1sc.org/Data.Release.shtml>: All of the data, images, and catalogs taken by PS1 for the PS1 Science Mission, which is funded by the member institutions of the PS1SC, will become public at the end of the PS1 Mission (2013).

Finally, by combining J-PAS with existing radio surveys in the Northern sky at 1.4 GHz, such as NVSS, FIRST, WENSS, and LOFAR, will allow us to constrain the properties of the nearby star-forming population, as well as those of the population of radio-loud AGN out to cosmological distances (see Sect. 4.2.5). The Square Kilometer Array (SKA) is an internationally-funded radio telescope, which will consist of more than one thousand of ~ 15 -meter size dishes in a central area of diameter ~ 5 km, surrounded by a similar number of dishes in an area stretching up to several thousands of km. The SKA will be much more sensitive than any existing radio telescope, aimed at answering some of the most fundamental questions of the Universe we live in (Carilli & Rawlings, 2004; Schilizzi, 2004). Since its construction is expected to be completed in 2022, several pathfinders have been, or are currently being, built. LOFAR (the Low Frequency Array, Röttgering et al., 2006) and Apertif (the updated Westerbork phased-array, Oosterloo et al., 2010) in the Northern Hemisphere, and ASKAP (the Australian SKA Pathfinder, Johnston et al., 2008) and MeerKat (the South African SKA Pathfinder, Booth et al., 2009) in the Southern Hemisphere can be considered as the SKA pathfinders. The pathfinder projects are expected to devote a significant amount of observing time to a number of “legacy” projects with the main aim of studying galaxy formation and evolution through cosmic time, e.g.:

WODAN, an Apertif legacy project, will observe at the relevant observing wavelength of 21 cm (continuum) all of the Northern sky at $\delta > 30$ deg, and down to a $1-\sigma$ rms noise figure of about $10\text{--}20\mu\text{Jy beam}^{-1}$ (a factor of 25-50 more sensitive than the NVSS). The angular resolution will be about 15 arcsec, a factor of three better than the angular resolution of the NVSS. ASKAP has a similar legacy project, called EMU (Evolutionary Mapping of the Universe). EMU is complementary to WODAN, as it will observe also in the 21 cm continuum band the whole Southern Sky and up to $\delta = +30$ deg (Norris et al., 2011). After about 1.5 yr of observation, EMU will reach an homogeneous $1-\sigma$ noise rms figure of about $10\mu\text{Jy beam}^{-1}$, with an angular resolution of about 10 arcsec.

Not surprisingly, the overall goals of these radio continuum surveys will match those pursued by J-PAS. In particular, EMU and WODAN will (i) trace the evolution of star-forming galaxies from $z \approx 2$ to the present day, using a wavelength mostly unbiased by dust or molecular emission, and (ii) trace the evolution of massive black holes throughout the history of the universe, and understand their relationship to star formation. Since J-PAS and WODAN/EMU will observe the same areas of the sky with very deep sensitivity at their corresponding bands, those surveys will detect and unambiguously identify many star-forming galaxies and accreting black holes at the low-mass end from the local universe up to $z \approx 2$. This region of the parameter space (low-masses and/or high-redshift) is so far largely uncharted territory. J-PAS will be in a unique position to provide the much needed high quality (photometric) redshifts for the ~ 100 million sources expected to be detected by WODAN/EMU, as spectroscopic redshifts for such a huge amount of galaxies is simply unaffordable. At the same time, J-PAS will provide information on the properties of the radio source host galaxies as well as their small- and large-scale environments.

In the HI line, the extension of ALFALFA (Arecibo Legacy Fast ALFA Extragalactic HI Survey, Haynes & ALFALFA Tea, 2008) and its spin-offs (High-Mass, SHIELD, GASS) will cover $\sim 13,000$ square degrees of sky, while AGES¹⁶ (Arecibo Galaxy Environment Survey) will provide a larger sample of clusters and groups of galaxies ($cz < 10000$ km s⁻¹) by covering 3,000 square degrees at 300 s integration time per beam (Giovanelli, 2008). Also, the combined WNSHS (APERTIF Westerbork Northern Sky HI Survey¹⁷) and WALLABY (Australian SKA Pathfinder HI All-sky Survey, Koribalski, 2012) programs will offer an unprecedented HI image of the whole sky (sensitivity of 0.65 and 0.55 mJy per 100 kHz beam at 30'' and 13'' angular resolutions, respectively).

¹⁶<http://www.naic.edu/~ages/>

¹⁷<http://www.astron.nl/~jozsa/wnshs/>

		Test Sample						
		306	345	222	97	9		
T_M	Irr				1%	89%		9
	SpL			11%	82%	11%		106
	SpE	4%	8%	73%	11%			212
	S0	13%	78%	15%	5%			348
	E	83%	14%					304
		F	S0	SpE	SpL	Irr		
							T_V	

Figure 33: Comparison between visual and MORPHOT 'broad' morphological classes for the galaxies of the MORPHOT test sample. At the top of the 2D-bins the percentages of the visual classes (Es, S0s, early spirals [SpE], late spirals [SpL] and irregulars) falling in different bins of the MORPHOT classification are shown. The percentages of the MORPHOT classes falling in different bins of the visual classification are shown at the right-hand side of the 2D-bins. Finally, on the top (columns) and on the right (rows) of the plot, we report the total number of galaxies in each 'broad' class of the visual and MORPHOT estimates, respectively.

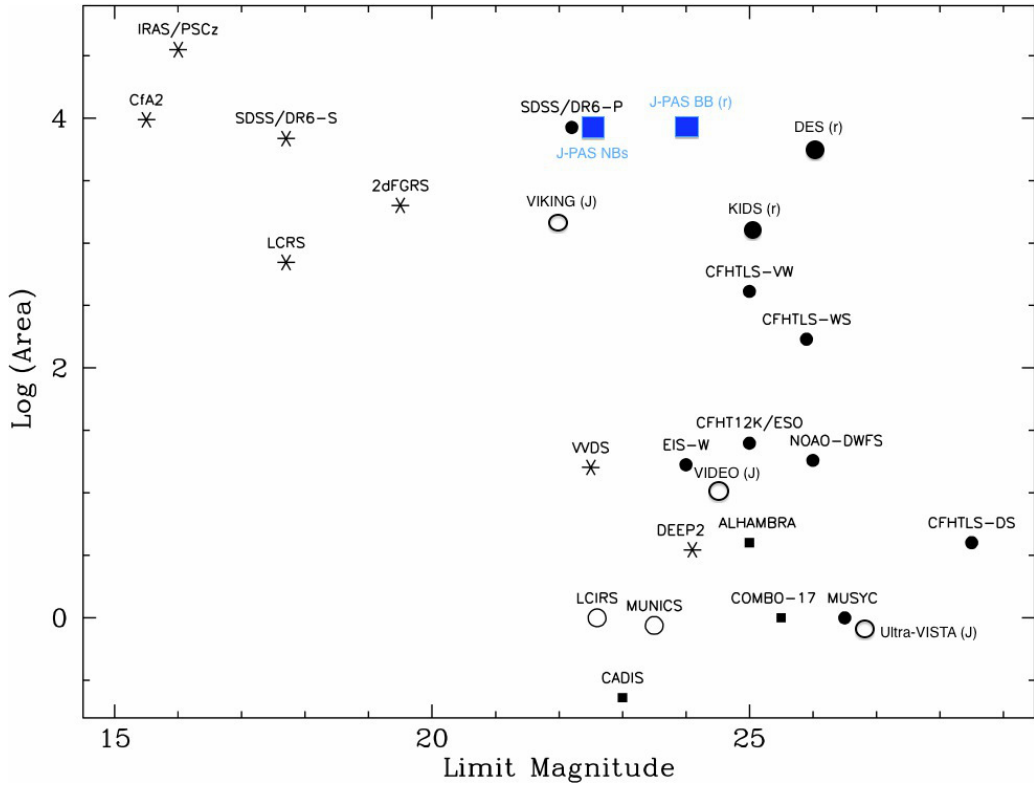


Figure 34: An overview of extra-galactic surveys in the area (square degrees) versus depth (limiting magnitude) plane. Circles correspond to broadband photometric surveys. Stars correspond to spectroscopic surveys. Squares correspond to multi-filter system photometric redshift surveys (i.e. CADIS, COMBO-17, ALHAMBRA and J-PAS). Filled symbols are surveys that are performed (primarily) in the optical, while open circles are surveys performed primarily in the near-infrared. The areas covered by the SDSS, DES and J-PAS are comparable. The J-PAS broad-band filters reach a depth of almost two magnitudes fainter than SDSS, while each of the J-PAS narrow-bands reaches a depth that is comparable to that only achieved by SDSS in the broad-bands. Both DES and KIDS will reach much fainter magnitudes in the optical than J-PAS, but will not have the great leverage in photometric redshifts achieved by the 56 filters of J-PAS. Note that the magnitude limits in general refer to a variety of bandpasses. Figure taken from Moles et al. (2008).

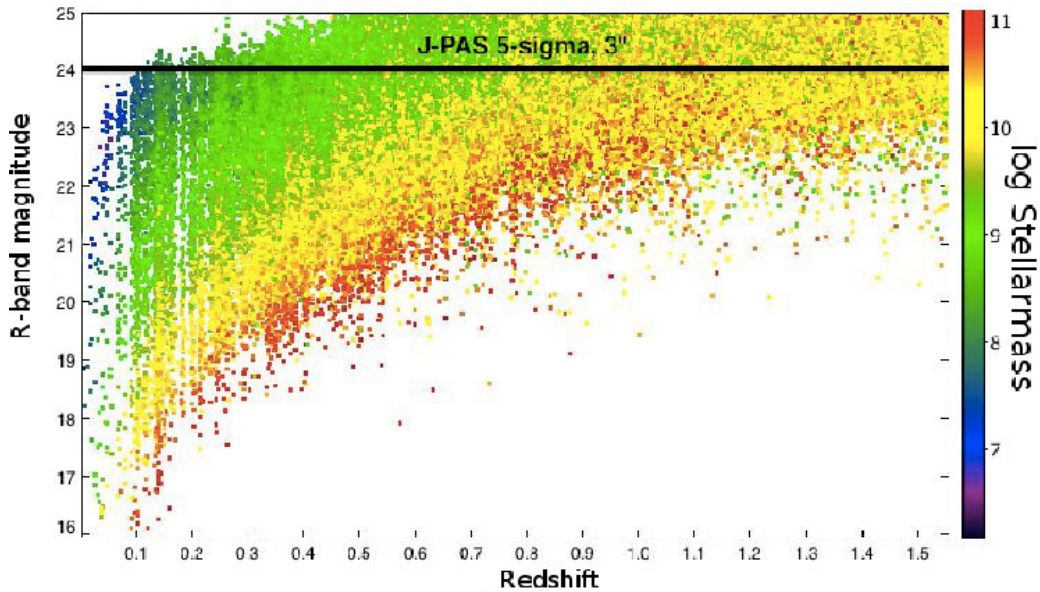


Figure 35: The range in stellar mass probed by J-PAS as a function of redshift and limiting magnitude in the R -band. The black horizontal line indicates the approximate limiting magnitude achieved by J-PAS (5σ , $3''$ aperture). Galaxies are colour-coded according to their stellar mass. J-PAS should be largely complete for galaxies more massive than $\sim 10^9 M_\odot$ out to $z \sim 0.4$ and $\sim 10^{10} M_\odot$ out to $z \sim 0.8$. This prediction is based on a 2 square degree mock galaxy redshift survey from the Millennium simulations (see Henriques et al., 2012; Overzier et al., 2013a).

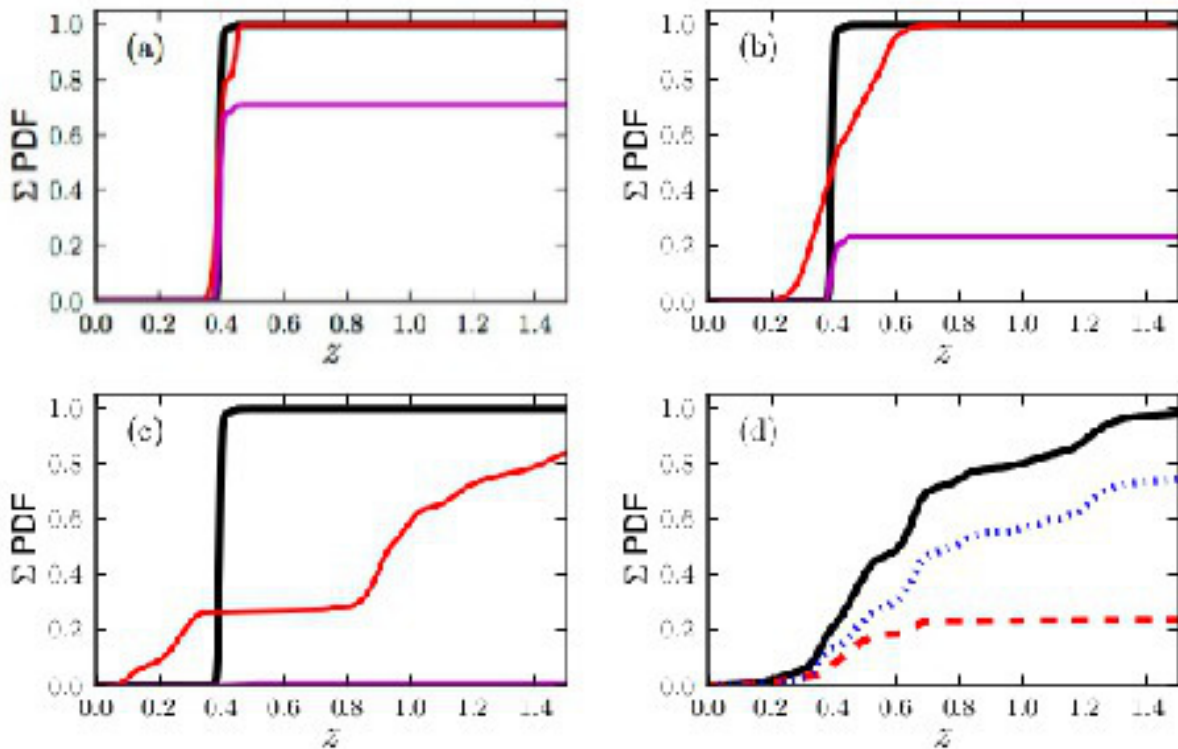


Figure 36: Cumulative probability distribution functions in the ALHAMBRA survey. *Panels (a), (b), and (c)* show a principal galaxy (black line) at $z = 0.395$ and a companion galaxy (red line) at $z = 0.395$, $z = 0.400$, and $z = 0.934$, respectively. The purple line shows the probability of both galaxies to be at the same redshift. The cumulative pair probability is 71%, 23%, and 0%, respectively. *Panel (d)* shows the PDF of a single source split by spectral types: red types (E+S0, red dashed line, 24%), blue types (S + starburst, blue dotted line 76%), and all the types (black solid line). We will be able to estimate reliable red and blue merger fractions.

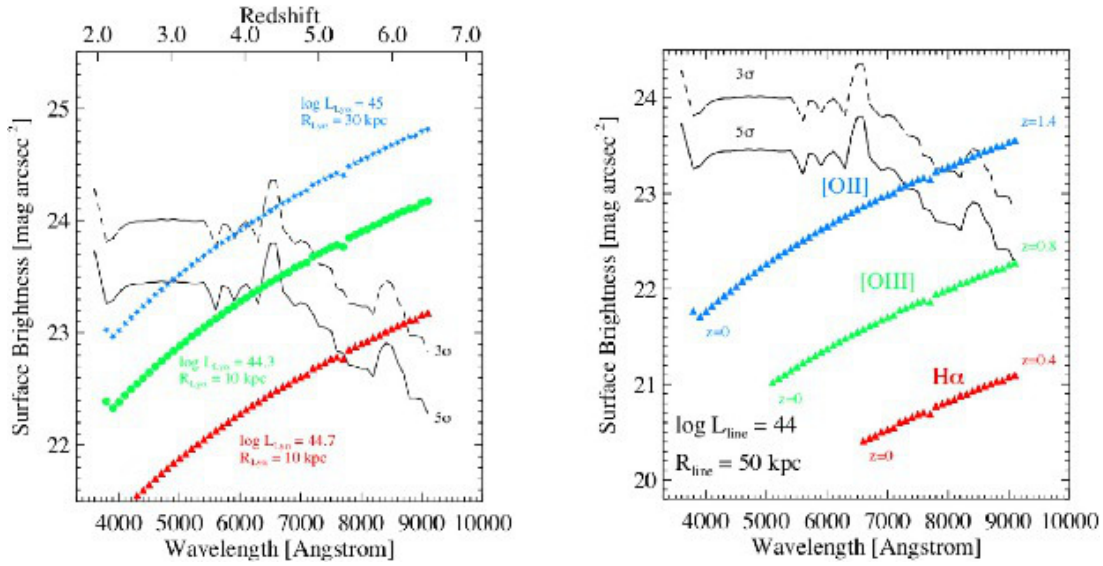


Figure 37: Detectability of LABs and other extended emission line objects. Left panel: The expected surface brightness of Ly α in each J-PAS filter for three types of LABs (blue points: $\log L_{Ly\alpha} = 45$, $R_{Ly\alpha} = 30$ kpc; green points: $\log L_{Ly\alpha} = 44.3$, $R_{Ly\alpha} = 10$ kpc; red points: $\log L_{Ly\alpha} = 44.7$, $R_{Ly\alpha} = 10$ kpc). The limiting surface brightness achieved by J-PAS is indicated by the solid (5σ) and dashed (3σ) curves. Right panel: Expected surface brightness of EELRs having a line luminosity of 10^{44} erg s⁻¹ and a radius of 50 kpc. Blue points: [OII] emission at $z = 0 - 1.4$, green points: [OIII] emission at $z = 0 - 0.8$, red points: H α emission at $z = 0 - 0.4$.

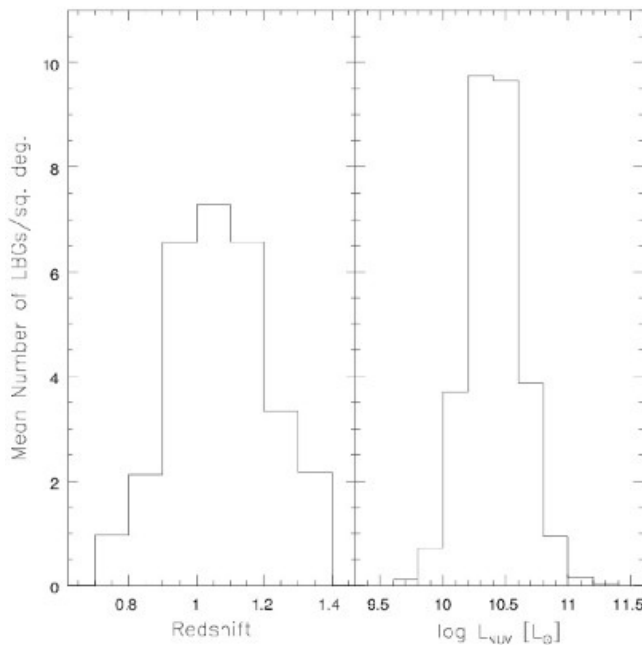


Figure 38: Photometric redshift and UV luminosity mean distributions of a GALEX selected LBG sample at the limiting magnitude of J-PAS, from a $\sim 125^\circ$ region with $55 \text{ deg} < b_{II} < 60 \text{ deg}$.

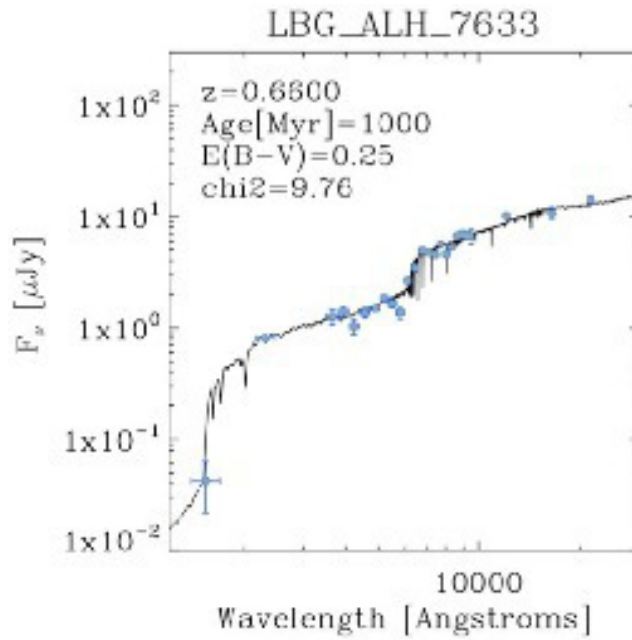


Figure 39: Template fitting (BC03) and derived parameters of a confirmed LBG in the ALHAMBRA survey. The two bluest dots correspond to GALEX photometry and the remaining ones to ALHAMBRA (optical + near-IR).

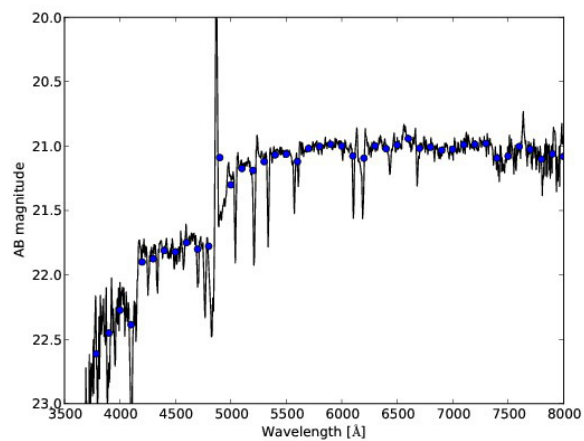


Figure 40: A composite spectrum of 811 LBGs of Shapley et al. (2003) (black line) and the corresponding synthesized J-spectrum (blue dots).

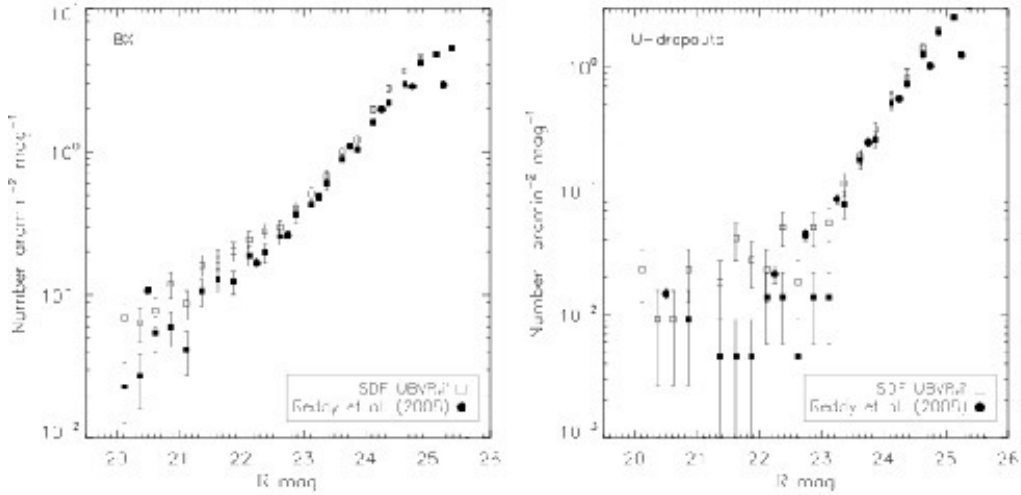


Figure 41: The LBG luminosity functions at $z \sim 2$ (left) and at $z \sim 3$ (right) from Ly et al. 2011.

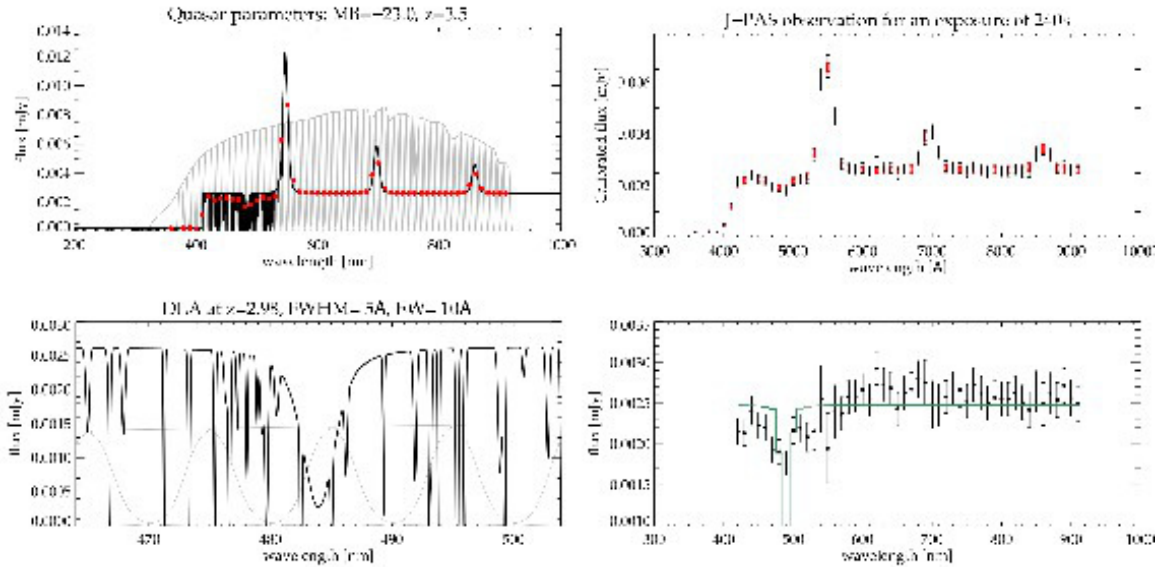


Figure 42: Illustration of the result for one simulation of a DLA observed by J-PAS. The quasar parameters are: $M_B = -23$ and $z = 3.5$. For the DLA, we chose $z_{DLA} = 2.98$, $FWHM = 5\text{\AA}$ and an $EW = 10\text{\AA}$. Since the profile is a Voigt profile, what we call FWHM is in fact $2.35 \times \sigma_{Voigt}$ at rest wavelength. The observed width is multiplied by a factor $(1 + z_{DLA})$. Top to bottom, left to right: (1) The full quasar simulated spectrum in black, the red dots mark the flux densities through the filters, and the grey curves show the filter transmissions. (2) A zoom on the DLA absorber, with the grey filter transmission curves in the region. (3) The resulting measurements through J-PAS for an exposure time of 240s. The red and thick bars show the computed values and the poisson noise, while the thin and black bars show a random draw for the measurement, like an actual observation, and the full uncertainty (quadratic sum of the poisson noise and 3% of the flux). (4) Residuals after a fit of the spectrum by a simple quasar model made of a flat continuum and three emission lines with a Voigt profile shape. A simple Voigt absorption fit is performed on this residual and is shown with the green line.

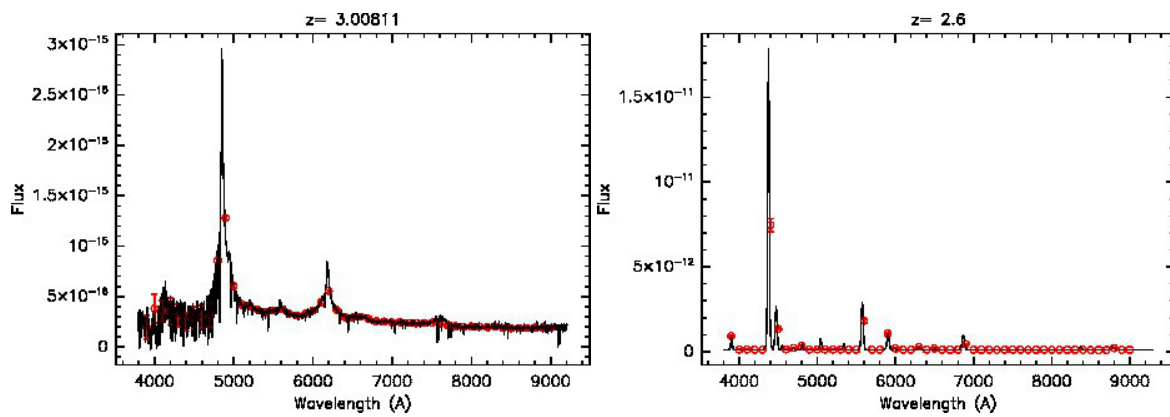


Figure 43: A QSO at $z = 3$ and a Seyfert-2 galaxy at $z = 2.6$ as they would be observed by J-PAS. The black line is the original spectrum at SDSS resolution and the red dots, with error bars, are the corresponding fluxes for the J-PAS narrow-band filters.

5. Scientific Goals III

5.1. Stars and the Galaxy

J-PAS is designed to obtain low-resolution spectroscopic of ~ 8000 squared degrees of the sky up to a limiting magnitude $R(AB) \sim 23.5$ with S/N ratio higher than 5. It can be considered the largest IFU survey ever carried out. Two different filter sets (12 for J-PLUS and 54+5 for J-PAS) define two distinct experiments with clearly differentiated telescopes and detectors and hence scientific goals, observational strategy, and timing. Between 200 and 500 million stars are expected to be listed in the final J-PAS catalogue which will provide one of the most detailed views of the Milky Way halo in the northern hemisphere sampled on 54 points of the optical spectrum.

5.1.1. Stellar Populations

Stellar populations, consisting of individual stars that share coherent spatial, kinematic, chemical, or age distributions, are powerful probes of a wide range of astrophysical phenomena. They describe different evolutionary stages, interior physics and phenomenology throughout the whole life of the stars, as well as the structure and evolution of different stellar systems.

The success of these studies will lie in the capability of J-PAS photometry to physically characterize the stellar populations and estimate their mean physical variables such as reddening, temperature, gravity and metallicity. Low resolution spectroscopy provided by J-PAS is what makes the difference compared to other photometric surveys such as SDSS, Pan-STARRS and LSST, and will allow a better taxonomy of the different stellar populations and a more accurate determination of physical properties. Experience acquired with the ALHAMBRA photometric system (Aparicio Villegas et al. 2010, 2011) will be very useful in defining the best strategy for characterizing the different stellar populations and to estimate their physical properties. Low-mass stars in the solar neighborhood; RR Lyrae variables that populate the thick disk and the halo, fantastic tracers of the structure of their respective Galactic subsystems; line-emission objects including planetary nebulae and cataclysm variables; and white dwarfs in a wide range of metallicities tracing the evolution time of different galactic subsystems – all these are, among others, good examples of the large variety of stellar objects that will be found in this survey.

RR Lyrae stars. Assuming the main halo metallicity $[Fe/H] = -1.5$ dex (Ivezić et al., 2008), RR Lyrae stars mean absolute magnitudes show very low dispersion $\langle M_V \rangle = 0.59 \pm 0.03$ (Cacciari & Clementini, 2003), so they can be used to measure distances and they are bright enough to be detected. For instance, SDSS has probed distances up to ~ 110 kpc (Sesar et al., 2010) with limiting magnitudes more restrictive than the present survey (see Sec 2.1), so the detection of this type of variable stars observed in different colors is conservatively expected (just considering the limiting magnitude 1 mag dimmer than that of SDSS) to occur at distances so far as ~ 190 kpc. Such detections have important implications on the formation history of our galaxy. At the same time, the survey will provide a large amount of SEDs that will significantly improve our understanding on the physics and the processes that take place at the interior of this kind of variable stars.

RR Lyrae stars are easy to identify by their characteristic light-curve, with periods from $P = 0.2$ days to $P = 1.2$ days, whenever it is sufficiently well-sampled. Nevertheless, they are expected to be identified in the survey by means of their color. RR Lyrae stars have been shown to be efficiently and robustly found in the past even with two-epoch data, using accurate multiband photometry obtained by the Sloan Digital Sky Survey (SDSS). The identification can even be feasible with single-epoch colors, due to the fact that RR Lyrae stars span a very narrow range of colors; e.g. for the SDSS (Ivezić et al., 2005):

$$\begin{aligned}
 0.99 &< u - g < 1.28 \\
 -0.11 &< g - r < 0.31 \\
 -0.13 &< r - i < 0.20 \\
 -0.19 &< i - z < 0.23
 \end{aligned}
 \tag{97}$$

Other ranges have been suggested more recently by Sesar et al. (2010). In that regard, a prediction on expected colors with the SDSS photometric system was conducted by Marconi et al. (2006). The approach of combining these color criteria and the, somehow limited, time-resolved observations will be adopted to look for this type of pulsating stars.

As it is well known, RR Lyrae have been demonstrated to be reliable tracers of the halo; as already mentioned, they are relatively bright and they obey a period-metallicity-luminosity relation (see Dambis et al. 2013; Catelan et al. 2004), so they can therefore serve as distance indicators, as well as kinematic and metallicity tracers. Some surveys for RR Lyrae stars (Sesar et al., 2010; Vivas et al., 2004; Ivezić et al., 2005) have already detected several substructures in the halo, and considering the extension that will be observed by J-PAS, 8500 square degrees, these observations will introduce strong constraints on the theoretical models and numerical simulations of the galactic halos formation (see e.g. Cooper et al. 2010).

The possibility of building a metallicity map of the galactic halo employing the J-PAS low resolution spectra will be explored. This is not straightforward due to the resolution of J-PAS spectra, and the changes undergone by the stellar spectrum with the phase of RR Lyrae’s oscillation coupled with the observation strategy of the survey.

RR Lyrae stars are not only bright stellar candles useful for drawing the structure of the outer regions of the galactic halo, but they represent unique probes for the study of stellar interiors and their response to internal perturbations. The observational strategy of the survey will provide 4 points, at least, per filter for all the stars in the sample, which will allow the discovery of new variables and a better coverage of the light curve for previously catalogued stars.

RR Lyrae stars populate the halo globular clusters. The mean pulsational period of cluster RRab stars (pulsating in the fundamental mode) is closely related to the metallicity of the cluster. If we represent the globular clusters into the $P(ab)$ vs. metallicity space they show a bimodal distribution forming two separated concentrations called Oosterhoff groups (Oosterhoff, 1939). Poor metal clusters present a mean fundamental period near to 0.65 days, while those with metallicity above -1.4 show a value of around 0.55, separated by a gap centered at 0.60 days. Although this phenomenon has been known for seventy years and there are numerous studies about the possible nature of this bimodality, its physical origin is still a matter of debate. The theoretical understanding of RR LyraeLyrae needs observations that not only cover the time domain but also the parameter space where this kind of pulsation is present. It is in this context that J-PAS will be unique in providing well sampled SEDs of these stellar pulsators.

White Dwarfs. White dwarfs are the end state of all main sequence stars less massive than $8M_{\odot}$, which means that 98% of all stars will end up as white dwarfs. First and foremost, J-PAS will allow us to discover many new white dwarfs. It will go deeper than SDSS; most of SDSS spectroscopically confirmed white dwarfs have a magnitude below 20.5, while J-PAS will be complete (5σ detections) down to 22.5 in each filter. So we should see white dwarfs 2.5 times farther than SDSS and therefore the total volume will be $(2.5^3 - 1 = 14.6)$ times larger. By definition every object in J-PAS will be spectroscopically observed, while in SDSS only chosen objects had their spectra taken, so our white dwarf sample will also be much more complete than SDSS.

White dwarfs in the J-PAS survey can be of great value for white dwarf studies as well as for other areas of stellar astrophysics:

1. Individual white dwarfs can be used as a distance indicator. Through analysis of their J-PAS multicolor and model stellar atmospheres, we can determine their T_{eff} and $\log g$. Using the well defined mass-radius relationship we can obtain a luminosity for these objects and therefore a distance. These distances can be very useful when the white dwarfs belong to a given star group.
2. In stellar groups we can use the cooling times of the coolest white dwarfs as an age indicator for the whole group. As the coolest white dwarfs come from the most massive main sequence stars, the main sequence lifetime for them is very short compared to the cooling time. White dwarfs can be used as chronometers in those cases when the coolest white dwarf in the group is detectable by J-PAS, which means the group distance modulus added to the absolute magnitude of the coolest white dwarfs is less than ≈ 22.5 , J-PAS magnitude limit. In particular we will scrutinize every open cluster within J-PAS coverage area in search of white dwarfs to determine their ages as well as to study the initial-final mass relationship.
3. Metal-line white dwarfs (DZ). These objects are associated with debris disk white dwarfs. Every white dwarf presenting a dust disk also presents metal lines. Currently 20 WDs are known to have infrared excess, and therefore a debris disk. About 100 WDs present metal lines in their spectra. J-PAS should allow at least an order of magnitude increase in the number of these objects.
4. White dwarf luminosity function (WDLF) in the halo and disk. The WDLF is of extreme importance to the studies of white dwarf physics, also as stated above it is very useful to date groups of stars, from open clusters ([Koester and Reimers, 1996]) to the Milky Way ([Winget et al, 1987], [DeGennaro et al, 2008]). The increase in the total numbers of white dwarfs obtained by J-PAS will allow a much improved WDLF of halo and disk white dwarfs as well as the luminosity function in clusters.
5. White dwarf mass function. The mass distribution of white dwarfs is closely related to mass loss for both single and binary stellar evolution. The large number of white dwarfs identified by J-PAS will allow us to improve the precision of the current white dwarf mass function.
6. Pulsating white dwarfs. J-PAS four visits to each field, times 56 exposures in all filters will allow us to search for variability among all the white dwarfs identified by the survey.

Cataclysmic Variables. Cataclysmic variables (CV) are an important component of the galactic population since they provide the closest and most abundant instance of accretion disks but are also a theoretical identified channel for the production of type I Supernovae. Estimations of the space density estimates of CVs vary. Cieslinski et al. (2003) suggested $\rho \leq 5 \times 10^{-7} \text{ pc}^{-3}$, for dwarf novae, the most common type of CV. The ROSAT North Ecliptic Pole Survey (Pretorius et al. 2007) gives $\rho = 1.1 \times 10^{-5} \text{ pc}^{-3}$. Rogel et al. (2008) adopt $\rho = 0.9 \times 10^{-5} \text{ pc}^{-3}$ in their model to predict the number of CVs in the galactic plane.

We adapted the Ortiz and Lapine (1993) Galactic star counts model to predict the high latitude counts of CVs. The luminosity function of Patterson (1998) purged from the super-soft sources was used in our estimate. We used $g = V - 0.14$ for a typical CV, and the very conservative assumption that the total density of CVs is $\rho = 1.0 \times 10^{-6} \text{ pc}^{-3}$. The corresponding cumulative counts (scaled to 8000 squared degrees) for $g < 22$ are ~ 600 and 200. Notice that these numbers would be ten times larger if the total density of CVs was $\rho = 1.0 \times 10^{-5} \text{ pc}^{-3}$, as in Pretorius et al. (2007) and Rogel et al. (2008).

Peculiar Stars Ap stars are chemically peculiar stars in, or just off, the main sequence. Their peculiarity is in the fact that they show a very high abundance of rare earth metals. We understand this phenomenon as being caused by radiative levitation from the inner core of an entirely radiative star. The existence of magnetic fields makes the radiative levitation deposit the rare earths close to the magnetic poles (Michaud, 1970, ApJ, 160, 641). The basic mechanism for the existence of these objects is understood; however, the reason why some A stars turn into Aps and others do not is still not known. Ap stars represent approximately 2% of all A stars, therefore we expect a large increase in the number of known Ap and other chemically peculiar stars. Statistic studies of such a large number of chemically peculiar objects will shed new light into their origin. In particular, studies relating the occurrence of Ap stars with the age of stellar groups, specially open clusters, are particularly important, as there is a possibility that the peculiarities increase in strength as the stars evolve.

J-PAS and metal-poor halo stars. In the J-PAS survey a great number of stars and minor systems will be also observed, which will provide a unique sample of galactic halo objects and will enable a deep study of the galactic structure and the halo stellar population. The stellar halo population is basically formed by stars of population II, which are old metal-poor stars, and the inferior limit of the distribution of metallicities of these stars is not defined yet. In fact, so far the poorest-metal old stars found are :

- The ultra-metal-deficient red giant CD-38 245 with $[Fe/H] = -4.5$ (Bessel & Norris 1984)
- The ultra-metal-poor and Carbon-rich HE 00557-4840 with $[Fe/H] = -4.75$ (Norris et al. 2007)
- The chemically ancient star HE0107-5240 with $[Fe/H] = -5.3$ (Christlieb et al. 2004)
- The most iron-poor star HE1327-2326 with $[Fe/H] = -5.6$ (Aoki et al. 2006)

These stars are in general giants and red subgiants with $V=13-15$ magnitudes, representing the extreme halo population II.

Some surveys with different characteristics from J-PAS did already study the galactic halo looking for metal-poor stars, such as the HK Survey (Beers et al. 1992), a low resolution spectroscopic survey developed with the 2.5m telescope, Du Pont, and centered on the HK line of Ca II; the Hamburg/ESO Survey (Wisotzki et al. 1996), a spectroscopic survey of QSOs that revealed white dwarfs, horizontal branch stars and metal-poor stars; or the Sloan Digital Sky Survey (SDSS, York et al. 2000) and its extension for the exploration of the galaxy SEGUE (Yanny et al. 2009) in operation from 2005 in the Apache Point Observatory. The success of these surveys incite the appearance of other new projects such as the SkyMapper (Keller et al. 2007), the counterpart of the SDSS in the South hemisphere, which began to operate in March of 2010 using a 1.35m telescope in the Siding Observatory and with a photometric system of 6 filters, 4 of them similar to the g, r, i, z SDSS filters, or the LAMOST project (Newberg et al. 2009) which was initiated in 2011 using a 4m telescope, and will provide low-resolution spectra for objects with $-10\text{degree} < \delta < +90\text{degree}$.

The 54 narrow-band filters of the J-PAS photometric system could be considered as a very low-resolution spectroscopy. With this idea in mind, the first approach for the study of these metal-poor stars will be done through the comparison of these observed “spectra” with theoretical J-PAS spectra from synthetic photometry, such as it is done in the methodology developed for the ALHAMBRA photometric system (Aparicio Villegas et al. 2010), the Q -Fit-Algorithm, a methodology for the estimation of the main physical stellar parameter (T_{eff} , $\log(g)$, $[Fe/H]$ and E_{B-V}) of stars of a great variety of spectral types and luminosity classes using reddening-free Q -parameters:

$$Q_{ijkl} = (m_i - m_j) - \frac{E_{ij}}{E_{kl}}(m_k - m_l), i = 1 : n - 3, j = i + 1, k = j + 1, l = k + 1 \quad (98)$$

where m_i is the magnitude in the band i of the photometric system of n bands, and E_{ij}/E_{kl} is the color excess ratio, which only depends on the interstellar extinction law.

In Aparicio Villegas et al. (2011) it can be found a brief resume of this method while a more complete paper is in preparation. Figure 44 presents an example of one of these possible fits using the 52 Q -parameters generated with the 53 correlative colors from the 54 J-PAS narrow-bands. The values of these Q -parameters are shown in the y-axis, while the x-axis is just the number of the Q -parameter in increasing order; red crosses are the Q -parameters of the star BD292091 of the Next Generation Spectral Library (NGSL, Gregg et al. 2004) and in black circles are represented the Q -parameters of one model from the theoretical library AMBRE (de Laverny et al. 2012); The main physical parameters of both, the star and the model, are described at the top of graph, together with the χ^2 value of the fit.

This methodology will be applied to the J-PAS narrow-band filter system in order to analyze the capability of this photometric system in the estimation of the main stellar parameters, such as was done for ALHAMBRA, but it can be also adjusted to be focused in classifying these metal-poor stars. For that task, it will be necessary the selection a priori of the filters which provide a greater information about the chemical composition of these objects; this could be handled with a qualitative criterion selecting the filters that contain absorption lines, like the lines of ionized Calcium at 3933Å and 3963Å, which are contained in filters JSCH3900 and JSCH4000, the molecule CH in 4300Å, situated in filter JSCH4300, the infrared triple of Calcium at 8498Å, 8542Å and 8662Å contained in filters JSCH8500 and JSCH8600, or the Magnesium line at 5183Å in filter JSCH5200. Or with a more statistical task, using PCA or generating linear regressions between color combinations and the values of stellar metallicity. The subset of filters chosen in each case would have a more weight in the fits in order to obtain more accurate metallicity determination.

Although this photometric system probably will not enable to determine the metallicity values of these stars with a spectroscopic accuracy, it will certainly allow the detection of these objects among all the other point-like objects that will be found in the J-PAS survey, and then a posterior high-resolution spectroscopic observation of these objects will be necessary to complete the study of their chemical composition and refine the results in metallicity with this methodology.

Halo post-AGB population: PNe and proto-PNe. The outer layers of the low- and intermediate-mass stars (0.8-8 M_{\odot}), which were enriched throughout their evolution, are ejected during the asymptotic giant branch (AGB) and post-AGB phases, and subsequently ionized by the remnant hot nucleus, forming the so-called planetary nebulae (PNe). Analysis of the ionization lines formed in the ejected envelopes of these evolved stars is one of the most important ways in which the chemical and physical characteristics of the gas are studied (for reviews, see Stasińska 2002; and Magrini, Stanghellini and Gonçalves 2012).

Such stars can be important sources of enrichment of He, N and C in the interstellar medium (ISM; e.g., Yin et al. 2010). Also, van den Hoek & Groenewegen (1997) and Marigo (2001) predicted theoretically the possibility that (PNe) progenitor stars produce O and Ne and dredge these elements up to the stellar surface - through the third dredge-up, TDU - resulting in enrichment of the ISM. The latter is a metallicity dependent effect, which happens mainly in low-metallicity environments (Pequignot et al. 2000; Magrini & Gonçalves 2009). In any case, PNe and their abundances are clearly important tools to study stellar evolution. By considering elements other than those just discussed, PNe can also reveal the imprint of ISM abundances when their progenitor stars were formed, in the Galactic as well as in the extragalactic context.

About 3,000 PNe are known in the Galaxy (Parker et al. 2012), and only a few, about 20, objects have been identified as halo PNe, from their location, kinematics and chemistry (see, for a recent ref., Otsuka et al. 2010). Halo PNe are able to reveal precious information for the study of low- and intermediate-mass star evolution and the early chemical conditions of the Galaxy.

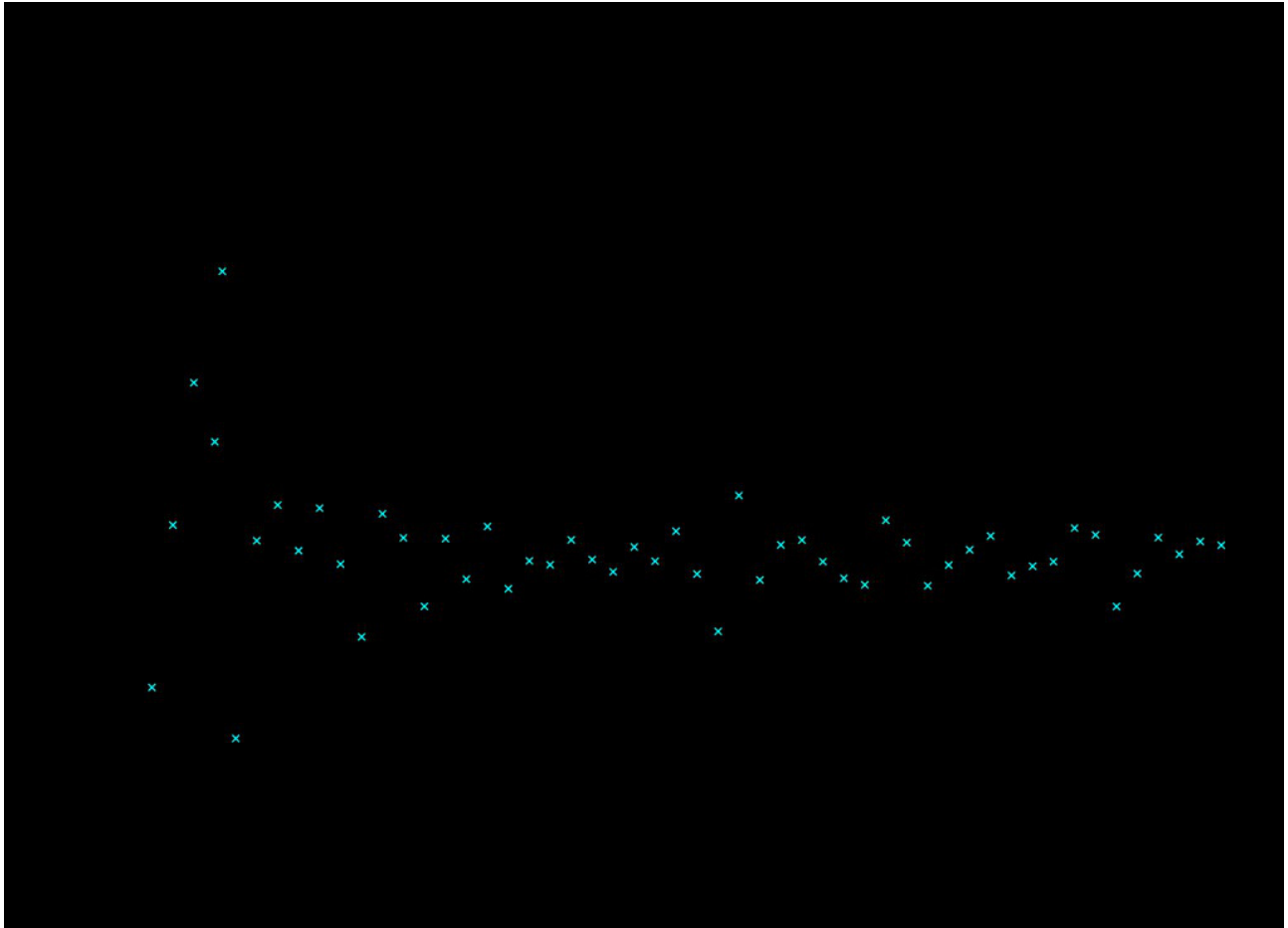


Figure 44: Example of fit using 52 Q -parameters generated with J-PAS synthetic photometry. Black circles corresponds to the Q -parameters of a model of the AMBRE library while the red crosses are the Q -parameters of the star BD292091 of the Next Generation Spectral Library. The main physical parameters of the star and of the model are described at the top of the graphic together with the χ^2 value of the fit.

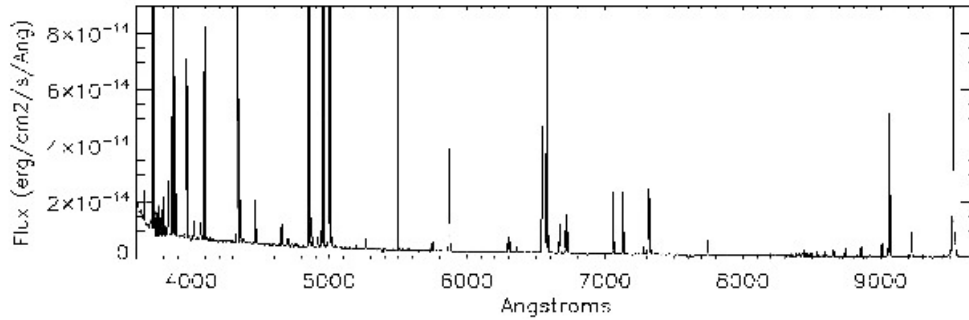


Figure 45: Observed medium-resolution optical spectrum of DdDm 1.

The progenitors of halo PNe are believed to be $\sim 0.8 M_{\odot}$ stars, as most of the stars of the halo. However, some halo PNe seems to have evolved from massive progenitors (Otsuka et al. 2010). According to the current stellar evolution models (e.g., Fujimoto et al. 2000) the TDU must take place in the late AGB phase. The TDU efficiency increases with increasing mass and/or decreasing metallicity. At halo metallicities, it is predicted that the TDU is efficient in stars with initial masses greater than $\sim 1 M_{sun}$ (Karakas 2010; Stancliffe 2010). Moreover, the stellar evolutionary models predict that the post-AGB evolution of a star with an initial mass $\sim 0.8 M_{\odot}$ proceeds too slowly for a visible PN to be formed. Therefore, clearly, the origin and evolution of halo PNe are still one of the unresolved big problems of stellar evolution.

So, interestingly enough from the point of view of the halo J-PAS survey, the study of the halo PNe - by determining their elemental abundances and ejected masses - will certainly enlighten not only the Galactic chemical evolution at early phases, but also our knowledge of the stellar evolution at environments other than the Galactic disk.

The characteristic low continuum and intense line emissions of PNe make them detectable at the halo distances. For example, the halo PNe BoBn 1, DdDm 1 and PS 1, located somewhere between 11 and 24 kpc from the Sun, have B magnitudes of 16, 14 and 13.4, respectively (Otsuka et al. 2010; Otsuka et al. 2009; Rauch et al. 2002). Such values are easily encompassed by J-PAS, since the typical limit magnitude of the survey will be about 22-23. Given the low number of halo PNe known so far, we plan a follow-up study for any possible candidate identified by the survey.

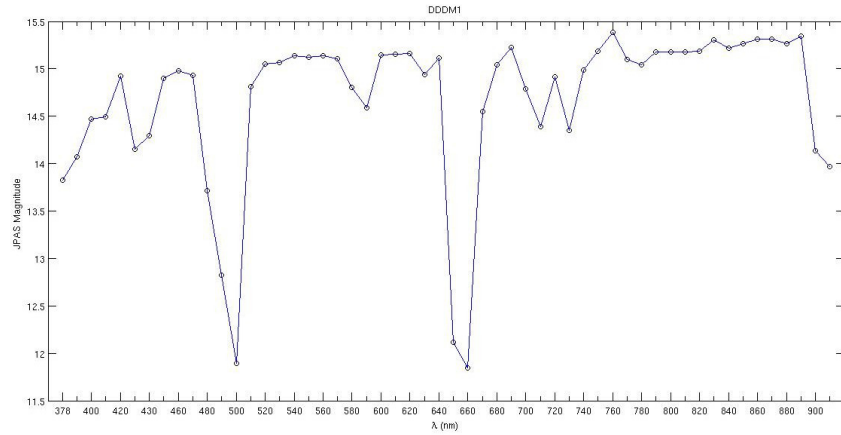


Figure 46: J-PAS convolved spectrum of DdDm 1 (J-PAS magnitudes versus wavelength).

To explore the possibility of using the J-PAS survey to detect halo PNe, we have convolved typical halo PNe spectra to simulate the corresponding J-PAS “spectrum” of these nebulae. In Figure 4.5 we show such a convolution, based on the medium-resolution optical spectrum of DdDm 1 (kindly provided by C. Pereira, and observed with the a configuration similar to that of Pereira & Miranda 2006), shown in Figure 45

From Figure 46 it is clear that the 54+5 J-PAS filters can easily detect the low-continuum, strong emission-line objects such as PNe. The intensity of the lines vary substantially with excitation, but using the halo PNe spectra available for our study so far, all of them are detectable by the J-PAS filter set.

There is another interesting class of post-AGB stars that is also likely detectable by survey, the proto-PNe. Theoretical calculations predict that post-AGB stars evolve with constant bolometric luminosity, while their radius shrinks and their effective temperature rises. When the temperature is high enough ($T_{eff} \sim 20,000$ K) to ionize the circumstellar nebula, the emission lines become detectable by spectral sky surveys, owing, first of all, to the presence of the H_{α} emission line. Hot post-AGB stars, or proto-PNe stars, are the immediate progenitors of the central stars of PNe. Hot candidate proto-PNe possess dust shells with temperatures ranging from 100 to 250 K, display spectra of early B-type stars with signs of a supergiant plus emission lines, and are usually located outside the Galactic plane (e.g. IRAS 19336-0400; Arkhipova et al. 2012).

On the other hand, in globular clusters, high luminosity F-G type post-AGB stars (yellow post-AGB) were observed. The most famous of those is RAO24 in Ω Cen (e.g., González & Wallerstein 1996). In the GC NGC5986, two A-F supergiants were discovered (Alves et al. 2001). Since the large Balmer jump of these stars is well traceable with a good choice of filters, more extensive specific surveys should discover post-AGB stars in the halo and external galaxies. Bond & Alves (2001) report upon the detection of yellow post-AGB stars in M31 and its dwarf elliptical NGC 205, yielding a good reproduction of the Cepheid distance to M31. Therefore, these stars are important as tracers of halo structure and dynamics, for studying advanced evolutionary stages of low-mass stars, and to provide new standard candle for measuring extragalactic distances.

We are now working on the construction of a grid of PNe and post-AGB nebular spectra, to widely prove their detectability using J-PAS photometry. Moreover, the latter can be better explored by applying appropriated color-color diagrams (Viironen et al. 2009), as well as performing the Q-fit algorithm, described in Aparicio-Villegas et al. (2010). The latter will provide the parameters (line ratios, for instance) that can distinguish these nebulae from other strong emission-line objects of the halo. Another important application of the synthetic grid of spectra we are creating is to identify the J-PAS filter ratios that can at least give limits to the abundance of the nebulae detected from the J-PAS spectra, even before the spectroscopic follow-up.

Hunting Tidal Stream Stars in the Milky Way with J-PAS. [a]

Within the hierarchical framework for galaxy formation (e.g., White & Rees 1978), the stellar bodies of massive galaxies are expected to form and evolve not only through the inflow of cold gas, but also via the infall and successive mergers of low-mass, initially bound systems (commonly referred to as satellites) that span a wide mass range. As a consequence, the stellar halos of these galaxies should contain a wide variety of diffuse structural features, such as stellar streams or shells, which result from interactions and mergers with dwarf satellites. The most spectacular cases of tidal debris are long, dynamically cold stellar streams, that wrap around the host galaxy's disk and roughly trace the orbit of the disrupted progenitor satellite.

Λ -CDM simulations predict that stellar streams may be detected nowadays, with sufficiently deep observations, in the outskirts of almost all nearby galaxies (Bullock & Johnston 2005; Cooper et al. 2010). Although the most luminous examples of diffuse stellar streams and shells around massive elliptical galaxies have been known for many decades (e.g. Arp 1966), recent studies have shown that fainter analogues of these structures are common around spiral galaxies in the local Universe (Martinez-Delgado et al. 2010), including the Milky Way (MW) and Andromeda (Belokurov et al. 2006; McConnachie et al. 2009).

Though it is now clear that these minor mergers likely played a prominent role in creating the halo of our Galaxy, the chemical abundance patterns of current MW "surviving" satellites are typically very different than those of halo stars (Venn et al. 2004), and the reason for these differences remains controversial (Majewski et al. 2002; Font et al. 2006). The J-PAS survey plans to test the bridge from dwarf galaxy to halo stars *directly* by exploring (for first time photometrically) the chemical trends of an extensive sample of M-star *bona-fide* members of known MW tidal streams (e.g. Sagittarius, Monoceros, Virgo). The membership of these stream stars was previously vetted by medium resolution radial velocity surveys. By selecting suitable J-PAS color indices sensitive to abundance patterns of the stream stars (e.g. $[\alpha/Fe]$), we plan to design a new method to identify new stream stars in the halo field and in the solar neighborhood and to search for abundance variations among known streams. This new census of stream stars will provide unprecedented information on the contribution of these merger events in the formation and chemical evolution of the Galactic halo.

5.1.2. *Additional topics*

Blue objects in the Galactic halo. Just to mention further details on the blue objects in the galactic halo: it would be nice to search for rare stars with B-type spectra (blue objects) in the halo and then select candidates for a spectroscopic follow-up in order to derive elemental abundances and then classify those objects as 1) B stars formed in situ; 2) runaway stars ejected from the disk; 3) evolved stars (BHB, hot post-AGBs, ..).

5.2. *Stellar Variability*

The timescale in which the brightness of astrophysical objects vary encompasses a considerably broad time-domain frequency range. These variations are observed with the most diverse shapes and amplitudes, sometimes affecting the entire electromagnetic spectrum, a specific band, a group of lines from chemical species or even a single line. In some cases the variability is periodic (such as on RR Lyr, pulsating stars and eclipsing binaries) but there are a number of cases where they are not (e.g. eruptive stars).

Despite the large amount of characteristics, the variability on astrophysical objects is classified either as intrinsic or extrinsic. Intrinsic variations are those related to changes in the physical properties of the object itself. These may be related to changes in the shape, temperature, instabilities and even magnetic properties which results in flux variability. Examples of intrinsically variable objects are solar-type and low mass active stars, pulsating stars, dwarf-novae, novae and supernovae. As the name suggests, extrinsic variations are those related to changes in the medium, surroundings or line of sight to the object. Eclipses and occultations in general are the classical cases of extrinsic variability.

Most variable objects display both types of variability and identifying and characterizing them is a fundamental step in understanding the underlying physics. These tasks are quite complementary and rely strongly on the observational strategy as well as on the properties of the variability itself (amplitude, period/recurrence and shape). Identifying a variable source is a much easier task than characterizing its variability. Usually, identification of a variable source requires only that the system is observed a sufficient number of times such that the scatter in flux, caused by variability, is larger than the scatter caused by uncertainty in the measurement. On the other hand, characterizing the variability - namely, obtaining periods/recurrence time, amplitude and shape - requires a much more detailed analysis. For instance, in case of periodic signals it is required that at least two cycles are observed with moderate time sampling (at least a 1/10 of cadence) in order to obtain reliable results.

As already mentioned, the J-PAS survey strategy will provide up to four epochs of observations in each of the 56 filters for each field, possibly separated by 20 – 30 days (see Section 3.4). In order to estimate the probability of finding variable sources with this setup we performed some Monte-Carlo simulations of variability detection and characterization. We separated the different types of variabilities into three groups;

Eclipsing binaries: In this case the variability is caused by occultation of one of the sources of the system by its companion. Since less light arrives at the observer when light is blocked, we observe a decrease in the flux of the system. A typical light curve of an eclipsing binary can be characterized by the duration and depth of the eclipses and the orbital period of the system.

Pulsating stars: Most commonly observed in RR Lyr and specific stages of white-dwarfs cooling evolution, pulsation is modeled by sinusoidal variations, single or multi-periodic, which are characterized by amplitude and period.

Transients: This type of variability may represent a vast class of objects, that display eruptive behavior. Here we can include solar and low-mass active stars during flares, dwarf novae and novae during eruption and much more. Also, supernovae may be considered as an eruptive event but this will be discussed in Section 3.4. Although the details in the shape of the variability can be quite different, it is possible to roughly model them by considering a simple two-parameter curve, represented by peak luminosity and a decay time (ΔT). The decay is modeled as a Gaussian, and therefore, the decay time is its FWHM. Since eruptive events are not periodic and may occur in the most different timescales we decided to considered only one such event for each run.

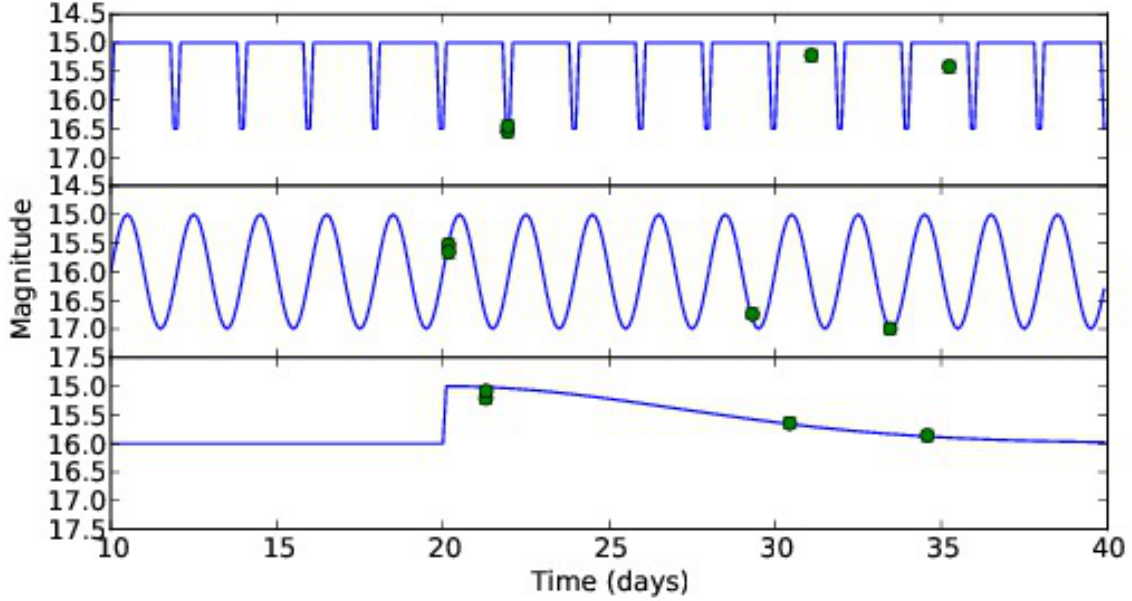


Figure 47: Example of model light curves (solid lines) representing the three types of variability used during the characterization of the survey strategy detectability efficiency. The points with error bars are the modeled observations, taking into consideration the survey strategy for each filter independently.

In Figure 47 we show an example light curve for each of these groups, with solid-lines representing the models and dots representing the observations. In order to estimate the detectability we generated a grid of light curves representing the three groups. For each light curve from a specific group we selected a different set of parameters, shown on Table 18. We then introduced uncertainty in the data to represent observations of stars with S/N from 5 to 220 (the saturation limit, http://jpaswiki.astro.ufsc.br/mediawiki/images/6/65/JPLUS_Exposure_Times.pdf).

Var. Type	Parameter	start	end	step	#
E	Orbital period	0.04 days	1.0 days	0.1 days	10
E	Orbital period	1.0 days	10.0 days	0.25 days	36
E	Eclipse Duration	0.01 $1/P_{orb}$	0.1 $1/P_{orb}$	0.01	10
E	Eclipse Depth	0.1 mag	1.0 mag	0.1 mag	10
P	Pulsation period	0.04 days	1.0 days	0.1 days	10
P	Pulsation period	1.0 days	10.0 days	0.25 days	36
P	Amplitude	0.01 mag	1.0 mag	0.02 mag	50
T	Decay time	0.04 days	1.0 days	0.1 days	10
T	Decay time	1.0 days	10.0 days	0.25 days	36
T	Amplitude	0.01 mag	1.0 mag	0.02 mag	50

Table 18: Set of parameters used to generate the model light curves for the detectability simulation. Note that the time grids, orbital/pulsation period and decay time, are separated in two sub-grids with different time resolution. This is important so we can better sample the lower end of the grid.

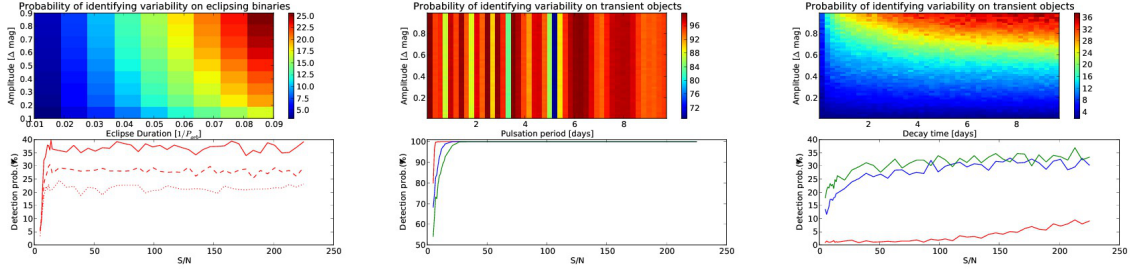


Figure 48: **Top panels:** Map of the averaged probability of detecting variability, obtained by the Monte-Carlo simulation. From left to right we show the results for eclipsing binaries, pulsations and transients, respectively (see text for details). These maps are averaged over S/N and, in the case of eclipsing binaries, also in orbital period. **Bottom panels:** S/N dependence of the identification probability for a set of parameters. For eclipsing binaries the solid, dashed and dotted lines are for orbital periods of $0.04d$, $1d$ and $9.5d$.

For each set of parameters and S/N we produced 1000 light curves with different observing epochs (following the observational strategy of four epochs, two back-to-back, another ~ 1 – and ~ 2 months subsequently), which resulted in a total of 9 200 000 simulated light curves. Finally, if the standard deviation of the modeled observations is larger than $3 - \sigma$ of the expected standard deviation, for each S/N (e.g. the magnitude of the object), it is possible to identify the variability of the target. By measuring the proportion between the number of targets for which variability is detected with those that are not, for each set of parameters, we estimate the probability of detecting variable sources.

The top panels of Figure 48 show a two-dimensional probability map of identifying variability for the three different types of light curves, for some selected set of parameters, and averaged over S/N. For eclipsing binaries, top left panel on Figure 48, we show the probability averaged over orbital period as well as on S/N. Here average probability ranges from $\sim 4\%$ in the worst case scenarios (shallow and short eclipses) to up to $\sim 25\%$ in the best cases (deep and long eclipses). The case is much better for pulsating binaries where (top middle panel on Figure 48) where we obtain virtually 100% detection probability for a large number of cases. Surprisingly, there is very little dependency of detecting pulsating objects with respect to the amplitude of the pulsation and a very strange pattern behavior with respect to pulsating period. This is likely to be caused by some sort of resonance between the observations and the pulsating period. For transients, the case is much similar to that obtained by eclipsing binaries where we have better average probability of finding large-amplitude and slow-decay events than finding small-amplitudes fast-decay, namely $\sim 36\%$ and $\sim 3\%$ respectively.

As expected there is a strong dependency with respect to the S/N of the data, as can be seen on the bottom panels of Figure 48 for some selected set of parameters. For the eclipsing binary case, bottom left panel, the different curves are for different orbital periods and same eclipse depth and relative eclipse duration. Here the solid lines are for a $0.04d$ orbital period, and has the larger identification probability. As can be seen, shorter orbital period (which means more frequent eclipses) results in easier variability identification. Typically, the detectability is practically zero for $S/N \lesssim 10$, increasing sharply between $10 \lesssim S/N \lesssim 20$ and then asymptotically for higher S/N.

Furthermore, in our simulations we considered only the observations of a single filter. It is not straightforward to consider the impact in the identification probability for observations of each target in all the 56 filters. The easiest approach would be to consider the observations individually. In this case the result would be more or less to increase the detection probability with the square root of the number of filters, e.g. a factor of $\sim \times 7$. A more refined analysis could be to evaluate the impact of variability on each filter for each kind of object. This task is very object-specific and which is beyond the scope of this work.

Overall, and even though the J-PAS survey was not designed for discovering variability, it will definitively provide means to identify a huge amount of sources. Most importantly, even though the variability in those cases won't be characterized (amplitudes, periods, etc.) the sources themselves will have a low resolution J-PAS spectra. This means that, in most cases, it will be possible to characterize automatically the source of the variability making the follow-up work much easier.

5.3. Minor planet science with J-PAS

The observation of a large number (tens of thousands) of minor planets is an added science bonus to large sky surveys like J-PAS. There are basically two science cases for minor solar system bodies observed in such surveys: the detection of previously unknown bodies, and characterization of the physical properties of those bodies.

5.3.1. Detection

The efficiency of the first science case is highly dependent on the cadence of the survey. However, even with the cadence constraints imposed by the main goal of the survey, J-PAS images would still be useful for detection of minor bodies. The 2+1+1 observation strategy that is to be adopted for most of the survey has implications for its ability to detect and track minor bodies.

During a visit, a pointing position will be imaged repeatedly for 16 (single exposures) or 30 minutes (double exposures), with individual exposures of 60 seconds. Therefore it will be possible to detect main belt and near earth objects within each visit. Slow-moving objects, like TNOs, on the other hand will be detected by comparing positions of the objects on the subsequent, one-month apart, visits. Considering all filter trays, each pointing position will be visited 13 times during the 7 years of the survey.

The individual frames, taken at different filters, have all limiting magnitudes around $m_{AB} = 22.1$ for single visits and $m_{AB} = 22.5$ for the visits with two exposures per filter. This last value is close to the detection limit of the PS1 Pan-STARRS telescope (Jedicke et al., 2007). However, the cadence of Pan-STARRS and other synodic surveys makes them more efficient than J-PAS for the discovery of minor bodies. That said, J-PAS can play an important role in the discovery of minor bodies in general and potentially hazardous objects in particular, since at this time the efforts to discover asteroids are based on observations made mostly in North America and Hawaii, with no major detection facility operating on Europe. Taken together with the detections of other surveys, the observations of minor bodies provided by J-PAS can significantly improve the chance of detection of potentially hazardous objects.

5.3.2. Physical properties: phase parameters

The variation of the observed magnitudes of minor bodies - phase curves - is a function of both the texture and of the composition of their surfaces. It is an important parameter, which however is still not known accurately for most objects.

The phase curve can be measured using the reduced magnitude ($M_\lambda(1, 1, \alpha)$, i.e., calibrated magnitude of the moving object, corrected from distance to the Sun (r) and Earth (Δ) against the phase angle (α).

The reduced magnitude is easily obtained as $M(1, 1, \alpha)_\lambda = M_\lambda - 5 \log(r\Delta)$, while α is the angle, on the moving object, that subtends the distance Earth-Sun, readily obtained from the object's orbital data. The technique is fairly simple: Observe calibrated magnitudes for different angles α and fit the widely used $H - G$ relationship (Bowell et al., 1989)

$$H_\lambda = M_\lambda(1, 1, \alpha) + 2.5 \log((1 - G)\Phi_1(\alpha) + G\Phi_2(\alpha)),$$

where H_λ is called the absolute magnitude, Φ_i are known function of the phase angle, and G a free parameter. Note that H_λ is $M(1, 1, 0)_\lambda$, an impossible geometrical configuration.

The absolute magnitude is related to both size, D , and geometric albedo, p_λ , of the moving target through

$$D [km] = C_\lambda \times 10^{(3-H_\lambda/5)} p_\lambda^{-0.5}$$

, where C_λ is a known constant. Thus obtaining a large number of H_λ will allow us to impose constraints on the size distribution of the populations of minor bodies.

Typical ranges of phase angles for minor bodies are many dozen degrees for Near Earth Objects, a few dozen degrees for Main belt asteroids, and no more than ten degrees for Centaurs and trans-Neptunian objects. In this last case the $H - G$ relation could be simplified to

$$H_\lambda = M_\lambda(1, 1, \alpha) + \beta\alpha$$

(Rabinowitz et al., 2008, see) because it reaches a nearly-linear region.

The cadence of J-PAS (2+1+1) spread in time could allow to obtain phase curves for TNOs and Centaurs provided they do not escape the field. In principle we will only have a maximum of three points in three different position which can then be fitted using the simplified version of the $H - G$ relationship. For other populations, with larger non-sidereal motions, we will rely on serendipitous observations of the same object in (likely) different fields in the same filter and, in this case, fit the full $H - G$ relation due to the, probable, larger span in phase angle coverage.

5.4. A target of opportunity program for the T80: Responding to GRB alerts provided by Swift and FERMI

The T80 mount reaches a maximum angular speed of $8^\circ/s$ with an acceleration of $1^\circ/s^2$, so it can point towards any sky direction in less than ~ 50 seconds. This makes the T80 telescope very suitable to respond to rapidly fading objects, mostly Gamma-Ray Burst (GRBs). To this end, it will be necessary to connect the T80 control system to the Gamma-ray Coordinates Network (GCN¹⁸) through a dedicated socket. The time necessary for the *Swift* high-energy satellite (Gehrels et al., 2004) to detect a GRB and disseminate its coordinates through the GCN network is ~ 15 seconds for observatories sited in the Iberian Peninsula (Jelínek, 2012). Therefore the T80 telescope could start acquiring data at most ~ 65 seconds after the GRB is detected.

The error boxes provided by *Swift* seconds after the GRB have error boxes radii of a few arc minutes, so they are well covered by the T80 field of view. In order to reduce the chip read out time (the $10k \times 10k$ CCD takes 20 second to read out) the detector could be windowed around the *Swift* GRB error box. One of the most interesting aspects of the T80 poses on its capabilities to respond also to alerts coming from *FERMI(LAT)* and *IPN* spacecraft. The large field of view of the T80 would cover most of the *FERMI(LAT)* and *IPN* error boxes with a single pointing, avoiding inefficient mosaics.

The GRB observations would be carried out through the *griz* SDSS filters that would be always mounted at the T80. Just after the GCN notice has arrived, a series of *griz*-band loops will be activated at the T80. The typical exposure time of the first loop would be of $\sim 15s$, $\sim 20s$, $\sim 30s$ and $\sim 60s$ in *griz* bands, respectively. These exposure times would yield AB limiting magnitudes of ~ 22 in *gri* and 21.3 in *z*-band, respectively (assuming S/N ratios of 5 in all bands, a seeing of $0.7''$, airmass=1.1 and dark time). Given that the optical source is expected to fade, the exposure times of the following loops would be enlarged. Thus, in each band, the exposure time of the subsequent n -th loop will be obtained scaling the exposure time of the first loop by a $(t_n/t_1)^2$ factor (being t_n and t_1 the time elapsed from the n -th and first loops to the gamma-ray event, respectively). This strategy is designed to keep roughly constant the S/N ratio of afterglows.

The combination of these deep *griz*-band limits with the T80 low reaction time are consistent with detecting a large fraction of the afterglows' population (see the compilation of light-curves by Kann et al., 2010, 2011). The afterglows detected in the *griz*-bands with the T80 would allow to test the spectral indexes and light-curves predicted by both the reverse (Meszaros & Rees, 1997) and forward shock scenarios (Sari et al., 1998).

¹⁸<http://gcn.gsfc.nasa.gov/>

For long lasting GRBs (durations > 1 min) the rapid T80 slewing capabilities could enable us to detect also the prompt optical flash contemporaneous to the gamma-ray emission (Piran, 1999). The non detections would also be useful to constrain the population of dark GRBs (Jakobsson et al., 2004) and their host galaxies (Rossi et al., 2012).

Considering the current GRB detection rate by *Swift* (~ 90 GRBs/yr) and assuming the real-time GRB visibility of Calar Alto ($\sim 20\%$ based on a close geographical location, Gorosabel et al., 2010, 2012), we expect ~ 18 GRBs/yr occurring at Javalambre's night. If we add the GRBs detected by *FERMI(LAT)* we would expect ~ 19 GRBs/yr. Taking into account the number of nights with clouds less than 50% (Moles et al., 2010) we foresee to acquire prompt data for ~ 12 GRBs/yr.

It is interesting to note that for GRB redshifts in the $3 \lesssim z \lesssim 6.5$ range, the Lyman- α dropout would be covered by the *griz* bands, so a rough redshift estimate could be possible in the first hours after the GRB, as done in the past (Haislip et al., 2006; Tagliaferri et al., 2005; Salvaterra et al., 2009; Tanvir et al., 2009). That would allow rapid and efficient triggers at large aperture telescopes (GTC, VLT,...) in order to determine spectroscopic redshifts based on afterglow metallic absorption lines (Fynbo et al., 2009).

We do not discard that the T80 could also be triggered by other high-energy events that might mimic GRBs, as already happened in the past with Magnetars (GRB070610/ SwiftJ195509.6+261406, Castro-Tirado et al., 2008), tidal disruption events (GRB110328A/ SwiftJ164449.3+573451, Levan et al., 2011), thermal high-energy mergers (GRB101225A, Thöne et al., 2011) or bright X-ray transients (GRB120916A/ SwiftJ174510.8-262411, Muñoz-Darias et al., 2013). In the future we might also implement T80 activations to high-energy/gravitational-wave alerts provided by *FERMI(GBM)*, *LIGO* or *VIRGO*.

6. Photometric calibration

Large scale structure analysis is very demanding on the homogeneity of the photometry on the whole area of the survey. This imposes strong requirements on the relative and absolute photometric calibration of the J-PAS photometry.

Large sky surveys carried out with large field of view cameras like J-PAS have to face a series of difficulties in their quest for obtaining accurate and homogeneous photometry. Some of the problems are connected with the instrumental setup and others are related with the variability of the observing conditions along the duration of the whole survey, which is of the order of several years in the case of J-PAS.

Among the problems connected with the instrumental setup that have to be controlled and corrected as much as possible we can list the following ones:

- Difficulties in obtaining suitable flat-fields. Given the large field of view, it is difficult to obtain homogeneously illuminated screens for dome flat-fields whereas for sky flat-fields taken at twilight the problem is the gradient of the sky illumination.
- Plate scale variations. Variations in the plate scale (or solid angle subtended by single pixels) from centre to edge introduce photometric distortions.
- Variations of the point spread function (PSF) along the whole camera. Although JST and JPCam have been designed from scratch to meet the best image quality in the whole focal plane, it is expected that some residual variations of the PSF will remain. They have to be taken into account when performing object photometry.
- Variations in the transmission curves of the filters. A particular problem in J-PAS connected with the large format of the narrow band filters is the presence of variations of the central wavelength across the filter. This means that objects at different positions on the filters are seen through slightly different bandpasses.
- Pupil ghost. J-PAS filters are very narrow and, therefore, reflect most of the incident light, this light reaches the field corrector and is reflected back to the camera but, generally speaking, on to a different filter with a different bandpass, hence allowing the corresponding wavelength range to pass to the CCD, creating a pupil ghost. After having detected this problem, several changes have been introduced in the manufacturing of the filters, the coating of the field corrector and the distribution of the filters in the filter trays which have almost, but not totally, eliminated this effect.
- Temporal variations of the performance of the different components (CCDs, filters, mirror coating,...). The stability of the system is another important factor in reaching an homogeneous final photometric catalog. Any change in the properties of any of the components either in the optical path or the detectors will be translated in a change in the effective transmission of the overall system and, hence, it will impact the photometry of the objects. Periodical tests of the performance of the different elements will help to control and mitigate these variations.

Many of these problems are dealt with during the reduction process (flat-fielding, photometric flat), nevertheless, some residuals should be taken into account in the calibration process.

Other problems related with the observational conditions are well known:

- Variations of the transparency of the atmosphere. They can appear, with different intensity and wavelength distribution, as a result of changes in the concentration of particular molecules (O_2, O_3, H_2O) in the atmosphere, dust concentration, or even barometric variations. To illustrate the importance of these effects, Padmanabhan et al. (2008) blame “the unmodeled atmospheric variations at Apache Point Observatory” as the main culprit of the limiting errors that they obtained in their ubercalibration of the SDSS data.
- Variations in the sky brightness. Observations at different moon phases will have different depth with equal exposure times just because of the reduction of the signal to noise due to the increase in the background flux.
- Seeing variations. The quality of the sky above the OAJ in the Pico del Buitre is superb with a median seeing of $\approx 0.5''$, but our observations will span a wide range of different seeing conditions and they have to be combined in an optimal way to impact as little as possible the quality of the photometry.

Finally, the ability of the photo-z codes to obtain accurate photometric redshifts or the success of any spectral fitting procedure depends on the absolute calibration of the photometry (although in many cases what really matters is the relative calibration between filters, i.e.. the accuracy of the colors). This means how accurate is the transformation from the observed instrumental magnitudes to calibrated magnitudes, which in the case of J-PAS are AB magnitudes. AB magnitudes are defined as (Oke, 1974; Bessell & Murphy, 2012):

$$m_{AB} = -2.5 \log \frac{\int f_{\nu}(\nu) S(\nu) d\nu / \nu}{\int S(\nu) d\nu / \nu} - 48.60 = -2.5 \log \frac{\int f_{\lambda}(\lambda) S(\lambda) \lambda d\lambda}{\int S(\lambda) \lambda d\lambda} - 48.60 \quad (99)$$

where $f_{\nu}(\nu)$ is the observed absolute flux in $\text{erg cm}^{-2} \text{s}^{-1} \text{Hz}^{-1}$, $f_{\lambda}(\lambda)$ is the observed absolute flux in $\text{erg cm}^{-2} \text{s}^{-1} \text{\AA}^{-1}$; and $S(\nu)$ and $S(\lambda)$ is the transmission curve from energy flux to photon flux. The advantage of the AB system is that magnitudes are directly related with the flux in physical units while other systems, as the Vega magnitudes, are based on the arbitrary fixed value set for the reference source (in that case, the magnitudes of the star Vega or α Lyr).

In practice, the calibration of the photometry, i.e.. the computation of the transformation from the instrumental magnitudes to the calibrated ones or, equivalently, the computation of the zero points, is based on the observation of standard stars (i.e.. stars with known calibrated magnitudes) allowing to compare their instrumental magnitudes with the calibrated ones and, afterward, applying the found zero points to the rest of objects with unknown calibrated magnitudes. Traditionally, this has been done interleaving observations of the target fields with observations of standard stars. However, several reasons make this procedure unfeasible for a project like J-PAS:

- Filters in the J-PAS filter system are non standard filters. This means that there aren't catalogs of standard stars available like there are, for example, for the Johnson system (Landolt, 1992, 2009) or the SDSS system (Smith et al., 2002). The only alternative is to use spectrophotometric standard stars (SPSS) to perform synthetic photometry (Howell, 1986). However, SPSS are scarce and even scarcer those that have spectrum available in the whole J-PAS wavelength range. This will improve in the near future thanks to the sample of SPSS that it is being compiled for the *Gaia* survey (Pancino et al., 2012). However, still the density of SPSS will be very low and this would mean that the telescope would have to move large angular distances from target fields to the closest SPSS and this is highly not recommended if one wants to keep the optical system as stable as possible.
- Many of the SPSS are quite bright for a 2.5m telescope.
- Large CCDs and large FoV cameras are prone to spatial variations of their sensitivity, and therefore, one would need to map that variation with the SPSS in order to calibrate different areas of the focal plane.

Already with the SDSS, it was realized that the photometric calibration of large sky surveys should rely on auxiliary systems (like the Photometric Telescope of the SDSS, Hogg et al., 2001). Also the experience of the SDSS has shown that the problem of calibrating a large survey with a lot of overlapping exposures can be split in two steps: first, a relative calibration of the overlapping exposures or ubercalibration (Padmanabhan et al., 2008); and then an absolute calibration which, in an ideal case, would be just a common zero point for all the objects in the survey. This procedure has been already applied in current large survey like Pan-STARRS1 (Schlafly et al., 2012).

The calibration procedure that J-PAS will incorporate try to overcome most of the difficulties described above using a mixture of the techniques already applied in SDSS and other large surveys. First, an auxiliary smaller telescope (an 83cm aperture telescope named Javalambre Auxiliary Survey Telescope or JAST) with a large field of view camera will image in advance the same area covered by J-PAS using a special set of filters. The goal of this preliminary survey will be to identify and classify millions of stars that will serve as secondary standard stars (SSS) for J-PAS. This preliminary survey will allow to perform other kind of scientific studies, especially of galaxies in the local universe, and has been named **Javalambre Photometric Local Universe Survey** or **J-PLUS** (see Section 6.1). With these SSS we will be able to calibrate each single exposure of J-PAS as well as tiles made of a combination of exposures. When a enough large area of J-PAS has been observed in any filter with at least 4 exposures, we will apply the ubercalibration to homogenize the relative calibration in that filter. Given the particular disposition of the filters in the JPCam, this situation will happen with at least 14 filters close in wavelength. This fact in combination with the use of SPSS falling in the observed area, will be used to tie the relative calibration between filters. And additional technique that will be used is that of the stellar locus in the version developed by Kelly et al. (2012). Finally, during the computation of the photometric redshift, another tool that will help to improve the photometric calibration (for photo-z estimation) will be the procedure developed by Molino et al (2014), who making use of the galaxies identified as emission line galaxies by the BPZ code Benítez (2000) compute offsets in the zero points which improve the resulting photo-z's providing values close to those obtained calibrating with a sample of spectroscopic redshifts.

In the following sections we will describe in more detail the key points in the calibration procedure for J-PAS.

6.1. Calibrating J-PAS with J-PLUS

6.1.1. Description of J-PLUS

The **Javalambre Photometric Local Universe Survey (J-PLUS)** will be a preliminary survey that will be carried out from the OAJ with the main goal of producing a catalog of millions of stars in the same area of J-PAS with accurate spectral type and, hence, accurate synthetic J-PAS magnitudes. As a side effect, the data resulting from J-PLUS will be used for many other astrophysical research with particular attention in the study of galaxies in the local Universe.

J-PLUS will be carried out with a 83cm-aperture telescope (the *Javalambre Auxiliary Survey Telescope* or *JAST*) with a field of view of 1.7° (diameter) with full performance and 2.0° if some vignetting is allowed. The camera mounted in the telescope (T80Cam) will have a large format CCD providing a plate scale of $0.55''/\text{pixel}$.

The key feature of J-PLUS will be the set of filters. The J-PLUS filter system (J-PLUS FS, hereafter) will consist of 4 Sloan filters (g, r, i, z) and 8 especially designed filters with different purposes:

- an u_J filter which is a modification of the Sloan u for better performance at these wavelengths;
- 5 filters located in particular absorption features: Ca HK lines ($\lambda_c = 3950\text{\AA}$), H δ ($\lambda_c = 4100\text{\AA}$), G band ($\lambda_c = 4300\text{\AA}$), Mgb-Fe band ($\lambda_c = 5150\text{\AA}$) and Ca Triplet ($\lambda_c = 8610\text{\AA}$);
- 2 filters in two regions directly related with the star formation in local galaxies: [OII] ($\lambda_c = 3780\text{\AA}$) and H α ($\lambda_c = 6600\text{\AA}$).

The election of filters located in the absorption features was based on the preparatory work for the *Gaia* survey (Jordi et al., 2006) in which it is explained how these bands and combinations between them can be used to determine different stellar parameters.

Meanwhile, the [OII] and H α filters were selected for studies of the star formation in galaxies in the local Universe. Be aware that the filter at $\lambda_c = 5150\text{\AA}$ can be used also for this purpose for galaxies with $0.001 < z < 0.0485$ using the [OIII] line at $\lambda = 5007\text{\AA}$.

Monte Carlo simulations with a library of theoretical stellar spectra have shown that with S/N per filter larger than 50 it is possible to recover the spectral type with enough accuracy.

The exposure times on the J-PLUS filters have been chosen to reach at least $m_{AB} = 18$ with S/N=50 in all the filters. For some filters with additional scientific value, apart from the calibration purposes, we have increased the exposure times:

- For the u_J we aim to reach $m_{AB} = 23$ with S/R=3.
- For g and r we will reach $m_{AB} > 23.2$ (S/N=3). For these 2 filters we will obtain 3 sets of 3 additional exposures with a time gap between each set of one week. This will help to study transient objects and to reach higher depth.
- For H α filter we will aim to $m_{AB} \sim 22.6$ (S/N=3).
- For i band the goal is $m_{AB} \sim 22.3$ (S/N=3).
- For z band the goal is $m_{AB} \sim 21.5$ (S/N=3).

6.1.2. Calibration of J-PLUS

The J-PLUS survey strategy will be focused on minimizing the variation of observing conditions of all the exposures on the different filters in each single pointing. For this reason, the imaging of each patch of the sky will consist of series of 3 exposures with small dithering in each filter (except additional exposures in the g and r filters that will be done at three additional epochs to detect transient objects).

The calibration of the J-PLUS images will rely on several exposures each night of one or more spectrophotometric standard stars that will be used to set the photometric zero points. In principle, the determination of the atmospheric extinction coefficients could be done with the same SSS given that they are observed at different airmasses. However, we decide to use an specific extinction monitor system. The next section describes the procedure used to determine the atmospheric extinction coefficients.

6.1.3. Determination of the atmospheric extinction

The monitoring of the atmospheric extinction is one of the key issues in the current era of large sky surveys. Padmanabhan et al. (2008) point out the unmodeled variations of the atmospheric conditions as the main source of the remaining uncertainties of the ubercalibration that they applied to the SDSS DR8 data.

The main components affecting the transmission of the atmosphere in the optical wavelength are three (Hayes & Latham, 1975):

- Rayleigh scattering.
- Absorption by molecules, in particular ozone and water.
- Mie scattering by small aerosol particles.

They have different dependence with the wavelength and with different atmospheric parameters. For a given location we can simplify their functional dependence with the wavelength like this:

- Rayleigh scattering: $\kappa_R \sim \lambda^{-\alpha_R}$
- Ozone absorption: $\kappa_O \sim k_O(\lambda)$.
- Aerosols scattering : $\kappa_{ae} \sim \lambda^{-\alpha_{ae}}$

where κ are the extinction coefficients of each component, α_R and α_{ae} condense the wavelength dependence of the Rayleigh and aerosols scattering and $k_O(\lambda)$ is the shape of the ozone absorption band. Once α_R , α_{ae} and $k_O(\lambda)$ are determined for a given location they are assumed to be constant or with a small temporal variation. The determination of the wavelength dependence of each component can be done observationally taken spectra of stars with known spectra outside the atmosphere or can be modeled using a code of atmospheric radiative transfer with the suitable parameters¹⁹.

The total atmospheric extinction curve will be the combination of these 3 components (see Fig. 49):

$$\kappa_{Total}(\lambda) = A_R \lambda^{-\alpha_R} + A_O k_O(\lambda) + A_{ae} \lambda^{-\alpha_{ae}} \quad (100)$$

The coefficients A_R , A_O and A_{ae} represent the relative importance of each component and their variation will be the responsible of the changes in the overall atmospheric extinction. In the case of A_R the main factor affecting it would be the local atmospheric pressure while for A_O and A_{ae} will be the concentration of ozone and aerosols in the atmosphere.

The task of the extinction monitor will be to allow the determination of the three parameters A_R , A_O and A_{ae} .

Currently, we have installed in the OAJ an extinction monitor developed by Dr. J. Aceituno called EX-CALIBUR (*EXtinction CAmera and LumInance BackgroUnd Register*). This consists on a commercial 11" aperture telescope with a SBig ST10 2184×1472 pixels camera and a set of 10 filters. The filter set includes Sloan u,g,r,i and 6 additional medium band filters at centered at wavelengths 4250Å, 4800Å, 5200Å, 5900Å, 7000Å and 8700Å. The goal of this set of filters is to suitably sample the atmospheric extinction curve.

¹⁹An example of open source radiative transfer code is libRadtran (<http://www.libradtran.org/>).

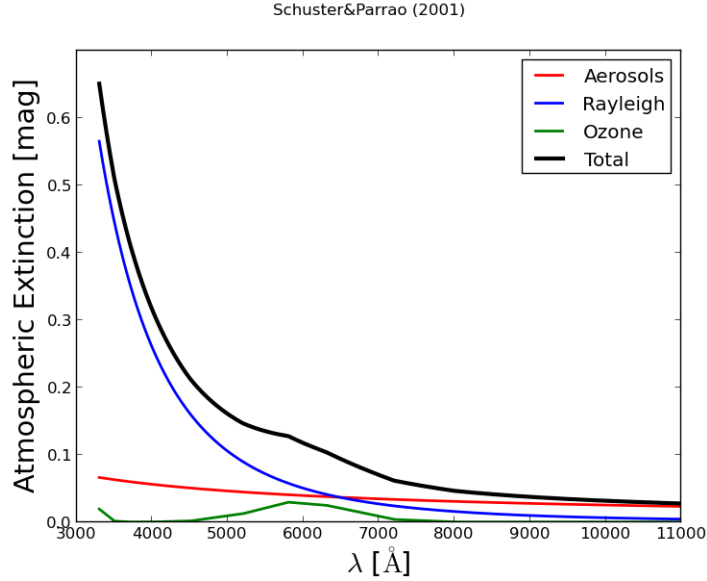


Figure 49: Illustration of the 3-components atmospheric extinction curve derived from Schuster & Parrao (2001). The blue, green and red lines corresponds to the three components: Rayleigh scattering, ozone absorption and aerosols' scattering. The black line is the total combined absorption.

The nightly procedure will consist in the observation of standard stars at different airmasses with the full filter set. This will allow to compute the extinction coefficients in each of the bands corresponding to the filter set. Then, Equation 100 will be fitted to the observed extinction coefficients and the fit will provide the nightly values of A_R , A_O and A_{ae} and, therefore, characterizing the nightly atmospheric extinction curve.

Once $\kappa_{Total}(\lambda)$ is known, it is possible to obtain the extinction coefficients in any other band like those of J-PLUS or even J-PAS (although some filters of the J-PAS will be highly affected by narrow absorption telluric lines, especially from water, that cannot be determined with this procedure).

6.1.4. Stellar spectral fitting

At the end of J-PLUS we will have absolute calibrated photometry in the J-PLUS filter system (FS) for millions of stars in the same area as J-PAS. However, except for the $H\alpha$ and the [OII] filters, J-PLUS FS and J-PAS FS are different and we need a way to transport the calibration in the J-PLUS FS to the J-PAS FS. To do this we will rely on the spectral fitting of the J-PLUS photometry of the SSS with a library of stellar spectra. Nowadays, there are several empirical and theoretical stellar libraries that can be used for this task. Empirical libraries like Pickles (1998) and MIUSCAT (Vazdekis et al., 2012; Ricciardelli et al., 2012) have the advantage of being based on real data, however, they don't cover the parameter space as much as the theoretical libraries like those of Coelho et al. (2005). Simulations will be carried out to check which one of the two possibilities or even an hybrid solution provide the most reliable reconstruction of the real spectra of the stars from the J-PLUS photometry.

The output of the spectral fitting will then be used to compute the synthetic magnitudes in the J-PAS filter system.

6.1.5. Calibration of the J-PAS exposures

The final calibration of the J-PAS exposures will be done identifying the SSS from J-PLUS in each J-PAS exposure. The zero point for each exposure will be a robust average of the difference between the synthetic magnitudes of the SSS and their instrumental magnitudes:

$$ZP = \langle m_{synth}^{SSS} - m_{instr}^{SSS} \rangle \quad (101)$$

In the construction of the final tiles in which several different exposures are combined, instead of calibrating each single image independently, the procedure will consist in, first, matching the flux of all the exposures using stars in common in different exposures (given the survey strategy this is more complex than just combine 4 exposures), and after the combination it will proceed with the calibration of the final tile using the same procedure as with the single exposures.

6.2. Improvements to the J-PAS calibration

With the advent of large sky surveys, and especially the SDSS, new procedures to improve the overall calibration of the survey have been developed. Two of these have been already applied with success and will be included in the calibration procedure of J-PAS: the ubercalibration (Padmanabhan et al., 2008) and the stellar locus (High et al., 2009). And additional procedure developed by members of the J-PAS team within the ALHAMBRA project will also help to improve the final quality of the photometric redshifts provided by J-PAS (Molino et al, 2014).

We describe briefly each of these procedures below.

6.2.1. Ubercalibration

The ubercalibration (Padmanabhan et al., 2008) is an *a posteriori* calibration procedure which takes advantage of the overlapping of many exposures in the survey. The result is an improvement of the relative calibration of the exposures included in the analysis and, for example, these authors reach a $\sim 1\%$ precision in the relative calibration in all the bands of the SDSS DR8, except for the *u* band where the uncertainties in the atmospheric extinction were larger and the precision was $\sim 2\%$.

Summarizing the description done for these authors, the photometric model that relates the *relative* calibrated magnitudes (m) with the instrumental ones (m_{ADU}) can be expressed mathematically as:

$$m = m_{ADU} + a(t) - k(t)x + f(i, j; t) + \dots, \quad (102)$$

where $a(t)$ is the photometric zero point and describes the temporal behavior of the optical response of the system, while $f(i, j; t)$ describes the spatial variation where i, j are the coordinates in the CCD. On the other hand, $k(t)$ is the atmospheric coefficient extinction per unit airmass (x). The actual functional form of any of these terms and the number of parameters to be determined in the model will depend on the amount of effects that the model should describe and their complexity. In the most simple model, $a(t)$ and $f(i, j; t)$ would be constant (for a perfect system) and $k(t)$ will change from night to night. In more real systems, $a(t)$ will be constant for rather long periods and $f(i, j; t)$ will have a spatial dependency but not a temporal one. In this case, $a(t) = a_\alpha$ where a_α is the photometric zero point in each of the period of constant value, $k(t) = k_\beta$ where k_β is the extinction coefficient for each night and $f(i, j) = f_\gamma$ where f_γ is the value in particular regions of the CCD (one would compute $f(i, j)$ in a grid instead of in each single pixel).

With this information, we can solve for the parameters $a_\alpha, k_\beta, f_\gamma$ with a χ^2 minimization procedure given that:

$$\chi^2[a_\alpha, k_\beta, f_\gamma] = \sum_i^{n_{star}} \chi_i^2, \quad (103)$$

and χ_i^2 is:

$$\chi_i^2 = \sum_{j \in O(i)} \left[\frac{m_i - m_{j,ADU} - a_{\alpha(j)} + k_{\beta(j)}x - f_{\gamma(j)}}{\sigma_j} \right]^2, \quad (104)$$

where j runs over the multiple observations, $O(i)$, of the i th star and σ_j is the error in $m_{j,ADU}$. The success of the procedure will depend on:

- the goodness of the model to represent the real behavior of the system;
- the complexity of the system (increasing the number of parameters);
- the stability of the system (less stable implies the need of more parameters in the model);
- the amount of observations and, in particular, the amount of observations of the same star in different conditions like different CCD location, different night, flat field, etc.

To provide an idea of the degree of complexity of a photometric model similar to the one that would be needed for J-PAS we can take a look to the work done for the first 1.5 years of Pan-STARRS1 data (Schlafly et al., 2012). For a model that includes the characterization of the photometric zero point (one parameter for each night), the atmospheric extinction (one parameter for each night), the illumination correction (8 parameters for each of the 60 CCDs) and an additional correction for the seeing (2 parameters for a quadratic model), the authors construct a model with ~ 900 parameters for each independent filter. The authors show that it is possible to reach accuracies of 10mmag with this procedure.

6.2.2. *Stellar locus and spectro-ubercalibration*

The shape of the spectral energy distribution (SED) of most of the stars is basically that of a blackbody with a temperature given by the effective temperature of the star (modified by the content in metals). This makes that the colors of most of the stars follow tight relations when plotted in color-color diagrams. The location of the majority of the stars in these color-color diagrams is called the stellar locus. Covey et al. (2007) computed the location of this locus in the color space defined by the ugriz Sloan bands and the JHK_S 2MASS bands for a sample of more than 300,000 stars in common in both surveys. High et al. (2009) developed a full calibration procedure making use of the stellar locus. Kelly et al. (2012) extended the stellar locus method to the case in which the observed photometric bands differ from those used to compute the standard stellar locus (mainly the SDSS bands) with the help of a library of stellar spectra. This will allow to apply the stellar locus procedure to the particular filter set of J-PAS.

However, J-PAS will go beyond the color-color diagrams and it will obtain accurate stellar spectral classifications. The comparison between the observed J-spectra of millions of stars with libraries of stellar spectra will help to obtain a relative calibration between different bands including the effects of the galactic extinction. The result will be a spectro-ubercalibration.

In the spectro-ubercalibration, white dwarves (WDs) will play an important role because of their relative simple spectra and the degree of accuracy that have been reached by synthetic models (Oke, 1974; Bohlin, 1996; Koester, 2010). Kleinman et al. (2013) have identified and classified more than 10,000 WDs. J-PAS will be able to identify many more WDs (this means several WDs per square degree) providing a grid of reliable spectroscopic anchors for the J-PAS calibration.

6.2.3. *Photometric redshifts*

One of the main goals of the photometric calibration is to reduce as much as possible the uncertainties in the computation of the photometric redshifts. The calibration of photometric redshifts can be improved by adjusting the photometric zero-points with the help of a subsample of galaxies with known spectroscopic redshift (Coe et al., 2006). However, in a survey as large as J-PAS it is not trivial to have enough galaxies with a wide enough spectroscopic redshift range in all the pointings (regarding this issue for future large photometric surveys, see Newman et al., 2013). Fortunately, as Molino et al (2014) have shown, it is possible to accurately calibrate the photometric zero points using the galaxies that are identified as emission line galaxies by the BPZ code. The offsets computed with these emission line galaxies not only improve their photo-z (by construction) but also improve the determination of the photo-z of galaxies with very different SEDs like early type galaxies.

7. Survey Operation

7.1. *Introduction*

The daily operation related to the J-PAS survey is strictly related with the daily activities of the OAJ and the UPAD (see appropriate sections in this paper). In general terms, one can think about each night as a normal observing run, with its main components: target selection, acquisition of the proper calibration frames, scientific observations and data reduction. Nevertheless, the large amount of pointings required in the survey and the enormous data rate make it impossible to manage the whole survey in “classical mode” and the workflow has been streamlined in such a way that it can be automated as much as possible. This section describes the operation flow. Since the flow has a period of 24 hours, the description arbitrarily starts with the day-time operations.

7.2. *Daytime Operation*

7.2.1. *Data Transfer and Analysis*

Immediately after an observation has been taken, the science frame is stored in the OAJ/CPD. The same image is also sent via radio-link to the UPAD, where the data is going to be reduced and analyzed (see data reduction section of this paper).

7.2.2. *Data Validation*

As in any observation, weather or technical issues (e.g. focus change) can affect an observation. Therefore, the validation of the data is crucial for the completion of the survey. It is important to note that, since observations are obtained every (about) two minutes, it is almost impossible to check all of them for people on the mountain (more in the “night time operation” section). It is foreseeable that only a sample of images will be visually inspected even in Teruel. To automate the data validation, when an image has been fully reduced, the system checks basic parameters of the image: if it fulfills the quality criteria set for the survey (both in terms of seeing and depth), the observation is considered as “valid” otherwise, it is set as “to be repeated”. For operational reasons, we estimate that all the data obtained during a night have been validated by noon of the following day.

7.2.3. *Night Scheduling*

After the data validation, the scheduling of the following night can be started. This deals with checking the “survey progress” table, which not only includes the ID and coordinates of the fields to be observed during the project but also information on when the field was observed and a quality flag (basically a field can be either “observed”, “to be observed” or “to be repeated”).

This task is performed by a software (the “scheduler”) which runs through all the targets and computes a series of figures of merits taking into account the minimum airmass of a field during the night, moon distance, and need for repeated observation (see Ederoclite et al. 2012, SPIE, 8448, 1). The total figure of merit is obtained by combining the partial figures of merit. The fields are then ordered on the basis of their figures of merit (the fields which are not observable are not included) and added to the “night target list”, which is then sent to the observatory (more in the “night-time operation” section).

7.2.4. OAJ Telescopes’ Afternoon Calibrations

Every day, bias frames are obtained before the opening of the telescope. At sunset (or sunrise), twilight flat fields are obtained on a daily basis (depending on cloud coverage). Dome-flats are not foreseen as the field of view of the OAJ telescope is too large to guarantee a uniform illumination. More in the “calibration plan” section.

7.3. Night-time Operation

7.3.1. The Weather and the Astronomical Conditions Monitoring

For normal astronomical observations, it is of the highest importance to monitor the weather and the “astronomical conditions” (seeing, extinction, . . .). For this purpose, at any given time, the telescope operators have continuous access to a webpage with the weather conditions (temperature, humidity, wind speed and direction). Humidity and wind speed are the two most relevant values for observations, as the telescopes must close with 90% humidity and with 18m/s of wind.

The astronomical conditions are constantly monitored with a RoboDIMM, an extinction monitor (“Excalibur”), and an all-sky camera (“AstMon”), which will provide the seeing, the atmospheric extinction and the cloud coverage.

7.3.2. The observing queue

It is of the highest importance to be able to take real-time decisions during an observing run. During a large survey, it is important that the decisions take into account a series of factors which have to do with contingencies (like the weather) but also strategical (like the possibility to re-observe a field, depending on the observation strategy which is foreseen). In a project which deals with thousands of pointings it is not possible to carry out such an effort manually (not even after the “scheduler” has reduced the amount of observable targets for a night). A software (the “sequencer”) is therefore in charge of preparing the observing queue taking into account: the current pointing of the telescope, the time, the position of the moon (if present) and the weather/astronomical conditions as given by the monitors (see “Weather and the Astronomical Conditions Monitoring” section). The sequencer takes a few seconds to run and is executed every hour (TBD) and prepares the observing queue for the following hour. Obviously, the more often the software is executed, the better will be the choice of the targets. This is done in order to take into account the possibility of weather change during the night which, obviously, make pointless the definition of an observing queue only once at the beginning of a night.

7.3.3. Observation Execution

The observing queue is ordered in such way that the first target of the list is the most suitable target for the observation. The observatory control system gets the information from the observing queue and moves to the field.

In general terms, the telescope is going to point to another target only few times during a night. Most of the observations will be comparatively small offsets.

When the T250/JST moves to a pointing, the telescope gets to position, it opens the shutter, sets up the guiding and the wavefront sensing. In fact, when the shutter opens, it allows some light into the science CCD array, the wavefront sensors and the guide camera.

7.3.4. *Data Quick Look*

When a scientific observation is obtained, it is moved from the computer control workstation to the OAJ/CPD. Here among other things (see UPAD section), the image is reduced for quick look. The main difference between this reduction and the “final” data reduction is the availability, in the UPAD, of the “main calibration frames”.

This quick look is used for the telescope operators to judge the performance of the telescope/camera system. The quick look will also continuously report a series of basic measurements like FWHM (to be compared with the seeing measured through the DIMM, see “Weather Station” section), the sky background, and the ellipticity.

The analysis of the image i of a night happens during the image $i + 1$ and, therefore, no reaction can happen before image $i + 2$.

7.3.5. *The calibration plan*

As in any observatory, the telescopes at OAJ have a calibration plan, which is meant to deal with both the scientific data reduction and the health-check of the telescope/camera systems. Each of the values being monitored will be accessible through a dedicated webpage.

Bias frames are obtained daily, before opening the telescopes. Sky flat fields are obtained on a daily basis as well (depending on the cloud coverage).

The readout noise is measured from the difference of bias images. Since bias frames are obtained daily, we plan to perform this measurement on a daily basis as well.

The gain, readout noise and linearity of the CCD are fundamental parameters in data reduction. We do not expect these value to vary significantly, and therefore the monitoring will happen on a weekly basis. It is important to notice that, for these images, dome-flats are normally used. Nevertheless, a “proper” dome-flat (i.e. useful to flatten science images) is not viable for our telescopes and, therefore, the “dome-flats” will be used by projecting light to the dome, which is a good enough approach to perform an illumination test, where the stability of the light source is more important than its uniformity.

Dark images are not expected to be required in a nitrogen-cooled CCD. For monitoring purposes, we will take darks once per month.

It is assumed that the shutter will not deteriorate quickly and, therefore, a test of the shutter opening is only foreseen to happen every three months. Roughly with the same cadence, a fringing frame is going to be created.

Bright time (less than 2 days from full moon), which is not suitable for the survey, is going to be used for calibration purposes.

The image quality (i.e. the fwhm, the ellipticity of the images and the sky-background) is going to be measured for each science image (both at the stage of quick look and of “final reduction”). Each science image will also be “astrometrized” with respect to the USNO catalogue.

The photometric calibration is treated in a dedicated section.

7.4. *Data Publication*

A project like J-PAS, with many researchers distributed all across the world, needs a way to distribute the data. Moreover, the success of such a project is directly related with the amount of researchers, not directly involved, who use the data for their research.

For this purpose, the collaboration is highly committed with the use of tools of the Virtual Observatory (VO). All the reduced images and the final catalogue will be accessible through VO-protocols.

Internal data releases will allow the researchers of the collaborations to take advantage of the observations.

8. Data Management

An important part of the OAJ project is the deployment of a data center UPAD (Unit for Data Processing and Archiving) for handling, analyzing and storing the significant amount of data produced by the OAJ telescopes during the survey development. J-PAS and J-PLUS surveys will produce about ~ 2.5 PB of information accounting for the raw and processed data. The two telescopes may produce up to ~ 1.5 TB per night. The processing and archiving of these data will be done in the UPAD datacenter, which is located in Teruel about 30 km away from the OAJ. For the transmission of the data from the OAJ to the UPAD, there is a radio-link with bandwidth 700 Mbps which allows to download the data as soon they are produced. More details concerning the data management pipelines, and the hardware solutions to store and process the survey data are given in the next sections. (see also Cristóbal-Hornillos et al. (2012)).

8.1. Image Format, Data Rates and Data Volumes

JPCam is a wide field camera of (3 deg diameter) that will be installed at the JST/T250. The focal plane includes a mosaic of 14 large format CCDs $\sim 9.2 \times 9.2$ kpix. The pixel size is $10\mu\text{m}$ producing a pixel scale of 0.23 arcsec/pix. The total image size produced by one of the CCDs considering overscan and pre-scan areas is ~ 180 MB. The J-PAS survey will be carried out using a set of 54 narrow band filters, 1 medium band and 1 broad band one that are arranged in four filter trays. Observations through an additional tray containing a broad band filter will be made in advance to serve, other than for specific scientific purposes, as reference for astrometric matching and source detection. In terms of data processing the images acquired by each CCD are processed independently since the light reaching each CCD pass through a different filter.

The JAST/T80 has a FoV of 2 deg diameter and the plate scale is 55.5 6arcsec/mm. The JAST/T80 camera is equipped with a detector of $\sim 9.2 \times 9.2$ kpix of $10\mu\text{m}$ that yields a pixel scale of 0.55 arcsec/pix . The raw images will be stored in 16 bits which gives an image size (considering the over and pre-scan) of 236 MB.

The data collected by each CCD in the cameras will be stored different FITS files. Each CCD has 16 amplifiers and the raw frame will contain overscan and pre-scan sections in both directions. To store this information the raw FITS files will have 17 Header and Data Units (HDUs), the primary HDU will only contain a header with the common metadata. The other HDUs will store the data corresponding to each amplifier and the headers that describe the electronics of the amplifier and the data organization inside the HDU. After the overscan or pre-scan correction and the trimming of the overscan and pre-scan areas, the image is reformatted to a single HDU containing the whole image and joining properly the information coming from the different amplifiers as is shown in Fig. 50.

8.2. Data Rates

The two telescopes at the OAJ will be mostly dedicated to the J-PLUS (JAST/T80) and J-PAS (JST/T250) surveys. For JPLUS observations, with individual exposures of 35 secs, the data rate after considering the overheads due to filter changes and telescope movements is ~ 13.8 GB/h.

The JST/T250 will capture simultaneous exposures in 14 CCDs producing 2.53 GB of data per reading. The JPCam camera at the JST/T250 telescope has four filter trays where the 56 J-PAS filters are distributed plus an additional tray containing the broad band reference filter. For J-PAS, the 3 bluer filter trays will be exposed ~ 240 secs, whereas the reddest tray will have a longer exposure time (~ 480 secs). The expected data rate without binning is 120 GB/h. Every day a set of 30 calibration frames (bias, and flat fields) has to be collected. Added with the science data each night the telescope produce 1.3 TB of data. When binning of 2×2 pixels is used, which is foreseen for the narrow band filters, the rate is 34GB/h and the total data ~ 340 TB.

The amount of data per year depends on the final observational strategy for J-PAS defining how the time along the year is allocated for the different trays. The exposure time in each tray is divided in four sub-exposures per sky position. The actual survey strategy plan is to collect the first two individual exposures of a pointing contiguously and revisit it twice, after one and two months. Considering an useful time of 1800h/year we expect ~ 230 TB/year on raw images during the first year of observations with the reference broad band filter. After that, the data of the J-PAS survey will be collected using a binning of 2×2 pixels and produce about ~ 62 TB/year.

Figure 51 shows the data collection rates. In the figure no binning it is considered. Periods of bad weather (15% of the time) are inserted randomly. The top panel shows the number of images (note that 14 images are produced in a single JPCam exposure) collected per night. The bottom panel shows the cumulated data volumes in raw, individual processed images and mosaics. It is assumed that as soon as the final deep mosaics are combined, the individual reduced images are deleted from the disk system.

8.2.1. Total data volumes

The JPCam pixel size is $0.23''/\text{pixel}$, which implies that a survey of $\sim 8500\text{M}^\circ$ will contain a total of ≈ 2 Tpix which is ≈ 4.0 TB of information for a sky pass. The total survey is observed through 59 filters with a total of 308 individual exposures per sky position. Considering the pre and over-scan areas and an increase of 10% of inefficiency due to the camera geometry, and that binning is being used in 56 filters the whole survey raw data (including calibration frames) amount to ~ 520 TB.

The coadded images (4 bytes image + 2 bytes weight map) amount to 760 TB of information considering a 10% increase due to geometrical issues. The initial approach is to produce the averaged calibration frames per month, this will lead to 2.4 TB in master calibration images during the six years of J-PAS data collection.

Taking all this data into account J-PAS needs ~ 2.5 PB to store the raw data plus 2 versions of processed data and auxiliary products. A ratio 2:1 of lossless compression is possible for the science raw data. Using this ratio of raw data the final number will be ~ 1.9 PB. Table 19 gives the data volumes expected by the J-PLUS and J-PAS surveys.

Table 19: Storage needs for the J-PLUS and J-PAS surveys. Only images

	J-PLUS	J-PLUS compressed	J-PAS	J-PAS compressed
			not binned — binned	
Night 10h	158 GB	79 GB	1290 — 340 GB	644 — 170 GB
Year raw data ¹	31.6 TB	15.8 TB	232 — 62 TB	116 — 31 TB
Total raw data ¹	42.8 TB	21.4 TB	520 TB	260 TB
Coadded data (1DR)	32.2 TB	-	760 TB ²	-
Coadded calibration	204 GB	-	2.4 TB	-

¹ Include calibration frames

² The weight map stored in 2 bytes.

8.3. OAJ-UPAD Data Flow

At the OAJ after data acquisition the images will be converted to the FITS format defined as input for the pipelines. The image headers will be filled with information from the telescope, the monitors and the meteorological station. This information will be provided by the Observatory Control System through a historic database. The image headers apart from the standard FITS keywords, will be complemented with HIERARCH special keywords containing the information needed for the image processing and quality check. The data processing pipeline will use this HIERARCH keywords to add some information during data processing.

The images are sent to the OAJ/CPD computing nodes to perform a quick data validation. The raw data will be archived in the storage system at OAJ and transferred to UPAD/CEFCA using the existing radio-link. The OAJ storage will contain a buffer of the 2 or 3 last months of operations. During day time two copies of the raw data in magnetic tapes will be done as backup.

In Fig. 52 it is shown the foreseen hardware to manage the data flow inside the OAJ, the data transmission to the UPAD, and the processing nodes.

8.4. Image processing pipeline

The processing of the images is divided in two main stages. The first one is related with the instrumental correction, the creation of the pixel mask for the individual frames, and also includes a first astrometric and photometric calibration. The second stage deals with the creation of the final tiles by combining the individual corrected frames and weight maps, the source extraction, and the insertion of the catalogs in the science database. Both parts of the pipeline are implemented in Python and use software from the astronomical community that have been integrated through Python wrappers.

8.4.1. Daily pipeline

The main steps performed by the pipeline are summarized in Fig. 53. The processing of each image is controlled through an administrative database. The Operative Archive is a table of this database which store the information about the raw frames and serve as the input to search for new images to process.

The daily pipeline use previously generated master calibration frames (bias, flat field, fringing pattern, etc). These frames are generated for predefined observing blocks. The master calibration frames metadata are stored in a table inside the administrative DB. As the OAJ telescopes are used mainly for a dedicated program the definition of each observing block will be done under the basis of instrumental stability.

The calibration images are created by an automatic algorithm that selects the individual frames acquired during the target observing block from the Operative Archive table. Then create the target master calibration frame, and finally apply it to each one of the input individual frames. The analysis of the residuals will indicate if the master calibration frame is appropriate to be used to correct the science images collected during the period or if the observing block shall be split in different dates. The time interval when each calibration frame is valid is uploaded to the database.

The operations done by the daily pipeline are independent for each image and can be managed by a batch-queue control system. In the first processing of a science image, just after acquisition, the master calibration frames from a previous observing block will be used for quality assessment. Once the current observing block is concluded the image processing will be repeated with the proper master calibration frames. All the operations performed on the images are stored in the Reduction Control table of the administrative DB.

After correcting the instrument signature the daily processing includes the creation of the mask associated to each individual frame. To produce the final image mask the pipeline uses the following strategies. The bad pixels are located through the hot and cold pixel mask associated with the bias and flat-field frames, respectively. To compute the cosmic ray mask SExtractor is used with a retina filter. The retina filter is a neural network which is trained using the cosmic ray mask created with LACOSim (Van Dokkum (2001)).

The linear patterns produced by satellite trajectories are identified and located using the Hough transformation to locate aligned detections among the centers of the sources computed in an initial catalog (computed using SExtractor Bertin & Arnouts (1996)).

The pixel mask is formatted as a compressed image in the second HDU of the individual processed images. A binary code is used to identify any problem affecting each pixel (bad pixel, cosmic ray, satellite trajectory, saturation) or if it is associated with an object. The compressed pixel masks and individual images catalogs occupy a factor ~ 200 and ~ 1200 , respectively, less than the associated raw data image. Considering that recomputing the pixel masks and catalogs requires a high CPU cost, those will be kept in the storage system for each data release. Eventually, keeping these products in the archive, together with the fact that the arithmetic operations and the identification of the master calibration frames applied over the raw data are stored in the Reduction Control Table, allows for reprocessing of the raw images or the recovery of the individual processed images whenever required.

The last step done by the daily pipeline is to compute the astrometric solution for each individual image, to this extent we are using SCAMP (www.astromatic.net Bertin et al. (2002)). The astrometric solution computed independently for each exposure can be improved when the final mosaics are combined by using the broadband image as a reference to produce the internal solution.

8.4.2. *Tile combination*

The goal of this part of the pipeline is to create a data-cube for each survey tile. The data-cube refers to the image mosaics in all the filters aligned so each pixel in the different filter images samples the same sky position. For the J-PLUS, as T80Cam has a unique CCD, the tile will be defined as the high S/N area after creating the combined images. For J-PLUS the dithering pattern will be a small fraction of the CCD to allow the correction of the bad zones of the CCD, and the removal of stellar haloes when computing background or fringing master frames. The telescope displacement between adjacent pointings will produce an overlap among the final tiles to allow for perform a zero point transportation. When creating the combined image we will use one of broad band images as a reference to re-calibrate the internal astrometric solution using SCAMP.

SWarp (www.astromatic.net Bertin et al. (2002)) is used to generate the mosaics from the individual images. Before producing the average mosaic, each image is scaled to match the photometry of a reference image in the tile. To compute the scaling factors the pipeline will make use of the calibration information generated for each observing night/run. It is foreseen to perform a relative calibration among the individual images using the stars inside the field. The results of both methods will be compared.

In the case of the J-PAS, due to the camera geometry and the fact that the light reaching each CCD pass through a different filter, it is not possible to define a pattern which is covered in the same way by the 14 filters arranged in a tray. The approach for the J-PAS tiles is to define a grid in the sky defined by the centers, pixel scale and image size. Each tile in the grid will be covered first by a broad band filter that will serve as an internal reference for the astrometric solution. The tile mosaic image in each filter will be created as soon as the four individual exposures are obtained. At this stage the individual image flux scaling is computed from the zero point assigned to them and using relative calibration. The procedure for the individual image calibration for the J-PAS data is described in Gruel et al. (2012).

8.5. *Final products for J-PAS*

The final products of J-PAS in terms of images will be provided as data-cubes. Data-cubes will be provided for each final sky tile and consist on the registered images for each filter. Along with the tile image those directories will contain the associated weight map, individual image mask, catalogs and validation plots (e.g. astrometric calibration).

Table 20: Size of the final coadded tiles and products for J-PAS.

Per tile per filter	
tile image + weight map	545 MB
tile catalog	10 MB
individual images plots (4 exposures)	8 MB
rendered images (")	2.5MB
individual image catalogs (")	20 MB
individual image masks(")	0.08 MB
Total products per tile (1 filter)	585.3 MB¹
Data-cube per tile	
Images + weight maps + catalogs (59 filters)	32.73 GB
Individual image (catalogs + rendered frames + masks + plots)	1.80 GB
Total products per data-cube	34.53 GB¹
Whole survey (~ 23700 tiles)	
Images + weight maps + catalogs	775 TB
Total products whole survey (1 DR)	817 TB¹

¹ Decimal units are used in the text (1KB = 1000B)

The size of the tiles will be close to the size of each CCD (0.6 x 0.6 sq degrees). A certain overlap area among adjacent tiles will be reserved for calibration (as SDSS ubercalibration) purposes. A summary of the data to be computed and preserved for each tile or data-cube is given in table 20. The J-PAS survey have ~ 23700 tiles (each in 59 filters). Considering the images, weight maps, catalogs, masks and plots produced for the individual images the total volume of a data release is ~ 817 TB.

8.6. Photometric pipeline

To reduce the J-PLUS and J-PAS data we will use the ALHAMBRA pipeline, which has been developed by J-PAS members and well tested with the ALHAMBRA dataset, which comprises 4° of imaging with 23 medium band filters and which, apart from its scientific value, it is a perfect testbed to develop the methods required for J-PAS. See ?, ? and Cristóbal et al., in preparation, for a detailed description.

8.7. Storage and Processing Facilities (UPAD)

The UPAD is the data center where the image archiving and data processing of the data coming from the OAJ telescopes is going to be performed.

The hardware at the UPAD will be deployed in two main phases. The first one provide the infrastructures to do the data transmission between the OAJ and the UPAD through the dedicated radio-link, disk storage system for the OAJ, OAJ computing nodes and the OAJ backup system. During this phase, the batch-queue manager, the processing nodes and the storage devices to manage the J-PLUS data will be implemented. Those systems are shown in Fig. 52 under the names OAJ-CPD and UPAD/T80. For J-PLUS the disk archive at UPAD have a capacity of ~100 TB. This storage system will allow to archive the raw and processed data for the J-PLUS survey until the whole infrastructure for the UPAD is deployed.

The second phase of the UPAD implementation will increase the storage capabilities and processing power to archive and process the data coming from the JPCam at JST/T250. Due to the large volumes of information that has to be stored, the storage system is divided in at least two different tiers. A storage disk system, that provides fast access to the hot data, and a tape library to do the data archive and an additional backup which will allow to increase the storage space to several PB.

Data compression. The raw images from both telescopes may be lossless compressed using Fpack (Pence et al. (2009)). A study with ALHAMBRA raw data and J-PAS simulated data yields that a 2:1 compression rate on science images with low background (noise) can be achieved. The numbers obtained using this compression rates on the raw data are given in table 19

Compression of processed science frames

The rate of lossless compression on the raw data can not be acquired on the processed frames containing floating point values. It is possible to acquire a higher rate of compression $\sim 4 : 1$ on the final processed images using a lossy algorithm. It has to be evaluated whether it is admissible to add some additional noise (< 1 ADU) on the final processed images in order to save a significant volume of storage.

Storage needs: Disk Storage System and Robotic Tape Library combination

As it is explained above the amount of data that has to be stored by the J-PAS survey is about 2.5 PB. It is pointed out that the volume of raw data to be stored for J-PAS is ~ 520 TB and the amount of information in processed combined images, catalogs and other products is ~ 820 TB.

To define the storage architecture it should be considered that:

- The amount of data to store, this is the raw data and several data revisions. The final data volume may grow up to several PB.
- That data will not be accessed at the same rate during their lifetime. For example raw data will be required by the processing nodes at a higher rate during the two months after data collection, which is the timescale to combine them into final mosaics due to observing strategy, and after that only eventually in a potential data reprocessing. Also old data releases will not be accessed frequently once the catalog are available.
- Due to the size of the images, the tier 1 storage shall provide a quick access to the data.

In this context, to store the raw data and products of the J-PAS and J-PLUS surveys a combination of a disk storage system and a robotic tape library will be used. Data will be stored in the adequate media depending on the access frequency. A schema of the architecture is shown in Fig 54

The disk storage system will be used as and big cache to do the data processing. The processing of J-PAS data is limited by I/O operations against storage. To hold the daily processing rate (and potential reprocessing) the storage has to provide an aggregated bandwidth of ~ 50 Gbps. With this bandwidth between the storage and the processing nodes, the time to read an image of 200MB is less than 20 secs in the case of a high network contention. Which produce an overhead of $< 10\%$ in the individual image processing. The network hardware shall be defined to provide this rates and that filesystem will be distributed.

The robotic library will be used as a near-line storage. It provides a more dense media to store the data at a lower initial and running cost. The tape library is a work space allowing the movement of big blocks of data (several days/months of raw data or sky areas of processed data to the disk storage). The robotic library will store a copy of the total raw data, the final combined images, associated information, and products (catalogs) for several data releases.

In the next section it is described which data is planned to be set in disks and in the tape library.

Disk storage system The disk storage will be dimensioned to store the data that are accessed frequently:

- *Raw and processed data collected during the last two months:* This data will be coadded into tiles and deleted from the disk space. Once they are removed from the disk system the copy in the library will allow automatic access to those data if needed. In case that we need to re-process an important part of the survey, some policies shall be defined to move data massively to the disks storage.
- *The last revision of the data-cubes and auxiliary data:* Include the tiles and weight maps per filter, and other data as the individual image masks, catalogs, and diagnostic plots.
- *A copy of the combined master frames:*. Bias, Flats and Fringing patterns. The master frames for older data releases can be also stored here to allow some data re-processing.
- *A copy of the auxiliary data and products (catalogs) from previous releases.*

Table 21 show the volumes needed in the disk storage system to archive the different products. Binning (2×2) in acquisition is considered in the 56 narrow band filters. Two kind of compression is used to estimate the volumes. 1) Lossless compression (2:1) only applied to the data stored in integers. 2) Lossless compression on integer images plus lossy compression (4:1) on the processed frames.

Table 21: Size of storage in DISK SYSTEM needed for J-PAS. Numbers in TB.

	binning in 56 filters		
	No Compression	Compression lossless	Compression lossy
Raw data (2 months)	20.4	10.2	10.2
Processed data (2 months)	36.5	36.5	9.2
Final tiles	760.7 ³	633.9 ⁴	253.6
Comb master CF (6DR)	4.2	4.2	1.1
Aux Products (3DR)	114.1	114.1	114.1
Sum	935.7	798.7	388.0

¹ Decimal units are used in the text (1KB = 1000B)

² Numbers for 59 filters

³ No compression used in Weight maps, stored in 16 bits.

⁴ Compression used in Weight maps, stored in 16 bits.

Robotic tape library. As mentioned before, the robotic library will be used to archive all the raw data and products. The raw data and older data releases not frequently requested will be stored here and moved to the disk storage if needed.

Table 22: Size of storage in TAPE LIBRARY needed for J-PAS. Numbers in TB.

	binning in 56 filters		
	No Compression	Compression (lossless)	Compression (lossy)
Raw data (J-PAS)	518.5	259.3	259.3
Final tiles	760.7 ³	633.9 ⁴	253.6
Comb Master CF (6DR)	4.2	4.2	1.1
Products (6DR)	339.9	339.9	339.9
Sum (2 DR images)	2383.8	1871.0	1107.3

¹ Decimal units are used in the text (1KB = 1000B)

² Numbers for 59 filters

³ No compression used in Weight maps, stored in 16 bits integers.

⁴ Compression used in Weight maps, stored in 16 bits integers.

⁵ Considered the sum of raw data plus 2 data releases of tiles and 6 releases of Master CF and products (catalogs, pixel mask, ...).

It is considered to store in the robotic library the following data.

- A near-line copy of all the raw data.
- A copy of the last released data-cubes. Also a copy of the images of some previous releases.
- A copy the master frames for all the releases.
- A copy of the products for all releases: individual image catalogs, validation plots, individual image masks, log files, etc.

Table 22 shown the volumes needed to store the enumerated data. In different columns is reflected the decrease in data volumes in case of conversion of the processed data to integers in 16 bits. Note that 2×2 binning during acquisition in the narrow band filters is assumed to compute the data volumes.

UPAD computing needs. The UPAD has to be equipped with computing power that allows the following actions:

1. Create the averaged Master Calibration Frames. During the instrument commissioning the UPAD team will verify the frequency for Calibration Frame updates.
2. Reduce and calibrate daily the individual frames obtained by the two telescopes.
3. Generate the averaged tiles from the individual frames once a sky area have been completed in a set of filters.
4. Extract the final catalogs from the final tiles.
5. Be able to reprocess the survey data with a sustained rate.
6. Execute other software developed by the collaborators.

The execution times to perform the first three task above have been evaluated using the alpha version of the J-PAS data processing pipeline and simulated images with similar characteristics that the ones collected for J-PAS. The test have been done in a development system with 3 nodes with similar characteristics than the target ones 3.2GHz processor, 12 cores, 48 GB RAM. Sun Grid Engine is used as batch-queue software. The average data reduction for one image is ~ 200 secs, and a tile of 4 images is combined in ~ 400 secs. Compute the final catalogs may take ~ 120 secs per frame. Taking into account that ~ 8000 science images will be collected per night, and that ~ 2000 tiles shall be combined, all this amount to 733 hours of CPU in daily processing.

The two surveys amount to 7.5×10^6 frames and 1.5×10^6 tiles so $\sim 6.3 \times 10^5$ CPU hours. A system with 300 cores shall be able to process daily the data in 4-5 hours and hold an adequate rate of data reprocessing.

There are some parts of the code that have not been taking into account like:

- Compute catalogs to run the photometric redshift code (BPZ) and photometric redshifts code.
- Other software developed by the J-PAS collaboration.

Science Database and External Access system. Once the final catalogs are computed the information frequently used by the scientific community will be ingested in a database. When J-PAS survey is finished the information stored in database will be ~ 20 TB. After studying different alternatives, a clustered SQL database engine is the current approach. The SQL data model is appropriate for the kind of data to store, the SQL queries are amply used by the astronomical community, and this approach allow an easier integration with the Virtual Observatory protocols. To share the processed data (images and catalogs) with the scientific community a system dedicated to the data distribution on demand is being considered (EDAM, External Data Access Machine). This system will contains a replica of the internal databases with the validated data that according with the release policies shall be public available. The EDAM will also provide access to final images or raw data under some restrictions on the demanded data volumes.

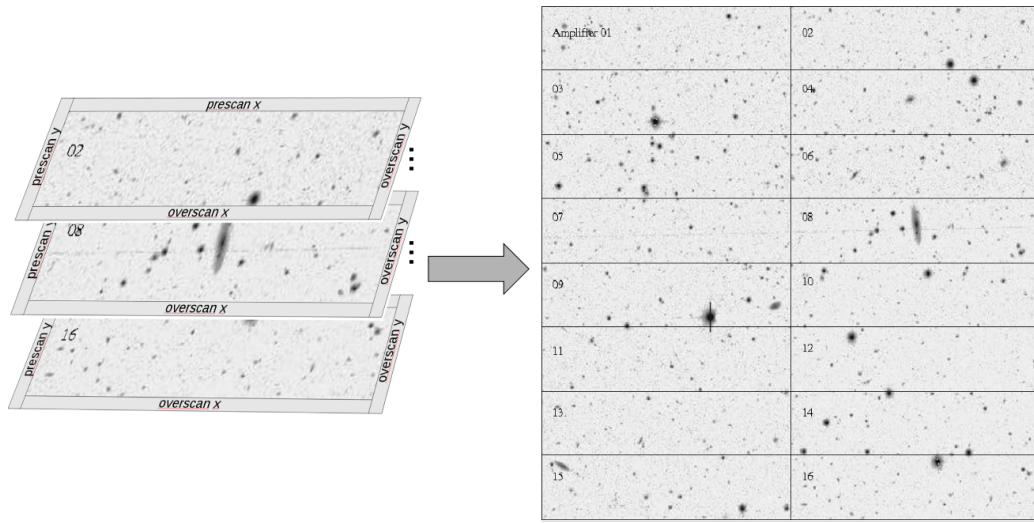


Figure 50: Schematics of the image format with the 16 amplifiers in different HDUs and how the images are reassembled using a single HDU after pre-scan or/and overscan correction and trimming.

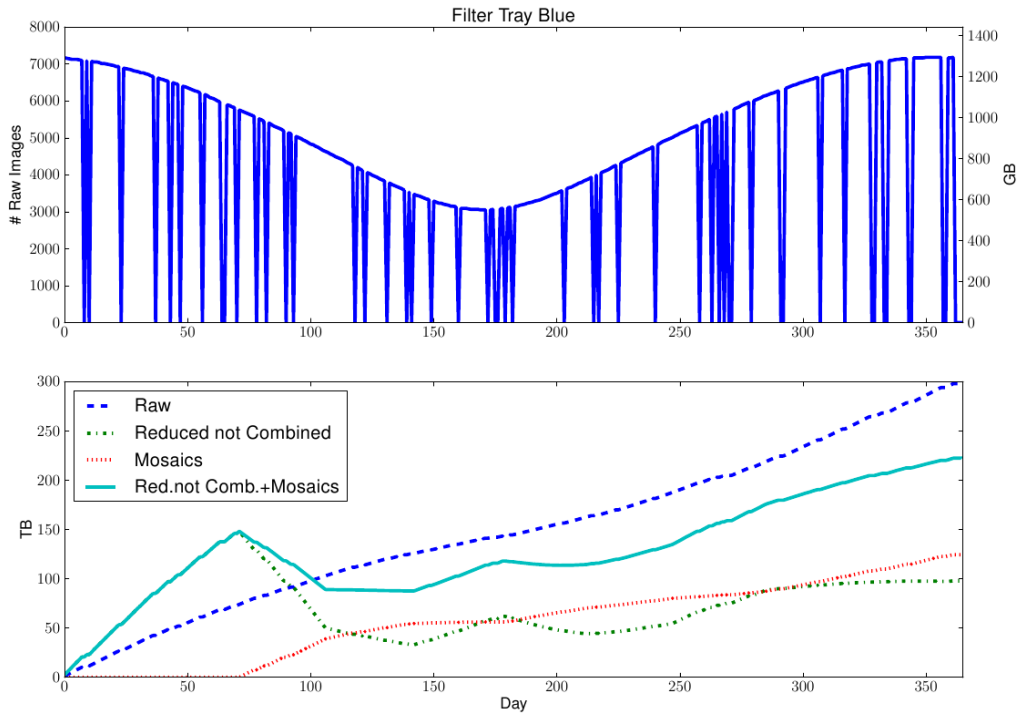


Figure 51: Estimated data rates obtained with the NB filter trays used with JPCam. The panels correspond to the number of images obtained by night at different epochs during the year (*top panel*), and the cumulative data volume during the year assuming that individual processed images are combined in deep mosaics and deleted from the storage system as soon as the 4 images are collected (*bottom panel*).

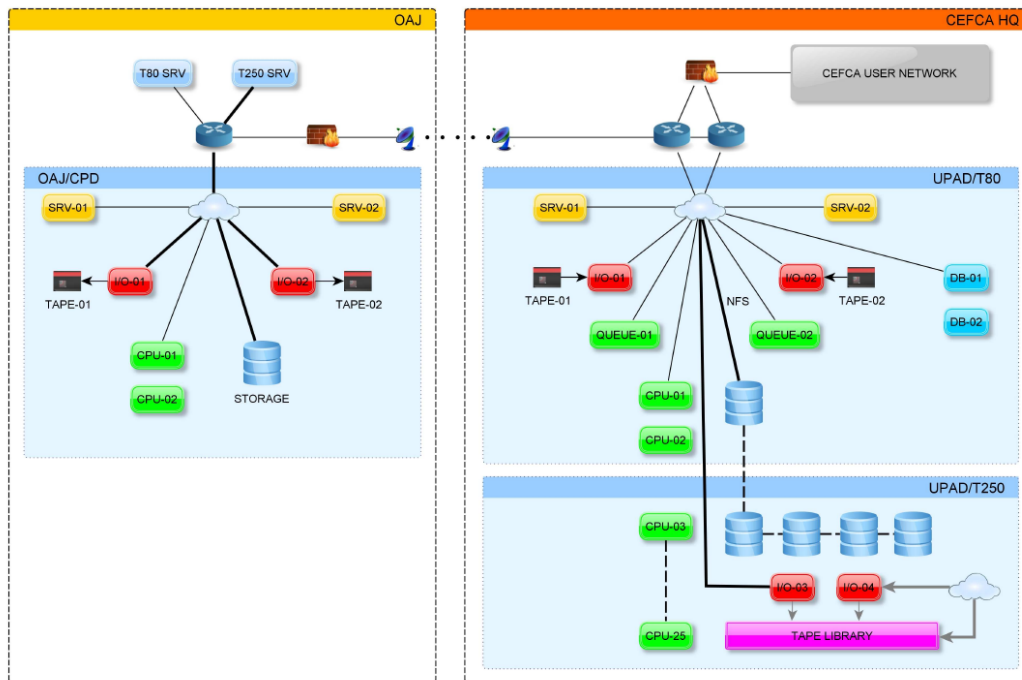


Figure 52: Schematics of the hardware involved in the data movement inside the Observatory and data transmission to the OAJ. On the right side there are two different phases. Above, the deployment hardware for data transmission, service machines and data processing for the JAST/T80 data it is shown. In the bottom part, it is shown the hardware dedicated to data reduction and catalog generation for the JST/T250 data.

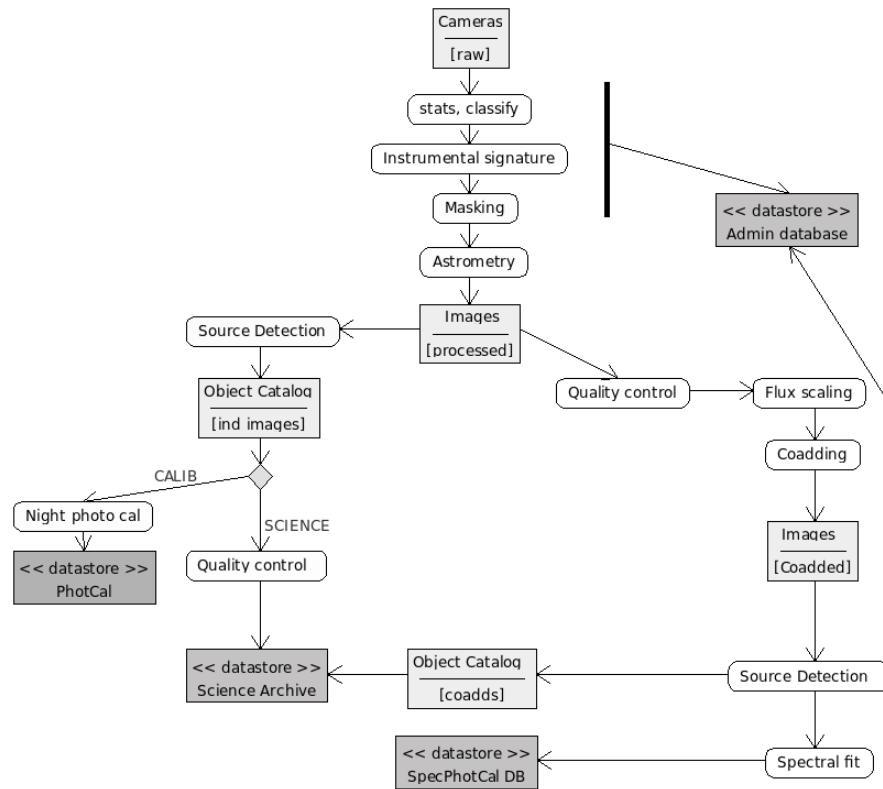


Figure 53: J-PLUS pipeline data flow. The calibration will be different for J-PAS which will make use of the previously calibrated stars, with their spectral type determined from J-PLUS, to calibrate each individual image (Gruel et al. (2012)).

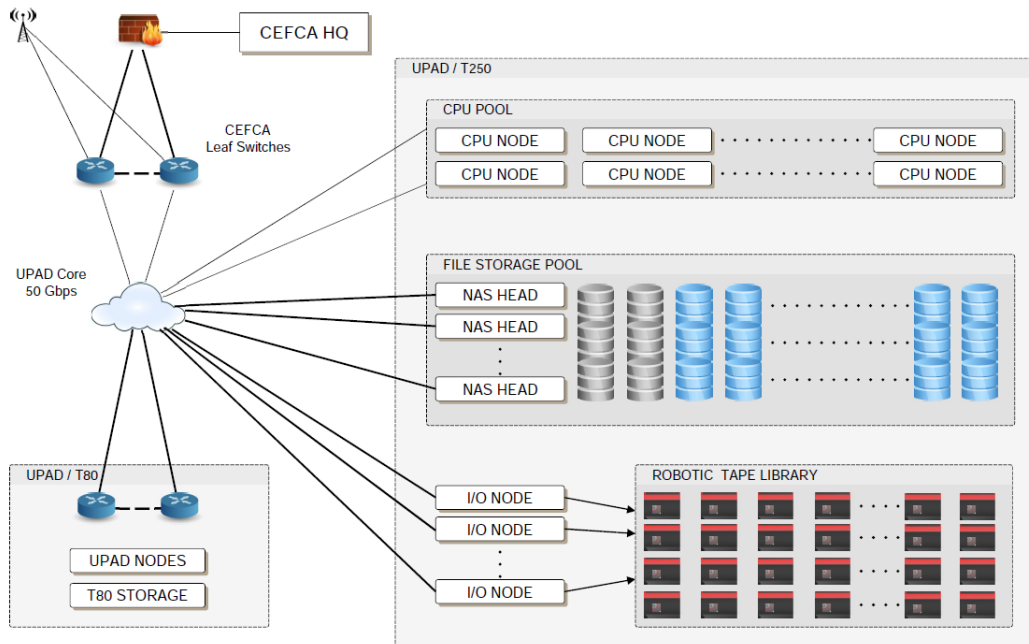


Figure 54: Schema of the storage and processing systems.

9. The Observatorio Astrofísico de Javalambre

9.1. Site and infrastructures

The *Observatorio Astrofísico de Javalambre* (hereafter OAJ) is the new astronomical facility at the *Pico del Buitre*, in the *Sierra de Javalambre* (Teruel, Spain), where J-PAS will be conducted from. The site has an altitude of 1957 m above the sea level, with excellent astronomical characteristics in terms of median seeing of 0.71 arcsec in *V* band, a fraction of totally clear nights of $\sim 53\%$ ($\sim 75\%$ with at least 30% of the night clear) and a remarkable darkness, a feature quite exceptional in continental Europe (see more details in Moles et al., 2010).

The OAJ is a facility specifically designed to carry out large sky surveys with two unique telescopes of unusually large fields of view (FoV). The main one is the Javalambre Survey Telescope (JST/T250) an innovative Ritchey-Chretien, alt-azimuthal, large-etendue telescope with a primary mirror diameter of 2.55 m and 3 deg (diameter) FoV. The JST/T250 is the telescope devoted to conduct J-PAS, making use of a unprecedented panoramic camera, JPCam, that will be described in Section 10. The second largest telescope at the OAJ is the Javalambre Auxiliary Survey Telescope (JAST/T80), a Ritchey-Chretien, german-equatorial telescope of 83 cm primary mirror and 2 deg FoV. The primary goal of JAST/T80 is to perform the Javalambre Photometric Local Universe Survey (J-PLUS), that will be described in a different paper. In short, J-PLUS will cover the same sky area of J-PAS using 12 filters in the optical range, which are specifically defined to allow the photometric calibration of J-PAS. These filters are: 4 SDSS filters (g,r,i,z) which allow to anchor the photometry to that of the SDSS, 6 filters of 200 – 400 Å width, centered on key absorption features (e.g. H δ , the G-band, Mgb/Fe lines, and the Ca triplet) for stellar classification and stellar population studies, and 2 narrow band filters in common with the J-PAS filter set which cover the [OII]/ λ 3727 and H α / λ 6563 lines, for anchoring the J-PAS calibration and also mapping the SFR in nearby galaxies ($z < 0.017$).

Overall, both JST/T250 and JAST/T80 have been particularly conceived by CEFCA to optimize the effective etendue. As part of the OAJ contract, the detailed design and manufacturing of the two telescopes is led by the belgian company AMOS, under CEFCA collaboration, review, and supervision. A detailed description of the OAJ and their telescopes can be found in (Cenarro et al., 2013), Cenarro et al. (2012), (Cenarro et al., 2011) and (Cenarro et al., 2010).

A general layout of the OAJ is presented in Figure 56. The JST/T250 building (top-left in Fig. 56; see also Fig. 57 left) consists of a main cylindrical insulated building of 21 m total height from the ground level, including the dome, which is air-conditioned and has a half-sphere geometry of ~ 13 m diameter, a double main shutter and a wind shield. Robotic openings around the static concrete structure of the telescope floor allows to control the air flow inside the dome preventing air stagnation and temperature gradients inside the dome. The building includes three working and storage levels, including an engineering control room. Aside the main JST/T250 building there is an underground room of ~ 6 m height with an overhead crane for storage, maintenance and mirror aluminizing procedures. A platform of 9 m² with capacity for up to 15 tons is used to transport the mirror in its cell from the telescope camera to the underground aluminizing area.

The JAST/T80 building (top-right in Fig. 56; see also Fig. 57 center) consists of the telescope floor, with a dome of 6.2 m diameter, an underground floor dedicated to storage and maintenance and an underground engineering control room. The monitor building (top-center in Fig. 56, between the two main telescope buildings; see also Fig. 57 right) contains the DIMM seeing monitor, the extinction monitor, and other devices for monitoring the sky night quality. The enclosure of this building consists of two openings in semicylindrical shape that deploy in opposite directions allowing observations for altitude values larger than ~ 20 deg.

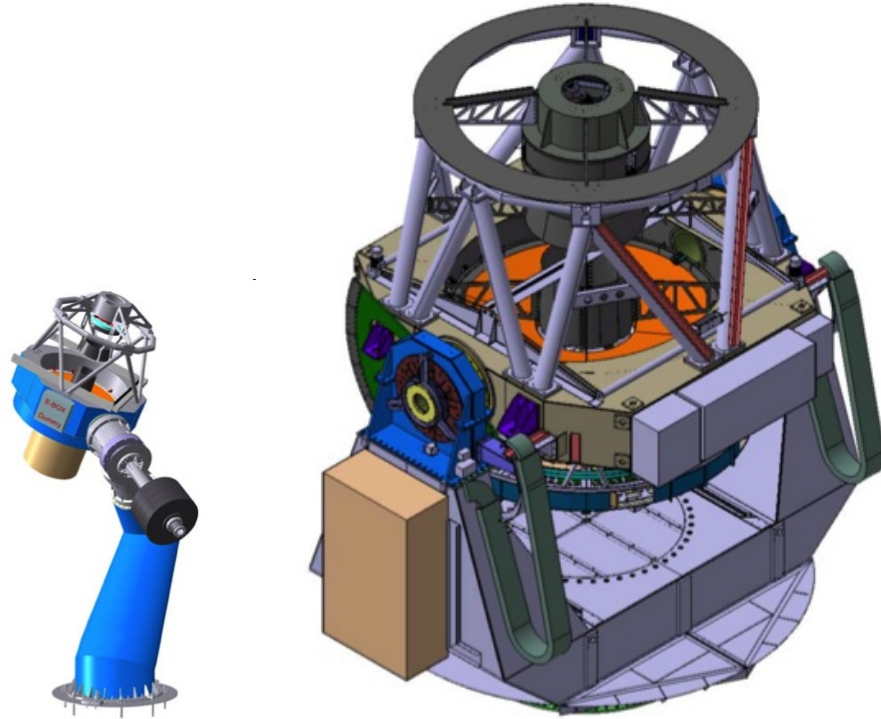


Figure 55: An illustration of the final designs of the 2.55 m Javalambre Survey Telescope (JST/T250; right) and the 83 cm Javalambre Auxiliary Survey Telescope (JAST/T80; left) in true relative scales.

The rest of buildings in Fig. 56 are devoted to host the general installations of the OAJ, the astronomical control room, laboratories, the data center and the residence. All the buildings communicate each other through underground tunnels, hence guaranteeing the safe use of the observatory in case of bad weather conditions as well as an efficient maintenance of the general OAJ installations.

9.2. The OAJ Telescopes

9.2.1. JST/T250

The centerpiece of the OAJ is the JST/T250 (Figure 58; left). JST/T250 and its panoramic camera JPCam are driven by the scientific requirements to conduct J-PAS. Motivated by the need of optimizing the etendue, JST/T250 is a very fast optics telescope (F#3.5) with a plate scale of 22.67 arcsec/mm. This leads to a very compact mechanical design, with a distance between the primary (M1) and secondary (M2) mirrors of just ~ 2.2 m. The focal plane of JST/T250 is flat and corresponds to a Cassegrain layout. The effective collecting area of JST/T250 is 3.75m^2 , yielding an etendue of $26.5\text{m}^2\text{deg}^2$. It is designed to support instruments at the Cassegrain focus of up to 1300 kg.

JST/T250 is optimized to provide a good image quality (EE50 diameter $< 10\ \mu\text{m}$) in the optical spectral range (330 – 1100 nm) all over the 48 cm diameter focal plane ($\sim 7\text{mrad}$). To achieve this goal JST/T250 includes a unique field corrector of 3 lenses of fused silica, with 4 aspherical surfaces and diameters in the range 50 – 60 cm. The geometry and optical performance of the J-PAS filters and the entrance window of JPCam were taken into account during the final optical design to simplify the aspheric departure of the field corrector of lenses. The lenses in the field corrector are supported inside a barrel of low carbon steel specifically designed to keep their relative positions during operation using a passive hexapod structure made of INVAR. The barrel is rigidly connected to the fixed flange of the instrument rotator and sealed to the entrance window of JPCam, keeping a dry, slightly hyperbaric atmosphere around the lenses.



Figure 56: Final design of the OAJ. See text for details.



Figure 57: Views of the main telescope buildings at the OAJ: the JST/T250 building and the maintenance area (left), the JAST/T80 building (center), and the DIMM seeing and extinction monitor building (right). See text for details

The JST/T250 guiding system consists of a set of 4 auxiliary CCDs at the edges of the JPCam focal plane. Also, in order to keep the system in focus and preserving the image quality during the survey execution, 8 additional CCDs located at the edges of the focal plane in extra and intra focal positions allow to perform wave-front curvature sensing corrections in real time. The control system of JST/T250 allows to work in continuous closed loop, analyzing the defocused images at the auxiliary CCDs and providing the Zernike coefficients to the telescope control system that converts it in M2 corrections in piston, tip and tilt to the M2 hexapod.

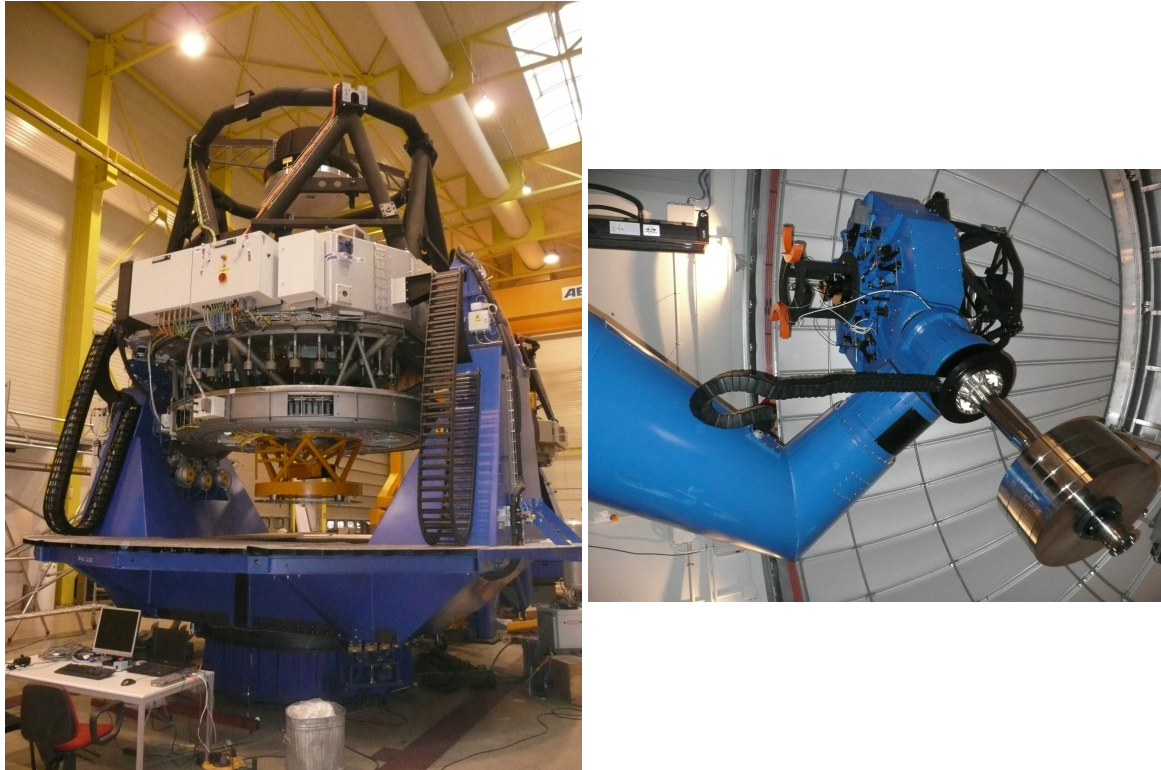


Figure 58: The OAJ main telescopes: JST/T250 at the integration hall in AMOS headquarters (left) and JAST/T80 at the OAJ (right).

For the alignment, testing and verification of JST/T250, the OAJ will make use of two independent verification cameras that can be independently displaced to any position of the focal plane by means of a set of x and z translation stages. Having two independent cameras allows for simultaneous testing of the image quality and telescope performance in different regions of the focal plane, which is essential given the large focal plane of JST/T250.

9.2.2. JAST/T80

The JAST/T80 has an 83 cm diameter M1 with a FoV of 2m° . It is also a fast optics telescope (F#4.5) driving a plate scale at the Cassegrain focal plane of 55.56 arcsec/mm. Mechanically, JAST/T80 has a German-equatorial mount (Fig. 58; right). The optical tube assembly has also a very compact layout, with just ~ 830 mm between M1 and M2. With a weight of around 2500 kg, JAST/T80 supports instruments at the Cassegrain focus of up to 80 kg. Together with its panoramic camera, T80Cam, JAST/T80 will be primarily devoted to perform J-PLUS and the photometric calibrations of J-PAS. Nevertheless, its large FoV and high sensitivity makes it ideal for many other scientific goals.

Like JST/T250, the optical design is based on a Ritchey-Chretien configuration plus a field corrector of three lenses of fused silica, in these case with just spherical surfaces and diameters are in the range 15 – 17 cm. The whole system is optimized to work in the optical range, yielding a polychromatic image quality better than $9.0\ \mu\text{m}$ (EE50; diameter) inside the 13 cm diameter focal plane ($\sim 3.1\text{m}^\circ$), after having accounted for all error sources in the error budget. The design is also optimized to account for the J-PLUS filters and the T80Cam entrance window in the optical path.

Guiding at JAST/T80 is carried by means of a 20 cm piggy-back telescope with an additional CCD camera. Because of the large FoV, keeping the system in focus and free of aberrations all over the FoV is expected to require small M2 corrections through the hexapod every few hours. For this reason, a specific procedure for wave-front curvature sensing has been designed at CEFCA, making use of the scientific CCD of T80Cam. Since JAST/T80 is not so demanding of this type of corrections as JST/T250 is, no auxiliary CCDs are necessary in this case.

10. The J-PAS Cameras

To carry out the J-PAS and J-PLUS surveys, the OAJ telescopes will be equipped with JPCam and T80Cam, two panoramic cameras designed to exploit survey capabilities of the JST/T250 and the JAST/T80, respectively. As the overall effective etendue of a telescope plus instrument system is ultimately determined by the CCD filling factor, JPCam and T80Cam have been designed to maximize the telescopes' focal plane coverage while maintaining the high image quality requirements.

JPCam and T80Cam are direct imaging instruments designed to work in a fast convergent beam at the Cassegrain foci that are based on state-of-the-art, large format CCDs. T80Cam will include a low-noise $9.2k \times 9.2k$, $10\mu\text{m}$ pixel, high efficiency CCD manufactured by e2V, providing a useful FoV of 2.1° (65% focal plane coverage) with a plate scale of 0.55 arcsec/pix . JPCam, on the other side, will include a mosaic of $14 \times 9.2k \times 9.2k$, $10\mu\text{m}$ pixel CCDs specially developed by e2V for J-PAS, providing a useful FoV of 4.7° (67% focal plane coverage) with a plate scale of $0.2267''/\text{pix}$. Moreover, JPCam will include 12 auxiliary detectors at the focal plane for guiding and wave front sensing.

The cameras are equipped with a filter unit designed to mount the complete J-PLUS and J-PAS filter sets. T80Cam includes two filter wheels with 7 positions each, this configuration allows the 12 J-PLUS filters to be permanently installed on the camera so no night-to-night filter exchange is required. Following the same low maintenance strategy, JPCam has been equipped with a filter tray magazine that includes up to five filter trays, each one mounting 14 filters. This filter unit design permits the 70 J-PAS physical filters to be permanently installed on JPCam.

The definition and procurement of JPCam and T80Cam is lead by a consortium of several funding institutions from Spain (CEFCA and IAA-CSIC) and Brazil (ON, IAG/USP, and CBPF). The funding of JPCam and T80Cam is guaranteed by that consortium, including the filter sets for both instruments. The commissioning of T80Cam and JPCam is planed for Q3 2013 and Q3 2015, respectively.

10.1. T80Cam, the wide field camera for the JAST/T80 telescope

JAST/T80 will be equipped with an instrument designed to exploit the telescope survey capabilities, the T80Cam. The JAST/T80 and T80Cam primary goal is to perform the photometric calibration of the JST/T250 surveys by means of the Javalambre-Photometric Local Universe Survey (J-PLUS). J-PLUS will image $\sim 8500^\circ$ of Northern Sky using 12 filters in the optical range. These are a combination of narrow- and broad-band filters carefully optimized to retrieve stellar parameters ($T, \log(g), [Fe/H]$) through flux calibrated stellar models fitting.

T80Cam is a wide field, direct imager that will be installed at the Cassegrain focus of the JAST/T80. It is equipped with an STA 1600 backside illuminated detector. This is a $9.2k \times 9.2k$, $10\mu\text{m}$ pixel, high efficiency CCD that is read from 16 ports simultaneously, allowing read times of 12s with a typical read noise of 3.5 electrons (RMS). This full wafer CCD covers a large fraction of the JAST/T80's FoV with a pixel scale of $0.55''/\text{pixel}$. Table 10.1 summarizes T80Cam performances.

FoV	$\varnothing = 1.7^\circ$ (full performance) $\varnothing = 2.0^\circ$ (reduced performance)
EE50	$\varnothing = 9\mu\text{m}$
EE80	$\varnothing = 18\mu\text{m}$
CCD format	9216×9232 pix $10\mu\text{m}/\text{pix}$
Pixel scale	$0.55''/\text{pix}$
FoV coverage	2.0° (fill factor 65%)
Read out time	12s
Read out noise	$3.5e^-/\text{pixel}$
Full well	$123ke^-$
CTE	0.99995
Dark current	$0.0008e^-/\text{pixel } s^{-1}$
Number of filters	12

Table 23: T80Cam parameters

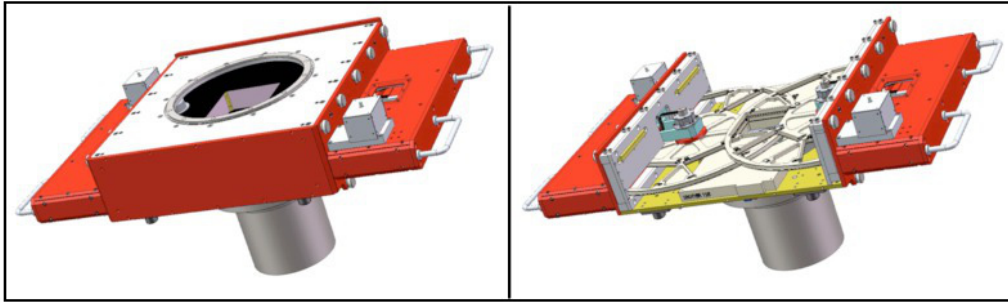


Figure 59: T80Cam design. Upper panel shows the complete assembled instrument. The two main subsystems can be clearly identified. The top part of the instruments represents the FSU containing the shutter and the two filter wheels. The cylindrical-shaped object underneath the FSU represents the camera subsystem. Lower panel shows the same view of T80Cam after cover removal to show the two filter wheels and the shutter.

The instrument consists of two main subsystems: the filter and shutter unit (FSU) and the camera subsystem (see Figure 59). The FSU holds two removable filter wheels and the shutter. The camera subsystem, below, comprises the cryostat, the cooling and vacuum systems, the CCD, an optically powered entrance window and the detector electronics.

10.1.1. The Camera System

The camera system is an 1110S camera manufactured by Spectral Instruments (Tucson, AZ, USA). It is equipped with a grade-1, backside illuminated E2V CCD, a $9.2k \times 9.2k$, $10\mu\text{m}$ pixel high efficiency CCD. This CCD has an image area of $92.16\text{mm} \times 93.32\text{mm}$ and has a broadband AR coating for optimized performance from 380 to 850nm. Figure 60 shows the 1110S camera with an engineering CCD mounted during its manufacture at Spectral Instruments premises.

The sensor is cryo-cooled to an operating temperature between -100°C and -110°C with a cryo-tiger refrigeration system, a closed-cycle Joule-Thomson effect cryogenic refrigerator system. The chamber will be evacuated to a level of 10^{-4} Torr using a turbo dry vacuum pump.

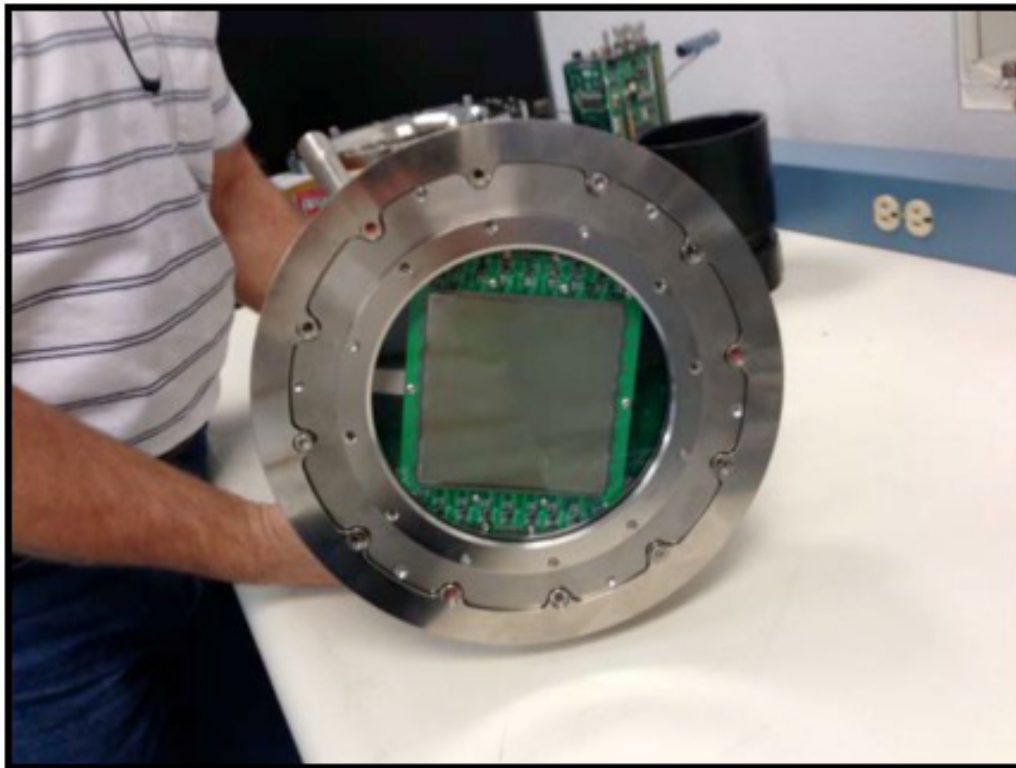


Figure 60: 1110S camera equipped with an engineering CCD during its manufacture at the Spectral Instruments premises

The camera entrance window is in fact the fourth element of the JAST/T80 field corrector, and together with the filters, it is part of the telescope optical design optimization. The window is a 10mm thick, weakly powered field-flattener with an 8mm distance between its inner surface and the focal plane. The entrance window has been manufactured by Harold Johnson Optical Laboratories (Gardena, CA, USA).

10.1.2. *The FSU System*

The FSU has been designed and manufactured by the Instituto Nacional de Pesquisas Espaciais (INPE) and CEFCA. It includes the filter unit, the shutter and the cryostat support flange. The latter allows for fine alignment of the camera system with respect to the telescope optical axis. The shutter is a 125mm clear aperture shutter that has been acquired through the Argelander Institut für Astronomie. The FSU holds two removable filter wheels, each one capable of holding 6 filters plus an empty position. As it can be seen, filters are operating in a converging beam and close to the detector. Figure 61 shows the FSU assembly during its final stages of integration and commissioning at CEFCA.

Summarizing, T80Cam design has been driven by the main science goals defined by the Science Working group inside the J-PAS collaboration. The instrument has therefore been optimized to develop the J-PLUS survey. The commissioning and acceptance of T80Cam is planned for the end of 2013. In this time scale, the J-PLUS survey to be performed with this camera will start in early 2014.

10.2. *JPCam, the 1.2Gpixel camera for the J-PAS survey*

The main scientific instrument for JST/T250 is JPCam, a 1.2 Gpixel camera that will be installed at the Cassegrain focus. JPCam has been designed to perform the J-PAS survey, so maximizing the efficiency of FoV and wavelength coverage while guaranteeing a high image quality over the whole focal plane have been the main instrument design drivers.



Figure 61: FSU during its AIV at CEFCALaboratory

JPCam is a wide field, direct imager equipped with a mosaic of 14 $9.2k \times 9.2k$, $10\mu m$ pixel backside illuminated, low noise detectors from e2V. Each science CCD is read from 16 ports simultaneously, allowing read times of 12s with a typical read noise of $4e^-$ (RMS, goal). Its filter unit has been designed to admit 5 filter trays, each mounting 14 square filters corresponding to the 14 CCDs of the mosaic. Each CCD will view only its corresponding filter avoiding optical cross-talk from their neighbors. The filters will operate close to, but up-stream from, the dewar window in a fast converging beam. With this configuration, JPCam will cover 4.7° (67% focal plane coverage) with a plate scale of $0.2267''/pix$ and will allow all the 70 required filters (56 main J-PAS filters plus several copies of the broad-bands) to be permanently installed on the camera, so no night-to-night filter exchange will be required.

Because of the JST/T250 telescope's very wide FoV combined with the confirmed excellence of the OAJ's intrinsic site seeing, JPCam is required to fully optimize and maintain the image quality across the full focal plane of the mosaic. Optical analysis reveals that it is necessary, not only to guide the telescope and keep it optically aligned by adjusting the position of its secondary mirror, but also of the focal plane itself. To perform this task JPCam includes an hexapod actuator system that is controlled thanks to a set of wavefront sensors in the periphery of the instrument's FoV. So the JPCam 14 science CCD mosaic is complemented with 12 auxiliary detectors, 4 for auto-guiding (AG) and 8 for wavefront sensing (WFS) tasks. The auxiliary detectors are E2V frame-transfer devices fed by light from broad-band filters mounted in the edges and corners of each filter tray. Table 10.2 summarizes JPCam performances.

Therefore, JPCam's final design includes the following three main subsystems (Figure 62):

- Actuator Subsystem: The hexapod actuator system (HAS) attach the cryostat to the Instrument Support Structure (ISS) through the Cryostat Support Structure (CSS) and provides the required focus and tilt adjustments to the focal plane. The HAS is being designed and manufactured by the company NTE-Sener (Barcelona, Spain).

- Filter and Shutter Unit Subsystem (FSU): The FSU is mounted directly to the ISS and comprises the filter tray exchange mechanism and the shutter. FSU is being designed and constructed by a Brazilian consortium led by INPE (Instituto Nacional de Pesquisas Espaciais). The massive 515mm aperture shutter is supplied by the Argelander-Institut fr Astronomie, Bonn.

FoV	$\varnothing = 1.7^\circ$
EE50	$\varnothing = 11\mu\text{m}$
EE80	$\varnothing = 22\mu\text{m}$
CCD format	Science (14X) $9.216k \times 9.232k\text{pix}^2$, $10\mu\text{m}/\text{pix}$ Guiding (4X) $1.024k \times 1.024k\text{pix}^2$, $13\mu\text{m}$ (frame transfer) Wavefront sensing (8X) $2.048k \times 2.048k\text{pix}^2$, $15\mu\text{m}$ (frame transfer)
Pixel scale	$0.2267''/\text{pix}$
FoV coverage	4.7° (fill factor 65%)
Read out time	12s
Read out noise	$4e^-/\text{pixel}$ (goal)
Full well	$130ke^-$
CTE	0.99995
Dark current	$0.0006e^-/\text{pixel } s^{-1}$
Number of filters	70

Table 24: JPCam parameters

- Camera Subsystem (CryoCam): The CryoCam comprises the dewar entrance window, the CCD mosaic and their associated controllers, the cooling and vacuum systems and the image acquisition electronics and control software. The CryoCam is being supplied by e2v under contract to J-PAS.

The three main subsystems are identified in the fully assembled JPCam design, as shown in Figure 63.

10.2.1. The Hexapod Actuator System (HAS)

The HAS is providing the CryoCam with focus and tip-tilt movement aimed to compensate the telescope deformation produced by the gravity and/or temperature changes. It will be able to move the CryoCam, whose weight is about 600Kg, with an accuracy of 4m (focus) and 20 arcsec (tip-tilt). The main elements of the HAS are (Figure 64):

- ISS: it interfaces with the Telescope flange, holds the FSU, and is the attachment to a set of actuators.
- CSS: supported by the set of actuators, it is in charge of keeping in place the CryoCam. It is the moving part of the HAS.
- Hexapod System and hexapod control electronics: Six actuators assemblies attached to both the ISS and CSS configure the hexapod system.

10.2.2. The Filter and Shutter Unit (FSU)

The FSU is designed to admit 5 filter trays. All five of which contain 14 square filters each corresponding to the 14 CCDs of the detector mosaic. Additionally, the filter trays also have filter holders for broad-band filtering of the 12 auxiliary WFS and AG chips. Details of the FSU are shown in Figure 65.

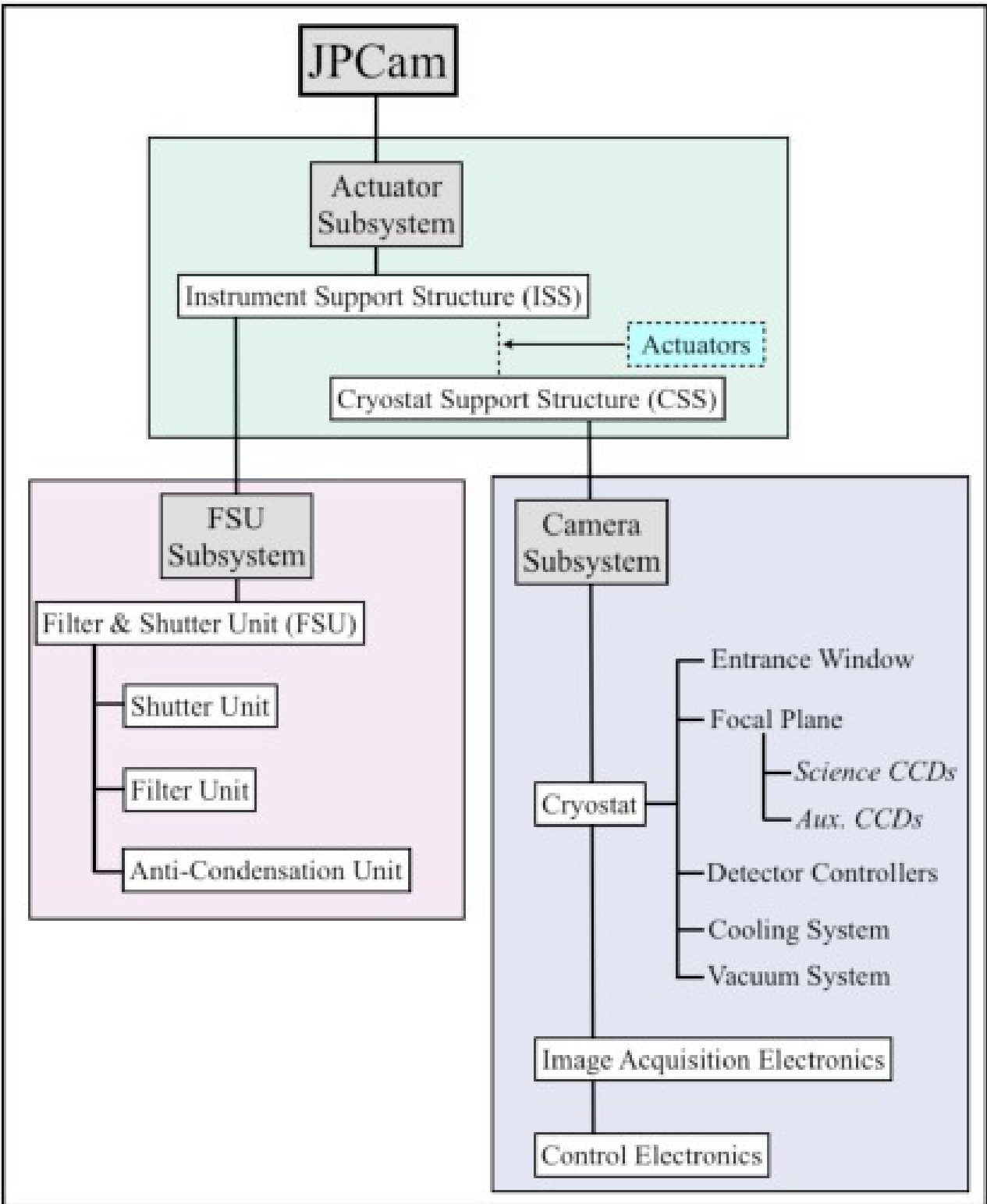


Figure 62: JPCam product tree

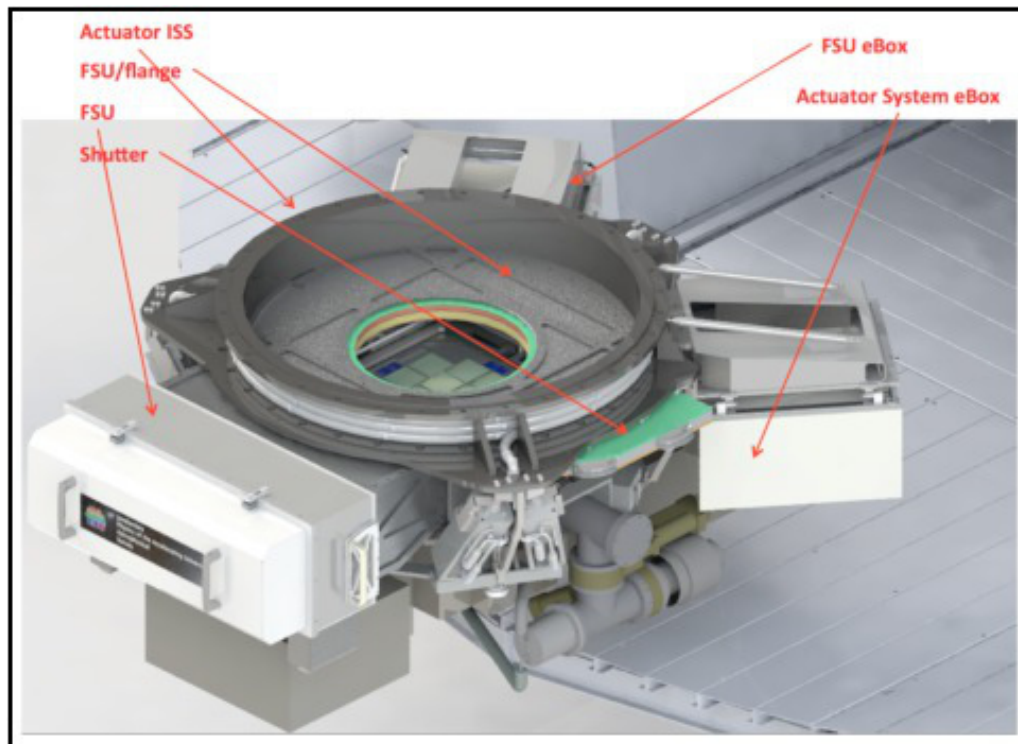


Figure 63: A view of JPCam fully assembled where the different subsystems are identified.

The 5 filter trays are selectable remotely so the FSU will include the motors and encoders and the control system needed for their operation. Each filter tray is designed to be easily and manually removable and exchangeable from the closed frame. Individual filters can be manually removable from their tray once the tray has been removed from the module.

The focal-plane of the T250 telescope is non-telecentric and hence, in order to retain the steepness of each intermediate-band filter bandpass profile and the uniformity of its wavelength centering, the filter must be held in each tray so as to induce a differential tilt in each of the 14 filters of the mosaic, so that each filter is perpendicular to the chief ray at its centre. This amounts to a maximum tilt of 3.5deg for the outer filters of the mosaic equivalent to a 6mm departure from a flat surface. Furthermore, in order to minimize the peripheral vignetting of the CCD by its corresponding filter, the distance between filters and CCDs is required to be as close as practical. A nominal gap of 4mm between the filters and the dewar window has been chosen to allow for filter tray deployment and the necessity of positioning the mosaic focal plane with the HAS.

The JPCam has a 515mm diameter aperture and is supplied by the Argelander-Institut für Astronomie, Bonn. It is a “two-curtain” shutter that guarantees an homogeneous illumination of the focal plane. It allow for exposures as short as 10ms with an exposure uniformity better than 1ms over the full FoV.

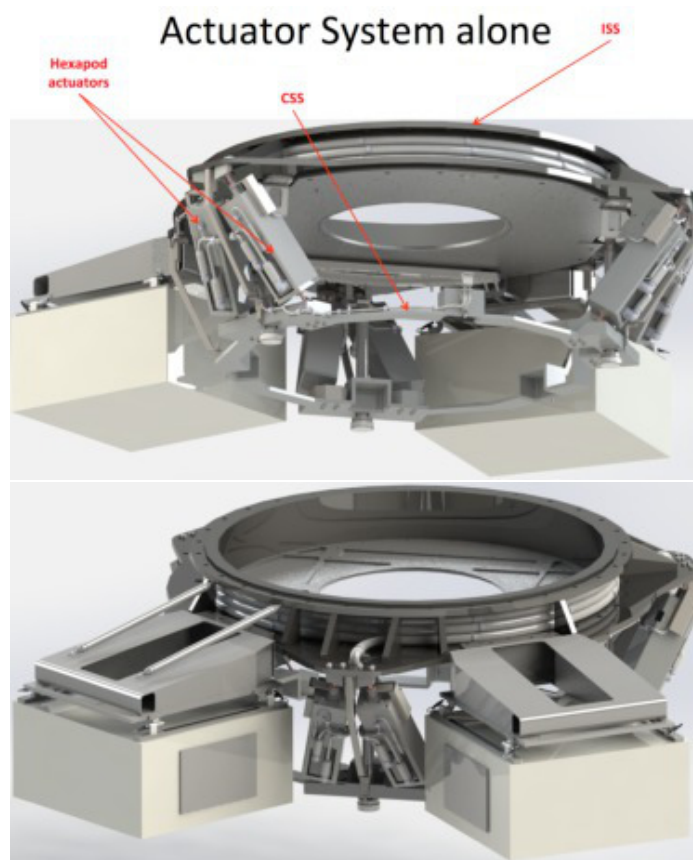


Figure 64: JPCam HEX

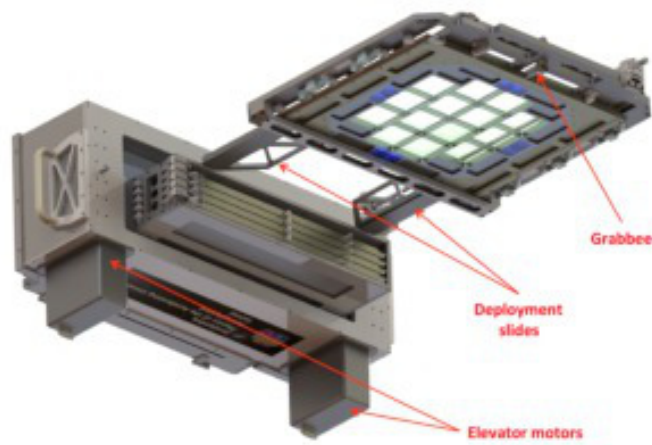
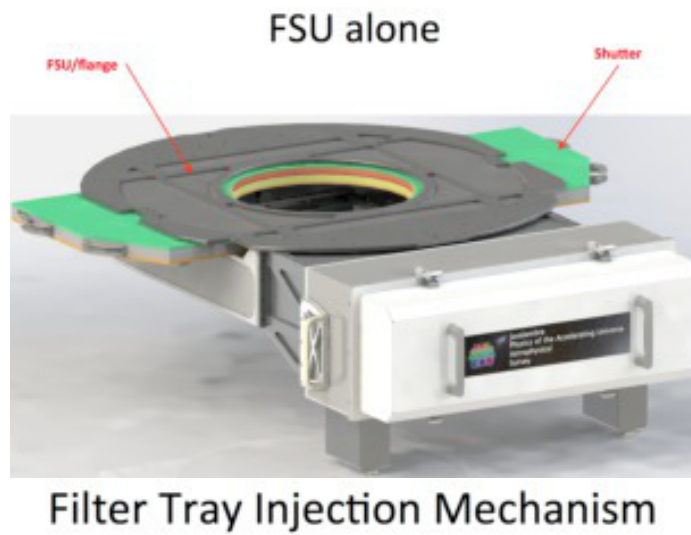


Figure 65: JPCam FSU (upper panel) and a closer view to the filter tray injection mechanism (lower panel)

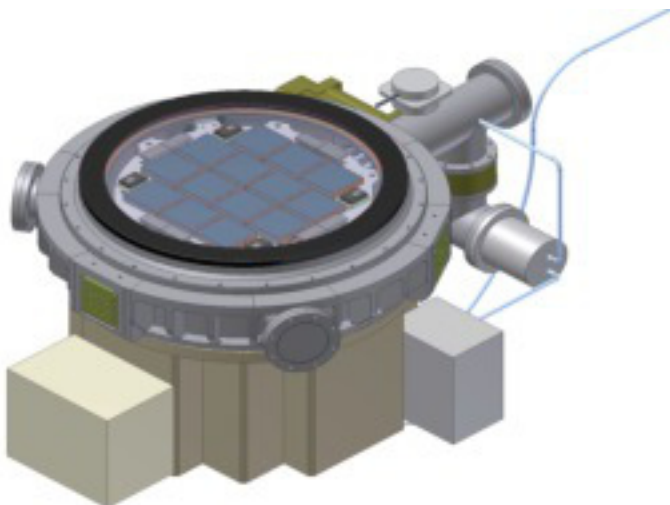


Figure 66: JPCam CryoCam design

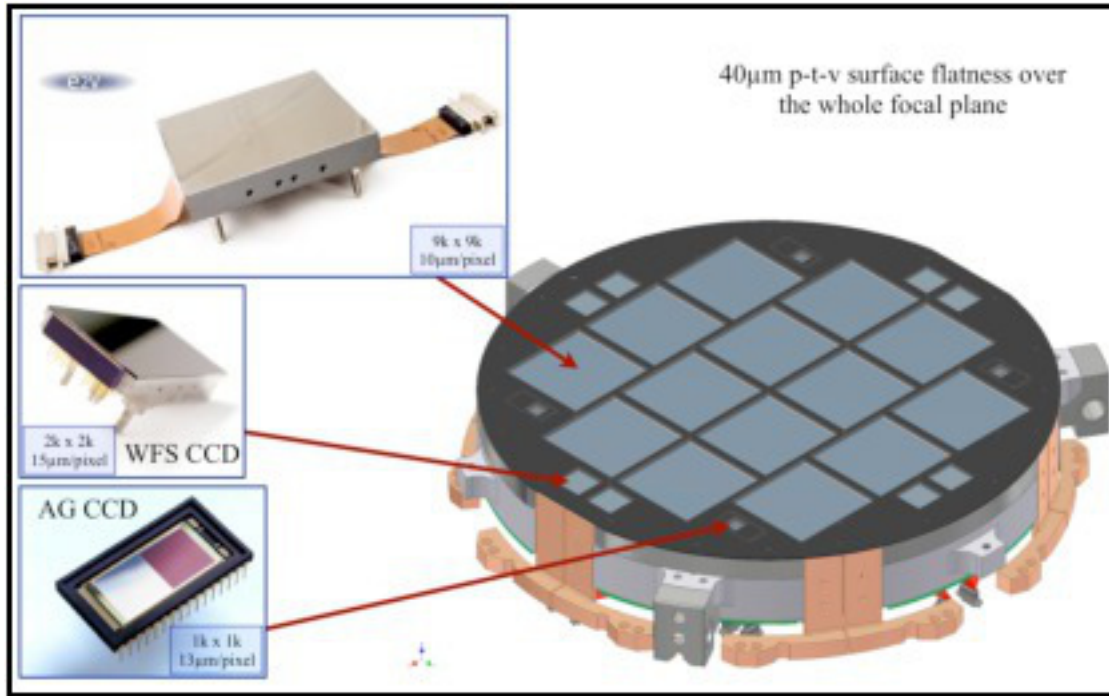


Figure 67: JPCam's focal plane layout as supplied by e2v. The 14 loosely packed, full-wafer, e2v science sensors are shown mounted on the FPCP. In the periphery are mounted 4, 1k2 frame-transfer (FT) guide CCDs and 4 pairs of 2k2 FT WFSs. The black surface on top of the CCD mosaic is the light baffle intended to remove any undesired reflections inside the CryoCam. Thermal links are also shown.

Finally, in order to prevent frost and/or condensation from forming on the large (about 550mm diameter) dewar window, the FSU will be sealed and over-pressured with N₂.

10.2.3. The Camera System(Cryocam)

The CryoCam is being supplied by e2v. The CryoCam design is shown in Figure 66, while the layout of the focal plane cold plate is given in Figure 67, where the 14 science sensors and 12 auxiliary guide and WFS CCDs are shown.

The data from the sensors is gathered in the Detector Electronics Box and transmitted via four Camera Link ports to three PCs, the science data, the AG and the WFS PCs. Two fibre optic channels are used to transmit the Science CCD data to reduce the data transmission time. The time to transfer a full image from JPCam to the science data PC is 8.4s, lower than the read out time.

The format of one science CCD image data is shown in Figures 68. The entire CCD is currently read out as if it were a single large image (9728 pixels wide x 9265 pixels high) and an additional line of status data is appended on the end.

The cryostat will be cryo-cooled to an operating temperature between -100C and -110C with cold nitrogen gas. A large LN₂ tank, mounted on the telescope fork, will feed the cryostat through routing of the flexible cooling lines via the telescope cable wraps, as required to accommodate both cassegrain and altitude rotation.

The chamber will be evacuated to a level of 10⁻⁶ Torr using a cryostat mounted turbo-pump that will run continuously into a Mini-Roots-dry-backing-pump mounted at some distance at the telescope fork where the liquid nitrogen tank is mounted. The two pumps will be connected through small bore flexible Stainless Steel Tubing routed through the telescope cable wrap.

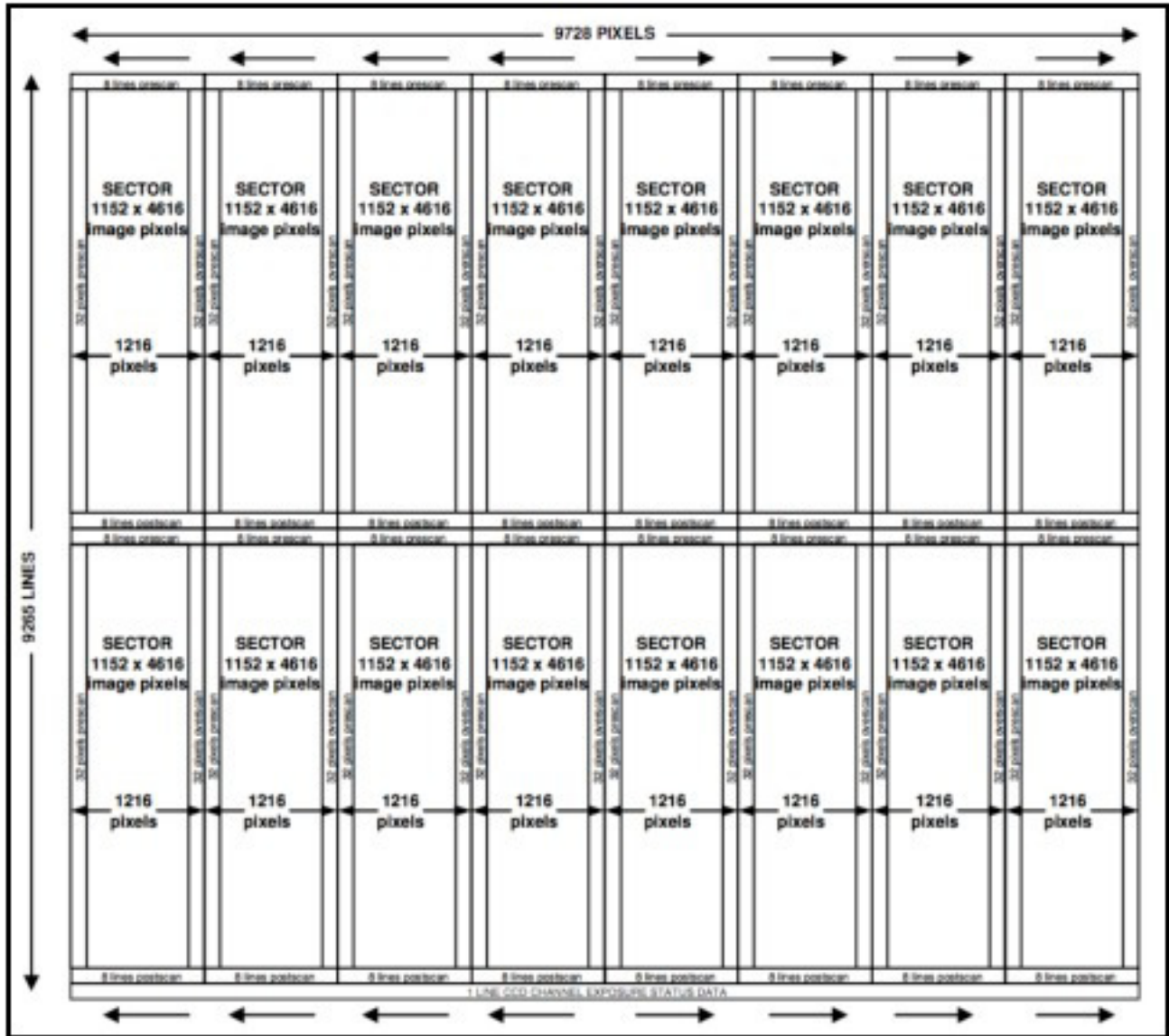


Figure 68: Science CCD array Camera Link frame format (no binning).

The camera entrance window is in fact the fourth element of the JST/T250 field corrector, and together with the filters, it is part of the telescope optical design optimization. The window is a 545mm diameter and 27mm thick, weakly powered field-flattener with an 8mm distance between its inner surface and the focal plane mosaic.

Summarizing, JPCam design has been driven by the main science goal defined by the J-PAS collaboration, that is, the J-PAS survey. The commissioning and acceptance of JPCam is planned for mid 2015, so the J-PAS survey should will start in late 2015.

11. The J-PAS Collaboration

11.1. A Brief History of J-PAS

J-PAS stands for Javalambre-PAU Astrophysical Survey, and its starting point was in 2006, when the Spanish Government opened a call for proposals focused on large projects, the so-called “Consolider” grants. A collaboration of Spanish groups, composed of High Energy physicists and astrophysicists, which called itself PAU (Physics of the Accelerated Universe), led by Enrique Fernández, a high energy physicist from IFAE, applied for funding for several Dark Energy projects in which they were involved. The proposal was received positively, but the referee appointed by the Ministry required the groups to focus on a new, single large Dark Energy project instead of scattering the grant money into different efforts.

At that time the most obvious niches in the field of Dark Energy Surveys were already filled, with PanSTARRS and DES covering the broad imaging field and BOSS, the spectroscopic options, so it was not trivial to find a new observational alternative which was truly competitive. Narciso (Txitxo) Benítez, working at the Instituto de Matemáticas and Física Fundamental (CSIC) in Madrid at the time, realized that it was feasible to use narrow band photometric redshifts to reach the precisions required to measure radial Baryonic Acoustic Oscillations $0.033(1+z)$, one of the most promising Dark Energy probes, and in early 2007 proposed the PAU collaboration carrying out a $8000 \square^\circ$ survey using a set of 40 – 50 narrow band filters. This was accepted as the basis of the new proposal, which was submitted to the Ministry, and received 5M€ of funding. The paper Benítez et al. (2009) describes the rationale behind that proposal and still gives a pretty accurate description of much of what J-PAS intends to do.

Almost simultaneously there was a proposal, led by Mariano Moles, of a new observatory at Javalambre, Teruel, Spain, to take advantage of the superb astronomical characteristics of the site, which he had identified in the early 90’s. Both proposals supported each other, PAU providing a competitive scientific case and the OAJ the required astronomical and technical infrastructure.

In 2009, the PAU collaboration split in two. A part of the collaboration decided to use the bulk of the PAU funds to build a $< 1 \square^\circ$ camera for the William Herschel Telescope to carry out a $100 - 200 \square^\circ$ survey with a similar observational set-up as the one described in Benítez et al. (2009), but with an area 80 times smaller and different scientific goals (Gaztañaga et al., 2012). They retained the name of PAU-Survey. The remainder of the collaboration, centered in Granada, Teruel and Valencia, decided to continue with the original survey idea and develop the project from Javalambre, where a dedicated 2.5m telescope is being specifically build for this project. The project was open to the Brazilian Astronomical community as equal partners in 2009 and founded again as J-PAS. Most of the funding for the construction of the JPCam has been provided by Brazilian grants led by Renato Dupke, Claudia Mendes de Oliveira y Laerte Sodré. The first of the J-PAS biannual meetings was held in Granada, in October of 2010.

11.2. Organizational structure

The Figure shows the management structure that is being used by the Collaboration to carry out the J-PAS project and by the Collaboration Board to oversee the J-PAS Project, including their interfaces with OAJ facilities. Finally, it is being used to organize and coordinate the scientific work of the Collaboration.

11.2.1. The Collaboration Board

The Collaboration Board is composed of one member from each Institution providing financial resources involved in the Collaboration. It conducts periodic reviews of the J-PAS Projects, costs, goals and scientific. The current members of the Collaboration Board are Narciso Benítez (IAA-CSIC), Renato Dupke (ON), Mariano Moles (CEFCA) and Laerte Sodré (IAG-USP).

11.3. The Survey Management Committee

The Survey Management Committee (SMC) is the body to organize, articulate and coordinate all the necessary activities to achieve the goals of the Collaboration. The SMC brings the skills and efforts of the Members and Participants into the Projects and assists the Project Managers in coordinating the contributions of the Collaboration and the Collaborating Institutions.

The OAJ Project Manager and the Cameras Project Manager are responsible for the preparation of the documents on the Installation and Commissioning Plans for the T80Cam and JPCam and for the Operations and Maintenance Plan.

Apart from the members of the Collaboration Board, which are natural part of the SMC, the other members are Javier Cenarro (CEFCA), Jordi Cepa (IAC), Alberto Fernández-Soto (UV), Antonio Marín (CEFCA), Claudia Mendes de Oliveira (IAG-USP) and Keith Taylor (ON).

11.3.1. Scientific Directors

The Scientific Directors coordinate the activities at the systems interfaces of the J-PAS Projects and the contributions of the Collaboration for the installation, commissioning and operation phases of the Survey; serve as the principal point of contact between the Survey Management Committee and the Collaboration Board and represent the Collaboration in interactions with the Collaboration Board and the Collaborating Institutions. They also are responsible for coordinating the scientific activities of the Science Working Groups (SWGs) and appointing the SWG and Science Groups (SG) heads.

The Scientific Directors of J-PAS are Narciso Benítez (IAA-CSIC) and Renato Dupke (ON).

11.3.2. Science Working Groups and Science Groups

The scientific activities of J-PAS are divided into broad Science Working Groups (SWG), namely Observational Cosmology, Theory, Galaxy Evolution, Resolved Stellar Populations, Transients and Solar System. The heads of the SWGs are responsible for assessing, assisting the SGs and evaluating the timetable to achieve the collaborations scientific immediate practical goals. The heads of these SWGs propose how to organize the research within each of these areas into smaller Science Groups, and nominate the SG heads.

11.4. Authorship Policy

The J-PAS collaboration recognizes three types of papers:

- core papers – Presentation paper and data releases. These are major which present a fundamental J-PAS aspect or dataset. The CB decides which papers are considered core papers. Any member has the right to sign a core paper. External Collaborators can sign the core papers if the coordinator of the corresponding SG can confirm their contribution
- regular papers – These papers are defined by the SWGs and SGs. Any member of the collaboration can propose a paper on a given subject and any other member of the collaboration can ask to be part of that publication.

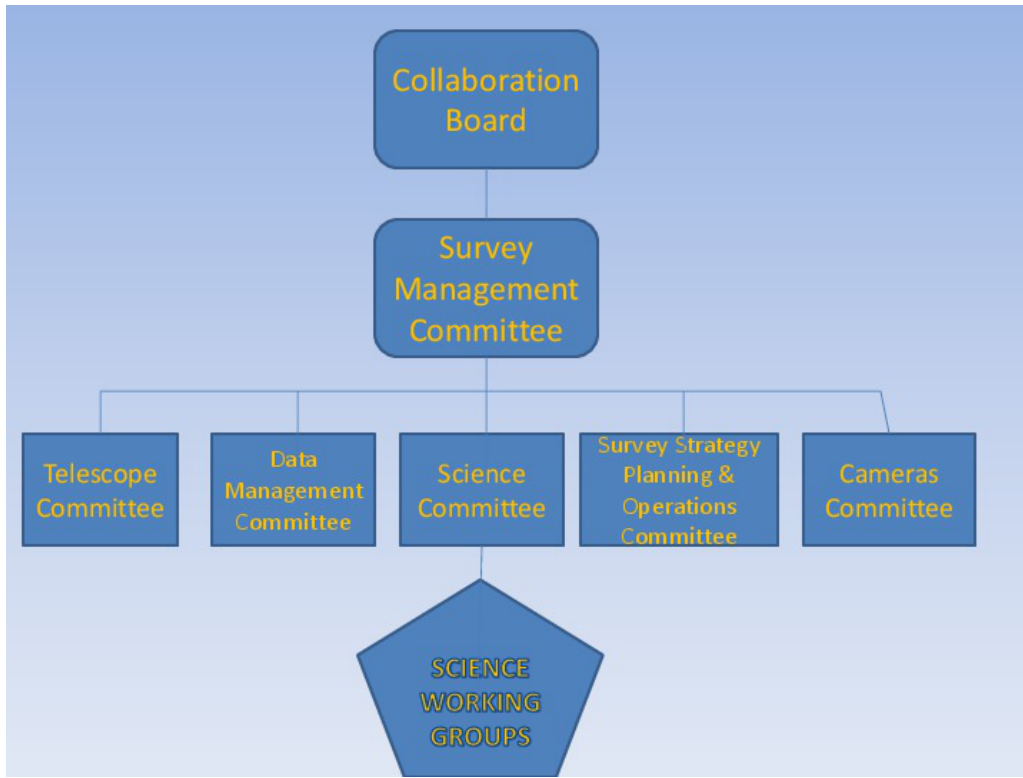


Figure 69:

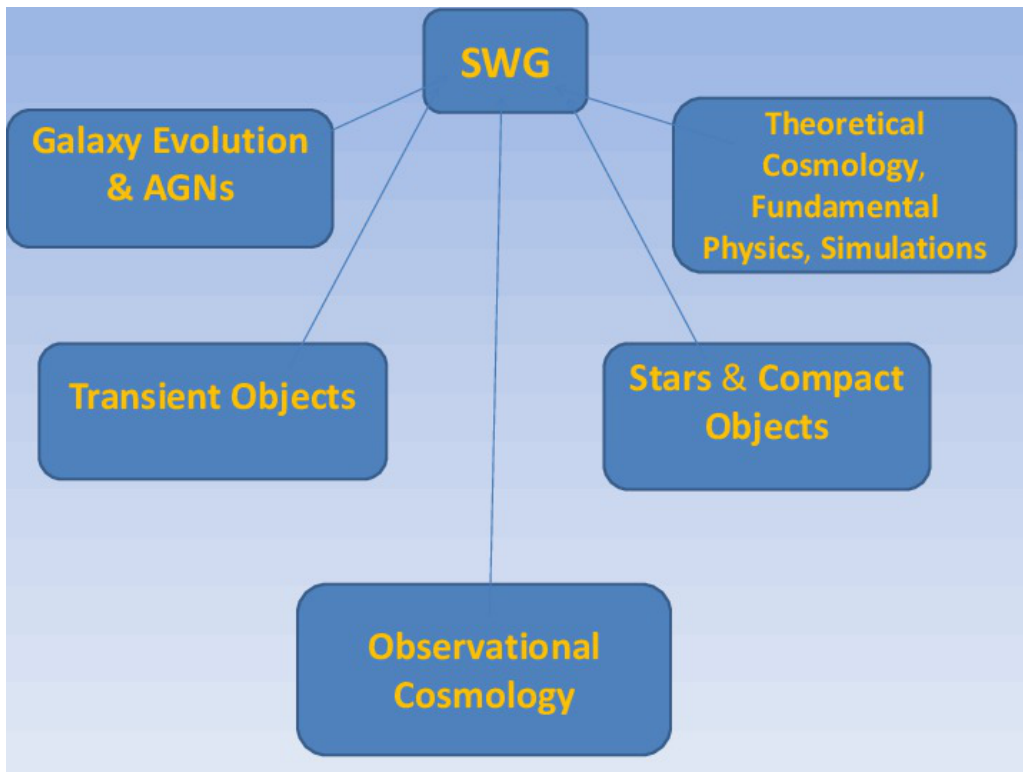


Figure 70:

SG heads in agreement with SWG heads decide who should lead the papers and the co-authors list, always encouraging the collaboration between the members; in case of doubt, or if a dispute arises regarding authorship, the Scientific Directors and ultimately the CB has the last word on issues of authorship. In cases of doubt, preferences will be given to junior collaborators.

Generally speaking, these papers can be signed only by the group that actually did the work (including technical contributions). In the case of papers led by graduate students, this rule should be applied even more stringently.

Builders have also the right to sign the 1st paper of each SG.

The SGs are responsible for determining the time at which a regular paper should be announced to the SG/WG and the rest of the collaboration. In principle, once first results are obtained, the paper should be announced at the SG/WG level. At first draft the collaboration should be aware and given the chance to comment and participate (at the minimum the collaboration shall have 2 weeks to review/comment)

- conference papers. Conference papers are defined as such by the SWGs and aim to publish J-PAS results in scientific meetings. Conference papers as well as seminars must be approved by the SG/SWGs; in case of doubt or dispute, the CB has the last word about who can speak on behalf of the collaboration. Conference papers can be signed by a few people + on behalf of J-PAS Collaboration.

Papers should be circulated to the SGs/SWGs and CB at least two weeks prior to submission or to making the paper public in any form. The authorship order in a paper should give preference to who did the work, including junior collaborators.

Members are not allowed to divulge or discuss either preliminary or final results, as well as any sensitive information relating to the core or parallel science of the project, without express and written agreement from the SGs/SWGs or the CB, if relevant.

11.5. Data Policy

Rights to scientific images and data, including, but not limited to, images, databases, catalogs, and scientific works will be determined in accordance with internal applicable data rights policies.

12. Acknowledgments

The main agencies supporting J-PAS are the Gobierno de Aragón, the Spanish MINECO, the Ministry of Science Technology and Innovation (MCTI) of Brazil, The National Observatory/MCTI, FAPERJ, FAPESP and CNPq.

References

- Abadi, M. G., Navarro, J. F., Steinmetz, M., & Eke, V. R. 2003, *Astrophys. J.*, 591, 499
- Abdalla, E., L. R. Abramo and J. C. C. de Souza, *Phys. Rev. D* **82**, 023508 2010
- Abdalla, E., L. R. W. Abramo, L. Sodré, Jr. and B. Wang, 2009 *Phys. Lett. B* **673**, 107
- Abramo, L. R. 2012, *Mon. Not. R. Astron. Soc.*, 420, 2042
- Abramo, L. R., Strauss, M. A., Lima, M., et al. 2012, *Mon. Not. R. Astron. Soc.*, 423, 3251
- Abramo, L. R. & Leonard, K. E. 2013, *Mon. Not. R. Astron. Soc.*, 432, 318
- Acquaviva, V. and Hajian, A. and Spergel, D. N. and Das, S., 2008, *Phys. Rev. D*, 78, 043514
- Adelberger K. L., Steidel C. C., 2005a, *Astrophys. J.*, 630, 50
- Adelberger K. L., Steidel C. C., 2005b, *Astrophys. J. Lett.*, 627, L1
- ADEPT 2008, http://www7.nationalacademies.org/ssb/BE_Nov_2006_bennett.pdf
- Aguerri, J. A. L., Iglesias-Paramo, J., Vilchez, J. M., & Muñoz-Tuñón, C. 2004, *Astron. J.*, 127, 1344
- Albrecht, A., et al. 2006, The Dark Energy Task Force (DETF) report, arXiv:astro-ph/0609591
- Alcaniz, J.S., Jain, D. and Dev, A., *Phys. Rev. D* 67 (2003) 043514;
- Alcaniz, J.S. and J. A. S. Lima, *Phys. Rev. D* **72**, 063516 2005
- Alcaniz, J. S. and Lima, J. A. S. *Astrophys. J.* 618 (2005) 16.
- Alcaniz J. S., Borges H. A., Carneiro S., Fabris J. C., Pigozzo C., Zimdahl W., 2012, *Phys. Lett. B*, 716, 165
- Alcock, C., Paczynski, B. 1979, *Nature* 281, 358
- Allen, S. W., Evrard, A. E., & Mantz, A. B. 2011, *Annu. Rev. Astron. Astrophys.*, 49, 409
- Alnes, H., Amarzguioui, M. and Grn, ., *Phys. Rev. D*, 73, 083519 2006
- Alves, David R.; Bond, Howard E.; Onken, Christopher 2001, *Astron. J.*, 121, 318
- Amblard A., Cooray A., Serra P., et al., 2010, *Astron. Astrophys.*, 518, L9
- Amendola, L. *Phys. Rev. D* **62**, 043511 2000
- Amendola, L., Appleby, S., Bacon, D., et al. 2012, arXiv:1206.1225
- Amendola, L., M. Kunz and D. Sapone, *JCAP* **0804**, 013 2008 .
- Anderson, L., Aubourg, E., Bailey, S., et al. 2013, arXiv:1303.4666
- Anderson, L., Aubourg, E., Bailey, S., et al. 2012, *Mon. Not. R. Astron. Soc.*, 427, 3435
- Andreon, S. 2008, *Mon. Not. R. Astron. Soc.*, 386, 1045
- Andreon, S., & Bergé, J. 2012, *Astron. Astrophys.*, 547, A117
- Angulo, R. E., Baugh, C. M., Frenk, C. S., & Lacey, C. G. 2008, *Mon. Not. R. Astron. Soc.*, 383, 755
- Angulo R. E., Springel V., White S. D. M., Jenkins A., Baugh C. M., Frenk C. S., 2012, *Mon. Not. R. Astron. Soc.*, 426, 2046

- Angulo R. E., Baugh C. M., Frenk C. S., Lacey C. G., 2013, ArXiv e-prints
- Aoki, W., Frebel, A., Christlieb, N., et al. 2006, Origin of Matter and Evolution of Galaxies, 847, 53
- Aparicio Villegas, T., Alfaro, E. J., Cabrera-Caño, J., et al. 2010, Astron. J., 139, 1242
- Aparicio Villegas, T., Alfaro, E. J., Cabrera-Caño, J., et al. 2011, Journal of Physics Conference Series, 328, 012004
- Aragón-Calvo M. A., Jones B. J. T., van de Weygaert R., van der Hulst J. M., 2007, Astron. Astrophys., 474, 315
- Arhipova, V. P.; Burlak, M. A.; Esipov, V. F.; Ikonnikova, N. P.; Komissarova, G. V. 2012, Astronomy Letters, 38, 157
- Armendariz-Picon, C., 2004, *JCAP*, **0407**, 007
- Arnalte-Mur, P., Martínez, V. J., Norberg, P., et al. 2013, arXiv:1311.3280
- Ascaso, B., Aguerri, J. A. L., Varela, J., Cava, A., Bettoni, D., Moles, M., & D'Onofrio, M. 2011, *Astrophys. J.*, 726, 69
- Ascaso, B., Wittman, D., & Benítez, N. 2012, *Mon. Not. R. Astron. Soc.*, 420, 1167
- Ascaso, B., Lemaux, B. C., Lubin, L. M., et al. 2013, arXiv:1309.6643
- Ascaso, B. 2013, Highlights of Spanish Astrophysics VII, 115
- Ascaso, B., Wittman, D., & Dawson, W. 2014, *Mon. Not. R. Astron. Soc.*, 242
- Ashman, K. M., & Zepf, S. E. 2001, *Astron. J.*, 122, 1888
- Astier, P., et al. 2006, *Astron. Astrophys.*, 447, 31
- Baker, N. 1966, in *Stellar Evolution*, ed. R. F. Stein, & A. G. W. Cameron (Plenum, New York) 333
- Baillard, A., Bertin, E., de Lapparent, V., et al. 2011, *Astron. Astrophys.*, 532, A74
- Baldwin, J. A., Phillips, M. M., & Terlevich, R. 1981, *PASP*, 93, 5
- Ballinger W. E., Peacock J. A, Heavens A. F. 1996, *Mon. Not. R. Astron. Soc.*, 281, 877
- Balluch, M. 1988, *A&A*, 200, 58
- Bardeen, J. M., Bond, J. R., Kaiser, N., & Szalay, A. S. 1986, *Astrophys. J.*, 304, 15
- Barreiro, R. B., Vielva, P., Hernandez-Monteagudo, C., & Martinez-Gonzalez, E. 2008, *IEEE Journal of Selected Topics in Signal Processing*, 2, 747
- Barreiro, R. B., Vielva, P., Marcos-Caballero, A., & Martinez-Gonzalez, E. 2012, ArXiv e-prints
- Bartelmann, M., Huss, A., Colberg, J. M., Jenkins, A., & Pearce, F. R. 1998, *Astron. Astrophys.*, 330, 1
- Bartelmann M., Schneider P., 2001, *Phys. Rep.*, 340, 291
- Barton, E. J., Geller, M. J., & Kenyon, S. J. 2000, *Astrophys. J.*, 530, 660
- Basett, B. et al. 2005, arXiv:astro-ph/0510272
- Baum, W. A. 1962, *Problems of Extra-Galactic Research*, 15, 390
- Baumgardt, H., Makino, J., & Ebisuzaki, T. 2004, *Astrophys. J.*, 613, 1143

Bayliss, M. B., Gladders, M. D., Oguri, M., et al. 2011, *Astrophys. J. Lett.*, 727, L26

Beck-Winchatz, B., & Anderson, S. F. 2007, *Mon. Not. R. Astron. Soc.*, 374, 1506

Becker, R. H., White, R. L., & Helfand, D. J. 1995, *Astrophys. J.*, 450, 559

Beers, T. C., Preston, G. W., & Schectman, S. A. 1992, *Bulletin of the American Astronomical Society*, 24, 824

Bekenstein, J. D., 2004 *Phys. Rev. D* **70**, 083509 [Erratum-ibid. *D* **71**, 069901 2005] [astro-ph/04(3694)].

Bell, E. F., Wolf, C., Meisenheimer, K., et al. 2004, *Astrophys. J.*, 608, 752

Beltrán Jimenez, J. and A. L. Maroto, 2009, *JCAP* **0902**, 025

Beltrán Jimenez, J. and A. L. Maroto, *JCAP*, 2009, **0903**, 016

Beltrán Jimenez, J. and A. L. Maroto, 2009, J. Beltran Jimenez and A. L. Maroto, *Phys. Rev. D* **80**, 063512

Benítez, N. 2000, *Astrophys. J.*, 536, 571

Benítez, N., Ford, H., Bouwens, R., et al. 2004, *Astrophys. J. S. S.*, 150, 1

Benítez, N., Gaztañaga, E., Miquel, R., et al. 2009, *Astrophys. J.*, 691, 241

Benítez, N., et al. 2009, *ApJL*, 692, 5L

Benítez, N., in preparation

Benítez-Llambay A., Navarro J. F., Abadi M. G., Gottlöber S., Yepes G., Hoffman Y., Steinmetz M., 2013, *Astrophys. J. Lett.*, 763, L41

Benjamin J., van Waerbeke L., Ménard B., Kilbinger M., 2010, *Mon. Not. R. Astron. Soc.*, 408, 1168

Bennett, C. L., Halpern, M., Hinshaw, G., et al., 2003, *Astrophys. J. S. S.*, 148, 1

Bennett, C. L., Hill, R. S., Hinshaw, G., et al., 2011, *Astrophys. J. S. S.*, 192, 17

Benson, A. J., Cole, S., Frenk, C. S., Baugh, C. M., & Lacey, C. G. 2000, *Mon. Not. R. Astron. Soc.*, 311, 793

Bentz, M. C. et al. 2004, *ApJ*, 600, 19

Bernardeau, F., Colombi, S., Gaztañaga, E., & Scoccimarro, R. 2002, *Phys. Rep.*, 367, 1

Bernardi, M., Hyde, J. B., Sheth, R. K., Miller, C. J., & Nichol, R. C. 2007, *Astron. J.*, 133, 1741

Bernstein, G. M. 1994, *Astrophys. J.*, 424, 569

Bernstein, G. and B. Jain 2004, *Astrophys. J.*, 600, 17

Bertin, E., & Arnouts, S. 1996, *A&AS*, 117, 393

Bertin, E., Mellier, Y., Radovich, M., et al. 2002, *Astronomical Data Analysis Software and Systems XI*, 281, 228

Bertolami, O., Sen, A. A., Sen, S. and Silva, P. T., *Mon. Not. Roy. Astro. Soc.*, 353 (2004) 329;

Bertschinger, E. 2006, *Astrophys. J.*, 648, 797

Bessell, M. S., & Norris, J. 1984, *Astrophys. J.*, 285, 622

Bessell, M. & Murphy, S. 2012, *PASP*, 124, 140

Best, P. N., Lehnert, M. D., Miley, G. K., Röttgering, H. J. A. 2003, *Mon. Not. R. Astron. Soc.*, 343, 1

Best, P. N. 2004, *Mon. Not. R. Astron. Soc.*, 351, 70

Best, P. N., Kauffmann, G., Heckman, T. M., & Ivezić, Ž. 2005, *Mon. Not. R. Astron. Soc.*, 362, 9

Best, P. N., & Heckman, T. M. 2012, *Mon. Not. R. Astron. Soc.*, 421, 1569

Bhattacharya, S., Habib, S., Heitmann, K., & Vikhlinin, A. 2013, *ApJ*, 766, 32

Bian, F., Fan, X., Jiang, L., et al. 2012, *Astrophys. J.*, 757, 139

Bica, E., Alloin, D., & Schmidt, A. A. 1990, *Astron. Astrophys.*, 228, 23

Bielby, R., Shanks, T., Sawangwit, U., et al. 2010, *Mon. Not. R. Astron. Soc.*, 403, 1261

Bilic, N., Tupper, G. B., and Viollier, R. D., *Phys. Lett. B*, 535 2002 ; Bento, M. C., Bertolami, O. and Sen, A. A., *Phys. Rev.*, D66 2002 , 043507;

Blake, C., Bridle, S. 2005, *Mon. Not. R. Astron. Soc.*, 363, 1329

Blake, C. & Bridle, S. 2005, *Mon. Not. R. Astron. Soc.*, 363, 1329

Blake, C., Davis, T., Poole, G. B., et al. 2011, *Mon. Not. R. Astron. Soc.*, 415, 2892

Blake, C., Kazin, E. A., Beutler, F., et al. 2011, *Mon. Not. R. Astron. Soc.*, 418, 1707

Blake, C., Glazebrook, K. 2003, *Astrophys. J.*, 594, 665

Blakeslee, J. P., et al. 2003, *Astrophys. J.*, 596, L143

Blanton, M. R., Eisenstein, D., Hogg, D. W., & Zehavi, I. 2006, *Astrophys. J.*, 645, 977

Berrier, J. C., Stewart, K. R., Bullock, J. S., et al. 2009, *Astrophys. J.*, 690, 1292

Blanc, G. A., Weinzirl, T., Song, M., et al. 2013, *Astron. J.*, 145, 138

Blanton, M. R., Hogg, D. W., Bahcall, N. A., et al. 2003, *Astrophys. J.*, 592, 819

Bohlin, R. C. 1996, *Astron. J.*, 111, 1743

Bolzonella, M., Kovač, K., Pozzetti, L., et al. 2010, *Astron. Astrophys.*, 524, A76+

Bond, Howard E.; Alves, David R. 2001 arXiv:104096

Bongiovanni, A., Oteo, I., Cepa, J., et al. 2010, *Astron. Astrophys.*, 519, L4

Booth, R. S., de Blok, W. J. G., Jonas, J. L., & Fanaroff, B. 2009, arXiv:0910.2935

Borgani, S., Rosati, P., Tozzi, P., Stanford, S. A., Eisenhardt, P. R., Lidman, C., Holden, B., Della Ceca, R., Norman, C., & Squires, G., 2001, *Astrophys. J.*, 561, 13

Borgani, S., Murante, G., Springel, V., et al. 2004, *Mon. Not. R. Astron. Soc.*, 348, 1078

Borges, H.A. and S. Carneiro, 2005, *Gen. Rel. Grav.* 37, 1385

Borges H. A., Carneiro S., Fabris J. C., Pigozzo C., 2008, *Phys. Rev. D*, 77, 043513

Bournaud, F., Chapon, D., Teyssier, R., et al. 2011, *Astrophys. J.*, 730, 4

Botzler, C. S., Snigula, J., Bender, R., & Hopp, U. 2004, *Mon. Not. R. Astron. Soc.*, 349, 425

Boughn, S. & Crittenden, R. 2004, *Nature*, 427, 45

Boughn, S. P. & Crittenden, R. G. 2002, *Physical Review Letters*, 88, 021302

Bowell et al. 1989, 524, Asteroids II, Ed. Binzel, Gehrels and Matthews, 524

Bower, R. G., Morris, S. L., Bacon, R., et al. 2004, Mon. Not. R. Astron. Soc., 351, 63

Bower, R. G., Benson, A. J., Malbon, R., et al. 2006, Mon. Not. R. Astron. Soc., 370, 645

Brammer, G. B., van Dokkum, P. G., Illingworth, G. D., et al. 2013, Astrophys. J. Lett., 765, L2

Brans, C. and R. H. Dicke, Phys. Rev. **124**, 925 1961.

Bridge, C. R., Carlberg, R. G., & Sullivan, M. 2010, Astrophys. J., 709, 1067

Bridge, C. R., Blain, A., Borys, C. J. K., et al. 2013, Astrophys. J., 769, 91

Broadhurst, T. J., Taylor, A. N., & Peacock, J. A. 1995, ApJ, 438, 49

Broadhurst, T., Benítez, N., Coe, D., et al. 2005, Astrophys. J., 621, 53

Brodie, J. P., & Strader, J. 2006, Annu. Rev. Astron. Astrophys., 44, 193

Brook, C. B., Kawata, D., Gibson, B. K., & Freeman, K. C. 2004, Astrophys. J., 612, 894

Brookes, M. H., Best, P. N., Peacock, J. A., Röttgering, H. J. A., & Dunlop, J. S. 2008, Mon. Not. R. Astron. Soc., 385, 1297

Brown, M. J. I., Dey, A., Jannuzi, B. T., Brand, K., Benson, A. J., Brodwin, M., Croton, D. J., & Eisenhardt, P. R. 2007, Astrophys. J., 654, 858

Bruzual A., G. 1983, Astrophys. J., 273, 105

Bruzual, G. & Charlot, S. 2003, MNRAS 344, 1000

Budavári, T., Szalay, A. S., Connolly, A. J., Csabai, I., & Dickinson, M. 2000, Astron. J., 120, 1588

Buitrago, F., Trujillo, I., Conselice, C. J., et al. 2008, Astrophys. J. Lett., 687, L61

Bullock, J. S., Kolatt, T. S., Sigad, Y., et al. 2001, MNRAS, 321, 559

Burgarella, D., Le Floch, E., Takeuchi, T. T., et al. 2007, Mon. Not. R. Astron. Soc., 380, 986

Burgarella, D. et al. 2011, ApJ 734, 12

Burke, C., & Collins, C. A. 2013, arXiv:1307.1702

Buttiglione, S., Capetti, A., Celotti, A., et al. 2010, Astron. Astrophys., 509, A6

Cabré, A. & Gaztañaga, E. 2009, Mon. Not. R. Astron. Soc., 396, 1119

Cacciari, C., & Clementini, G. 2003, Stellar Candles for the Extragalactic Distance Scale, 635, 105

Caldwell, R.R. and M. Kamionkowski, Ann. Rev. Nucl. Part. Sci. **59**, 397 2009

Caldwell, R. R. and Linder, E. V., Phys.Rev.Lett. 95 2005 141301; Alcaniz, J. S. et al. Class.Quant.Grav. 26 2009 105023

Calvi, R., Poggianti, B. M., Vulcani, B., & Fasano, G. 2013, Mon. Not. R. Astron. Soc., 432, 3141

Camera, S., Santos, M. G., Bacon, D. J., et al. 2012, Mon. Not. R. Astron. Soc., 427, 2079

Campbell, H. et al. 2013 . ApJ, 763, 88.

Capak, P. et al. 2007, arXiv:0704.2430

Capozziello, S. and M. Francaviglia, *Gen. Rel. Grav.* **40**, 357 2008

Cappellari, M., Emsellem, E., Krajnović, D., et al. 2011, *Mon. Not. R. Astron. Soc.*, 416, 1680

Cardelli, J. A., Clayton, G. C., & Mathis, J. S. 1989, *Astrophys. J.*, 345, 245

Carilli, C. L., & Rawlings, S. 2004, *New Astronomy Reviews*, 48, 979

Carneiro S., Pigozzo C., Borges H. A., Alcaniz J. S., 2006, *Phys. Rev. D*, 74, 023532

Carneiro S., Dantas M. A., Pigozzo C., Alcaniz J. S., 2008, *Phys. Rev. D*, 77, 083504

Carroll, S.M., V. Duvvuri, M. Trodden and M. S. Turner, *Phys. Rev. D* **70**, 043528 2004

Carroll, S. M., Duvvuri, V., Trodden, M., & Turner, M. S. 2004, *Phys. Rev. D*, 70, 043528

Carvalho, J. C., Lima, J. A. S. and Waga, I., *Phys. Rev. D*46 (1992) 2404;

Cassata, P., Cimatti, A., Franceschini, A., et al. 2005, *Mon. Not. R. Astron. Soc.*, 357, 903

Castander et al. 2012, 8446

Castro-Tirado, A. J., de Ugarte Postigo, A., Gorosabel, J., et al. 2008, *Nature*, 455, 506

Catelan, M., Pritzl, B. J., & Smith, H. A. 2004, *Astrophys. J. S. S.*, 154, 633

Celerier, M.N. 2000, *Astron. Astrophys.* 353, 64

Cen, R. & Ostriker, J. P. 1999, *Astrophys. J.*, 514, 1

Cen, R. & Ostriker, J. P. 2006, *Astrophys. J.*, 650, 560

Cenarro, A. J., Beasley, M. A., Strader, J., Brodie, J. P., & Forbes, D. A. 2007, *Astron. J.*, 134, 391

Cenarro, A. J., Moles, M., Cristóbal-Hornillos, D., et al. 2010, *Proc. SPIE*, 7738,

Cenarro, A. J., Cristóbal-Hornillos, D., Gruel, N., et al. 2011, *Highlights of Spanish Astrophysics VI*, 680

Cenarro, A. J., Cristóbal-Hornillos, D., Gruel, N., et al. 2011, *Highlights of Spanish Astrophysics VI*, 771

Cenarro, A. J., Moles, M., Cristóbal-Hornillos, D., et al. 2012, *Proc. SPIE*, 8448,

Cenarro, A. J., Moles, M., Cristóbal-Hornillos, D., et al. 2013, *Highlights of Spanish Astrophysics VII*, 862

Cezario, E., Coelho, P. R. T., Alves-Brito, A., Forbes, D. A., & Brodie, J. P. 2013, *Astron. Astrophys.*, 549, A60

Chen, Y.-M., Kauffmann, G., Heckman, T. M., et al. 2013, *Mon. Not. R. Astron. Soc.*, 429, 2643

Chevallier, M. & Polarski, D. 2001, *Int. J. Mod. Phys. D*, 10, 213

Chiang, Y.-K., Overzier, R., & Gebhardt, K. 2013, arXiv:1310.2938

Chiba, T., Smith, T. L., & Erickcek, A. L. 2007, *Phys. Rev. D*, 75, 124014

Chilingarian, I. V. 2009, *Mon. Not. R. Astron. Soc.*, 394, 1229

Chiosi, C., & Carraro, G. 2002, *Mon. Not. R. Astron. Soc.*, 335, 335

Christensen, L., Jahnke, K., Wisotzki, L., & Sánchez, S. F. 2006, *Astron. Astrophys.*, 459, 717

Christlieb, N., Gustafsson, B., Korn, A. J., et al. 2004, *Astrophys. J.*, 603, 708

Choudhury, T. R., & Ferrara, A. 2006, *Mon. Not. R. Astron. Soc.*, 371, L55

Cid Fernandes, R., Mateus, A., Sodr , L., Stasińska, G., & Gomes, J. M. 2005, *Mon. Not. R. Astron. Soc.*, 358, 363

Clausen, D., & Eracleous, M. 2011, *Astrophys. J.*, 726, 34

Clausen, D., Sigurdsson, S., Eracleous, M., & Irwin, J. A. 2012, *Mon. Not. R. Astron. Soc.*, 424, 1268

Clements D. L., Rigby E., Maddox S., et al., 2010, *Astron. Astrophys.*, 518, L8

Coe, D., Benítez, N., Sánchez, S. F., et al. 2006, *Astron. J.*, 132, 926

Coe, D., Fuselier, E., Benítez, N., et al. 2008, *Astrophys. J.*, 681, 814

Coe, D. & Moustakas, L. A. 2009, *ApJ* 706, 45

Coelho, P., Barbuy, B., Meléndez, J., Schiavon, R. P., & Castilho, B. V. 2005, *Astron. Astrophys.*, 443, 735

Coelho, P., Mendes de Oliveira, C., & Cid Fernandes, R. 2009, *Mon. Not. R. Astron. Soc.*, 396, 624

Coil A. L., Hennawi J. F., Newman J. A., Cooper M. C., Davis M., 2007, *Astrophys. J.*, 654, 115

Colberg, J. M., White, S. D. M., Yoshida, N., et al. 2000, *MNRAS*, 319, 209

Cole S., Hatton S., Weinberg D. H., Frenk C. S., 1998, *Mon. Not. R. Astron. Soc.*, 300, 945

Cole, S., Lacey, C. G., Baugh, C. M., & Frenk, C. S. 2000, *Mon. Not. R. Astron. Soc.*, 319, 168

Cole, S. et al. 2005, *Mon. Not. R. Astron. Soc.*, 362, 505

Colistete Jr., R., Fabris, J. C., Gonçalves, S. V. B., and de Souza, P. E., *Int. J. Mod. Phys. D*13 (2004) 669;

Colless, M., Dalton, G., Maddox, S., et al. 2001, *Mon. Not. R. Astron. Soc.*, 328, 1039

Collins, C. A., Stott, J. P., Hilton, M. et al. 2009, *Nature*, 458, 603

Condon, J. J., Cotton, W. D., Greisen, E. W., et al. 1998, *Astron. J.*, 115, 1693

Conley, A. et al. 2011 . *ApJS*, 192, 1.

Conroy, C., Wechsler, R. H., & Kravtsov, A. V. 2007, *Astrophys. J.*, 668, 826

Conselice, C. J., Gallagher, J. S., III, & Wyse, R. F. G. 2001, *Astrophys. J.*, 559, 791

Conselice, C. J. 2003, *Astrophys. J. S. S.*, 147, 1

Conselice, C. J., Rajgor, S., & Myers, R. 2008, *Mon. Not. R. Astron. Soc.*, 386, 909

Cool, R. J., Eisenstein, D. J., Johnston, D., Scranton, R., Brinkmann, J., Schneider, D. P., & Zehavi, I. 2006, *Astron. J.*, 131, 736

Cooper, A. P., Cole, S., Frenk, C. S., et al. 2010, *Mon. Not. R. Astron. Soc.*, 406, 744

Coupon, J., Ilbert, O., Kilbinger, M., et al. 2009, *Astron. Astrophys.*, 500, 981

Coupon, J., Broadhurst, T., & Umetsu, K. 2013, *ApJ*, 772, 65

Courteau S. & Dekel A. 2001, Proceedings of the “Astrophysical Ages and Time Scales” Conference, ASP Conference series, Vol. 245, p. 584, eds. von Hippel, Manset & Simpson. [arXiv:astro-ph/01(5470)]

Couch, W. J., Ellis, R. S., MacLaren, I., & Malin, D. F. 1991, *Mon. Not. R. Astron. Soc.*, 249, 606

Costa, F.E.M and J. S. Alcaniz, *Phys. Rev. D* **81**, 043506 2010

- Covey, K. R., Ivezić, Ž., Schlegel, D., et al. 2007, *Astron. J.*, 134, 2398
- Covone, G., Sereno, M., Kilbinger, M., & Cardone, V. F. 2014, arXiv:1402.4815
- Cowie, L. L., & Hu, E. M. 1998, *Astron. J.*, 115, 1319
- Cowie, L. L., Barger, A. J., & Hu, E. M. 2010, *Astrophys. J.*, 711, 928
- Cowie, L. L., Hu, E. M., & Songaila, A. 2011, *Astrophys. J. Lett.*, 735, L38
- Cox, J. P. 1980, *Theory of Stellar Pulsation* (Princeton University Press, Princeton) 165
- Cox, A. N., & Stewart, J. N. 1969, *Academia Nauk, Scientific Information* 15, 1
- Cristóbal-Hornillos, D., Aguerri, J. A. L., Moles, M., et al. 2009, *Astrophys. J.*, 696, 1554
- Cristóbal-Hornillos, D., Gruel, N., Varela, J., et al. 2012, *Proc. SPIE*, 8451
- Crittenden, R. G. & Turok, N. 1996, *Physical Review Letters*, 76, 575
- Crocce, M. & Scoccimarro, R. 2006, *Phys. Rev. D*, 73, 063519
- Crocce, M., & Scoccimarro, R. 2008, *Phys. Rev. D* 77, 023533
- Croom, S.M., et al. 2009, *MNRAS*, 399, 1755
- Croom, S. M., Lawrence, J. S., Bland-Hawthorn, J., et al. 2012, *Mon. Not. R. Astron. Soc.*, 421, 872
- Cucciati, O., Iovino, A., Kovač, K., et al. 2010, *Astron. Astrophys.*, 524, A2+
- Cucciati, O., Iovino, A., Marinoni, C., et al. 2006, *Astron. Astrophys.*, 458, 39
- Cuesta A. J., Jeltama T. E., Zandanel F., et al., 2011, *Astrophys. J. Lett.*, 726, L6
- Cunha, C., Huterer, D., & Doré, O. 2010, *Phys. Rev. D*, 82, 023004
- Cypriano, E.S, A. Amara, L. M. Voigt, S. L. Bridle, F. B. Abdalla, A. Réfrégier, M. Seiffert, and J. Rhodes., 2010, *Mon. Not. R. Astron. Soc.*, 405,494
- Da Ângela, J., Outram, P. J., Shanks, T., et al. 2005, *Mon. Not. R. Astron. Soc.*, 360, 1040
- D'Abrusco, R., Staiano, A., Longo, G., Brescia, M., Paolillo, M., De Filippis, E., & Tagliaferri, R. 2007, *Astrophys. J.*, 663, 752
- Daddi, E., Renzini, A., Pirzkal, N., et al. 2005, *Astrophys. J.*, 626, 680
- Dalal, N., Doré, O., Huterer, D., & Shirokov, A. 2008, *Phys. Rev. D*, 77, 123514
- Dalton, G. B., Maddox, S. J., Sutherland, W. J., & Efstathiou, G. 1997, *Mon. Not. R. Astron. Soc.*, 289, 263
- Das, S., Sherwin, B. D., Aguirre, P., et al. 2011, *Physical Review Letters*, 107, 021301
- Dambis, A. K., Berdnikov, L. N., Kniazev, A. Y., et al. 2013, *Mon. Not. R. Astron. Soc.*, 435, 3206
- Davis, M. & Geller, M. J. 1976, *Astrophys. J.*, 208, 13
- Davis, M. & Huchra, J. 1982, *Astrophys. J.*, 254, 437
- Davis, M., & Peebles, P. J. E. 1983, *Astrophys. J.*, 267, 465
- De Breuck, C., van Breugel, W., Röttgering, H. J. A., & Miley, G. 2000, *??jnlA&AS*, 143, 303
- De Felice, A. and Tsujikawa, S., 2010, *Liv. Rev. Relat.*, 13, 3

De Felice, A. and S. Tsujikawa, *Living Rev. Rel.* **13**, 3 2010

De Felice, A. T. Kobayashi and S. Tsujikawa, *Phys. Lett. B* **706**, 123 2011 ; A. De Felice and S. Tsujikawa, *JCAP* **1202**, 007 2012 .

De Felice, A., R. Kase and S. Tsujikawa, *Phys. Rev. D* **83**, 043515 2011 ; H. Okada, T. Totani and S. Tsujikawa, *Phys. Rev. D* **87**, 103002 2013 .

De Jong, R. S, Bellido-Tirado, Chiappini, C., Depagne, É., Haynes, R. and Johl, D. and Schnurr, O. and Schwobe, A., et al., 2012, *SPIE Conference Series*, 8446,1206.6885

De Lucia, G., & Blaizot, J. 2007, *Mon. Not. R. Astron. Soc.*, 375, 2

De Ravel, L., Kampczyk, P., Le Fèvre, O., et al. 2011, *Astron. Astrophys.*, submitted [ArXiv: 1104(5470)]

De Ravel, L., Le Fèvre, O., Tresse, L., et al. 2009, *Astron. Astrophys.*, 498, 379

De Rham, C. and G. Gabadadze, 2010, *Phys. Rev. D* **82**, 044020

De Rham, C., G. Gabadadze, L. Heisenberg and D. Pirtskhalava, 2011 *Phys. Rev. D* **83**, 103516

DeDeo S., Spergel D. N., Trac H., 2005, *ArXiv Astrophysics e-prints*

Deffayet, C., X. Gao, D. A. Steer and G. Zahariade, *Phys. Rev. D* **84**, 064039 2011 ; T. Kobayashi, M. Yamaguchi, J. 'i. Yokoyama, *Prog. Theor. Phys.* **126**, , 511-529 2011 .

Deharveng, J.-M., Small, T., Barlow, T. A., et al. 2008, *Astrophys. J.*, 680, 1072

Dekel, A. & Lahav, O. 1999, *Astrophys. J.*, 520, 24

De Laverny, P., Recio-Blanco, A., Worley, C. C., & Plez, B. 2012, *Astron. Astrophys.*, 544, A126

DES 2008, <http://www.darkenergysurvey.org>

Desjacques, V. & Sheth, R. K. 2010, *Phys. Rev. D*, 81, 023526

Dev, A., Jain, D. and Alcaniz, J. S., *Phys. Rev. D* 67 (2003) 023515;

Dey, A., Bian, C., Soifer, B. T., et al. 2005, *Astrophys. J.*, 629, 654 Heckman, T. M. 2010, *Mon. Not. R. Astron. Soc.*, 407, 1078

Diamond-Stanic, A. M., Moustakas, J., Tremonti, C. A., et al. 2012, *Astrophys. J. Lett.*, 755, L26

L. M. Diaz-Rivera, L. Samushia and B. Ratra, 2006 *Phys. Rev. D* **73**, 083503, [astro-ph/0601153].

Dickinson C., et al. 2004, *Mon. Not. R. Astron. Soc.*, 353, 732

Dijkstra, M., & Loeb, A. 2009, *Mon. Not. R. Astron. Soc.*, 400, 1109

Dodelson, S., *Modern cosmology*, 2003

Dodelson, S., Narayanan, V. K., Tegmark, M., et al. 2002, *Astrophys. J.*, 572, 140

Dolag K., Grasso D., Springel V., Tkachev I., 2005, *JCAP*, 1, 9

Dolgov, A. D. & Kawasaki, M. 2003, *Physics Letters B*, 573, 1

Donoso, E., Best, P. N., & Kauffmann, G. 2009, *Mon. Not. R. Astron. Soc.*, 392, 617

Donoso, E., Li, C., Kauffmann, G., Best, P. N., & Heckman, T. M. 2010, *Mon. Not. R. Astron. Soc.*, 407, 1078

Douspis, M., Castro, P. G., Caprini, C., & Aghanim, N. 2008, *Astron. Astrophys.*, 485, 395

Dressler, A. 1980, *Astrophys. J.*, 236, 351

Dressler, A., Oemler, A., Jr., Couch, W. J., et al. 1997, *Astrophys. J.*, 490, 577

Duffy, A. R., Schaye, J., Kay, S. T., & Dalla Vecchia, C. 2008, *MNRAS*, 390, L64

Dubois, Y., Pichon, C., Devriendt, J., et al. 2013, *Mon. Not. R. Astron. Soc.*, 428, 2885

Dunlop, J. S., & Peacock, J. A. 1990, *Mon. Not. R. Astron. Soc.*, 247, 19

Dunlop, J. S. 2013, *Astrophysics and Space Science Library*, 396, 223

Dupé, F.-X., Rassat, A., Starck, J.-L., & Fadili, M. J. 2011, *Astron. Astrophys.*, 534, A51

Dupke, R. A., & Bregman, J. N. 2001. *Astrophys. J.* 547, 705

Dupke, R. A., & Bregman, J. N. 2001. *Astrophys. J. S. S.* 161, 224

Dvali, G., G. Gabadadze and M. Porrati, 2000, *Phys. Lett.* **B485**, 208

Eales S., Dunne L., Clements D., et al., 2010, *PASP*, 122, 499

Efstathiou, G., Sutherland, W. J. , Maddox, S. J. , 1990 *Nature*, 348, 705-707.

Eggen, O. J., Lynden-Bell, D., & Sandage, A. R. 1962, *Astrophys. J.*, 136, 748

Einasto, M. et al. 2011, arXiv:1105.2124; arXiv:1105.1632.

Eisenstein, D. J., Hu, W., & Tegmark, M. 1998, *Astrophys. J. Lett.*, 504, L57

Eisenstein, D. J., et al. 2003, *Astrophys. J.*, 585, 694

Eisenstein, D. J., et al. 2005, *Astrophys. J.*, 633, 560

Eisenstein, D. J., Seo, H.-J., Sirko, E., & Spergel, D. N. 2007, *Astrophys. J.*, 664, 675

Eisenstein, D. J., Seo, H.-J., & White, M. 2007, *Astrophys. J.*, 664, 660

Eisenstein, D. J., & Hu, W. 1998, *Astrophys. J.*, 496, 605

Ellis, R., Takada, M., Aihara, H., et al. 2012, arXiv:1206.0737

Ellison, S. L., Patton, D. R., Mendel, J. T., & Scudder, J. M. 2011, *Mon. Not. R. Astron. Soc.*, 418, 2043

Ellison, S. L., Patton, D. R., Simard, L., & McConnachie, A. W. 2008, *Astron. J.*, 135, 1877

Elmegreen, B. G., & Efremov, Y. N. 1997, *Astrophys. J.*, 480, 235

Erb, D. K., Bogosavljević, M., & Steidel, C. C. 2011, *Astrophys. J. Lett.*, 740, L31

Faber, S. M., Willmer, C. N. A., Wolf, C., et al. 2007, *Astrophys. J.*, 665, 265

Falco, E. E., Gorenstein, M. V., & Shapiro, I. I. 1985, *Astrophys. J. Lett.*, 289, L1

Fan, L., Lapi, A., De Zotti, G., & Danese, L. 2008, *Astrophys. J. Lett.*, 689, L101

Fasano, G., Vanzella, E., Dressler, A., et al. 2012, *Mon. Not. R. Astron. Soc.*, 420, 926

Fassbender, R., Nastasi, A., Böhringer, H., et al. 2011, *Astron. Astrophys.*, 527, L10

Feldman, H.A., Kaiser, N., Peacock, J.A. 1994, *Astrophys. J.*, 426, 23

Feng, C. Bin Wang, E. Abdalla, Ru-Keng Su. *Phys. Lett.* **B665** 2008 111-119.

Fernandes, C., et al. 2014, in preparation

Fine, S., Shanks, T., Nikoloudakis, N., & Sawangwit, U. 2011, *Mon. Not. R. Astron. Soc.*, 418, 2251

Finkelstein, S. L., Cohen, S. H., Malhotra, S., & Rhoads, J. E. 2009a, *Astrophys. J.*, 700, 276

Finkelstein, S. L., Cohen, S. H., Malhotra, S., et al. 2009b, *Astrophys. J. Lett.*, 703, L162

Fisher, K. B., Davis, M., Strauss, M. A., Yahil, A., & Huchra, J. P. 1993, *Astrophys. J.*, 402, 42

Foley, R. J., Andersson, K., Bazin, G., et al. 2011, *Astrophys. J.*, 731, 86

Folkes, S., Ronen, S., Price, I., et al. 1999, *Mon. Not. R. Astron. Soc.*, 308, 459

Ford, J., Hildebrandt, H., Van Waerbeke, L., et al. 2012, *ApJ*, 754, 143

Foreman, S. et al., 2010, *Phys. Rev. D* 82, 103532

Forero-Romero J. E., Hoffman Y., Gottlöber S., Klypin A., Yepes G., 2009, *Mon. Not. R. Astron. Soc.*, 396, 1815

Fosalba, P., Gaztañaga, E., & Castander, F. J. 2003, *Astrophys. J. Lett.*, 597, L89

Fosalba, P., Gaztañaga, E., Castander, F., & Manera, M. 2007, *arXiv:astro-ph/0711.1540*

Francis, P. J., Woodgate, B. E., Warren, S. J., et al. 1996, *Astrophys. J.*, 457, 490

Francis, P. J., Williger, G. M., Collins, N. R., et al. 2001, *Astrophys. J.*, 554, 1001

Francis, C. L. & Peacock, J. A. 2010, *Mon. Not. R. Astron. Soc.*, 406, 2

Frieman, J. A. et al. *Phys.Rev.Lett.* 75 1995 2077-2080

Frieman, J. A. et al. 2008 . *AJ*, 135(1):338.

Fynbo, J. P. U., Jakobsson, P., Prochaska, J. X., et al. 2009, *Astrophys. J. S. S.*, 185, 526

Fu, H., & Stockton, A. 2009, *Astrophys. J.*, 690, 953

Fujimoto, Masayuki Y.; Ikeda, Yasufumi; Iben, Icko, Jr. 2000, *Astrophys. J.*, 529, 25

Gal, R. R., de Carvalho, R. R., Odewahn, S. C., Djorgovski, S. G., & Margoniner, V. E. 2000, *Astron. J.*, 119, 12

Gal, R. R., de Carvalho, R. R., Lopes, P. A. A., Djorgovski, S. G., Brunner, R. J., Mahabal, A., & Odewahn, S. C. 2003, *Astron. J.*, 125, 2064

Gallagher, J. S., Garnavich, P. M., Caldwell, N., Kirshner, R. P., Jha, S. W., Li, W., Ganeshalingam, M., and Filippenko, A. V. 2008 . *ApJ*, 685, 752.

Gao, L., Navarro, J. F., Cole, S., et al. 2008, *MNRAS*, 387, 536

Garcia-Bellido, J. and Haugboelle, T., *JCAP* 0909 2009 028

Gawiser, E., Francke, H., Lai, K., et al. 2007, *Astrophys. J.*, 671, 278

Gaztañaga, E., Eriksen, M., Crocce, M., et al. 2012, *Mon. Not. R. Astron. Soc.*, 422, 2904

Geach, J. E., Matsuda, Y., Smail, I., et al. 2005, *Mon. Not. R. Astron. Soc.*, 363, 1398

Gehrels, N., Chincarini, G., Giommi, P., et al. 2004, *Astrophys. J.*, 611, 1005

Giannantonio, T., Scranton, R., Crittenden, R. G., et al. 2008, *Phys. Rev. D*, 77, 123520

Gilbank, D. G., Gladders, M. D., Yee, H. K. C., & Hsieh, B. C. 2011, *Astron. J.*, 141, 94

Giovanelli, R. 2008, *The Evolution of Galaxies Through the Neutral Hydrogen Window*, 1035, 328

Gladders, M. D., & Yee, H. K. C. 2000, *Astron. J.*, 120, 2148

Gladders, M. D., & Yee, H. K. C. 2005, *Astrophys. J. S. S.*, 157, 1

Gladders, M. D., Yee, H. K. C., Majumdar, S., Barrientos, L. F., Hoekstra, H. H., Patrick B. & Infante, L., 2007, *Astrophys. J.*, 655, 128

Glazebrook, K., et al. 2007, *Proceedings of the Durham “Cosmic Frontiers” Conference*, ASP Conference Series, Vol. 379, p. 72. eds. Metcalfe & Shanks. [arXiv:astro-ph/07(1876)].

Glikman, E., Bogosavljević, M., Djorgovski, S. G., et al. 2010, *Astrophys. J.*, 710, 1498

Gonzalez, A. H., Tran, K.-V. H., Conbere, M. N., & Zaritsky, D. 2005, *Astrophys. J. Lett.*, 624, L73

Gonzalez, A. H., Zaritsky, D., & Zabludoff, A. I. 2007, *Astrophys. J.*, 666, 147

Gonzalez, Guillermo; Wallerstein, George 1996, *Mon. Not. R. Astron. Soc.*, 280, 515

González-Nuevo, J., Lapi, A., Negrello, M., et al. 2014, arXiv:1401.4094

Gorgas, F. J., Faber, S. M., Burstein, D., Gonzalez, J. J., Courteau S. & Prosser, C. 1993, *Astrophys. J. S. S.*, 86, 153

Gorosabel, J., Kubánek, P., Jelínek, M., et al. 2010, *Advances in Astronomy*, 2010, 55

Gorosabel, J., Kubánek, P., Lara-Gil, O., et al. 2012, *Astronomical Society of India Conference Series*, 7, 303

Goto, T., et al. 2002, *Astron. J.*, 123, 1807

Granett B. R., Neyrinck M. C., Szapudi I., 2009, *Astrophys. J.*, 701, 414

Grazian, A., Fontana, A., de Santis, C., et al. 2006, *Astron. Astrophys.*, 449, 951

Gregg, M. D., et al. 2004, *Bulletin of the American Astronomical Society*, 36, 1496

Griffin M. J., Abergel A., Abreu A., et al., 2010, *Astron. Astrophys.*, 518, L3

Gronwall, C., Ciardullo, R., Hickey, T., et al. 2007, *Astrophys. J.*, 667, 79

Gruel, N., Moles, M., Varela, J., et al. 2012, *Proc. SPIE*, 8448,

Guaita, L., Gawiser, E., Padilla, N., et al. 2010, *Astrophys. J.*, 714, 255

Gunn J. E., 1967, *Astrophys. J.*, 147, 61

Guo, Q., White, S., Boylan-Kolchin, M., et al. 2011, *Mon. Not. R. Astron. Soc.*, 413, 101

Guy, J. et al. 2007. *A&A*, 46, 11.

Haas, M. R., Schaye, J., & Jeason-Daniel, A. 2012, *Mon. Not. R. Astron. Soc.*, 419, 2133

Haberzettl, L., Williger, G. M., Lauroesch, J. T., et al. 2009, *Astrophys. J.*, 702, 506

Haberzettl, L. et al. 2012, *ApJ* 745, 96

Hahn O., Porciani C., Carollo C. M., Dekel A., 2007, *Mon. Not. R. Astron. Soc.*, 375, 489

Haislip, J. B., Nysewander, M. C., Reichart, D. E., et al. 2006, *Nature*, 440, 181

Hamaus, N., Seljak, U., & Desjacques, V. 2011, *Phys. Rev. D*, 84, 083509

Hamaus, N., Seljak, U., & Desjacques, V. 2012, *Phys. Rev. D*, 86, 103513

Hamaus, N., Seljak, U., Desjacques, V., Smith, R. E., & Baldauf, T. 2010, *Phys. Rev. D*, 82, 043515

Hamilton, A. J. S. 1997, *Mon. Not. R. Astron. Soc.*, 289, 285

Hamilton, A. J. S. 1998, in *Astrophysics and Space Science Library*, Vol. 231, *The Evolving Universe*, ed. D. Hamilton, 185

Hand, N., Addison, G. E., Aubourg, E., et al. 2012, *Physical Review Letters*, 109, 041101

Hao, J., McKay, T. A., Koester, B. P., et al. 2010, *Astrophys. J. S. S.*, 191, 254

Harris, W. E., & Racine, R. 1979, *Annu. Rev. Astron. Astrophys.*, 17, 241

Harris, W. E., & van den Bergh, S. 1981, *Astron. J.*, 86, 1627

Harris, W. E., Harris, G. L. H., & McLaughlin, D. E. 1998, *Astron. J.*, 115, 1801

Harris, W. E. 1991, *Annu. Rev. Astron. Astrophys.*, 29, 543

Harris, W. E. 2001, *Saas-Fee Advanced Course 28: Star Clusters*, 223

Hart, Q. N., Stocke, J. T., Evrard, A. E., Ellingson, E. E., & Barkhouse, W. A. 2011, *Astrophys. J.*, 740, 59

Hardcastle, M. J., Evans, D. A., & Croston, J. H. 2007, *Mon. Not. R. Astron. Soc.*, 376, 1849

Häußler, B., Bamford, S. P., Vika, M., et al. 2013, *Mon. Not. R. Astron. Soc.*, 430, 330

Hawkins, E., Maddox, S., Cole, S., et al. 2003, *Mon. Not. R. Astron. Soc.*, 346, 78

Hayes, D. S. & Latham, D. W. 1975, *Astrophys. J.*, 197, 593

Hayes, M., Östlin, G., Schaerer, D., et al. 2010, *Nature*, 464, 562

Haynes, M. P., & ALFALFA Team 2008, *The Evolution of Galaxies Through the Neutral Hydrogen Window*, 1035, 238

He, J.H., B. Wang, E. Abdalla and D. Pavon, *JCAP* **1012**, 022 2010

He, J.B., B. Wang and E. Abdalla, *Phys. Rev. D* **83**, 063515 2011

Heckman, T. M., Miley, G. K., Lehnert, M. D., & van Breugel, W. 1991, *Astrophys. J.*, 370, 78

Heckman, T. M., Kauffmann, G., Brinchmann, J., et al. 2004, *Astrophys. J.*, 613, 109

Heckman, T. M., Hoopes, C. G., Seibert, M., et al. 2005, *Astrophys. J. Lett.*, 619, L35

Heckman, T. M., Borthakur, S., Overzier, R., et al. 2011, *Astrophys. J.*, 730, 5

Henriques, B. M. B., White, S. D. M., Lemson, G., et al. 2012, *Mon. Not. R. Astron. Soc.*, 421, 2904

Henriques B. M. B., White S. D. M., Thomas P. A., Angulo R. E., Guo Q., Lemson G., Springel V., 2013, *Mon. Not. R. Astron. Soc.*, 431, 3373

Henry, J. P., 2000, *Astrophys. J.*, 534, 565

Henry, J. P., Evrard, A. E., Hoekstra, H., Babul, A., & Mahdavi, A. 2009, *Astrophys. J.*, 691, 1307

Hildebrandt, H., Muzzin, A., Erben, T., et al. 2011, *ApJL*, 733, L30

Hine, R. G., & Longair, M. S. 1979, *Mon. Not. R. Astron. Soc.*, 188, 111

Heavens, A. F., Matarrese, S., & Verde, L. 1998, *Mon. Not. R. Astron. Soc.*, 301, 797

Heavens, A. F. & Taylor, A. N. 1997, *Mon. Not. R. Astron. Soc.*, 290, 456

Hernandez-Monteagudo, C., et al. 2006, *Astrophys. J.*, 643, 598

Hernández-Monteagudo, C., Génova-Santos, R., & Atrio-Barandela, F. 2006, in *American Institute of Physics Conference Series*, Vol. 841, *A Century of Relativity Physics: ERE 2005*, ed. L. Mornas & J. Diaz Alonso, 389–392

Hernández-Monteagudo, C. 2008, *Astron. Astrophys.*, 490, 15

Hernández-Monteagudo, C. & Ho, S. 2009, *Mon. Not. R. Astron. Soc.*, 398, 790

Hernández-Monteagudo, C. 2010, *Astron. Astrophys.*, 520, A101

Hernandez-Monteagudo, C., Ross, A., Cuesta, A., et al. 2013, *ArXiv e-prints*

Heß S., Kitaura F.-S., Gottlöber S., 2013, *Mon. Not. R. Astron. Soc.*

HETDEX 2008, <http://www.as.utexas.edu/hetdex>

Hickson, P., Gibson, B. K., & Callaghan, K. A. S. 1994, *Mon. Not. R. Astron. Soc.*, 267, 911

High, F. W., Stubbs, C. W., Rest, A., Stalder, B., & Challis, P. 2009, *Astron. J.*, 138, 110

Hildebrandt, H., Erben, T., Kuijken, K., et al. 2012, *Mon. Not. R. Astron. Soc.*, 421, 2355

Hildebrandt, H., Arnouts, S., Capak, P., et al. 2010, *Astron. Astrophys.*, 523, A31

Hildebrandt, H., Wolf, C., & Benítez, N. 2008, *Astron. Astrophys.*, 480, 703

Hill, G. J., & Lilly, S. J. 1991, *Astrophys. J.*, 367, 1

Hill, G. et al. 2004, *Mitchell symposium: "The HET Dark Energy Experiment"*

Hill, G.J., Gebhardt, K., Komatsu, E., Drory, N., MacQueen, P.J., Adams, J.A., Blanc, G.A., Koehler, R., Rafal, Roth, 2008, *ASP Conference Series*, 339, 115

Hinshaw, G. 2008, *arXiv:0803.0732v1*

Hirata, C.M, R. Mandelbaum, M. Ishak, U. Seljak, R. Nichol, K. A. Pimblet, N. P. Ross, and D. Wake 2007, *Mon. Not. R. Astron. Soc.*, 381,1197

Hlavacek-Larrondo, J., Fabian, A. C., Edge, A. C., & Hogan, M. T. 2012, *Mon. Not. R. Astron. Soc.*, 424, 224

Ho, S., Hirata, C., Padmanabhan, N., Seljak, U., & Bahcall, N. 2008, *Phys. Rev. D*, 78, 043519

Ho S., Dedeo S., Spergel D., 2009, *ArXiv e-prints*

Hogg, D. W., Finkbeiner, D. P., Schlegel, D. J., & Gunn, J. E. 2001, *Astron. J.*, 122, 2129

Holland, W. S., Bintley, D., Chapin, E. L., et al. 2013, *Mon. Not. R. Astron. Soc.*, 430, 2513

Homeier, N. L., et al. 2006, *Astrophys. J.*, 647, 256

Hopkins, P. F., Lidz, A., Hernquist, L., et al. 2007, *Astrophys. J.*, 662, 110

Hopkins, P.F., Richards, G.T., Hernquist, L., 2007, *ApJ*, 654, 731

Hopkins, P. F., Bundy, K., Hernquist, L. et al. 2010, *Mon. Not. R. Astron. Soc.*, 401, 1099

Hopkins, P. F., & Hernquist, L. 2006, *Astrophys. J. S. S.*, 166, 1

Hopkins, P. F., Cox, T. J., Kereš, D., & Hernquist, L. 2008, *Astrophys. J. S. S.*, 175, 390

Hopkins, P. F., Hernquist, L., Cox, T. J., Dutta, S. N., & Rothberg, B. 2008, *Astrophys. J.*, 679, 156

Horesh, A., Maoz, D., Hilbert, S., & Bartelmann, M. 2011, *Mon. Not. R. Astron. Soc.*, 418, 54

Horndeski, G.W., *Int. J. Theor. Phys.* 10, 363-384 1974.

Howell, S. B. 1986, *Astron. J.*, 91, 171

Hu, W. & Haiman, Z. 2003, *Phys. Rev. D*, 68, 063004

Hu, W., & Kravtsov, A. V. 2003, *Astrophys. J.*, 584, 702

Hu, W. & Sawicki, I. 2007, *Phys. Rev. D*, 76, 104043

Hu, W. and I. Sawicki, *Phys. Rev. D* **76**, 064004 2007 .

Huchra, J. P., & Geller, M. J. 1982, *Astrophys. J.*, 257, 423

Huertas-Company, M., Rouan, D., Tasca, L., Soucail, G., & Le Fèvre, O. 2008, *Astron. Astrophys.*, 478, 971

Hunt, P. & S. Sarkar, *MNRAS* 401, 547 2010 ;

Huterer, D. & Linder, E. V. 2007, *Phys. Rev. D*, 75, 023519

Hütsi, G. 2006, *Astron. Astrophys.*, 449, 891

Ilbert, O., Capak, P., Salvato, M., et al. 2009, *Astrophys. J.*, 690, 1236

Iovino, A., Cucciati, O., Scodeggio, M., et al. 2010, *Astron. Astrophys.*, 509, A40+

Irwin, J. A., Brink, T. G., Bregman, J. N., & Roberts, T. P. 2010, *Astrophys. J. Lett.*, 712, L1

Ivezić, Ž., Vivas, A. K., Lupton, R. H., & Zinn, R. 2005, *Astron. J.*, 129, 1096

Ivezić, Ž., Sesar, B., Jurić, M., et al. 2008, *Astrophys. J.*, 684, 287

Ivezic, Z., Tyson, J. A., Acosta, E., et al. 2008, arXiv:0805.2366

Iverson, R. J. et al. 2005, *MNRAS* 362, 535

Iye, M., Ota, K., Kashikawa, N., et al. 2006, *Nature*, 443, 186

Jackson, N. 2007, *Living Reviews in Relativity*, 10, 4

Jackson, N., & Rawlings, S. 1997, *Mon. Not. R. Astron. Soc.*, 286, 241

Jain, B. & Bertschinger, E. 1994, *Astrophys. J.*, 431, 495

Jain, B., Lima M., 2011, *Mon. Not. R. Astron. Soc.*, 411, 2113

Jain, B. and A. Taylor. 2003, *Physical Review Letters*, 91(14), 141302

Jakobsson, P., Hjorth, J., Fynbo, J. P. U., et al. 2004, *Astrophys. J. Lett.*, 617, L21

Janssen, R. M. J., Röttgering, H. J. A., Best, P. N., & Brinchmann, J. 2012, *Astron. Astrophys.*, 541, A62

Janz, J., Laurikainen, E., Lisker, T., et al. 2012, *Astrophys. J. Lett.*, 745, L24

Jasche, J., Kitaura, F. S., Li, C., & Enßlin, T. A. 2010, *Mon. Not. R. Astron. Soc.*, 409, 355

Jasche J., Kitaura F.-S., 2010, *Mon. Not. R. Astron. Soc.*, 407, 29

Jasche J., Wandelt B. D., 2012, *Mon. Not. R. Astron. Soc.*, 425, 1042

Jedicke, R. and Pan-STARRS, 2007, *BAAS*, 39, 421

Jelínek, J., 2012, priv. comm.

Jenkins, A., Frenk, C. S., White, S. D. M., et al. 2001, *Mon. Not. R. Astron. Soc.*, 321, 372

Jennings, E., Baugh, C. M. and Pascoli, S., 2011, *MNRAS*, 410, 2081

Jiang, F., van Dokkum, P., Bezanson, R., & Franx, M. 2012, *Astrophys. J. Lett.*, 749, L10

Jiménez-Teja, Y., & Benítez, N. 2012, *Astrophys. J.*, 745, 150

Jing, Y. P. 1998, *Astrophys. J. Lett.*, 503, L9

Jing, Y. P., & Suto, Y. 2000, *ApJL*, 529, L69

Joachimi B., Taylor A. N., Kiessling A., 2011, *Mon. Not. R. Astron. Soc.*, 418, 145

Jogee, S., Miller, S. H., Penner, K., et al. 2009, *Astrophys. J.*, 697, 1971

Johnston, D. E., Sheldon, E. S., Tasitsiomi, A., et al. 2007, *ApJ*, 656, 27

Johnston, S., Taylor, R., Bailes, M., et al. 2008, *Experimental Astronomy*, 22, 151

Jones, W. C., et al. 2006, *Astrophys. J.*, 647, 823

Jordi, C., Høg, E., Brown, A. G. A., et al. 2006, *Mon. Not. R. Astron. Soc.*, 367, 290

Jullo, E., Kneib, J.-P., Limousin, M., et al. 2007, *New Journal of Physics*, 9, 447

Kaiser, N. 1984, *Astrophys. J. Lett.*, 284, L9

Kaiser, N., *Mon. Not. Roy. Astron. Soc.* **227**, 1 1987;

Kaiser N., 1992, *Astrophys. J.*, 388, 272

Kaiser, N., Aussel, H., Burke, B. E., et al. 2002, *Proc. SPIE*, 4836, 154

Kaiser, N., & Squires, G. 1993, *ApJ*, 404, 441

Kamenshchik, A., Moschella, H., and Pasquier, V., *Phys. Lett. B* 511 2001 265

Kampczyk, P., Lilly, S. J., de Ravel, L., et al. 2013, *Astrophys. J.*, 762, 43

Kann, D. A., Klose, S., Zhang, B., et al. 2011, *Astrophys. J.*, 734, 96

Kann, D. A., Klose, S., Zhang, B., et al. 2010, *Astrophys. J.*, 720, 1513

Karakas, Amanda I.; Campbell, Simon W.; Stancliffe, Richard J. 2010 *Astrophys. J.*, 713, 374

Kasuya, S. *Phys. Lett. B* 515 (2001) 121;

Kauffmann, G., White, S. D. M., Heckman, T. M., et al. 2004, *Mon. Not. R. Astron. Soc.*, 353, 713

Keel, W. C., White, R. E., III, Chapman, S., & Windhorst, R. A. 2009, *Astron. J.*, 138, 986

Keller, S. C., Schmidt, B. P., Bessell, M. S., et al. 2007, *Publications of the ASA*, 24, 1

Kelly, P. L., Hicken, M., Burke, D. L., Mandel, K. S., and Kirshner, R. P. 2010 . *ApJ*, 715, 743.

Kelly, P. L., von der Linden, A., Applegate, D. E., et al. 2012, ArXiv e-prints

Kennicutt, R. C., Jr. 1998, *Annu. Rev. Astron. Astrophys.*, 36, 189

Kepner, J., Fan, X., Bahcall, N., Gunn, J., Lupton, R., & Xu, G. 1999, *Astrophys. J.*, 517, 78

Kessler, R. et al. 2009 . *PASP*, 121, 1028.

Kessler, R. et al. 2013 . *ApJ*, 764, 48.

Kewley, L. J., Geller, M. J., & Barton, E. J. 2006, *Astron. J.*, 131, 2004

Kim, R. S. J., et al. 2002, *Astron. J.*, 123, 20

Kiselev, V.V. *Class. Quant. Grav.*, 2004 **21**: 3323,

Kitaura F.-S., Enßlin T. A., 2008, *Mon. Not. R. Astron. Soc.*, 389, 497

Kitaura F.-S., Erdoğan P., Nuza S. E., Khalatyan A., Angulo R. E., Hoffman Y., Gottlöber S., 2012, *Mon. Not. R. Astron. Soc.*, 427, L35

Kitaura F.-S., Gallerani S., Ferrara A., 2012, *Mon. Not. R. Astron. Soc.*, 420, 61

Kitaura F.-S., Angulo R. E., 2012, *Mon. Not. R. Astron. Soc.*, 425, 2443

Kitaura F.-S., Yepes G., Prada F., 2013, arXiv:1307.3285

Kitaura F.-S., 2013, *Mon. Not. R. Astron. Soc.*, 429, L84

Kitching, T.D., S. T. Balan, S. Bridle, N. Cantale, F. Courbin, T. Eifler, M. Gentile, M. S. S. Gill, S. Harmeling, C. Heymans, M. Hirsch, K. Honscheid, T. Kacprzak, D. Kirkby, D. Margala, R. J. Massey, P. Melchior, G. Nurbaeva, K. Patton, J. Rhodes, B. T. P. Rowe, A. N. Taylor, M. Tewes, M. Viola, D. Witherick, L. Voigt, J. Young, and J. Zuntz, 2012, *Mon. Not. R. Astron. Soc.*, 423, 3163

Kleinman, S. J., Kepler, S. O., Koester, D., et al. 2013, *Astrophys. J. S. S.*, 204, 5

Klypin A., Hoffman Y., Kravtsov A. V., Gottlöber S., 2003, *Astrophys. J.*, 596, 19

Knapen, J. H. & James, P. A. 2009, *Astrophys. J.*, 698, 1437

Kneib, J. P., Mellier, Y., Fort, B., & Mathez, G. 1993, *Astron. Astrophys.*, 273, 367

Kneib, J.-P., & Natarajan, P. 2011, *A&AR*, 19, 47

Kobayashi, M. A. R., Totani, T., & Nagashima, M. 2007, *Astrophys. J.*, 670, 919

Koester, B. P., et al. 2007, *Astrophys. J.*, 660, 221

Koester, D. *Mem. Soc. Astron. Italiana*, 81, 921, 2010

Koleva, M., Prugniel, P., de Rijcke, S., & Zeilinger, W. W. 2011, *Mon. Not. R. Astron. Soc.*, 417, 1643

Kolodzig, A., Gilfanov, M., Sunyaev, R., Sazonov, S., & Brusa, M. 2013a, *Astron. Astrophys.*, 558, A89

Kolodzig, A., Gilfanov, M., Hütsi, G., & Sunyaev, R. 2013b, *Astron. Astrophys.*, 558, A90

Komatsu, E., Smith, K. M., Dunkley, J., et al. 2011, *Astrophys. J. S. S.*, 192, 18

Komatsu, E., Dunkley, J., Nolta, M., et al. 2009, *Astrophys. J. S. S.*, 180, 330

Komatsu, E. 2010, *Class. Q. Grav.*, 27, 124010

Komatsu, E., Smith, K. M., Dunkley, J., et al. 2011, *Astrophys. J. S. S.*, 192, 18

Koribalski, B. S. 2012, *Publications of the Astronomical Society of Australia*, 29, 359

Kormendy, J., Fisher, D. B., Cornell, M. E., & Bender, R. 2009, *Astrophys. J. S. S.*, 182, 216

Kovač, K., Somerville, R. S., Rhoads, J. E., Malhotra, S., & Wang, J. 2007, *Astrophys. J.*, 668, 15

Kovač, K., Lilly, S. J., Cucciati, O., et al. 2010, *Astrophys. J.*, 708, 505

Koyama, K. & Silva, F. P. 2007, *Phys. Rev. D*, 75, 084040

Krisciunas et al. 1997, *PASP*, 109, 108

Kroupa, P. 2002, *Mon. Not. R. Astron. Soc.*, 330, 707

Kuhlen M., Vogelsberger M., Angulo R., 2012, *Physics of the Dark Universe*, 1, 50

Kulkarni, V. P., Meiring, J., Som, D., et al. 2012, *Astrophys. J.*, 749, 176

Kunz, M., 2012, *Comptes Rendus Physique* **13**, 539

Laing, R. A., Jenkins, C. R., Wall, J. V., & Unger, S. W. 1994, *The Physics of Active Galaxies*, 54, 201

Lagos C. d. P., Bayet E., Baugh C. M., Lacey C. G., Bell T. A., Fanidakis N., Geach J. E., 2012, *Mon. Not. R. Astron. Soc.*, 426, 2142

Lambas, D. G., Tissera, P. B., Alonso, M. S., & Coldwell, G. 2003, *Mon. Not. R. Astron. Soc.*, 346, 1189

Lampeitl, H. et al. 2010. *ApJ*, 722, 566.

Landolt, A. U. 1992, *Astron. J.*, 104, 340

Landolt, A. U. 2009, *Astron. J.*, 137, 4186

Landy, S. D. & Szalay, A. S. 1993, *Astrophys. J.*, 412, 64

Lapi A., González-Nuevo J., Fan L., et al., 2011, *Astrophys. J.*, 742, 24

Larson, R. B. 1996, *Formation of the Galactic Halo...Inside and Out*, 92, 241

Laszlo, I. & Bean, R. 2008, *Phys. Rev. D*, 77, 024048

Laureijs, R., Amiaux, J., Arduini, S., et al. 2011, *ArXiv e-prints*

Lawrence, A., Warren, S. J., Almaini, O., et al. 2007, *Mon. Not. R. Astron. Soc.*, 379, 1599

Le Fèvre, O., Abraham, R., Lilly, S. J., et al. 2000, *Mon. Not. R. Astron. Soc.*, 311, 565

Levan, A. J., Tanvir, N. R., Cenko, S. B., et al. 2011, *Science*, 333, 199

Levi, M., Chris Bebek, Timothy Beers, Robert Blum, Robert Cahn, Daniel Eisenstein, Brenna Flaugher, Klaus Honscheid, Richard Kron, Ofer Lahav, Patrick McDonald, Natalie Roe, David Schlegel, representing the DESI collaboration, 2013, *astro-ph/1308.0847*

Lewis, A. & Bridle, S. 2002, *Phys. Rev. D*, 66, 103511

Lewis, A., Challinor, A., & Lasenby, A. 2000, *Astrophys. J.*, 538, 473, <http://camb.info>

Libeskind N. I., Knebe A., Hoffman Y., Gottlöber S., Yepes G., Steinmetz M., 2011, *Mon. Not. R. Astron. Soc.*, 411, 1525

Lidman, C. E., & Peterson, B. A. 1996, *Astron. J.*, 112, 2454

Lilly, S. J., Le Brun, V., Maier, C., et al. 2009, *Astrophys. J. S. S.*, 184, 218

Lima, M., & Hu, W. 2004, *Phys. Rev. D*, 70, 043504

Lima, M., & Hu, W. 2005, *Phys. Rev. D*, 72, 043006

Lima, M., & Hu, W. 2007, *Phys. Rev. D*, 76, 123013

Limousin, M., Ebeling, H., Ma, C.-J., et al. 2010, *Mon. Not. R. Astron. Soc.*, 405, 777

Lin, L., Koo, D. C., Willmer, C. N. A., et al. 2004, *Astrophys. J. Lett.*, 617, L9

Lin, Y.-T., Mohr, J. J., 2004, *Astrophys. J.*, 617, 879-895.

Lin, L., Patton, D. R., Koo, D. C., et al. 2008, *Astrophys. J.*, 681, 232

Lin, L., Cooper, M. C., Jian, H., et al. 2010, *Astrophys. J.*, 718, 1158

Linder, E. V. 2003, *Physical Review Letters*, 90, 091301

Linder, E. V. 2005, *Phys. Rev. D*, 72, 043529

Linder, E. V. *Phys. Rev. D* **72**, 043529 2005 .

Linder, E. V. & Cahn, R. N. 2007, *Astroparticle Physics*, 28, 481

Linder, E. V. & Jenkins, A. 2003, *Mon. Not. R. Astron. Soc.*, 346, 573

Lintott, C. J., Schawinski, K., Slosar, A., et al. 2008, *Mon. Not. R. Astron. Soc.*, 389, 1179

Liske, J., Lemon, D. J., Driver, S. P., Cross, N. J. G., & Couch, W. J. 2003, *Mon. Not. R. Astron. Soc.*, 344, 307

Lisker, T., Grebel, E. K., Binggeli, B., & Glatt, K. 2007, *Astrophys. J.*, 660, 1186

Liu, F. S., Hsieh, B. C., Ho, P. T. P., Lin, L., & Yan, R. 2008, *Astrophys. J.*, 681, 1046

Liu, F. S., Mao, S., Deng, Z. G. et al. 2009, *Mon. Not. R. Astron. Soc.*, 396, 2003

Liu, F. S., Guo, Y., Koo, D. C., et al. 2013, *Astrophys. J.*, 769, 147

Lopes, P. A. A., de Carvalho, R. R., Gal, R. R., Djorgovski, S. G., Odewahn, S. C., Mahabal, A. A., & Brunner, R. J. 2004, *Astron. J.*, 128, 1017

López-Corredoira, M., Sylos Labini, F., & Betancort-Rijo, J. 2010, *Astron. Astrophys.*, 513, A3

López-Cruz, O., Barkhouse, W. A., & Yee, H. K. C. 2004, *Astrophys. J.*, 614, 679

López-Sanjuan, C., Balcells, M., García-Dabó, C. E., et al. 2009a, *Astrophys. J.*, 694, 643

López-Sanjuan, C., Balcells, M., Pérez-González, P. G., et al. 2010, *Astron. Astrophys.*, 518, A20

López-Sanjuan, C., Balcells, M., Pérez-González, P. G., et al. 2009b, *Astron. Astrophys.*, 501, 505

López-Sanjuan, C., Le Fèvre, O., de Ravel, L., et al. 2011, *Astron. Astrophys.*, 530, A20

López-Sanjuan, C., Le Fèvre, O., Ilbert, O., et al. 2012, *Astron. Astrophys.*, 548, A7

López-Sanjuan, C., Le Fèvre, O., Tasca, L. A. M., et al. 2013, *Astron. Astrophys.*, 553, A78

Lotz, J. M., Davis, M., Faber, S. M., et al. 2008, *Astrophys. J.*, 672, 177

- Lotz, J. M., Jonsson, P., Cox, T. J., et al. 2011, *Astrophys. J.*, 742, 103
- Loverde M., Hui L., Gaztañaga E., 2008, *Phys. Rev. D*, 77, 023512
- LSST Science Collaboration, Abell, P. A., Allison, J., et al. 2009, arXiv:0912.0201
- Ly, C., Malkan, M. A., Hayashi, M., et al. 2011, *Astrophys. J.*, 735, 91
- Ma, C.-P. & Fry, J. N. 2000, *Astrophys. J.*, 543, 503
- Maddox S. J., Sutherland W. J., Efstathiou G., Loveday J., 1990, *MNRAS*, 243, 692.
- Makler, M., de Oliveira S. Q. and Waga, I. *Phys. Lett. B* 68, (2003) 123521;
- Mármol-Queraltó, E., Trujillo, I., Pérez-González, P. G., Varela, J., & Barro, G. 2012, *Mon. Not. R. Astron. Soc.*, 422, 2187
- MacArthur, L. A., González, J. J., & Courteau, S. 2009, *Mon. Not. R. Astron. Soc.*, 395, 28
- MacKenzie, T., Braglia, F. G., Gibb, A. G., et al. 2011, *Mon. Not. R. Astron. Soc.*, 415, 1950
- Madau, P. et al. 1998, *ApJ* 498, 106
- Macciò, A. V., Dutton, A. A., & van den Bosch, F. C. 2008, *Mon. Not. R. Astron. Soc.*, 391, 1940
- Magliocchetti, M., Maddox, S. J., Hawkins, E., et al. 2004, *Mon. Not. R. Astron. Soc.*, 350, 1485
- Magorrian, J., Tremaine, S., Richstone, D., et al. 1998, *Astron. J.*, 115, 2285
- Magrini, Laura; Stanghellini, Letizia; Gonçalves, Denise R. 2012, arXiv:1110.1186
- Magrini, Laura; Gonçalves, Denise R. 2009, *Mon. Not. R. Astron. Soc.*, 398, 280
- Mandelbaum, R., C. M. Hirata, M. Ishak, U. Seljak, and J. Brinkmann, 2006, *Mon. Not. R. Astron. Soc.*, 367, 611
- Mandelbaum, R., C. Blake, S. Bridle, F. B. Abdalla, S. Brough, M. Colless, W. Couch, S. Croom, T. Davis, M. J. Drinkwater, K. Forster, K. Glazebrook, B. Jelliffe, R. J. Jurek, I.-H. Li, B. Madore, C. Martin, K. Pimbblet, G. B. Poole, M. Pracy, R. Sharp, E. Wisnioski, D. Woods, and T. Wyder, 2011, *Mon. Not. R. Astron. Soc.*, 410, 844
- Mannucci, F. et al. 2007, *MNRAS*, 377, 1229
- Mantz, A., Allen, S. W., Rapetti, D., & Ebeling, H. 2010, *Mon. Not. R. Astron. Soc.*, 406, 1759
- Marconi, M., Cignoni, M., Di Criscienzo, M., et al. 2006, *Mon. Not. R. Astron. Soc.*, 371, 1503
- Marigo, P. 2001 *Astron. Astrophys.*, 370, 194
- Martin, D. C., Fanson, J., Schiminovich, D., et al. 2005, *Astrophys. J. Lett.*, 619, L1
- Martínez-Sansigre, A., & Rawlings, S. 2011, *Mon. Not. R. Astron. Soc.*, 414, 1937
- Marulli, F., M. Baldi and L. Moscardini, *Mon. Not. Roy. Astron. Soc.* **420**, 2377 2012
- Marulli, F., Bianchi, D., Branchini, E., et al. 2012, *Mon. Not. R. Astron. Soc.*, 426, 2566
- Massey, R., C. Heymans, J. Bergé, G. Bernstein, S. Bridle, D. Clowe, H. Dahle, R. Ellis, T. Erben, M. Heterscheidt, F. W. High, C. Hirata, H. Hoekstra, P. Hudelot, M. Jarvis, D. Johnston, K. Kuijken, V. Margoniner, R. Mandelbaum, Y. Mellier, R. Nakajima, S. Paulin-Henriksson, M. Peeples, C. Roat, A. Refregier, J. Rhodes, T. Schrabback, M. Schirmer, U. Seljak, E. Semboloni, and L. van Waerbeke, 2007, *Mon. Not. R. Astron. Soc.*, 376, 13

- Mateo, M. L. 1998, *Annu. Rev. Astron. Astrophys.*, 36, 435
- Mathis H., Lemson G., Springel V., Kauffmann G., White S. D. M., Eldar A., Dekel A., 2002, *Mon. Not. R. Astron. Soc.*, 333, 739
- Matsuda, Y., Yamada, T., Hayashino, T., et al. 2004, *Astron. J.*, 128, 569
- Matsuda, Y., Nakamura, Y., Morimoto, N., et al. 2009, *Mon. Not. R. Astron. Soc.*, 400, L66
- Matsuda, Y., Yamada, T., Hayashino, T., et al. 2011, *Mon. Not. R. Astron. Soc.*, 410, L13
- Matsubara, T. 2008, *Phys. Rev. D*, 77, 063530
- Matthews D. J., Newman J. A., 2010, *Astrophys. J.*, 721, 456
- Matthews D. J., Newman J. A., 2012, *Astrophys. J.*, 745, 180
- Mattila, S. et al. 2012, *ApJ*, 756, 111
- Maturi, M., Mizera, S., & Seidel, G. 2013, arXiv, 1305.3608
- McCarthy, P. J., Spinrad, H., Dickinson, M., et al. 1990, *Astrophys. J.*, 365, 487
- McConnell, N. J., Ma, C.-P., Gebhardt, K., et al. 2011, *Nature*, 480, 215
- McDonald, P. & Seljak, U. 2009, *JCAP*, 10, 7
- McEwen, J. D., Wiaux, Y., Hobson, M. P., Vandergheynst, P., & Lasenby, A. N. 2008, *Mon. Not. R. Astron. Soc.*, 384, 1289
- McNamara, B. R., & Nulsen, P. E. J., 2007, *Ann. Rev. Astr.*, 45, 117
- McNamara, B. R., Rohanizadegan, M., & Nulsen, P. E. J. 2011, *Astrophys. J.*, 727, 39
- McQuinn M., White M., 2013, *Mon. Not. R. Astron. Soc.*, 433, 2857
- Medezinski, E., Broadhurst, T., Umetsu, K., Benítez, N., & Taylor, A. 2011, *MNRAS*, 414, 1840
- Mehta K. T., Cuesta A. J., Xu X., Eisenstein D. J., Padmanabhan N., 2012, *Mon. Not. R. Astron. Soc.*, 427, 2168
- Mehta, K. T., Cuesta, A. J., Xu, X., Eisenstein, D. J., & Padmanabhan, N. 2012, *Mon. Not. R. Astron. Soc.*, 427, 2168
- Mei, S., Holden, B. P., Blakeslee, J. P., et al. 2006, *Astrophys. J.*, 644, 759
- Meiksin, A., White, M., & Peacock, J. A. 1999, *Mon. Not. R. Astron. Soc.*, 304, 851
- Melchior, P. and M. Viola, 2012, *Mon. Not. R. Astron. Soc.*, 424, 2757
- Menanteau, F., Sifón, C., Barrientos, L. F., et al. 2012, arXiv:1210.4048
- Ménard B., Scranton R., Fukugita M., Richards G., 2010, *Mon. Not. R. Astron. Soc.*, 405, 1025
- Ménard B., Scranton R., Schmidt S., Morrison C., Jeong D., Budavari T., Rahman M., 2013, ArXiv e-prints
- Méndez-Abreu, J., Aguerri, J. A. L., Corsini, E. M., & Simonneau, E. 2008, *Astron. Astrophys.*, 478, 353

- Merson, A. I., Baugh, C. M., Helly, J. C., et al. 2013, *Mon. Not. R. Astron. Soc.*, 429, 556
- Meszaros, P., & Rees, M. J. 1997, *Astrophys. J.*, 476, 232
- Metropolis, N., Rosenbluth, A. W., Rosenbluth, M. N., Teller, A. H., & Teller, E. 1953, *J. Chem. Phys.*, 21, 1087
- Micheletti, S.M.R. *JCAP* **1005**, 009 2010
- Micheletti, S., E. Abdalla, Bin Wang *Phys. Rev. D* **79** 2009 123506; Shaoyu Yin, Bin Wang, E. Abdalla, Chi-Yong Lin *Phys. Rev. D* **76** 2007 124026; A.B. Pavan, E. G.M. Ferreira, S. Micheletti, J.C.C. de Souza, E. Abdalla *Phys. Rev. D* **86** 2012 103521.
- Mihos, J. C., & Hernquist, L. 1994, *Astrophys. J. Lett.*, 437, L47
- Milgrom, M., 1983, *Astrophys. J.* **270**, 365
- Milkeraitis, M., van Waerbeke, L., Heymans, C., Hildebrandt, H., Dietrich, J. P., & Erben, T. 2010, *Mon. Not. R. Astron. Soc.*, 701
- Miller, C. J., et al. 2005, *Astron. J.*, 130, 968
- Miller, L., C. Heymans, T. D. Kitching, L. van Waerbeke, T. Erben, H. Hildebrandt, H. Hoekstra, Y. Mellier, B. T. P. Rowe, J. Coupon, J. P. Dietrich, L. Fu, J. Harnois-Déraps, M. J. Hudson, M. Kilbinger, K. Kuijken, T. Schrabback, E. Semboloni, S. Vafaei, and M. Velander, 2013, *Mon. Not. R. Astron. Soc.*, 429, 2858
- Minchev, I., & Famaey, B. 2010, *Astrophys. J.*, 722, 112
- Mizuno H. 1980, *Prog. Theor. Phys.*, 64, 544
- Mo, H. J. & White, S. D. M. 1996, *Mon. Not. R. Astron. Soc.*, 282, 347
- Moessner R., Jain B., Villumsen J. V., 1998, *Mon. Not. R. Astron. Soc.*, 294, 291
- Moles, M., et al. 2005, arXiv:astro-ph/0504545
- Moles, M., Benítez, N., Aguerri, J. A. L., et al. 2008, *Astron. J.*, 136, 1325
- Moles, M., et al. 2010, *PASP*, 122, 363
- Mori, M., Yoshii, Y., & Nomoto, K. 1999, *Astrophys. J.*, 511, 585
- Molino, A., Benítez, N., Moles, M., et al. 2014, *MNRAS*, in press, arXiv: 1306.4968
- Mountrichas G., Sawangwit U., Shanks T., Croom S. M., Schneider D. P., Myers A. D., Pimblett K., 2009, *Mon. Not. R. Astron. Soc.*, 394, 2050
- Murante, G., Giovalli, M., Gerhard, O., et al. 2007, *Mon. Not. R. Astron. Soc.*, 377, 2
- Mukhanov, V. 2005, *Physical Foundations of Cosmology*, Cambridge University Press, 2005
- Mukherjee, P., Kunz, M., Parkinson, D., & Wang, Y. 2008, *Phys. Rev. D*, 78, 083529
- Munari, E., Biviano, A., Borgani, S., Murante, G., & Fabjan, D. 2013, *Mon. Not. R. Astron. Soc.*, 430, 2638
- Muñoz-Darias, T., de Ugarte Postigo, A., Russell, D. M., et al. 2013, *Mon. Not. R. Astron. Soc.*, 432, 1133
- Myers A. D., White M., Ball N. M., 2009, *Mon. Not. R. Astron. Soc.*, 399, 2279
- Naab, T., Jesseit, R., & Burkert, A. 2006, *Mon. Not. R. Astron. Soc.*, 372, 839

Nadathur, S. & S. Sarkar, 2011, Phys. Rev. D 83, 063506

Nagai, D., Vikhlinin, A., & Kravtsov, A. 2007 Astrophys. J.655, 98

Nagai, D., & Lau, E. 2011 Astrophys. J. Lett.731, 10

Navarro, J. F., Frenk, C. S., & White, S. D. M. 1997, ApJ, 490, 493

Navarro, J. F., Ludlow, A., Springel, V., et al. 2010, MNRAS, 402, 21

Neto, A. F., Gao, L., Bett, P., et al. 2007, MNRAS, 381, 1450

Newberg, H. J., China, L. p. o., in LAMOST, P., & (PLUS), U. 2009, Bulletin of the American Astronomical Society, 41, #416.14

Newman J. A., 2008, Astrophys. J., 684, 88

Newman, J., Abate, A., Abdalla, F., et al. 2013, ArXiv e-prints

Neyrinck M. C., Szapudi I., Szalay A. S., 2009, Astrophys. J. Lett., 698, L90

Nicol, M.-H., Meisenheimer, K., Wolf, C., & Tapken, C. 2011, Astrophys. J., 727, 51

Nicolis, A. R. Rattazzi and E. Trincherini, Phys. Rev. D **79**, 064036 2009 ; C. Deffayet, G. Esposito-Farese and A. Vikman, Phys. Rev. D **79**, 084003 2009 .

Nilsson, K. K., & Møller, P. 2009, Astron. Astrophys., 508, L21

Norberg, P., Baugh, C. M., Hawkins, E., et al. 2002, Mon. Not. R. Astron. Soc., 332, 827

Norris, J. E., Christlieb, N., Korn, A. J., et al. 2007, Astrophys. J., 670, 774

Norris, R. P., Hopkins, A. M., Afonso, J., et al. 2011, Publications of the Astronomical Society of Australia, 28, 215

Oguri, M., & Marshall, P. J. 2010, Mon. Not. R. Astron. Soc., 405, 2579

Oguri, M., & Hamana, T. 2011, MNRAS, 414, 1851

Oguri, M., & Takada, M. 2011, PhysRevD.83.023008

Okabe, N., & Umetsu, K. 2008, PASJ, 60, 345

Oke, J. B. 1974, Astrophys. J. S. S., 27, 21

O'Hanlon, J. Phys. Rev. Lett. **29**, 137 1972; T. Chiba, Phys. Lett. B **575**, 1 2003 ; T. P. Sotiriou and V. Faraoni, Rev. Mod. Phys. **82**, 451 2010 ; A. De Felice and S. Tsujikawa, Living Rev. Rel. **13**, 3 2010 .

Oliver S. J., Bock J., Altieri B., et al., 2012, Mon. Not. R. Astron. Soc., 424, 1614

Oliver S. J., Wang L., Smith A. J., et al., 2010, Astron. Astrophys., 518, L21

Oosterhoff, P. T. 1939, The Observatory, 62, 104

Oosterloo, T., Verheijen, M., & van Cappellen, W. 2010, ISKAF2010 Science Meeting,

Östlin, G., Hayes, M., Kunth, D., et al. 2009, Astron. J., 138, 923

Oteo, I., Bongiovanni, A., Pérez García, A. M., et al. 2011, *Astrophys. J. Lett.*, 735, L15

Oteo, I., Bongiovanni, A., Pérez García, A. M., et al. 2012a, *Astron. Astrophys.*, 541, A65

Oteo, I., Bongiovanni, A., Pérez García, A. M., et al. 2012b, *Astrophys. J.*, 751, 139

Oteo et al. 2013a, *A&A* 554L, 3

Oteo et al. 2013b, *MNRAS*, accepted (arXiv: 1302.2327)

Oteo et al. 2013c, *MNRAS*, accepted (arXiv: 1306.1121)

Oteo et al. 2013d, *MNRAS*, submitted (arXiv: 1307.0971)

Otsuka, Masaaki; Tajitsu, Akito; Hyung, Siek; Izumiura, Hideyuki 2010, *Astrophys. J.*, 723, 658

Otsuka, Masaaki; Hyung, Siek; Lee, Seong-Jae; Izumiura, Hideyuki; Tajitsu, Akito 2009, *Astrophys. J.*, 705, 509

Ouchi, M., Shimasaku, K., Akiyama, M., et al. 2008, *Astrophys. J. S. S.*, 176, 301

Overduin, J. M. and Cooperstock, F. I., *Phys.Rev. D*58 1998 043506;

Overzier, R. A., Röttgering, H. J. A., Kurk, J. D., & De Breuck, C. 2001, *Astron. Astrophys.*, 367, L5

Overzier, R. A., Röttgering, H. J. A., Rengelink, R. B., & Wilman, R. J. 2003, *Astron. Astrophys.*, 405, 53

Overzier, R. A., Bouwens, R. J., Cross, N. J. G., et al. 2008, *Astrophys. J.*, 673, 143

Overzier, R. A., Heckman, T. M., Tremonti, C., et al. 2009, *Astrophys. J.*, 706, 203

Overzier, R., Lemson, G., Angulo, R. E., et al. 2013a, *Mon. Not. R. Astron. Soc.*, 428, 778

Overzier, R. A., Nesvadba, N. P. H., Dijkstra, M., et al. 2013b, *Astrophys. J.*, 771, 89

Oyaizu, H. 2008, *Phys. Rev. D*, 78, 123523

Oyaizu, H., Lima, M., Cunha, C. E., Lin, H., Frieman, J., & Sheldon, E. S. 2008, *Astrophys. J.*, 674, 768

Oyaizu, H., Lima, M., & Hu, W. 2008, *Phys. Rev. D*, 78, 123524

Padmanabhan, T. and Choudhury, T. R. *Phys. Rev. D*66 (2002) 081301;

Padmanabhan, N., et al. 2007, *Mon. Not. R. Astron. Soc.*, 378, 852

Padmanabhan, N., Schlegel, D. J., Finkbeiner, D. P., et al. 2008, *Astrophys. J.*, 674, 1217

Padmanabhan N., White M., Norberg P., Porciani C., 2009, *Mon. Not. R. Astron. Soc.*, 397, 1862

Padmanabhan N., Xu X., Eisenstein D. J., Scalzo R., Cuesta A. J., Mehta K. T., Kazin E., 2012, *Mon. Not. R. Astron. Soc.*, 427, 2132

Padmanabhan, N., Xu, X., Eisenstein, D. J., et al. 2012, *Mon. Not. R. Astron. Soc.*, 427, 2132

Pancino, E., Altavilla, G., Marinoni, S., et al. 2012, *Mon. Not. R. Astron. Soc.*, 426, 1767

Pan-STARRS 2008, <http://pan-starrs.ifa.hawaii.edu/public/>

Parker, Q. A.; Frew, D. J.; Acker, A.; Miszalski, B., 2012, *IAUS*, 283, 9

Passmoor, S., Cress, C., Faltenbacher, A., et al. 2013, *Mon. Not. R. Astron. Soc.*, 429, 2183

Patat, F. 2004, *The Messenger*, 115, 1

Patton, D. R. & Atfield, J. E. 2008, *Astrophys. J.*, 685, 235

Patton, D. R., Carlberg, R. G., Marzke, R. O., et al. 2000, *Astrophys. J.*, 536, 153

Patton, D. R., Ellison, S. L., Simard, L., McConnachie, A. W., & Mendel, J. T. 2011, *Mon. Not. R. Astron. Soc.*, 412, 591

Peacock, J. A. 1992, in *Lecture Notes in Physics*, Berlin Springer Verlag, Vol. 408, *New Insights into the Universe*, ed. V. J. Martinez, M. Portilla, & D. Saez, 1

Peacock, J. A., Cole, S., Norberg, P., et al. 2001, *Nature*, 410, 169

Peacock, J. A., et al. 2006, [arXiv:astro-ph/0610906](http://arxiv.org/abs/astro-ph/0610906)

Peacock, J. A. & Dodds, S. J. 1996, *Mon. Not. R. Astron. Soc.*, 280, L19

Peebles, P. J. E., *The large-scale structure of the universe*, (Princeton University Press, Princeton, 1980)

Peebles, J. and B. Ratra, *Ap. J. Lett.* 325, L17 (1988)

Pence, W. D., Seaman, R., & White, R. L. 2009, *PASP*, 121, 414

Peng, C. Y., Ho, L. C., Impey, C. D., & Rix, H.-W. 2002, *Astron. J.*, 124, 266

Peng, Y., Lilly, S. J., Kovač, K., et al. 2010, *Astrophys. J.*, 721, 193

Piquinot, D.; Walsh, J. R.; Zijlstra, A. A.; Dudziak, G. 2000, *Astron. Astrophys.*, 361L, 1

Percival, W. J., Verde, L., & Peacock, J. A. 2004, *Mon. Not. R. Astron. Soc.*, 347, 645

Percival W. et al. 2007, *Astrophys. J.*, 657, 645

Percival, W. J., Cole, S., Eisenstein, D. J., Nichol, R. C., Peacock, J. A., Pope, A. C., & Szalay, A. S. 2007, *Mon. Not. R. Astron. Soc.*, 381, 1053

Percival, W. J., Reid, B. A., Eisenstein, D. J., et al. 2010, *Mon. Not. R. Astron. Soc.*, 401, 2148

Pereira, C. B.; Miranda, L. -F 2007, *Astron. Astrophys.*, 467, 1249

Peter, P. & Uzan, J. 2009, *Primordial cosmology*, Oxford graduate texts (Oxford University Press)

Pickles, A. J. 1998, *PASP*, 110, 863

Pietrobon, D., Balbi, A., & Marinucci, D. 2006, *Phys. Rev. D*, 74, 043524

Pigozzo C., Dantas M. A., Carneiro S., Alcaniz J. S., 2011, *JCAP*, 1108, 022

Pilbratt G. L., Riedinger J. R., Passvogel T., et al., 2010, *Astron. Astrophys.*, 518, L1

Piran, T. 1999, *Phys. Rep.*, 314, 575

Planck 2008 , <http://planck.esa.int>

Planck Collaboration, Aghanim, N., Arnaud, M., et al. 2011, *Astron. Astrophys.*, 536, A12
Planck Collaboration, Ade, P. A. R., Aghanim, N., et al. 2012, ArXiv e-prints
Planck Collaboration, Ade, P. A. R., Aghanim, N., et al. 2013a, ArXiv e-prints
Planck Collaboration, Ade, P. A. R., Aghanim, N., et al. 2013b, arXiv:1303.5077
Planck Collaboration, Ade, P. A. R., Aghanim, N., et al. 2013c, ArXiv e-prints
Planck Collaboration, Ade, P. A. R., Aghanim, N., et al. 2013d, ArXiv e-prints
Planck Collaboration, Ade, P. A. R., Aghanim, N., et al. 2013e, arXiv:1303.5062
Planck Collaboration, Ade, P. A. R., Aghanim, N., et al. 2013f, arXiv:1303:5082
Planck Collaboration, Ade, P. A. R., Aghanim, N., et al. 2013g, arXiv:1303.5083
 Porciani, C., Magliocchetti, M., & Norberg, P. 2004, *Mon. Not. R. Astron. Soc.*, 355, 1010
 Postman, M., Lubin, L. M., Gunn, J. E., Oke, J. B., Hoessel, J. G., Schneider, D. P., & Christensen, J. A. 1996, *Astron. J.*, 111, 615
 Postman, M., Lauer, T. R., Oegerle, W., & Donahue, M. 2002, *Astrophys. J.*, 579, 93
 Postman, M., Franx, M., Cross, N. J. G., et al. 2005, *Astrophys. J.*, 623, 721
 Postman, M., Lauer, T. R., Donahue, M., et al. 2012, *Astrophys. J.*, 756, 159
 Pović, M., Huertas-Company, M., Aguerri, J. A. L., et al. 2013, *Mon. Not. R. Astron. Soc.*, 2221
 Pozzetti, L., Bolzonella, M., Zucca, E., et al. 2010, *Astron. Astrophys.*, 523, A13
 Prescott, M. K. M., Dey, A., & Jannuzi, B. T. 2013, *Astrophys. J.*, 762, 38
 Prieto, M., Aguerri, J. A. L., Varela, A. M., & Muñoz-Tuñón, C. 2001, *Astron. Astrophys.*, 367, 405
 Puxley 2008 , <http://www.gemini.edu/sciops/ObsProcess/obsConstraints/ocSkyBackground.html>
 Quillen, A. C., Minchev, I., Bland-Hawthorn, J., & Haywood, M. 2009, *Mon. Not. R. Astron. Soc.*, 397, 1599
 Rabinowitz et al. 2008, *ApJ*, 136, 1502
 Ramella, M., Boschini, W., Fadda, D., & Nonino, M. 2001, *Astron. Astrophys.*, 368, 776
 Ramella, M., Geller, M. J., Pisani, A., & da Costa, L. N. 2002, *Astron. J.*, 123, 2976
 Rassat, A., Land, K., Lahav, O., & Abdalla, F. B. 2007, *Mon. Not. R. Astron. Soc.*, 377, 1085
 Rauch, T.; Heber, U.; Werner, K. 2002, *Astron. Astrophys.*, 381, 1007
 Rawlings, S., & Saunders, R. 1991, *Nature*, 349, 138
 Readhead A.C.S., et al. 2004, *Astrophys. J.*, 609, 498
 Rees, M. J. & Sciama, D. W. 1968, *Nature*, 217, 511
 Rees, M. J. 1988, *Nature*, 333, 523
 Refregier, A., Amara, A., Kitching, T. D., et al. 2010, arXiv:1001.0061
 Reichardt C. L. et al. 2008, arXiv:0801.149

Reid, B. A. and White, M., 2011, MNRAS, 417, 1913

Rengelink, R. B., Tang, Y., de Bruyn, A. G., et al. 1997, A&AS, 124, 259

Rettura, A., Rosati, P., Nonino, M., et al. 2010, Astrophys. J., 709, 512

Rettura, A., Mei, S., Stanford, S. A., et al. 2011, Astrophys. J., 732, 94

R. Reyes, R. Mandelbaum, J. E. Gunn, R. Nakajima, U. Seljak, and C. M. Hirata, 2011, ArXiv e-prints

Rhoads, J. E. & Malhotra, S. 2001, ApJ 563, L5

Ricciardelli, E., Vazdekis, A., Cenarro, A. J., & Falcón-Barroso, J. 2012, Mon. Not. R. Astron. Soc., 424, 172

Ricciardelli, E., Vazdekis, A., Cenarro, A. J., & Falcón-Barroso, J. 2012, Mon. Not. R. Astron. Soc., 424, 172

Richard, J., Smith, G. P., Kneib, J.-P., et al. 2010, Mon. Not. R. Astron. Soc., 404, 325

Riess A. et al. 2007, Astrophys. J., 659, 98

Robaina, A. R., Bell, E. F., Skelton, R. E., et al. 2009, Astrophys. J., 704, 324

Ross, N. P., Shen, Y., Strauss, M. A., et al. 2009, Astrophys. J., 697, 1634

Rossi, A., Klose, S., Ferrero, P., et al. 2012, Astron. Astrophys., 545, A77

Ross, N. P., Shen, Y., Strauss, M. A., et al. 2009, Astrophys. J., 697, 1634

Rothberg, B. & Fischer, J. 2010, Astrophys. J., 712, 318

Rothberg, B. & Joseph, R. D. 2006a, Astron. J., 131, 185

Rothberg, B. & Joseph, R. D. 2006b, Astron. J., 132, 976

Röttgering, H. J. A., Braun, R., Barthel, P. D., et al. 2006, arXiv:astro-ph/0610596

Rozo, E., Wechsler, R. H., Rykoff, E. S., Annis, J. T., Becker, M. R., Frieman, J. A., Hansen, S. M., Hao, J., Johnston, D. E., Koester, B. P., McKay, T. A., Sheldon, E. S., & Weinberg, D. H. 2010, Astrophys. J., 708, 645

Rozo, E., Rykoff, E. S., Evrard, A., et al. 2009, Astrophys. J., 699, 768

Rozo, E., Wu, H.-Y., & Schmidt, F. 2011, Astrophys. J., 735, 118

Rozo, E., & Schmidt, F. 2010, arXiv:1009.5735

Rubin, K. H. R., Weiner, B. J., Koo, D. C., et al. 2010, Astrophys. J., 719, 1503

Rubin, K. H. R., Prochaska, J. X., Koo, D. C., et al. 2013, arXiv:1307.1476

Rudick, C. S., Mihos, J. C., & McBride, C. K. 2011, Astrophys. J., 732, 48

Ryś, A., Falcón-Barroso, J., & van de Ven, G. 2013, Mon. Not. R. Astron. Soc., 428, 2980

Sachs, R. K. & Wolfe, A. M. 1967, Astrophys. J., 147, 73

Sahni, V. and A. A. Starobinsky, *Int. J. Mod. Phys D9*, 373 2000 ; P. J. E. Peebles and B. Ratra *Rev. Mod. Phys.* **75**, 559 2003 ; T. Padmanabhan, *Phys. Rept.* **380**, 235 2003 ; E. J. Copeland, M. Sami and S. Tsujikawa, *Int. J. Mod. Phys. D* **15**, 1753 2006 ; R. R. Caldwell and M. Kamionkowski, *Ann. Rev. Nucl. Part. Sci.* **59**, 397 2009 ;

Sahni, V. & P. Coles, 1995, *Physics Reports* 262 1-135

Sahni, V., B.S. Sathyaprash & S.F. Shandarin, 1998, *ApJ* 495, L5

Sako, M. et al. 2011 *ApJ* 738, 162.

Salvaterra, R., Della Valle, M., Campana, S., et al. 2009, *Nature*, 461, 1258

Sánchez, A. G., Kazin, E. A., Beutler, F., et al. 2013, *Mon. Not. R. Astron. Soc.*

Sánchez, S. F., Kennicutt, R. C., Gil de Paz, A., et al. 2012, *Astron. Astrophys.*, 538, A8

Schönrich, R., & Binney, J. 2009, *Mon. Not. R. Astron. Soc.*, 399, 1145

Sánchez-Blázquez, P., Courty, S., Gibson, B. K., & Brook, C. B. 2009, *Mon. Not. R. Astron. Soc.*, 398, 591

Sandage, A., Binggeli, B., & Tammann, G. A. 1985, *Astron. J.*, 90, 1759

Sansom, A. E., de Castro Milone, A., Vazdekis, A. & Sanchez-Blazquez, P. 2013, *Mon. Not. R. Astron. Soc.*, 435, 952

Santos, J. F. C. J., Alloin, D., Bica, E., & Bonatto, C. 2002, *Extragalactic Star Clusters*, 207, 1

Sari, R., Piran, T., & Narayan, R. 1998, *Astrophys. J. Lett.*, 497, L17

Sawangwit, U., Shanks, T., Abdalla, F. B., et al. 2011, *Mon. Not. R. Astron. Soc.*, 416, 3033

Sawangwit, U., Shanks, T., Cannon, R. D., et al. 2010, *Mon. Not. R. Astron. Soc.*, 402, 2228

Sawangwit, U. et al. 2011, *arXiv:1108.1198*

Schiavon, R. P., Caldwell, N., & Rose, J. A. 2004, *Astron. J.*, 127, 1513

Schiavon, F., Finelli, F., Gruppuso, A., et al., *MNRAS*, 427, 3044 (2012)

Schilizzi, R. T. 2004, *Proc. SPIE*, 5489, 62

Schlafly, E. F., Finkbeiner, D. P., Juric, M., et al., *ApJ*, 756, 158, (2012)

Schlegel, D. J., Blanton, M., Eisenstein, D., et al. 2007, in *Bulletin of the American Astronomical Society*, Vol. 39, American Astronomical Society Meeting Abstracts, 132.29

Schlegel, D., White, M., & Eisenstein, D. 2009, *astro2010: The Astronomy and Astrophysics Decadal Survey*, 2010, 314

Schmidt S. J., Ménard B., Scranton R., Morrison C., McBride C. K., 2013, *Mon. Not. R. Astron. Soc.*, 431, 3307

Schneider, P., King, L., & Erben, T. 2000, *A&A*, 353, 41

Schneider, P., & Seitz, C. 1995, *A&A*, 294, 411

Schoenell, W. 2010, MSc. Thesis, Universidade Federal de Santa Catarina

Schoenell, W., Cid Fernandes, R., Benítez, N., & Vale Asari, N. 2013, *Highlights of Spanish Astrophysics VII*, 405

Schulz A. E., 2010, *Astrophys. J.*, 724, 1305

Schuster, W. J. & Parrao, L. 2001, *RMxAA*, 37, 187

Scoccimarro, R. 2004, *Phys. Rev. D*, 70, 083007

Scranton R., Ménard B., Richards G. T., et al., York D. G., 2005, *Astrophys. J.*, 633, 589

Scudder, J. M., Ellison, S. L., Torrey, P., Patton, D. R., & Mendel, J. T. 2012, *Mon. Not. R. Astron. Soc.*, 426, 549

Sefusatti, E. & Komatsu, E. 2007, *Phys. Rev. D*, 76, 083004

Seljak, U. 2000, *Mon. Not. R. Astron. Soc.*, 318, 203

Seljak, U., A. Makarov, R. Mandelbaum, C. M. Hirata, N. Padmanabhan, P. McDonald, M. R. Blanton, M. Tegmark, N. A. Bahcall, and J. Brinkmann, 2005, *Phys. Rev. D*, 71, 043511

Seljak, U. 2009, *Physical Review Letters*, 102, 021302

Seljak, U. & Zaldarriaga, M. 1996, *Astrophys. J.*, 469, 437

Sellwood, J. A., & Binney, J. J. 2002, *Mon. Not. R. Astron. Soc.*, 336, 785

Seo H.-J., Eckel J., Eisenstein D. J., et al., 2010, *Astrophys. J.*, 720, 1650

Seo, J. J., Eisenstein, D. J. 2003, *Astrophys. J.*, 598, 720

Seo, H.-J. & Eisenstein, D. J. 2007, *Astrophys. J.*, 665, 14

Serber W., Bahcall N., Ménard B., Richards G., 2006, *Astrophys. J.*, 643, 68

Sesar, B., Ivezić, Ž., Grammer, S. H., et al. 2010, *Astrophys. J.*, 708, 717

Shankar, F., Marulli, F., Bernardi, M., et al. 2013, *Mon. Not. R. Astron. Soc.*, 428, 109

Sheldon, E.S., D. E. Johnston, R. Scranton, B. P. Koester, T. A. McKay, H. Oyaizu, C. Cunha, M. Lima, H. Lin, J. A. Frieman, R. H. Wechsler, J. Annis, R. Mandelbaum, N. A. Bahcall, and M. Fukugita, *Astrophys. J.*, 703, 2217

Shen, Y., Strauss, M. A., Oguri, M., et al. 2007, *Astron. J.*, 133, 2222

Shapley, A. E., Steidel, C. C., Pettini, M., & Adelberger, K. L. 2003, *Astrophys. J.*, 588, 65

Shectman, S. A. 1985, *Astrophys. J. S. S.*, 57, 77

Sherwin, B. D., Das, S., Hajian, A., et al. 2012, *Phys. Rev. D*, 86, 083006

Sheth, R. K. & Tormen, G. 1999, *Mon. Not. R. Astron. Soc.*, 308, 119

Sheth, R.K. & A. Diaferio, 2011, arXiv:1105.3378

Silk, J., 1968 *Astrophys. J.* 151, 459

Silverman, J. D., Green, P. J., Barkhouse, W. A., et al. 2008, *Astrophys. J.*, 679, 118

- Skrutskie, M. F., Schneider, S. E., Stiening, R., et al. 1997, *The Impact of Large Scale Near-IR Sky Surveys*, 210, 25
- Smith, J. A., Tucker, D. L., Kent, S., et al. 2002, *Astron. J.*, 123, 2121
- Smith, R. E., Scoccimarro, R., & Sheth, R. K. 2007, *Phys. Rev. D*, 75, 063512
- Smith, M. et al. 2012 . *ApJ*, 755, 61.
- Smoot, G. F., Bennett, C. L., Kogut, A., et al. 1992, *Astrophys. J. Lett.*, 396, L1
- Sobral, D., Best, P. N., Geach, J. E., et al. 2009, *Mon. Not. R. Astron. Soc.*, 398, L68
- Sodré, L., Jr., Boris, N. V., Lima Neto, G. B., et al. 2009, *Revista Mexicana de Astronomia y Astrofisica Conference Series*, 35, 243
- Song, Y.S. and W. J. Percival, *JCAP* **0910**, 004 2009 .
- Sotiriou, T. P. & Faraoni, V. 2010, *Rev. Mod. Phys.*, 82, 451
- SPACE 2008, <http://sci.esa.int/science-e/www/object/index.cfm?fobjectid=42266>
- Spergel, D. N., Verde, L., Peiris, H. V., et al. 2003, *Astrophys. J. S. S.*, 148, 175
- Spergel, D. et al. 2007, *Astrophys. J. S. S.*, 170, 377
- Spinelli, P. F., Seitz, S., Lerchster, M., Brimiouille, F., & Finoguenov, A. 2012, *Mon. Not. R. Astron. Soc.*, 420, 1384
- Springel, V. 2005, *Mon. Not. R. Astron. Soc.*, 364, 1105
- Springel, V., White, S. D. M., Jenkins, A., et al. 2005, *Nature*, 435, 629
- Stabenau, H. F. & Jain, B. 2006, *Phys. Rev. D*, 74, 084007
- Stancliffe Richard J. 2010, *Mon. Not. R. Astron. Soc.*, 403, 505
- Starobinsky, A.A. *JETP Lett.* **68**, 757 1998; B. Boisseau, G. Esposito-Farese, D. Polarski and A. A. Starobinsky, *Phys. Rev. Lett.* **85**, 2236 2000 [gr-qc/00(1066)].
- Starobinsky, A.A. *JETP Lett.* **86**, 157 2007 .
- Stasinska, G. 2002 arXiv:/0207500
- Steidel, C. C., Adelberger, K. L., Shapley, A. E., et al. 2000, *Astrophys. J.*, 532, 170
- Sterken, C. (ed.) 2007, “The Future of Photometric, Spectrophotometric and Polarimetric Standardization,” *ASP Conference Series*, Vol. 364
- Storchi-Bergmann, T., Kinney, A. L., & Challis, P. 1995, *Astrophys. J. S. S.*, 98, 103
- Storchi-Bergmann, T., González Delgado, R. M., Schmitt, H. R., Cid Fernandes, R., & Heckman, T. 2001, *Astrophys. J.*, 559, 147
- Storchi-Bergmann, T., Riffel, R. A., Riffel, R., et al. 2012, *Astrophys. J.*, 755, 87
- Stott, J. P., Collins, C. A., Burke, C., Hamilton-Morris, V., & Smith, G. P. 2011, *Mon. Not. R. Astron. Soc.*, 414, 445

Strader, J., Brodie, J. P., Cenarro, A. J., Beasley, M. A., & Forbes, D. A. 2005, *Astron. J.*, 130, 1315

Strauss, M. A., Yahil, A., Davis, M., Huchra, J. P., & Fisher, K. 1992, *Astrophys. J.*, 397, 395

Strauss M., Willick, J. 1995, *Phys. Rep.* 261, 271

Strubbe, L. E., & Quataert, E. 2009, *Mon. Not. R. Astron. Soc.*, 400, 2070

Suarez-Velásquez I., Kitaura F.-S., Atrio-Barandela F., Mücke J. P., 2013, *Astrophys. J.*, 769, 25

Sunyaev, R. A. & Zeldovich, I. B. 1980, *Mon. Not. R. Astron. Soc.*, 190, 413

Sunyaev, R. A. & Zeldovich, Y. B. 1972, *Comments on Astrophysics and Space Physics*, 4, 173

Sullivan, M. et al. 2006 . *ApJ*, 648, 868.

Sullivan, M. et al. 2010 . *MNRAS*, 406, 782.

Sutherland, W., *Science from the Next Generation Imaging and Spectroscopic Surveys*, 2012

Szapudi, I. & Colombi, S. 1996, *Astrophys. J.*, 470, 131

Tadhunter, C. N., Morganti, R., Robinson, A., et al. 1998, *Mon. Not. R. Astron. Soc.*, 298, 1035

Tagliaferri, G., Antonelli, L. A., Chincarini, G., et al. 2005, *Astron. Astrophys.*, 443, L1

Takahashi, R., Yoshida, N., Takada, M., et al. 2011, *Astrophys. J.*, 726, 7

Tanvir, N. R., Fox, D. B., Levan, A. J., et al. 2009, *Nature*, 461, 1254

Taruya, A., Nishimichi, T., Saito, S., & Hiramatsu, T. 2009, *Phys. Rev. D*, 80, 123503

Tasca, L. A. M., Kneib, J.-P., Iovino, A., et al. 2009, *Astron. Astrophys.*, 503, 379

Tasitsiomi, A., Kravtsov, A. V., Gottlöber, S., & Klypin, A. A. 2004, *ApJ*, 607, 125

Taylor, A. N., Kitching, T. D., Bacon, D. J., & Heavens, A. F. 2007, *MNRAS*, 374, 1377

Taylor, E. N., Franx, M., Glazebrook, K., et al. 2010, *Astrophys. J.*, 720, 723

Tegmark, M. 1997, *Phys. Rev. D*, 55, 5895

Tegmark, M. 1997, *Physical Review Letters*, 79, 3806

Tegmark, M., Hamilton, A. J. S., Strauss, M. A., Vogeley, M. S., & Szalay, A. S. 1998, *Astrophys. J.*, 499, 555

Tegmark M. et al. 2004, *Astrophys. J.*, 606, 702

Tegmark, M., et al. 2006, *Phys. Rev. D*, 74, 123507

Tempel E., Saar E., Liivamägi L. J., Tamm A., Einasto J., Einasto M., Müller V., 2011, *Astron. Astrophys.*, 529, A53

Tempel E., Stoica R. S., Saar E., 2013, *Mon. Not. R. Astron. Soc.*, 428, 1827

Terlevich, R. 1992, in *ASP Conf. Ser. 31, Relationships between Active Galactic Nuclei and Starburst Galaxies*, ed. A. V. Filippenko, 13

The Dark Energy Survey Collaboration. 2005, *ArXiv Astrophysics e-prints*

Thöne, C. C., de Ugarte Postigo, A., Fryer, C. L., et al. 2011, *Nature*, 480, 72

Tinker, J., Kravtsov, A. V., Klypin, A., et al. 2008, *Astrophys. J.*, 688, 709

Toft, S., van Dokkum, P., Franx, M., et al. 2007, *Astrophys. J.*, 671, 285

Toloba, E., Boselli, A., Cenarro, A. J., et al. 2011, *Astron. Astrophys.*, 526, A114

Tomita, K., 2001, *Prog. Theor. Phys.* 106, 929

Tonry, J. L., Stubbs, C. W., Lykke, K. R., et al. 2012, *Astrophys. J.*, 750, 99

Toomre, A. & Toomre, J. 1972, *Astrophys. J.*, 178, 623

Tremonti, C. A., Moustakas, J., & Diamond-Stanic, A. M. 2007, *Astrophys. J. Lett.*, 663, L77

Trujillo, I., Feulner, G., Goranova, Y., et al. 2006, *Mon. Not. R. Astron. Soc.*, 373, L36

Trujillo, I., Conselice, C. J., Bundy, K., et al. 2007, *Mon. Not. R. Astron. Soc.*, 382, 109

Trujillo, I., Cenarro, A. J., de Lorenzo-Cáceres, A., et al. 2009, *Astrophys. J. Lett.*, 692, L118

Trujillo, I., Carrasco, E. R., & Ferré-Mateu, A. 2012, *Astrophys. J.*, 751, 45

Trotta, R., Kunz, M., Mukherjee, P., & Parkinson, D., Bayesian experimental design and model selection forecasting, ed. M. P. Hobson, A. H. Jaffe, A. R. Liddle, P. Mukeherjee, & D. Parkinson, 2010, 99

Tscharnuter W. M. 1987, *A&A*, 188, 55

Tsujikawa, S., R. Gannouji, B. Moraes and D. Polarski, *Phys. Rev. D* **80**, 084044 2009 .

Tsujikawa, S., *Class.Quant.Grav.* 30 2013 214003

Tversky A., and D. Kahneman, *Science*, vol. 185, no. 4157, 1124 (1974)

Umetsu, K. 2013, *ApJ*, 769, 13

Umetsu, K., & Broadhurst, T. 2008, *ApJ*, 684, 177

Umetsu, K., Broadhurst, T., Zitrin, A., Medezinski, E., & Hsu, L. 2011, *ApJ*, 729, 127

Umetsu, K., Medezinski, E., Nonino, M., et al. 2012, *ApJ*, 755, 56

Vale A., Ostriker J. P., 2004, *Mon. Not. R. Astron. Soc.*, 353, 189

Van Breukelen, C., & Clewley, L. 2009, *Mon. Not. R. Astron. Soc.*, 395, 1845

Van den Hoek, L. B.; Groenewegen, M. A. T. 1997 *AAS*, 123, 305

Van Dokkum, P. G. 2001, *PASP*, 113, 1420

Van Engelen, A., Keisler, R., Zahn, O., et al. 2012, *Astrophys. J.*, 756, 142

Vazdekis, A., & Arimoto, N. 1999, *Astrophys. J.*, 525, 144

Vazdekis, A., Sánchez-Blázquez, P., Falcón-Barroso, J., et al. 2010, *Mon. Not. R. Astron. Soc.*, 404, 1639

Vazdekis, A., Ricciardelli, E., Cenarro, A. J., et al. 2012, *Mon. Not. R. Astron. Soc.*, 424, 157

Vielva, P., Martínez-González, E., & Tucci, M. 2006, *Mon. Not. R. Astron. Soc.*, 365, 891

Viironen, K.; Greimel, R.; Corradi, R. L. M.; Mampaso, A.; Rodriguez, M.; Sabin, L.; Delgado-Inglada, G.; Drew, J. E.; Solares, E. A.; and 5 coauthors

Vikhlinin, A., Kravtsov, A. V., Burenin, R. A., Ebeling, H., Forman, W. R., Hornstrup, A., Jones, C., Murray, S. S., Nagai, D., Quintana, H., & Voevodkin, A. 2009, *Astrophys. J.*, 692, 1060

Vivas, A. K., Zinn, R., Abad, C., et al. 2004, *Astron. J.*, 127, 1158

Venemans, B. P., Röttgering, H. J. A., Miley, G. K., et al. 2007, *Astron. Astrophys.*, 461, 823

Verde, L., Wang, L., Heavens, A. F., & Kamionkowski, M. 2000, *Mon. Not. R. Astron. Soc.*, 313, 141

Vogeley, M. S. & Szalay, A. S. 1996, *Astrophys. J.*, 465, 34

Volonteri, M., & Ciotti, L. 2013, *Astrophys. J.*, 768, 29

von der Linden, A., Best, P. N., Kauffmann, G., & White, S. D. M. 2007, *Mon. Not. R. Astron. Soc.*, 379, 867

Vulcani, B., Poggianti, B. M., Aragón-Salamanca, A., et al. 2011, *Mon. Not. R. Astron. Soc.*, 412, 246

Vulcani, B., Poggianti, B. M., Fasano, G., et al. 2012, *Mon. Not. R. Astron. Soc.*, 420, 1481

Vulcani, B., Poggianti, B. M., Oemler, A., et al. 2013, *Astron. Astrophys.*, 550, A58

Waddington, I., Dunlop, J. S., Peacock, J. A., & Windhorst, R. A. 2001, *Mon. Not. R. Astron. Soc.*, 328, 882

Walcher, J., Groves, B., Budavári, T., & Dale, D. 2011, *MNRAS*, 331, 1

Walker, X. 1987, *NOAO Newsletter*, 10, 16

Wang, B., J. Zang, C. -Y. Lin, E. Abdalla and S. Micheletti, *Nucl. Phys. B* 778, 69 2007

Wang, B., Yun-gui Gong, E. Abdalla *Phys. Lett.* **B624** 2005 141-146;

Wang, B., Chi-Yong Lin, E. Abdalla *Phys. Lett.* **B637** 2006 357-361.

Wang H., Mo H. J., Yang X., van den Bosch F. C., 2013, *Astrophys. J.*, 772, 63

Wang, L. & Steinhardt, P. J. 1998, *Astrophys. J.*, 508, 483

Wang L., Cooray A., Farrah D., et al., 2011, *Mon. Not. R. Astron. Soc.*, 414, 596

Wang, S., Khoury, J., Haiman, Z., & May, M. 2004, *Phys. Rev. D*, 70, 123008

Wang, Y., Percival, W., Cimatti, A., et al. 2010, *Mon. Not. R. Astron. Soc.*, 409, 737

Wang, Y., 2006, *Astrophys. J.*, 647, 1

Watson W. A., Iliev I. T., Diego J. M., Gottlöber S., Knebe A., Martínez-González E., Yepes G., 2013, *ArXiv e-prints*

Watterich, C. *Phys. Rev. D* 65 (2002) 123512

Weinberg, D.H., M. J. Mortonson, D. J. Eisenstein, C. Pirata, A. G. Riess, and E. Rozo, *Phys. Rep.*, 530, 87

Weinmann, S. M., Lisker, T., Guo, Q., Meyer, H. T., & Janz, J. 2011, *Mon. Not. R. Astron. Soc.*, 416, 1197

White M., Tinker J. L., McBride C. K., 2013, *arXiv:1309.5532*

White S. D. M., Davis M., Efstathiou G., Frenk C. S., 1987, *Nature*, 330, 451

Williams, R. J., Quadri, R. F., & Franx, M. 2011, *Astrophys. J. Lett.*, 738, L25

Willott, C. J., Rawlings, S., Blundell, K. M., Lacy, M., & Eales, S. A. 2001, *Mon. Not. R. Astron. Soc.*, 322, 536

Willott, C. J., Delorme, P., Reylé, C., et al. 2010, *Astron. J.*, 139, 906

Wilson, G., et al. 2008, *Infrared Diagnostics of Galaxy Evolution*, 381, 210

- WiggleZ 2008, <http://astronomy.swin.edu.au/karl/Karl-Home/Home.html>
- Wisotzki, L., Koehler, T., Groote, D., & Reimers, D. 1996, *MNRAS*, 115, 227
- Wolf, C., et al. 2001, *Astron. Astrophys.*, 365, 681
- Wolf, C., Meisenheimer, K., Rix, H.-W., Borch, A., Dye, S., & Kleinheinrich, M. 2003, *Astron. Astrophys.*, 401, 73
- Wolf, C., Hildebrandt, H., Taylor, E. N., & Meisenheimer, K. 2008, *Astron. Astrophys.*, 492, 933
- Wolfe, A. M., Gawiser, E., & Prochaska, J. X. 2005, *Annu. Rev. Astron. Astrophys.*, 43, 861
- Wolz, L., Kilbinger, M., Weller, J., & Giannantonio, T. 2012, *JCAP*, 9, 9
- Wood-Vasey, W. M. et al. 2007, *Astrophys. J.*, 666, 694
- Worthey, G., Faber, S. M., Gonzalez, J. J., & Burstein, D. 1994, *Astrophys. J. S. S.*, 94, 687
- Wright, E. L., Eisenhardt, P. R. M., Mainzer, A. K., et al. 2010, *Astron. J.*, 140, 1868
- Wucknitz, O. 2002, *Mon. Not. R. Astron. Soc.*, 332, 951
- Xavier, H. S. et al. 2013, *MNRAS*, 434, 1443.
- Xu, X., Padmanabhan, N., Eisenstein, D. J., Mehta, K. T., & Cuesta, A. J. 2012, *Mon. Not. R. Astron. Soc.*, 427, 2146
- Yahil, A., Sandage, A., & Tammann, G. A. 1980, *Astrophys. J.*, 242, 448
- Yang, Y., Zabludoff, A., Tremonti, C., Eisenstein, D., & Davé, R. 2009, *Astrophys. J.*, 693, 1579
- Yanny, B., Rockosi, C., Newberg, H. J., et al. 2009, *Astron. J.*, 137, 4377
- Yin, J.; Magrini, L.; Matteucci, F.; Lanfranchi, G. A.; Gonçalves, D. R.; Costa, R. D. D. 2010 *Astron. Astrophys.*, 520, 55
- Yoachim, P., & Dalcanton, J. J. 2008, *Astrophys. J.*, 683, 707
- Yoachim, P., Roškar, R., & Debattista, V. P. 2012, *Astrophys. J.*, 752, 97
- Yoo, J. and U. Seljak, 2012, *Phys. Rev. D*, 86(8), 083504
- York, D. G., Adelman, J., Anderson, Jr., J. E., et al. 2000, *Astron. J.*, 120, 1579
- York, D. G., Adelman, J., Anderson, J. E., Jr., et al. 2000, *Astron. J.*, 120, 1579
- Yuma, S., Ouchi, M., Drake, A. B., et al. 2013, *Astrophys. J.*, 779, 53
- Zandivarez, A., Díaz-Gimenez, E., Mendes de Oliveira, C., Ascaso, B., Benítez, N., Dupke, R., Sodr e Jr., L., Irwin, J. 2014, *Astron. Astrophys.*, 561, A71
- Zehavi I., Zheng Z., Weinberg D. H., Blanton M. R., Bahcall N. A., Berlind A. A., Brinkmann J., Frieman J. A., Gunn J. E., Lupton R. H., Nichol R. C., Percival W. J., Schneider D. P., Skibba R. A., Strauss M. A., Tegmark M., York D. G., 2011, *Astrophys. J.*, 736, 59
- Zimdahl W., Borges H. A., Carneiro S., Fabris J. C., Hipolito-Ricaldi W. S., 2011, *JCAP*, 1104, 28
- Zimdahl, W. and Pavon, D., *Phys. Lett. B* 521 2001 133-138;

- Zirm, A. W., Dey, A., Dickinson, M., & Norman, C. J. 2009, *Astrophys. J. Lett.*, 694, L31
- Zitrin, A., Broadhurst, T., Bartelmann, M., et al. 2012a, *Mon. Not. R. Astron. Soc.*, 423, 2308
- Zitrin, A., Broadhurst, T., Rephaeli, Y., & Sadeh, S. 2009a, *Astrophys. J. Lett.*, 707, L102
- Zitrin, A., Menanteau, F., Hughes, J. P., et al. 2013a, *Astrophys. J. Lett.*, 770, L15
- Zitrin, A., Broadhurst, T., Umetsu, K., et al. 2009b, *Mon. Not. R. Astron. Soc.*, 396, 1985
- Zitrin, A., Rosati, P., Nonino, M., et al. 2012b, *Astrophys. J.*, 749, 97
- Zitrin, A., Meneghetti, M., Umetsu, K., et al. 2013b, *Astrophys. J. Lett.*, 762, L30
- Zlosnik, T.G, P. G. Ferreira and G. D. Starkman, 2007, *Phys. Rev. D* **75** 044017
- Zuntz, J., T. Kacprzak, L. Voigt, M. Hirsch, B. Rowe, and S. Bridle, 2013, *Mon. Not. R. Astron. Soc.*, 434, 1604